Satellite Geophysical Investigation of the Moon

by

Laramie V. Potts

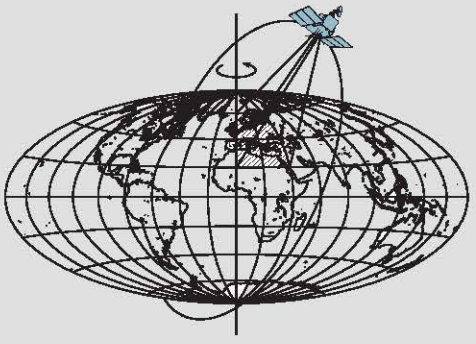

Report No. 458

Geodetic Science and Surveying
Department of Civil and Environmental Engineering and Geodetic Science
The Ohio State University
Columbus, Ohio 43210-1275

December 2000

ABSTRACT

Lunar mass variations for the region $\pm 64^{o}$ latitude related to composition, structure, isostatic and tectonic development of the crust, mantle, and core were developed using gravity and topography from Lunar Prospector, Clementine, and earlier satellite observations. Computed terrain gravity effects were spectrally correlated with the free-air anomalies to differentiate the terrain-correlated and -decorrelated free-air components. Annihilating terrain gravity effects, obtained by subtracting the terrain-correlated anomalies from the terrain gravity effects, were used to estimate the lunar Moho and crustal thicknesses by least squares inversion assuming compensation by crustal thickness variations. Inversion of the terrain-correlated anomalies obtained a radial adjustment model of the Moho that equilibrates the lunar topography. Terrain-decorrelated anomalies were differentiated into crustal and subcrustal components based on their correlation spectrum with the free-air anomalies. Inversion of the terrain-decorrelated crustal maxima over central basins predicted mare fill thicknesses up to a few kilometers. Inversion of the subcrustal components inferred boundary undulations for the core-mantle, asthenosphere-lithosphere, and middle-upper mantle during bombardment time.

Nearly all major nearside basins exhibit mascon gravity anomalies reflecting mass concentrations from superisostatic mantle plugs plus mare fill, while farside basins mostly involve maslite gravity anomalies from mass deficiencies due to subisostatic mantle plugs with marginal or no mare fill. The preponderance of farside maslites suggests a weaker nearside lithosphere due to higher thermal gradients from enhanced abundances of radioactive elements in the nearside mantle and crust than the farside. Comparing crustal thicknesses with transient cavity diameters suggests a critical crustal thickness of about 30 km presumably differentiated the development of superisostatic and subisostatic mantle plugs on the farside. Inferred subcrustal boundary undulations tend to support mantle convection on the nearside involving diapiric rise of magma, whereas viscous entrainment on the farside inhibited basalt flooding of basins. The elevated core-mantle boundary beneath the Procellarum-Imbrium basins is consistent with uplifting effects of the Imbrium impact involved with the "Great Lunar Hotspot". Comparison of the gravity and topography spectra of the terrestrial planets suggests the Moon has the lowest temperature gradient and hydrostatic equilibrium.

ACKNOWLEDGMENTS

I am grateful to my advisors Drs. Ralph von Frese and Christopher Jekeli for their brilliant tutelage, constructive discussions as well as professional guidance that enabled me to accomplish this research. Their enthusiastic guidance motivated me to further stretch the scientific envelope of selenodesy and lunar geophysics.

It all began with the enthusiasm and initiative of Dr. John Bossler who wanted lunar missions to accurately map the farside of the moon using space geodetic techniques. But it is the SELENE mission, scheduled for launch in 2003, that will finally realize his dream. However, to him I owe special thanks for securing funding that enabled a first-ever comprehensive investigation of the geophysical properties of the Moon.

My gratitude and appreciation also go to Drs. Merry and Shum for their expert advice and comments during my research and the reviews of this manuscript. Special thanks are also due to Dr. Jens Munk, Hyung Rae Kim, Timothy Leftwich, and LeeAnn Munk for helpful discussions and to Brent Curtiss for computer assistance.

This work has been partially supported by grants from NASA Goddard Space Flight Center (PO S-97647-Z), Center for Mapping at The Ohio State University, and the Ohio Supercomputer Center.

Contents

List of Figures

List of Tables

1 Introduction

Analyses of gravity and topography provide some of the few means available for probing the internal properties of a planet. Lunar satellite gravity observations in combination with radar altimetry-derived topographic data are used here to obtain new insights on the subsurface properties of the Moon. In particular, the focus of this research is geophysical modeling of the crustal and subcrustal properties of the Moon using spectrally correlated free-air and terrain gravity effects.

Lunar data sets considered in this study include the LIDAR-mapped terrain model GLTM-2 from NASA's Clementine mission (Nozette et al., 1996; Smith et al., 1997) and the spherical harmonic gravity field model LP75G derived from the Lunar Prospector (LP) mission (Konopliv et al., 1998). This research is timely because the recent Clementine and Lunar Propector satellite mapping missions have significantly improved lunar gravity and topography models.

1.1 Background and Motivation

Prior to the first manned explorations and sample returns, greatly simplified views were held about the bulk composition of the Moon and its internal structure. For example, astronomers in the seventeenth century observing the Moon through telescopes concluded that it had seas and dry land like the Earth. Since then the dark areas on the Moon have been called seas or maria (singular mare) and the light areas called continents or terrae (singular terra). The first maps of the Moon by Riccioli in 1651 also featured lakes (lacus), marshes (palus) and bays (sinus). It was held that the Moon influenced the Earth's weather, which would be fine when the Moon was waxing and cloudy, rainy and stormy when the Moon was waning. Riccioli may have been mindful of this idea when inventing names for the maria such as the Sea of Tranquillity (Mare Tanquilitatis), the Sea of Serenity (Mare Serenitatis) or the Sea of Storms (Oceanus Procellarum), etc. (Rukl, 1976).

Initial studies of the lunar craters suggested two basic propositions for their origin; namely that the craters had developed from a) endogenous forces, such as volcanism, lunar tectonics, and other subsurface processes, and b) exogenous causes, such as bolloidal impacts (Spudis, 1993). It was also suggested that the lunar surface evolved by both external and internal processes (Cattermole, 1996). Hence, before the Apollo missions, selenologists were faced with two fundamentally contrasting views. Volcanists, for example maintained that at least 95% of the lunar landscape was the result of endogenous activity with the remaining 5% being possibly caused by the impact of the meteorites or volcanically ejected lunar rocks. Exogenous purporters, on the other hand, held that the surface formations resulted predominantly from the impact of meteorites and related secondary impacts of the ejected lunar material.

With the Apollo era, analyses of a variety of *in situ* measurements provided new fundamental insights on the compositional and structural attributes of the Moon. As a result, the majority of selenologists now hold that most of the craters are due to meteorite impact and their secondary effects (Rukl, 1976). Subsequently, the existences of a lunar core and mantle have also been subjected to intense investigation. In particular, the sizes and chemical compositions of these features are fundamental constraints for understanding lunar differentiation and evolution. Additional studies of lunar seismic,

electromagnetic sounding, laser ranging and paleomagnetic data tested the hypothesis that the Moon accreted as a cold body (Runcorn, 1996; Stevenson, 1980). Inversion of limited seismic data premitted a "first look" into the internal structure of the Moon (Nakamura et al., 1979; Nakamura et al., 1982; Nakamura, 1983). Velocities were interpreted for radial density models of the Moon's crust and upper mantle (e.g., Taylor, 1982; Hood, 1986; Hood and Jones, 1987) with constraints from other geophysical and geochemical observations. However, lunar seismic velocity models and/or interpretations are based on very limited seismic observations and hence do not strongly constrain the compositional and density properties of the middle and lower mantle. The lunar moments of inertia also have yielded little definitive evidence for the existence of a metallic core because of their observational limits.

Most recently, improved models for metal-silicate separation have been developed that may provide further insight on the differentiation of the terrestrial planets (e.g., Agee, 1998; Alley and Parmentier, 1998). Major new lunar data bases from analyses of its surface chemistry and thermal evolution (Konrad and Spohn, 1997), as well as its gravitational figure and moments of inertia (Bills, 1995), have become available to help revise the radial density structure of the Moon. In addition, the lunar gravity field has been significantly updated by the satellite observations from the Clementine (Nozette et al., 1996) and Lunar Prospector missions (Konopliv et al., 1998). These data bases provide mutual constraints on the ill-posed inverse problem of evaluating the internal properties of the Moon.

1.2 Objectives

This study seeks to 1) develop a model of internal mass variations that comprehensively accounts for the lunar free-air gravity anomaly field and gravity effects of the terrain, and 2) investigate the significance of this model for new insight on the lunar evolution. In particular, near-global models are developed for the lunar Moho and related crustal thickness variations, incipient radial adjustments of the Moho that possibly may equilibriate the lunar lithosphere, and subcrustal mass variations related possibly to undulations of the core-mantle boundary, and the surfaces of the lower and middle mantle. In addition, the attributes of the selenoid are investigated for insights on basin mare basalt flooding and evolution of the lunar tidal bulge.

A near-global crustal thickness model is developed for insight on lunar lithospheric evolution during bombardment time. Crustal properties are inferred for the giant Procelluram and South Pole-Aitken basins, as well as for 27 major lunar basins for insight on the nearside and farside dichotomies in crustal rheologies. Comparing the crustal properties of the major basins reveals that their central underlying masses may reflect both positive (i.e., mascon) and negative (i.e., maslite) density contrasts that points to a more comprehensive gravimetric characterization of the lunar basins.

Incipient radial adjustments of the Moho (RAM) that nullify the terrain-correlated free-air anomalies are developed for inferrences on the crustal stress field components due possibly to bollide impacts. The relationships between photogeologically determined basin rings and the RAM data are investigated for further insights on the poorly understood lithospheric processes of basin ring formation and evolution. The RAM data are also analyzed for additional insights on the lithospheric dichotomy

in mechanical properties between the near and far sides using the dimensional relationship between the transient cavity diameter and lithospheric viscosity (Melosh, 1982).

Undulations of the core, lower, and middle mantle surfaces are developed for insight on possible internal mass distributions from surface basin-size bollide impacts. Inferrences on the development of the "Great Lunar Hotspot" may also be reflected by core-mantle boundary estimates. Subcrustal lateral mass transport may also be inferred from correlations between impact basin centers and undulations of the lithopshere-asthenosphere boundary. Additionally, the topography of the lithopshere-asthenosphere boundary may provide constraints on the composition of the mare basalts. In particular, magmas presumably were extruded vertically through conduits that tapped subsurface reservoirs. However, the depths of these conduits in turn may have been constrained by tensional and compressive forces in the near and far sides, respectively (Runcorn, 1974).

Inferrences on the nonhydrostatic shape of the Moon are suggested from correlations between selenoid heights and subcrustal undulation models of mass variations. In particular, the core-mantle and lithopshere-asthenosphere boundaries are strongly displaced towards the Earth. Earth's influence on the internal mass distribution during the early evolution of the Moon is also apparent in the RAM data. The hypothesis that the mare floors describe a lunar equipotential surface is investigated. The secular Love number k_s and the topography and gravity spectra of the 4 inner terrestrial planets are compared.

Undulations of a density interface boundary may be obtained from inversion of gravity anomaly data. For this study, least squares inversion procedures are developed based on modeling the gravity effects of an array of spherical prisms by Gauss-Legendre quadrature (GLQ) integration. Several undulation models are produced by inversion of the anomaly data that are derived from the wavenumber correlation analysis (WCA) of the free-air and terrain gravity effects. In particular, a Moho undulation model is developed to produce a near-global model of crustal thickness, as well as topographic undulation models at the density discontinuities between the middle and upper mantle, and at the core-mantle boundary.

1.3 Methodology

The topography of the Moon is quite rugged relative to that of the Earth (von Frese et al., 1997b). Hence, terrain gravity modeling has a much greater impact on the use of gravity observations for subsurface studies. However, lunar terrain gravity effects (*TGE*) can be accurately and efficiently modelled in spherical coordinates by GLQ integration (von Frese et al., 1981). Using this approach, crustal and subcrustal mass models are developed for the Moon that satisfy constraints imposed by independent lunar gravity and topographic observations.

Free-air gravity anomalies (*FAGA*) are evaluated from the Lunar Prospector spherical harmonic model (LP75G) at a satellite altitude of 100 km above the mean radius of the Moon. The terrain gravity effects (*TGE*) are also computed in lunar spherical coordinates at the same altitude for the Goddard model of lunar topography (GMLT-2) that incorporates the Clementine LIDAR observations. Details concerning these calculations and the spherical harmonic gravity and terrain models are found in Appendices A and B, respectively.

The correlation spectrum (von Frese et al., 1997a) is used to identify wavenumber components in *FAGA* and *TGE* that show high positive and negative correlations. Inversely transforming the wavenumber components of *FAGA* yields estimates of the terrain-correlated free-air gravity anomalies (*TCFAGA*) that may reflect isostatic mass imbalances of the lunar crust (von Frese et al., 1997b). Subtracting *TCFAGA* from *FAGA* and *TGE*, respectively, estimates the terrain-decorrelated free-air gravity anomalies (*TDFAGA*) and compensated terrain gravity effects (*CTGE*) that may reflect non-isostatic mass variations of the lunar subsurface (von Frese et al., 1997b). Accordingly, the *CTGE* may be interpreted by least squares inversion for mantle topography and crustal thickness variations assuming an appropriate crustal compensation model. In this context, the *TCFAGA* also can provide insight on possible equilibriating adjustments of the mantle topography that may influence the residual stress field of the crust, and hence its response to faulting (Golombek, 1985) and ring tectonism (Solomon and Head, 1980; Melosh, 1989; Spudis, 1993). In particular, the lunar Moho (and crustal thicknesses) may be studied for the internal effects to bolloidal impacts and the nature of mascons (Muller and Sjogren, 1968). Moreover, the notion that mascon basins were not supporting stresses before mare flooding is complicated by the gravity results of the Lunar Prospector mission (Konopliv et al., 1998). This new gravity model revealed new mascons for the nearside Humboltianum, Mendel-Rydberg, and Schiller-Zucchius, and the farside Hertzprung, Coulomb-Sarton, Freundlich-Sharonov, and Moscovience impact basins. However, visible evidence of mare fill is lacking for the Schiller-Zucchius, Coulomb-Sarton, and Freundlich-Sharonov basins. Accordingly, the LP75G model is best suited for investigating the evolution of lunar mass variations.

The processes of basin ring formation and evolution are investigated from the incipient radial adjustments of the Moho that nullify *TCFAGA*. These adjustments may reflect Moho subsidence and uplift that are required to equilibriate topography fully by crustal thickness variations. The RAM data may also provide clues regarding transient cavity diameters and basin excavation depths. In particular, the relationship between crustal thickness and transient cavity diameters may reflect insights on the dichotomy in lithospheric rheology between the lunar near and far sides. Also, the estimates on excavation depths may provide constraints for interpreting the crustal settings of returned lunar samples.

Studies of local lunar features such as Mare Orientale (von Frese et al., 1997b) suggested that the *FAGA* may be related mostly to large scale features of the lower crust and upper mantle. However, an analysis of the correlation spectrum between the more global *TDFAGA* and *FAGA* has revealed striking associations over several wavelength bands that may also reflect deeper systematic lunar mass differentiations within the mantle and at the core-mantle boundary (von Frese et al., 1998). Spectral correlation filtering between *FAGA* and *TDFAGA* is used to estimate the *TDFAGA* components for modeling these deeper density interfaces by least squares inversion. Effective modeling of these deeper structures can facilitate interpreting lunar thermal history (Konrad and Spohn, 1997), mantle dynamics and other sources of subcrustal density variations (Zuber et al., 1994).

After removing the possible effects of these subcrustal density interfaces, the residual *TDFAGA* tend to be dominated by high-frequency anomalies that may include the effects of crustal density variations, as well as data measurement and processing errors. These inferred crustal elements (*CTDFAGA*) of *TDFAGA* are perhaps the most appropriate components of the *FAGA* to relate to remote sensing imagery and other surface constraints in crustal analysis.

The selenoid and hydrostatic components in the lunar figure parameters are computed and the results are investigated for inferences on effects of mass distribution on shape distortions.

The relationship between surface elevations and selenoid heights at basin centers is investigated regarding the hypothesis that nearside mare floors constitute an lunar equipotential surface. Nearside basins tend to show evidence for mare basalt flooding whereas farside basins are mostly characterized by an apparent lack of mare fill. For this study, the selenoid is computed from Bruns' formula (Heiskanen and Moritz, 1967) and the disturbing potential evaluated from the spherical harmonic model (LP75G). The secular Love number k_s and the topography and gravity spectra of the 4 inner terrestrial planets are also compared for insight on planetary evolution under diverse geologic processes.

1.4 Scope and Organization

This research is focussed on imaging and analyzing the subsurface density variations of the Moon for the near-global region between $\pm\ 64^0$ latitude that had been mapped by the Clementine (Nozette et al., 1996) and Lunar Prospector (Binder, 1998) satellite missions. The study region, includes most of the major lunar nearside and farside basins.

In Chapter 2, a crustal thickness model is developed and analyzed. The major basins are compared for their rheological and lithological properties to gain insight on lunar nearside and farside dichotomies in crustal thickness, mechanical and thermal properties. The definition for a mascon is extended to characterize other possible sources of central basin mass anomalies.

In Chapter 3, the evolution of lunar basin rings is investigated from the spectrally correlated gravity and topographic data. Models of incipient crustal adjustment are investigated to infer basin ring diameters and spacing, and basin excavation depths.

In Chapter 4, the spectral correlation analysis of the gravity and topographic data is extended to develop possible scenarios for lunar subcrustal mass differentiation. Models of density variations across the core-mantle, lower and middle mantle boundaries are inferred to investigate the possible effects of bollide impacts on the redistribution of mass in the lunar interior.

In Chapter 5, the lunar selenoid was computed from spherical harmonic coefficients of the LP75G model (Konopliv et al., 1998) and the state of hydrostatic equilibrium was inferred from the estimates of the secular Love number k_s. The second zonal harmonic in the gravitational potential of the planets was computed from the geometrical flattening of the reference ellipsoid and rotational parameter q. Correlations of the selenoid with topographic and subsurface undulation models as well as point data, centered on the basins, are computed for inference on the shape distortions of the Moon.

Coefficient models for the Earth, Venus, and Mars were obtained from analyses of satellite tracking data. Hence, variances, correlations of gravity and topography, spectral slopes, and the secular Love number k_s of the Earth, Venus, Mars and the Moon are compared.

Chapter 6 highlights the major conclusions and recommendations for future investigations of this study.

Several Appendices are also provided to supplement these chapters. In particular, Appendix A includes definitions for the selenodetic parameters used in this study. Appendix B describes the attributes of the satellite-derived gravity and topography data models used in this research, as well as the calculations of *TGE*. Appendix C reviews the geologic history and major surface features of the Moon.

A least squares inversion procedure based on modeling spherical prisms using GLQ integration is developed in Appendix D. This approach is tested on the $64^0 \times 64^0$ region centered on the Mare Orientale basin. Appendix E presents crustal cross-sections and gravity profiles for the 27 major basins considered in this study. Regional maps of crustal thickness and incipient radial Moho adjustments over $64^0 \times 64^0$ regions centered on each of these basins are also provided. Appendix G describes geochemical and geophysical constraints used for developing the standard lunar model of internal radial density distributions. A glossary of the technical terms and acronyms used in this study is also provided in appendix H.

2 Lunar Crustal Modeling from Spectrally Correlated Free-air and Terrain Gravity Data

2.1 Introduction

The topography of the Moon is large when scaled to that of the Earth, so that the use of simple Bouguer gravity anomalies which ignore lunar terrain gravity effects may be seriously limited for subsurface investigations, particularly in regions of rugged topography. Accurate topographic gravity modeling that removes these effects can greatly enhance the utility of satellite gravity observations for developing new details on subsurface mass variations related to the composition, structure, isostasy, and tectonic evolution of the lunar crust. In general, the role of the simple Bouguer anomaly in modern lunar investigations is rather limited, because the gravity effects of the terrain can be readily calculated in spherical coordinates anywhere on the topographic surface or above it by Gauss-Legendre quadrature (GLQ) integration (von Frese et al., 1981).

Another innovation for modern subsurface studies of the Moon is the use of correlation filtering (von Frese et al., 1997a; 1997b) to break out the free-air gravity anomalies (*FAGA*) on the basis of their correlations with the terrain gravity effects (*TGE*). In particular, *FAGA* may be separated into terrain-correlated (*TCFAGA*) and terrain-decorrelated (*TDFAGA*) components for effective constraints on modeling differential crustal and subcrustal mass variations.

Early efforts to map the regional variations of lunar crustal thickness dealt with Apollo mission gravity and topography data (e.g., Bills and Ferrari, 1977; Thurber and Solomon, 1978; Bratt et al., 1985) that were limited in accuracy, resolution and spatial coverage. These studies also were limited by incorporating excessively large thickness estimates for the mare basalt fill (Williams and Zuber, 1998). However, the 1994 Clementine mission (Nozette et al., 1996) provided greatly enhanced, near-global topography coverage (Smith et al., 1997) and improved regional gravity observations (Lemoine et al., 1997) that resulted in improved lunar crustal thickness estimates (e.g., Zuber et al., 1994; Neumann et al., 1996; von Frese et al., 1997b; Wieczorek and Phillips, 1998). Most recently, a greatly enhanced lunar gravity model was also obtained from the Lunar Prospector mission (Konopliv et al., 1998). In this chapter, the combined near-global topography and gravity models are investigated for new insight on the crustal structure of the Moon. Additional details of these data models are given in Appendix B.

To investigate lunar subsurface density variations, least squares inversion procedures were developed based on modeling the gravity effects of spherical crustal prisms by GLQ integration (see Appendix D). In particular, the GLQ inversion procedures were applied to estimate the lunar Moho and related crustal thickness variations between $\pm 64^o$ latitude. For additional insight on the development of the lunar lithosphere, the contrasting crustal attributes were also investigated between the major regional basins with diameters of about 300 km and larger of the nearside in Figure 1(A) (i.e., Balmer-Kapetyn, Crisium, Cruger, Grimaldi, Humboltianum, Humorum, Imbrium, Mutus-Vlacq, Nectaris, Procellarum, Schiller-Zuchius, Serenitatis, and Smythii) and the farside in Figure 1 (B) (i.e., Apollo, Australe, Birkhoff, Coulomb-Sarton, Freundlich-Sharonov, Hertzprung,

Ingenii, Keeler-Heaviside, Korolev, Lorenz, Mendeleev, Mendel-Rydberg, Moscovience, Orientale, South Pole-Aitken, and Tsiolkovskiy-Stark).

Section 2 considers current methodologies and basic assumptions for modeling crustal thickness variations of the Moon. Section 3 describes the use of spectral correlation theory to separate correlative and noncorrelative features in the free-air and terrain gravity anomaly data. Models of the lunar Moho and crustal thickness variations are obtained. Incipient radial adjustments of the Moho that nullify the terrain-correlated free-air anomalies are also inferred for constraints on the stress field of the lunar crust. In addition, terrain-decorrelated free-air anomalies are estimated that may reflect nonisostatic crustal and subcrustal mass variations. Section 4 considers the significance of these results for investigating nearside and farside dichotomies in crustal rheologies, and the crustal properties of the giant Procelluram and South Pole-Aitken basins. Crustal models for 27 of the major basins are also developed that include estimates of their mare fill thicknesses. Section 5 develops a new, more comprehensive gravimetric characterization of the major basins where the central underlying masses may reflect both positive (i.e., mascon) and negative (i.e., maslite) density contrasts. The major results and conclusions are summarized in section 6.

2.2 Gravity-Based Crustal Modeling Reviewed

Muller and Sjogren (1968) processed pertubations in the Lunar Orbiter tracking data for free-air gravity anomaly (*FAGA*) estimates. Prominent positive gravity anomalies were discovered over the nearside basins of the Moon that were taken to reflect crustal mass excesses or mass concentrations (mascons) in the mare regions. Remnants of colliding iron asteroids of the order of tens of kilometers in diameter were inferred for the sources of the mascons. In particular, a 100-km diameter nickel-iron object buried at a depth of 50 km was estimated for the Imbrium mascon. However, it was noted that such an object would produce stresses exceeding the strength of granite and therefore it would sink to the center of the Moon. Hence, to maintain the object in the outer part of the Moon, isostatic compensation of the lunar topography was inferred, whereby the crust could be floated on a mechanically weak interior in general accordance with Archimedes' principle (O'Keefe, 1968).

The sources of the nearside mascons were attributed to lava filled maria generated from the deeper interior by pressure-release melting that subsequently flooded the crater (Stipe, 1968). By this model, the mare fill may be represented by a thin circular disk of more massive rock at the lunar surface (Conel and Holstrom, 1968). For Serenitatis, a mare fill thickness of 8 km was estimated using a density contrast of 0.5 g/cm^3 between basalt and the lunar crust.

Another interpretation for the mascons suggested that mass excess may also involve a mantle plug that formed after the deep crater was produced by meteorite impact (Wise and Yates, 1970). For the Mare Orientale basin, analysis of radio-tracking data from four Apollo 15 subsatellite orbits and another orbit from Lunar Orbiter V found that the basin is characterized by a broad negative gravity anomaly with a sharp central, relatively positive peak or "mascon-type" anomaly (Sjogren and Smith, 1976). These gravity anomalies were found to be modeled best with an upper crustal body of enhanced mass that is underlain by an elevated Moho according to the Bowin et al. (1975)

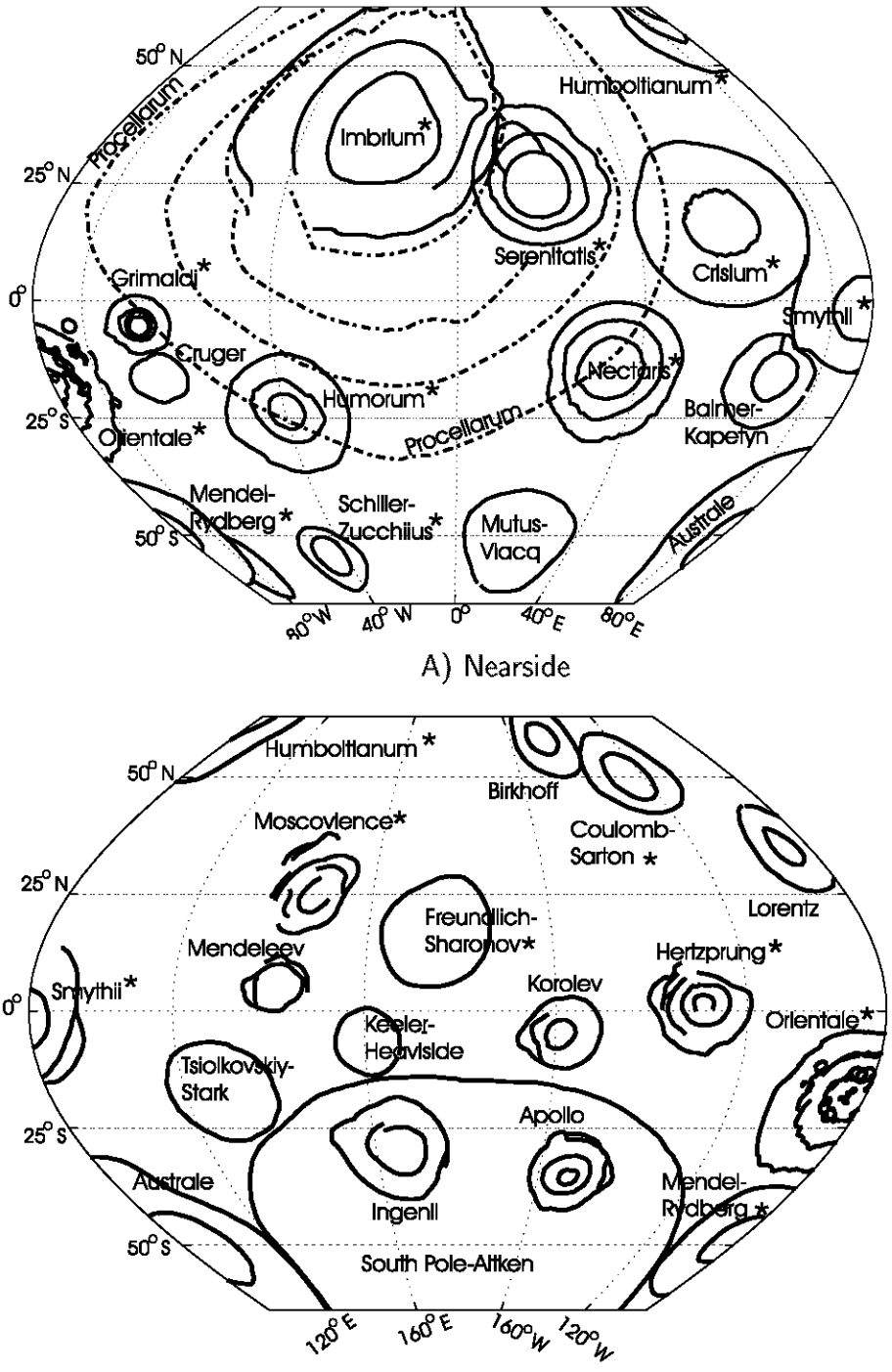

Figure 1: Major lunar basins of the A) nearside and B) farside adapted from Solomon and Head (1979; 1980) and Wilhelms (1987), respectively. Basins identified in the literature (e.g., Neumann et al., 1996; Konopliv et al., 1998) as mascon-bearing are marked by asterisks.

mascon model (Muller and Sjogren, 1968)

Bratt et al. (1985) computed crustal models beneath impact basins from an inversion of nearside Apollo gravity and topographic data. Mare fill thicknesses of 3.5 - 4.5 km for the younger nearside mare basins and 0.5 - 1.3 km for the older buried basins (e.g., Fucenditatits and Nubium) were applied. Terrain gravity effects (*TGE*) were computed in spherical coordinates using 5^o x 5^o blocks of averaged terrain and subtracted from *FAGA* to obtain complete Bouguer anomalies. For these calculations crustal and mantle densities of 2.9 and 3.4 g/cm^3, respectivley, were assumed. The crustal thickness estimates yielded 6.5 mGal residuals relative to the Bouguer anomaly estimates.

The results suggested thinner crust and elevated Moho beneath all the nearside basins. A general decrease in mantle uplift with basin age was noted that might reflect enhanced rates of ductile flow of crustal material in the early history of the Moon. A smoother Moho and surface topography for the older basins was taken to reflect a younger, thinner elastic lithosphere. For the nearside basins in particular, subsurface heating due possibly to large amounts of preferrentially emplaced radiogenic elements on the nearside (Stevenson, 1980) may have facilitated their development of higher states of isostatic equilibrium. For younger large impact basins, excavation may have extended to the base of the crust, but significant mantle excavation may have been impeded by the abrupt increase in strength across the Moho. However, these results were limited by the low resolution and poor coverage of the available lunar gravity and topographic data.

The Clementine mission (Nozette et al., 1996) resulted in greatly improved models of lunar gravity (Lemoine et al., 1997) and topography (Smith et al., 1997). Zuber et al. (1994) obtained a preliminary crustal thickness model for the Moon from these data by downward continuation of the Bouguer anomalies to an equivalent mass sheet at a depth of 64 km. To stabilize the downward continuation, a filter that minimizes the slope and curvature of the lunar topography was applied to the Bouguer gravity anomalies. In particular, the filter suppressed features at large wavenumbers that could not be resolved in the presence of noise while short wavelengths were smoothed or truncated. However, crustal thickness estimates were close to zero beneath the central portions of Mare Orientale, Mare Crisium and portions of the South Pole-Aitken basin.

The crustal modeling approach of Zuber et al. (1994) was extended by Neumann et al. (1996) to include the contributions from mare basalt fill thicknesses for eight major nearside basins that had been estimated up to 10 km (Solomon and Head, 1980). In particular, Neumann et al. (1996) computed Bouguer corrections from a spherical harmonic expansion of the gravity-topography admittance for an Airy compensation. The results of this correction matched the gravity field only at intermediate degrees 10 through 30. Global crustal thickness estimates were computed by downward continuing of the Bouguer anomalies to an equivalent mass sheet 64 km below the nominal equatorial radius of 1738 km to match the seismically estimated crustal thickness of 55 km near the Apollo 12 and 14 landing sites (Toksöz et al., 1974). The Moho was estimated by assuming a mantle density contrast of 0.5 g/cm^3 with crust (e.g., Bowin et al., 1975; Sjogren and Smith, 1976; Bratt et al., 1985).

For more localized variations beneath a basin, additional terrain corrections were computed over a 2048-km-square regions centered on the basin using the FFT admittance between topography and gravity. Downward continuation of these anomalies produced localized Moho undulations that were

constrained by the averaged depth to the Moho from the global solution.

The results showed that both mare and non-mare basins may be characterized by a centrally upwarped Moho that is surrounded by thickened crustal rings mainly within the basin rims. Moho variations for large basins with diameters greater than about 300 km appeared to be uncorrelated with diameter, but negatively correlated with age. Hence the lithosphere perhaps became competent to support the stresses of multi-ring basins that were out of isostatic equilibrium prior to mare emplacement. These results may be limited, however, by the use of Bouguer anomalies and poorly estimated thicknesses of the mare basalt fill. Instabilities due to the downward continuation of the gravity data in the presence of noise may also have degraded the results.

Wieczorek and Phillips (1997; 1998) tested the use of a stratified crust for modeling the Moho. The spherical harmonic expansion of the gravity anomalies was related to crustal models of vertically stratified densities based on seismically inferred discontinuities at 20 km below the Apollo 12 and 14 sites (Toksöz et al., 1974). The method failed for crustal models with more than two layers, which in fact produced "Moho islands" rising above the surface topography. However, reasonable crustal thickness estimates were obtained for a dual-density layered crust, although their thinnest estimate for the nearside crust of 5 km beneath Crisium is difficult to justify by previous studies (Bratt et al., 1985; Neumann et al., 1996; Arkani-Hamed, 1998). This method permits simultaneous computation of upper and lower crustal thickness variations with compensation occuring at both mid-crustal and crust-mantle interfaces. However, the use of simple Bouguer anomalies can be problematic in studies of lunar subsurface mass variations, due to terrain density errors and errors in accounting for terrain gravity effects in rugged relief.

The Clementine-era data were also investigated by Arkani-Hamed (1998) who determined the thicknesses of the crust and mare flows for mascon basins assuming they were Airy compensated before the mascons formed. Mare fill thicknesses ranging between 3-6 km were estimated from the anti-variant harmonics of the gravity and topography over the central basins. Mantle relief, on the other hand, involved estimates based on covariant central basin negative gravity anomalies that were adjusted for the mare fill thicknesses. In this approach, the mascons were attributed entirely to the mare fill. Also, global or regional applications may be limited by the flat moon approximation used to develop this analysis. Furthermore, the resolution of the results may be problematic because the analysis was restricted to the degree 40 and lower harmonics.

The above crustal thickness studies involve several limitations that affect applications of the results. For example, the gravity and the topographic data sets used in these studies were not of the quality of the LP-era data sets. Also the reduction of gravity for terrain effects was first order at best. In particular, the use of the simple Bouguer anomaly based on the infinite slab approximation of the topography on a small-diameter body such as the Moon can be quite problematic, especially in regions of rugged relief (von Frese et al., 1997b). Furthermore, these studies present obscure characterizations of the actual residual gravity components attributed to the crustal thickness variations, as well as the remaining anomaly noise and regional components, which complicate assessing the veracity of the crustal thickness models.

The present study uses the modern LP-era gravity and terrain data to estimate crustal thickness variations for the near-global region between $\pm\ 64^o$ latitude. Terrain gravity effects are determined in

spherical coordinates by GLQ integration to accuracies that are commensurate with the accuracies of the elevation and related density data. Possible gravity effects of crustal thickness variations are isolated in terms of the correlations between *FAGA* and *TGE*. In the subsequent chapters, the remaining gravity anomalies are analyzed for possible subcrustal and intracrustal density variations. These gravity effects together with the effects of the crustal thickness estimates account almost completely for *FAGA* and *TGE* that were obtained from independent observations of the lunar gravity and topography.

2.3 Spectral Correlation Analysis of Crustal *FAGA* and *TGE*

Establishing the correlations between the gravity effects of the topography and free-air gravity anomalies at satellite altitude can be used to estimate lunar Moho and variations of crustal thickness (von Frese et al., 1997b). The *FAGA* (defined in Appendix A) and terrain elevation data (described in Appendix B) considered in this study are given in Figures 2 and 3, respectively. The topographic gravity effects at 100 km above the mean surface radius are efficiently modeled by GLQ integration. In particular, a 100-m error in elevation and a density error of 0.05 g/cm^3 are negligible at altitude Z = 100 km. Accordingly, the free-air gravity model (LP75G) in Figure 2 was evaluated at 100 km altitude above the mean surface radius (= 1738 km) of the Moon. This is a common practice in lunar studies (e.g., Muller and Sjogren, 1968; Bills and Ferrari, 1977; Bratt et al., 1985; von Frese et al., 1997b). However, these gravity data incorporate the tracking of the spacecraft in circular polar orbit at 100 km altitude by the Deep Space Network (DSN) that measured line-of-sight velocities from the Doppler shift to an accuracy of 0.2 mm/s over 10-s intervals. The listed attributes of this and subsequent maps include the minimum (MIN) and maximum (MAX) amplitudes, the amplitude mean (AM), amplitude standard deviation (ASD), amplitude unit (AU), grid interval (GI) and contour interval (CI). The amplitude mean (AM) is defined as

$$AM = \frac{\sum_{i=1}^{n} y_i^{obs}}{n}, \tag{1}$$

and the amplitude standard deviation (ASD) as

$$ASD = \left[\frac{\sum_{i=1}^{n}(y_i^{obs} - AM)^2}{n-1}\right]^{\frac{1}{2}}, \tag{2}$$

respectively, where y_i^{obs} is the $i-th$ of n observations.

Data from continuous LP-tracking were combined with data from the Lunar Orbiter (LO), Apollo, and Clementine missions to produce a degree and order 75 spherical harmonic gravity model (Konopliv et al., 1998). The Clementine data, obtained from tracking the spacecraft in its elliptical orbit with periapsis altitude of 400 km, improved the low degree (n=2, 3) and sectorial terms (to degree 20) of the gravity field (Konopliv et al., 1998). Over the lunar farside the LP could not be viewed from Earth, so that the lunar farside gravity field was less well determined than the nearside field. In particular, information was obtained by observing the changes in the spacecraft orbit due to accumulated accelerations of the farside as it would come out of occulation (Konopliv et al., 1998).

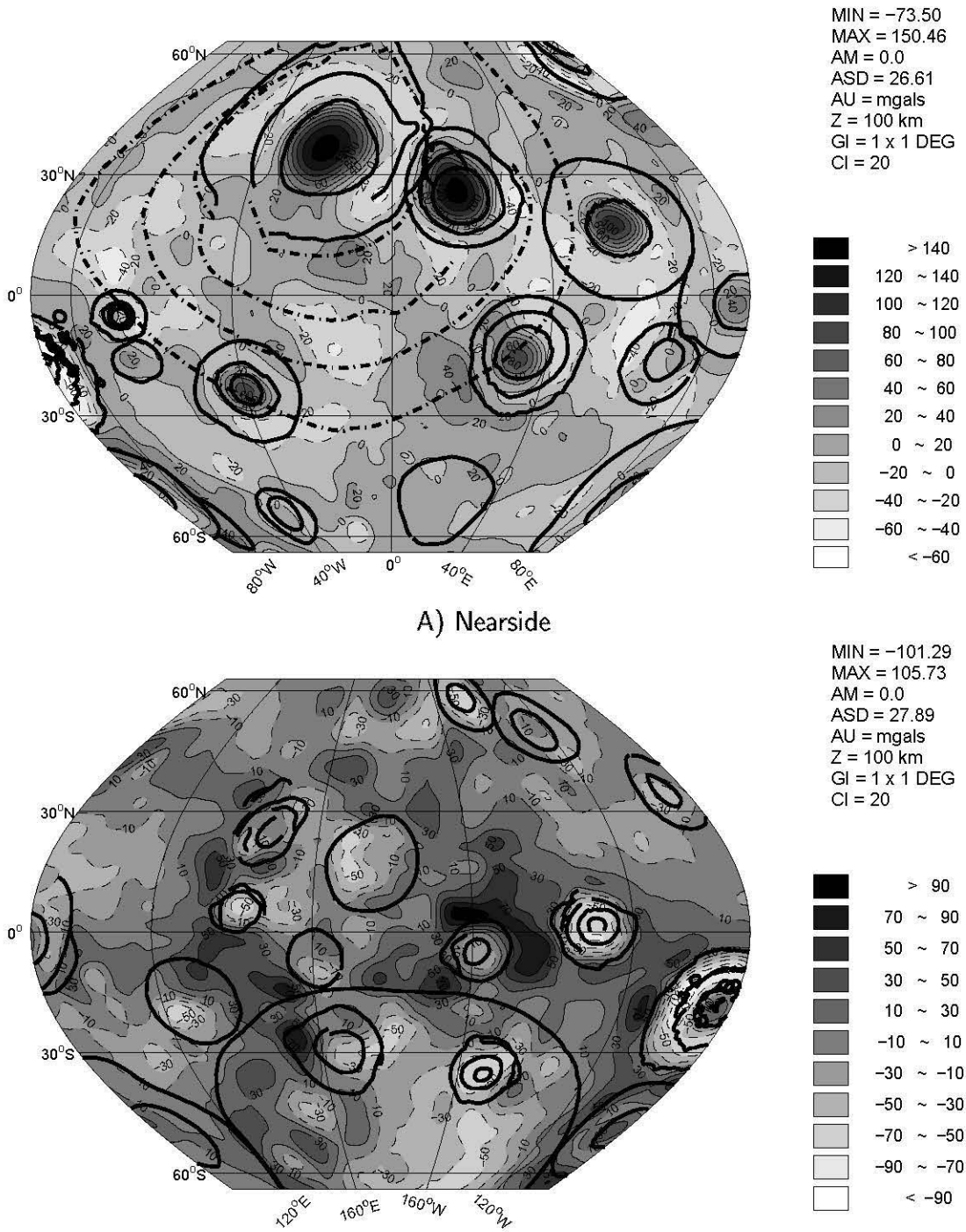

Figure 2: Free-air gravity anomalies (FAGM) evaluated at an altitude (Z) of 100 km from the spherical harmonic coefficients of the Lunar Prospector gravity model (Konopliv et al., 1998). These and subsequent maps are in pseudocylindrical equal-area projection (Snyder, 1987).

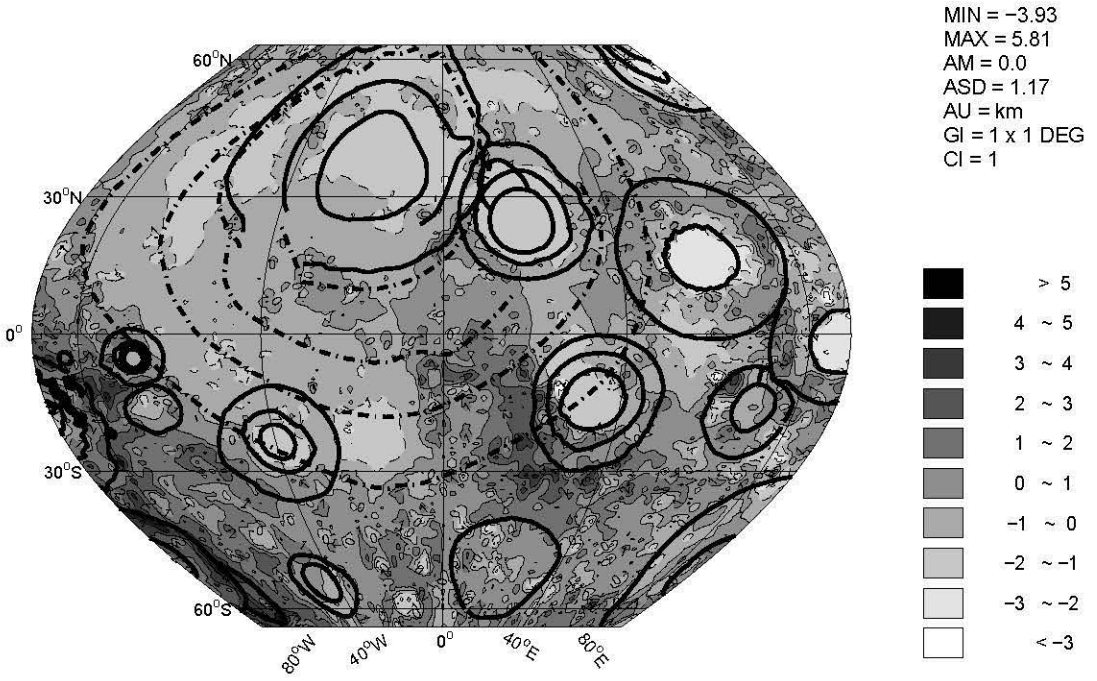

A) Nearside

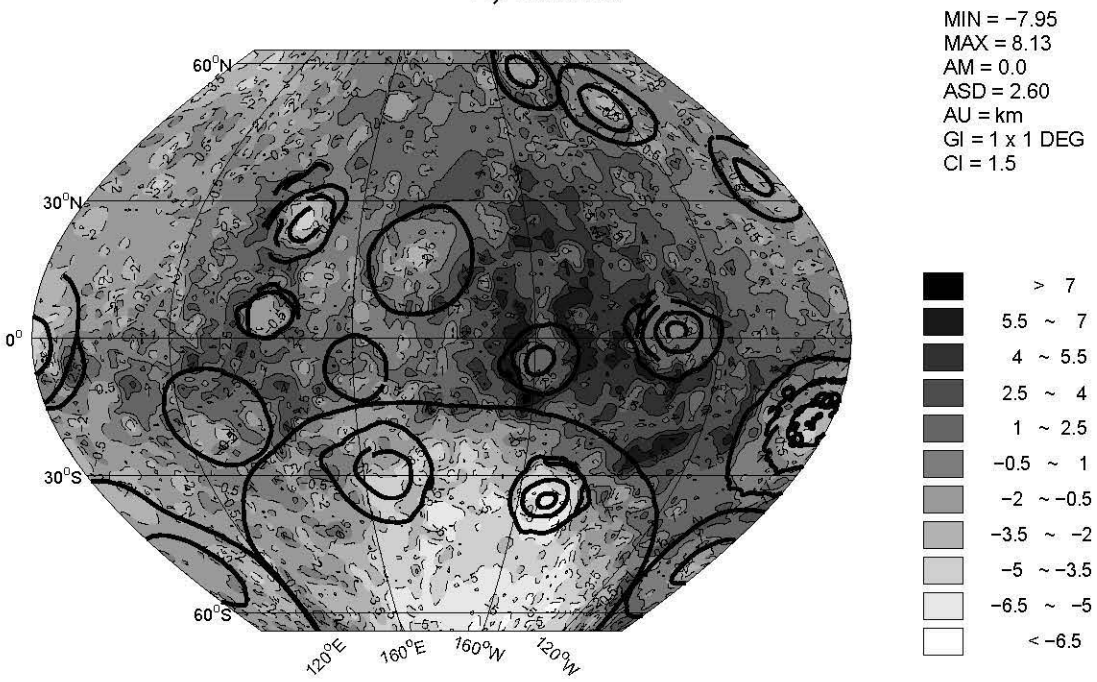

B) Farside

Figure 3: Crustal topography evaluated from the spherical harmonic coefficients of the Goddard Lunar Terrain Model-2 (Smith et al., 1997). Elevations are referenced to the mean lunar radius of 1738 km.

The surface gravity errors are estimated to be about 20-40 mGals for the nearside and 30-50 mGals for the farside. At the 100 km altitude these gravity errors are near the 1-5 mGal level (A. Konopliv, personal communication, 2000) that is consistent with anomaly error variance shown in Figure 49.

Figure 3 shows the lunar topography of the $128^o \times 360^o$ study region at 1^o intervals between $\pm 64^o$ latitude that includes over 16 km of relief. The spherical harmonic coefficients for this topographic model (GLMT-2) were derived from laser altimeter data obtained by the Clemetine satellite mission (Nozette et al., 1996). A laser ranging instrument (LIDAR) was carried that measured the slant range from the spacecraft to the lunar surface (Nozette et al., 1996). Elevations were referenced to a ellipsoid of equatorial radius 1738 km and flattening 1/3234.94. The flattening corresponds to the C_{20} spherical harmonic term obtained from the Clementine lunar gravity field (GLGM-2) (Lemoine et al., 1997). The degree and order 72 spherical harmonic expansion model of the lunar topography was developed with about 100 m total radial error (Smith et al., 1997). This total error was estimated from the root sum square of the statistically independent error sources that include orbital errors (10 m), system instrumental errors (40 m), selenoid error (10 m), pointing errors (meter-scale) and the roughness of the lunar surface. To account for additional unmodelled errors, a contingency radial error of about 30 m was also incorporated (Smith et al., 1997).

Figure 4 shows the terrain gravity effects (*TGE*) (given by equation 62 in Appendix A) of the lunar topography of Figure 3 modeled at 100-km altitude by GLQ integration (von Frese et al., 1981; von Frese et al., 1997b) assuming a 2.8 g/cm^3 density contrast of the terrain with the near-vacuum of space. The modeling procedure involves distributing point sources within the anomalous body according to the GLQ decomposition of its volume and computing the integrated gravity effects of the point sources for comparison with *FAGA*. The numerical procedure used in estimating *TGE* is accurate because of the orthogonality of the Legendre polynomials used to represent the elemental volume elements of the anomalous mass (e.g., Stroud and Secrest, 1966). For the terrain modeling, spherical prismatic elements were used with flat tops at the average altitudes provided by the GLTM-2 file of $1^o \times 1^o$ topographic estimates. At 100 km elevation, the calculation errors in using this simplified representation of the topography are negligible compared to the error budget for the LP75G file of FAGA estimates.

Comparing *TGE* (Figure 4) and *FAGA* (Figure 2) suggests that the *TGE* are relatively poorly represented in *FAGA*. Indeed the correlation coefficient (CC) between the two datasets is only 0.27. Hence, to the degree that the *TGE* have been accurately modeled, the existence of a compensating anomaly field can be inferred. Assuming that the lunar topography may be compensated by thickness variations of the crust (e.g., Bowin et al., 1975; Bratt et al., 1985; Zuber et al., 1994; Neumann et al., 1996; von Frese et al., 1997b; Wieczorek and Phillips, 1997), the annihilating effects can be analyzed for mantle topography and crustal thickness variations.

However, unmasking the compensated terrain gravity effects can be complicated by the gravity effects of the crustal topography that are incompletely compensated. These effects when they occur will be marked by *FAGA* components that are correlated either positively or negatively with features in the *TGE*, although clearly not every terrain-correlated free-air anomaly necessarily reflects incompletely compensated topography (e.g., von Frese et al., 1997). In general, spectral correlation filters (von Frese et al., 1997a) can be designed using *TGE* to separate *FAGA* into terrain-correlated

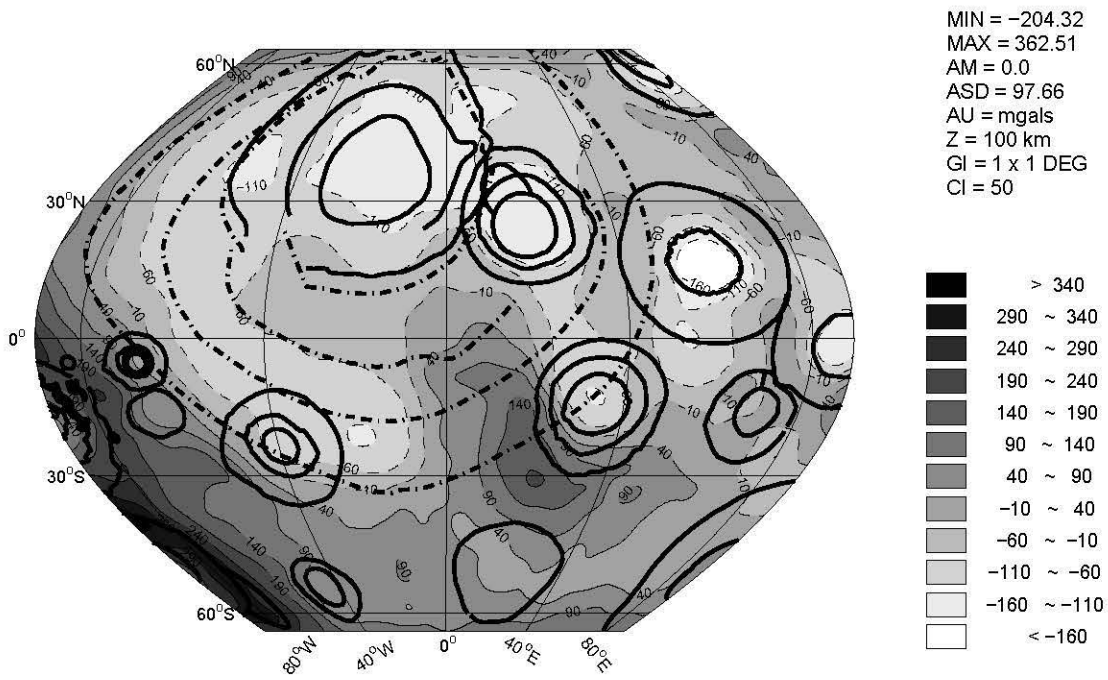

A) Nearside

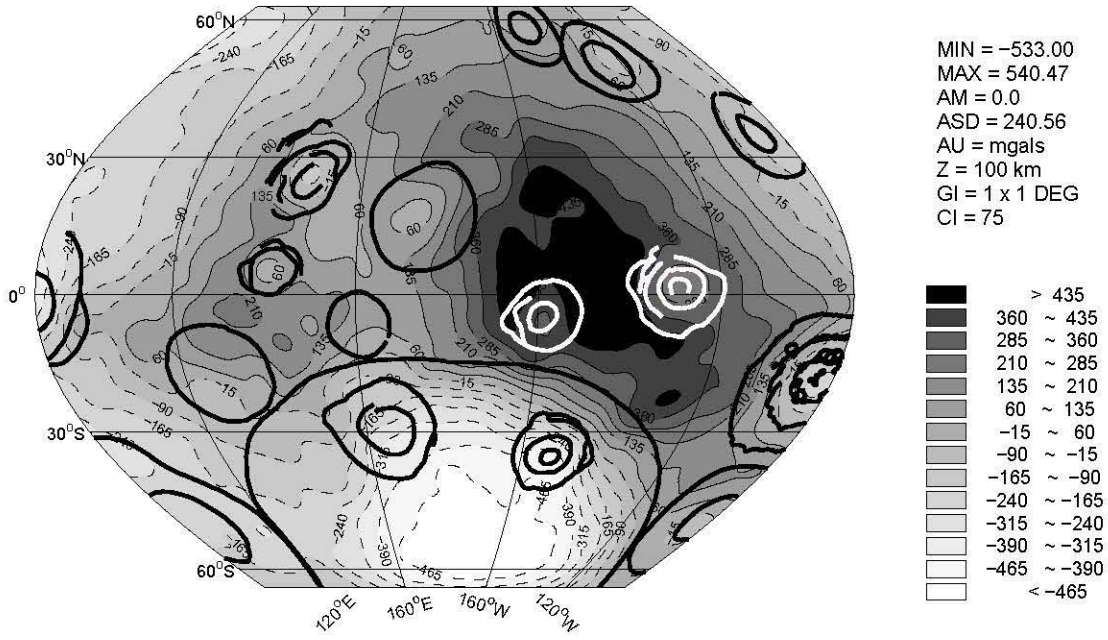

B) Farside

Figure 4: Terrain gravity effects obtained from modeling Figure 3 in lunar spherical coordinates by GLQ integration using a density contrast of 2.8 g/cm^3 for the surface terrain.

(*TCFAGA*) and terrain-decorrelated (*TDFAGA*) components and expressed as

$$FAGA = TCFAGA + TDFAGA. \tag{3}$$

Assuming crustal thickness variations are maintained in disequilibrium by the strengh of the lithosphere, the compensated terrain gravity effects (*CTGE*) are obtained by subtracting the terrain-correlated free-air gravity anomalies (*TCFAGA*) from *TGE* and expressed as

$$CTGE = TGE - TCFAGA. \tag{4}$$

For correlation filtering, the fast Fourier transforms **F** and **D** of *FAGA* and *TGE*, respectively, are evaluated for their correlation spectrum as given by:

$$CC(k) = cos(\Delta\Theta_k) = [Re\frac{\mathbf{F}(k)}{\mathbf{D}(k)}] \times \frac{|\mathbf{D}(k)|}{|\mathbf{F}(k)|}, \tag{5}$$

where $CC(k)$ is the correlation coefficient between the wavenumber components $\mathbf{F}(k)$ and $\mathbf{D}(k)$ with amplitude spectra given by $|\mathbf{F}(k)|$ and $|\mathbf{D}(k)|$, respectively, and Re denotes taking the real parts of the wavenumber components. $CC(k)$ is most simply evaluated from the cosine of the phase difference ($\Delta\Theta_k$) between the two k-th wavenumber components.

Inversely transforming *FAGA* wavenumber components that show high positive and negative correlation with *TGE* components yields *TCFAGA* that may be useful for evaluating isostatic properties of the crust. In particular, where crustal topography is incompletely compensated, *TCFAGA* can significantly constrain the related mass imbalances.

Effective correlation filtering commonly involves picking a range of values of the correlation coefficient for isolating features with the desired correlation properties. If the range is too small, the extracted features may be of little or no utility because they have amplitudes in the noise range of the data. On the other hand, if the range is too large, the resolution of correlative features can be severely degraded.

To evaluate threshold values of the correlation coefficient for effectively estimating *TCFAGA*, the power ratio spectra for *FAGA* and *TGE* in Figure 5 were considered. Here each spectrum gives the percentages of the input power that are output by the correlation filtered data. In the right half of the plot, the pass-range of the correlation coefficients (CCs) includes the value for the point though 1, whereas in the left half the pass-range includes the CCs for the point through -1. For example, inversely transforming all wavenumber (k) components of *TGE* that have $0 \leq CC(k) \leq 1$ with respect to the spectral *FAGA* components yields signals with output power that is about 70% of the original *TGE* power, whereas the *TGE* components with $-1 \leq CC(k) \leq 0$ yield an output power of about 30%. Note in Figure 5 that only for this case are the two ranges mutually exclusive so that the output powers effectively sum to 100% within round-off error.

Figure 5 was used to explore the data sets for their broad correlation structures as indicated by abrupt changes in slope in the spectra. For example, maps of the *FAGA* components in the ranges $-1 \leq CC(k) \leq -0.4, -0.3, -0.2, -0.1$, and 0.0 will all be quite similar, but very different from the map with components in the range $-1 \leq CC(k) \leq -0.5$. Of course, comparing maps at different

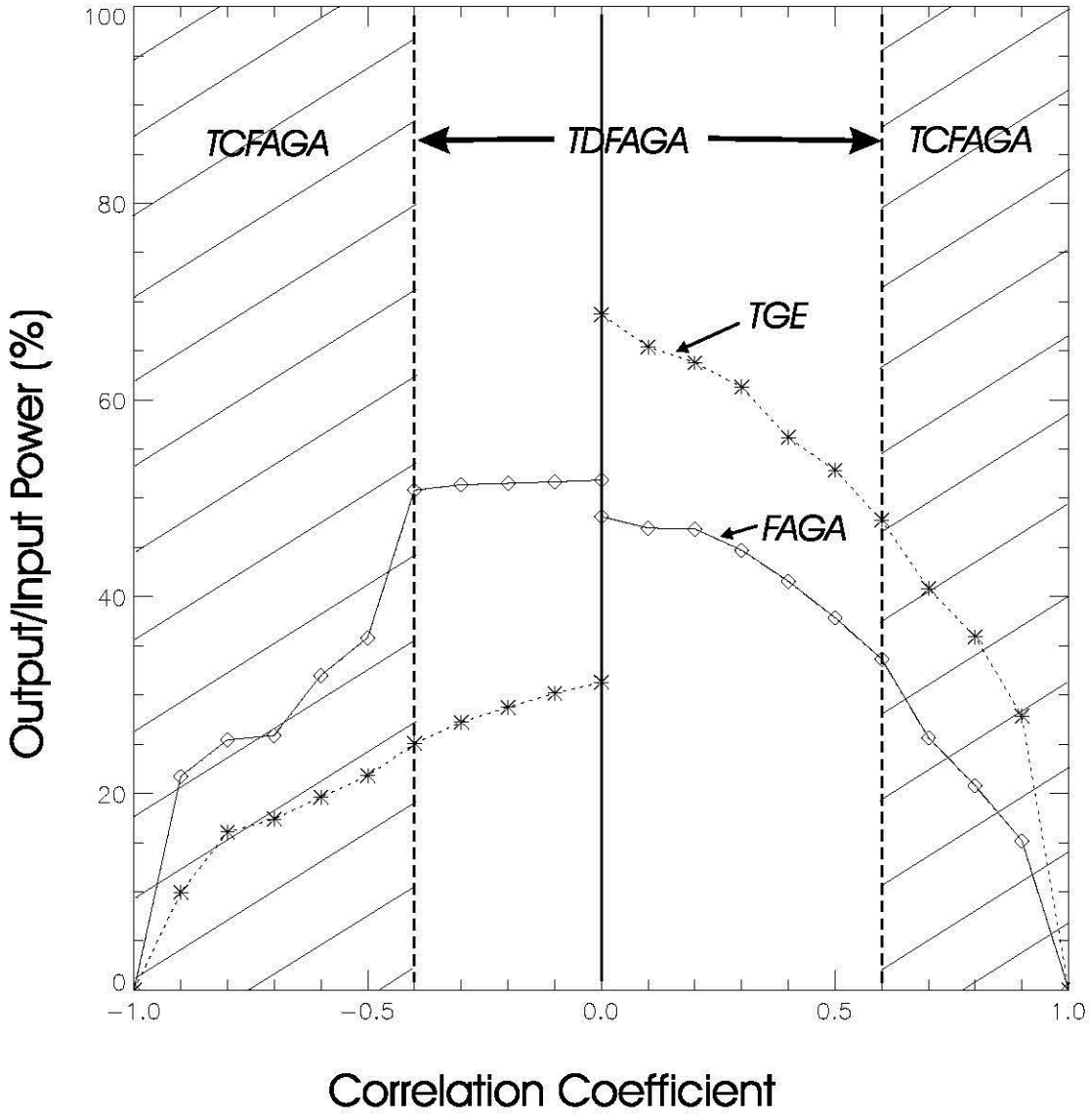

Figure 5: Percentages of output-to-input power for *FAGA* and *TGE* at 0.1 intervals of the correlation coefficient.

thresholds (e.g., $CC(k) \leq -0.4$ vs. $CC(k) \leq -0.5$) will highlight the features in *FAGA* that are affected by the different threshold values.

Broadly guided by the correlation power ratio spectra in Figure 5, *TCFAGA* were estimated by inversely transforming only those *FAGA* wavenumber components that exhibited high positive [$CC(k) \geq 0.6$] and negative [$CC(k) \leq -0.4$] correlations to the wavenumber components of *TGE*. These threshold $CC(k)$ were also selected to insure that the remaining *TDFAGA* and *CTGE* have effectively zero correlation, and hence may be independently analyzed for the properties of the lunar subsurface.

The estimated *TCFAGA* and *TDFAGA* components of *FAGA* are shown in Figures 6 and 7, respectively. Figure 8 gives the compensated terrain effects *CTGE* estimated by subtracting Figure 6 from Figure 4. The *TDFAGA* and *CTGE* were determined by spectral correlation analysis to have effectively zero correlation.

However, even though the compensated terrain gravity effects are not represented in the free-air anomalies, they must still contribute to the gravity field of the region by virtue of the horizontal density contrasts that constitute the topography. Their absence can be explained by reversing the polarities of these effects to produce annihilating signals (*-CTGE*) that may be interpreted in terms of upper mantle topography by an appropriate compensation model for the crust.

In particular, mantle topography (i.e., the Moho) was estimated from these annihilating gravity effects by inversion assuming the crust is compensated by its thickness variations with a -0.5 g/cm^3 density contrast to the mantle (e.g., Bowin et al., 1975; Bills and Ferrari, 1977; Thurber and Solomon, 1978; Bratt et al., 1985; Neumann et al., 1996; von Frese et al., 1997b; Wieczorek and Phillips, 1998). The inversion used GLQ integration to estimate the thicknesses of 1^o spherical prisms about a reference depth of 64 km below the mean surface radius of the Moon (von Frese et al., 1997b; Appendix B.3). This reference depth has been determined from calibrating a global crustal thickness model to seismically determined thicknesses at Apollo 12 and 14 landing sites (Zuber et al., 1994). The use of this reference depth for the inversion yielded a crustal thickness value of about 54.6 km in the vicinity of the Apollo 12 and 14 landing sites ($\approx 3^o$ S, 20^oW) that is in good agreement with the 55 km value estimated from seismic refraction measurements (Toksöz et al., 1974; Nakamura et al., 1979; Goins et al., 1981).

Figure 9 gives the crustal thickness estimates for the Moon where the crustal topography (Figure 3) was combined with the Moho estimates from the annihilating signals *-CTGE* (Figure 8). The inversion obtained Moho variations that produced gravity effects which matched 99% of the *CTGE* with 0.02-mGals standard error. The results suggest an average thickness of about 69.9 km for the farside, which is roughly 13 km thicker than the 56.7 km average of the nearside crust. These results compare favourably to the 12 km difference in crustal thicknesses between the farside and nearside that Neumann et al. (1996) obtained.

Crustal thickness variations provide insight on the tectonic features and evolution of the crust. In addition, these variations may constrain the local stress field in the crust because they tend to flow and concentrate compressive and tensional stresses in the thinner and thicker regions of the crust (Artyushkov, 1973). Further insight on the residual stress field of the lunar crust may be inferred from the *TCFAGA* (Figure 6) to the extent that they reflect incomplete isostatic compensation.

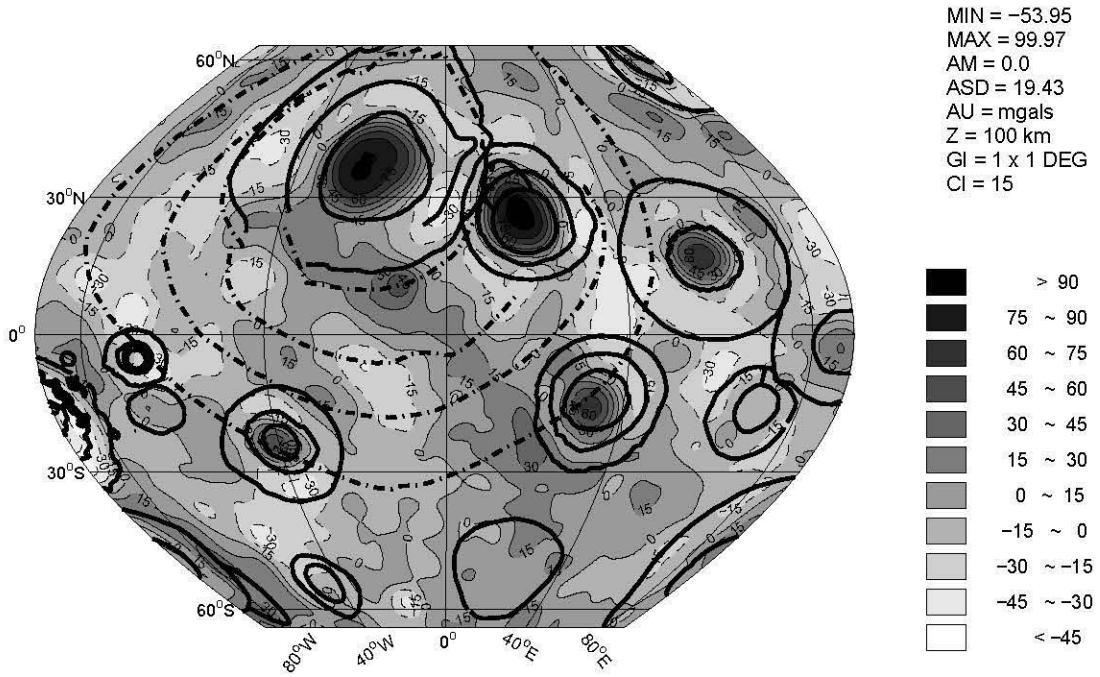

A) Nearside

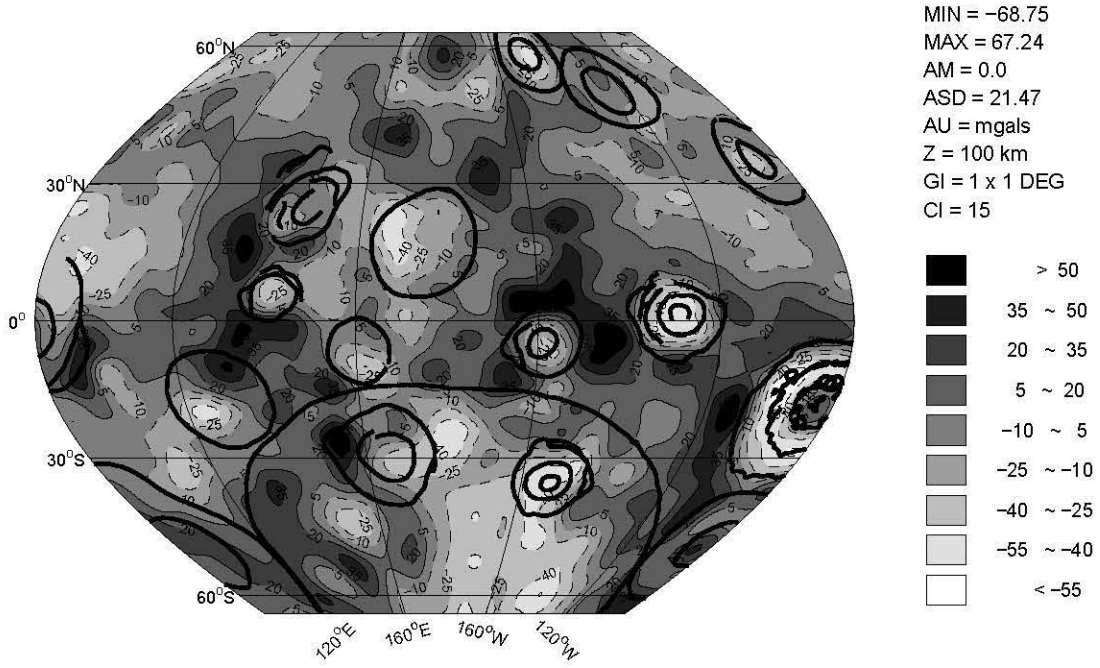

B) Farside

Figure 6: Terrain-correlated free-air gravity anomalies (*TCFAGA*).

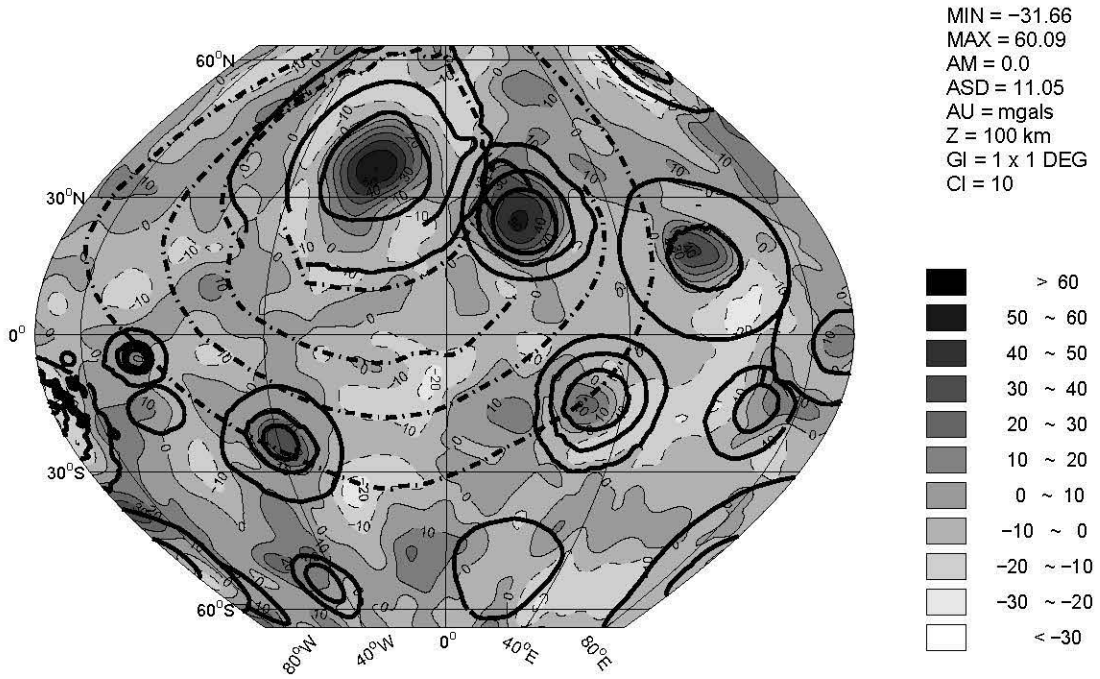

A) Nearside

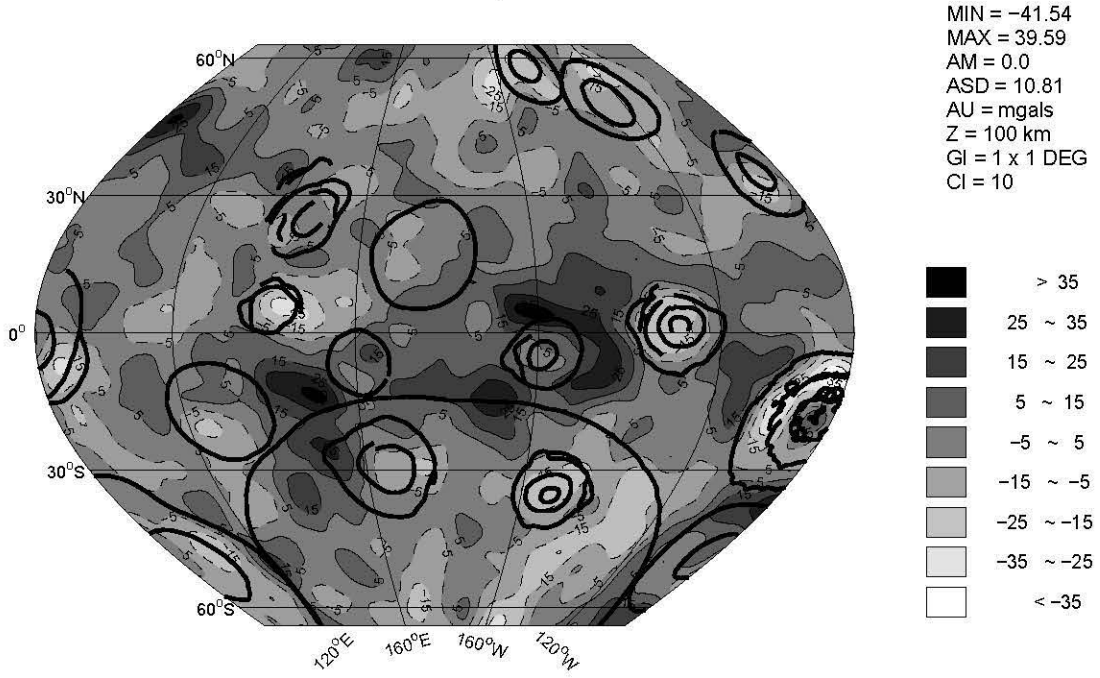

B) Farside

Figure 7: Terrain-decorrelated free-air gravity anomalies (*TDFAGA*).

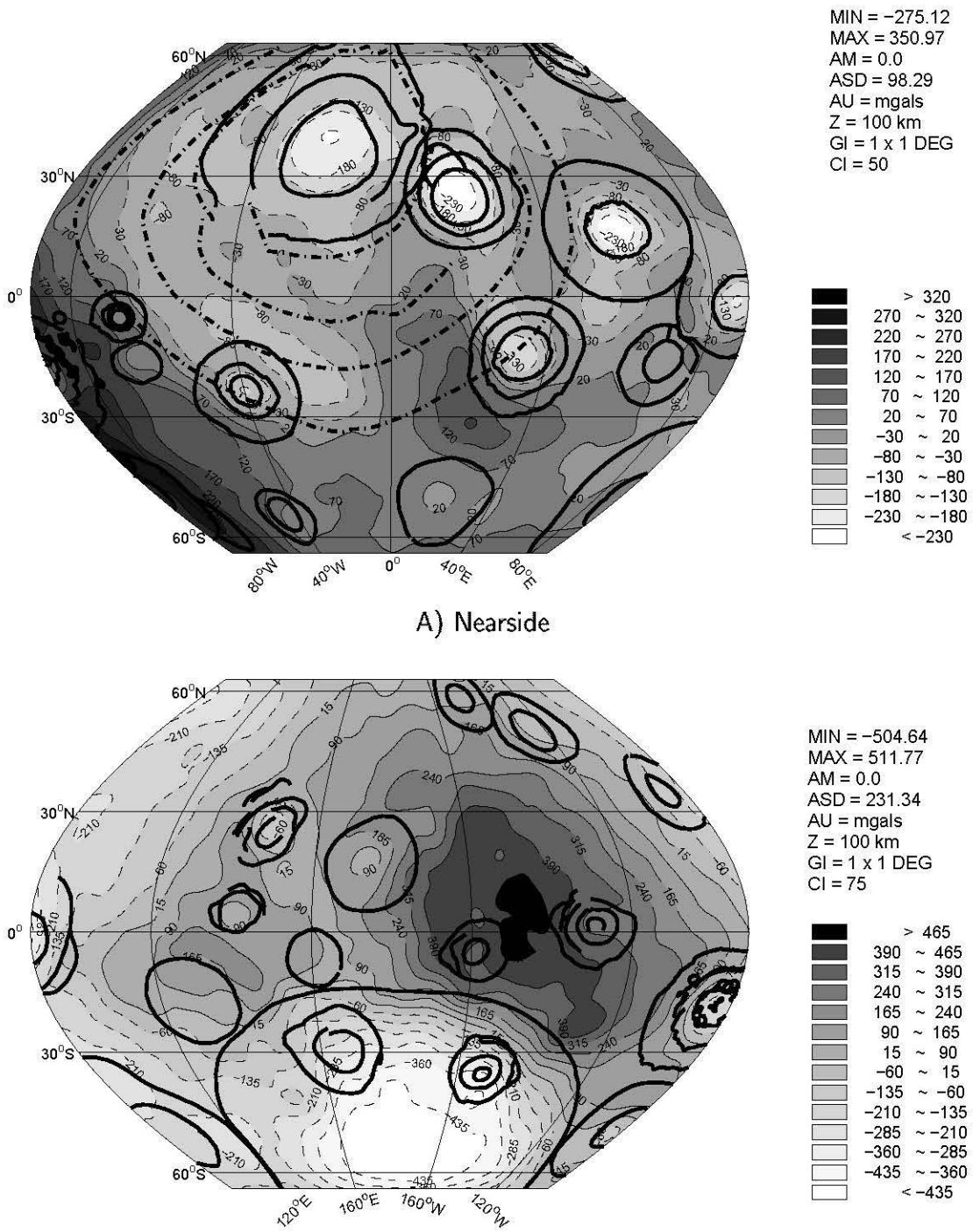

Figure 8: Compensated terrain gravity effects (*CTGE*) that by polarity reversal yield annihilating signals (*-CTGE*) for modeling the Moho assuming the crust is compensated by its thickness variation.

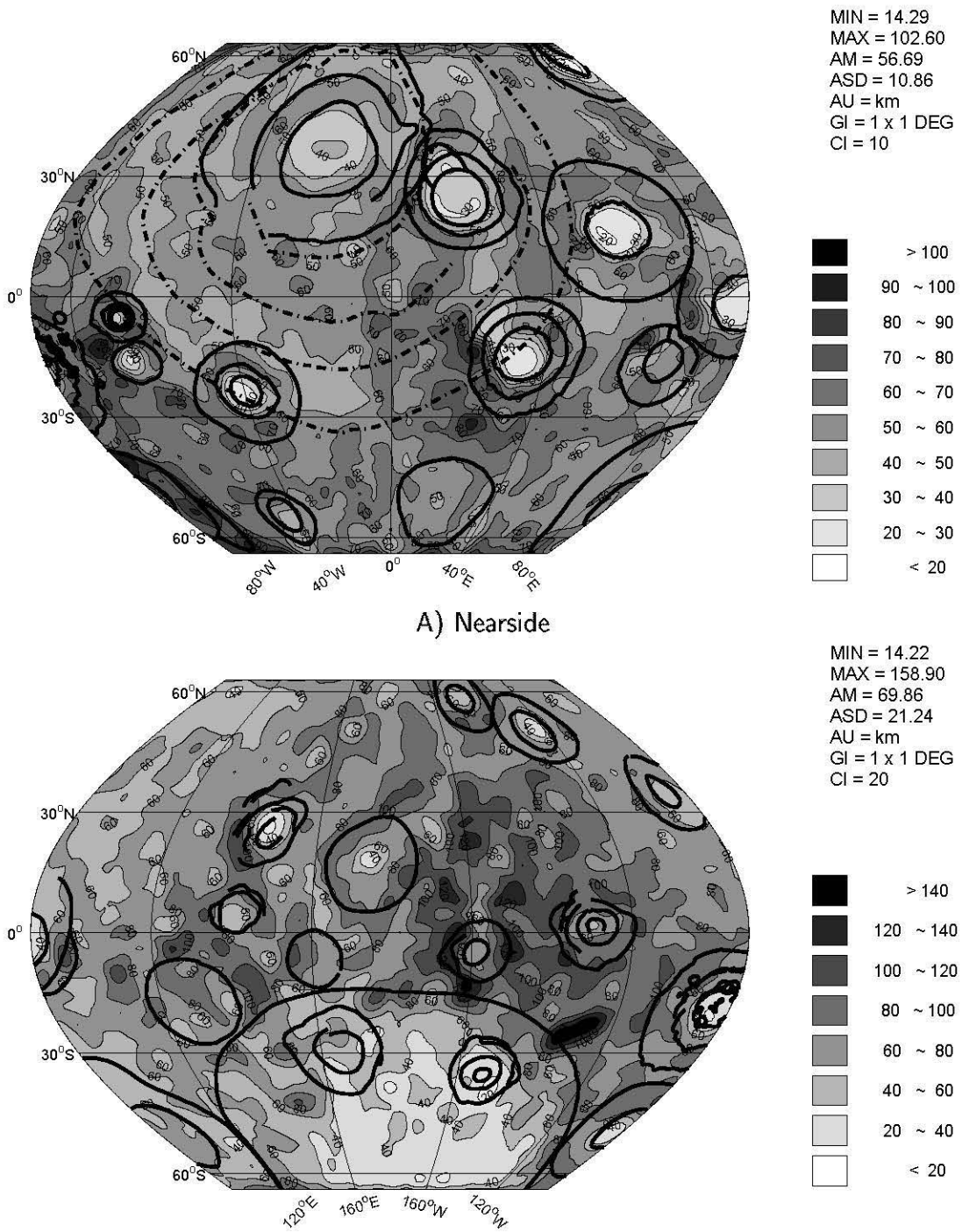

Figure 9: Crustal thickness model obtained by combining crustal topography (Figure 3) with Moho estimates from the inversion of -*CTGE* (Figure 8).

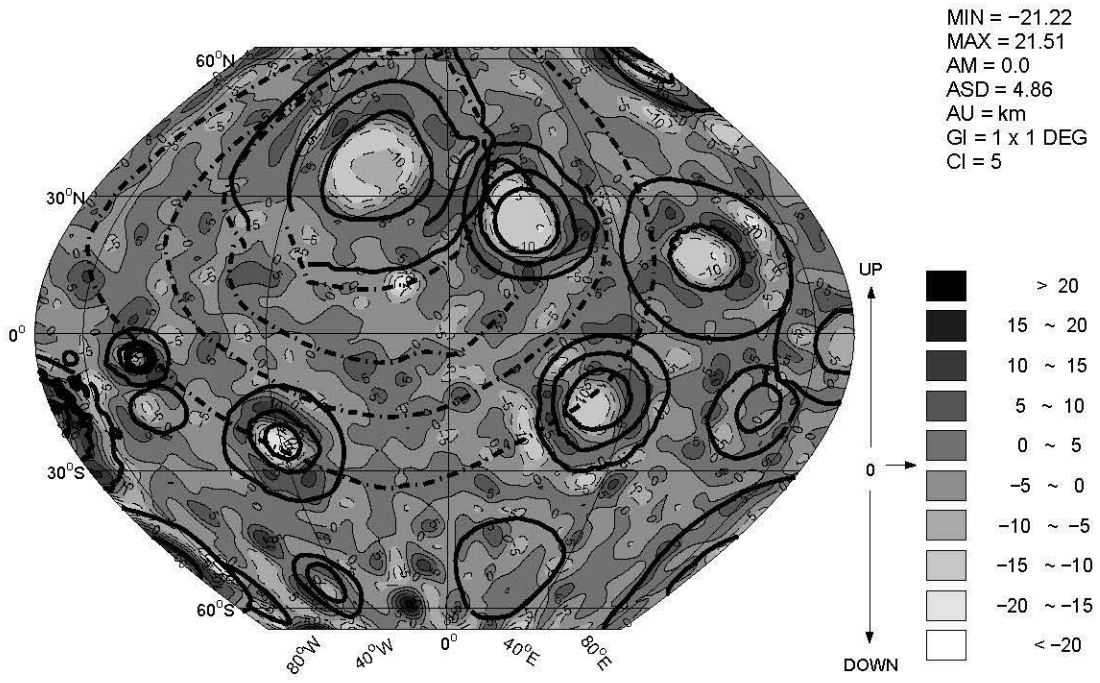

A) Nearside

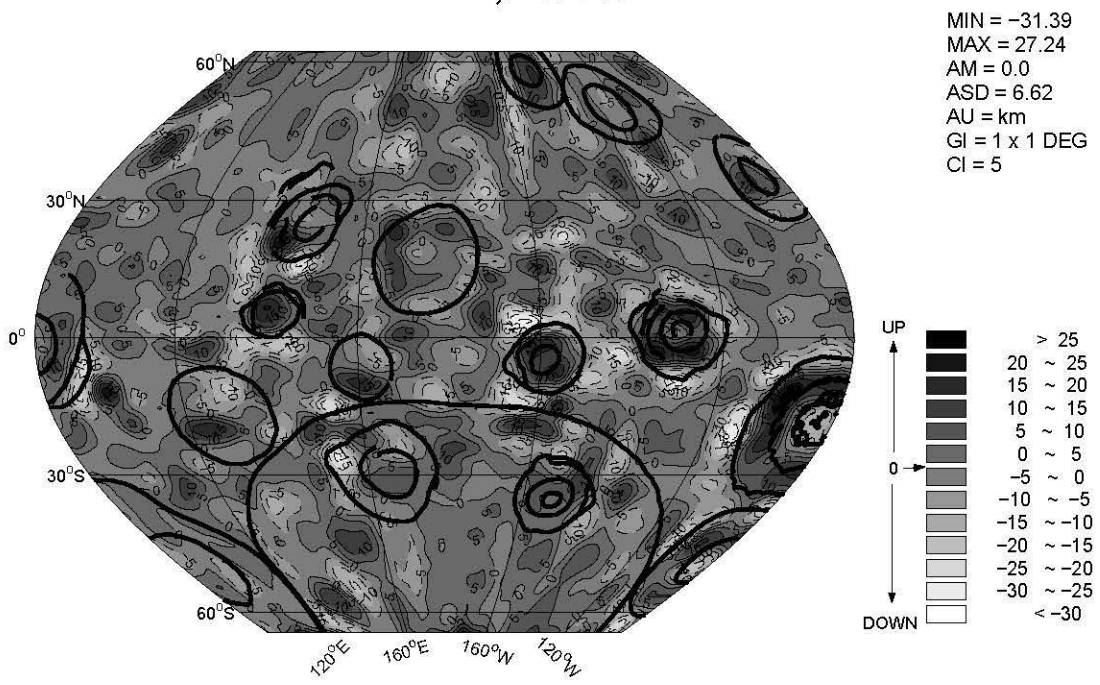

B) Farside

Figure 10: Incipient radial adjustments of the lunar Moho inferred from the GLQ inversion of *TCFAGA* (Figure 6).

Figure 10 gives the radial adjustments of the Moho for the crustal thickness estimates of Figure 9 that nullify the *TCFAGA* of Figure 6. *TCFAGA* is interpreted to reflect uncompensated terrain. Here, GLQ inversion was used to estimate thickness variations of 1^o spherical prisms about the estimated Moho that account for the *TCFAGA* assuming the crust is compensated by its thickness variations with a -0.5 g/cm^3 density contrast to the mantle (e.g., von Frese et al., 1997b; Appendix D). The inversion produced incipient Moho adjustments with gravity effects that matched more than 99% of the *TCFAGA* with 0.03-mGal standard error.

The negative and positive contours in Figure 10 give the amount of subsidence and uplift, respectively, that is required of the estimated Moho to equilibriate the topography fully by crustal thickness variations and hence nullify *TCFAGA*. Assuming that the lunar crust is evolving towards equilibrium and a zero mean free-air gravity anomaly, these Moho adjustments may contribute superposed loads to the crustal stress field. Hence, the global stress field related to lunar thermal evolution (e.g., (Solomon and Head, 1980) may be locally augmented by the superposed stress effects due to the crustal thickness variations and these incipient Moho adjustments (von Frese et al., 1997b).

The remaining *FAGA* components to account for in the development of a lunar crustal model are the *TDFAGA* of Figure 7. To first order, these anomalies may be separated into crustal (*CTDFAGA*) and subcrustal (*STDFAGA*) components on the basis of Figure 11, which gives their correlation spectrum with the LP-gravity model (LP75G). Several branches are apparent in Figure 11, the most prominent of which is the flat branch related to anomaly components for degree and order 25 and higher that may largely reflect the shorter wavelength effects of crustal density contrasts. These anomalies are low-amplitude, high-frequency features that may also reflect measurement and processing noise. However, as described below, many of these anomalies show systematic associations with basins that may provide additional constraints on their crustal properties.

Figure 12 shows the possible crustal components of *TDFAGA* in Figure 7. These *CTDFAGA* were obtained by inversely transforming all wavenumber components of Figure 7 that are positively correlated with wavenumber components of the LP-gravity model (LP75G) of degree and order 25 and higher. The north-south stratification of the anomalies appear artificial and may include orbital errors. The north-south stratification can be removed by applying a strike sensitive filter to the data. However, these anomaly estimates are perhaps the most appropriate components of *FAGA* to relate to remote sensing imagery and other near-surface constraints on the poorly understood lunar crust. For example, von Frese et al. (1997) found that gravity anomalies with the wavelength and amplitude properties of *CTDFAGA* may readily reflect crustal mass inhomogeneities involving density contrasts up to $\pm$ 0.5 g/cm^3 with respect to the non-mare crust. Possible sources of these inhomogeneities include higher density mare basaltic fill, ejected deposits of impact melts, as well as lower density unconsolidated deposits of ejecta, fractured and brecciated crust, and accumulations of anorthosite.

Another prominent branch in the correlation spectrum of Figure 11 occurs for degree and order 24 and lower where the slope increases abruptly. The lower frequency components involved in this branch can be largely interpreted for the longer wavelength effects of subcrustal density variations as shown in Chapter 4. Figure 13 gives these possible subcrustal components of *TDFAGA* that are most strongly correlated with the degree and order 24 and lower wavenumber components of LP-gravity model (LP75G).

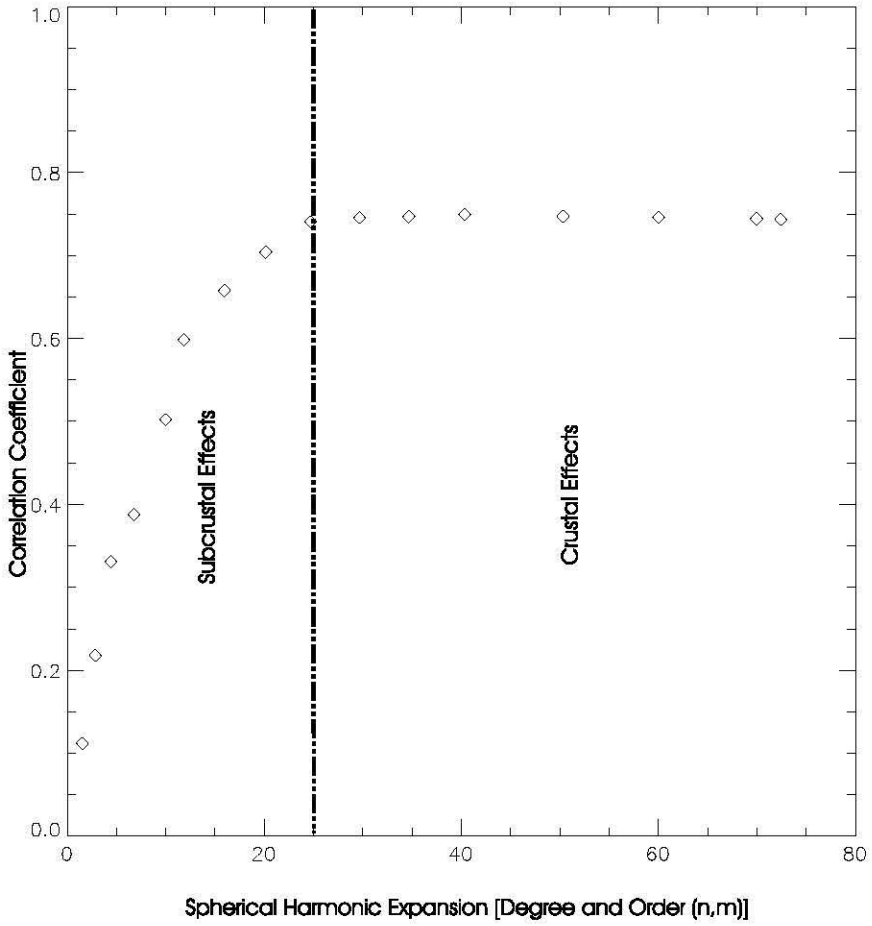

Figure 11: Correlation spectrum between *TDFAGA* and *FAGA* (LP75G). The spherical harmonic model expansion of the gravity field was evaluated at degree and order 2, 3, 5, 7, 10, 12, 15, 20, 25, 30, 35, 40, 50 and 75. The curve may be interpreted for two slopes possibly differentiating the effects of lateral density variations of the crust ($n \geq 25$) and subcrust ($n \leq 24$).

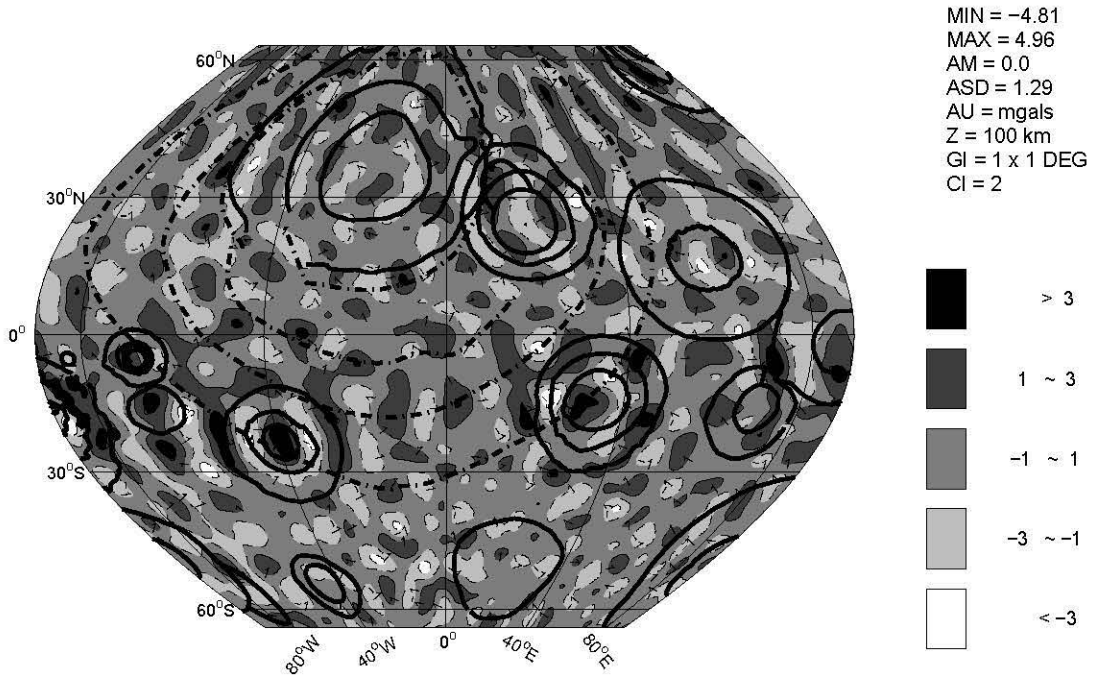

A) Nearside

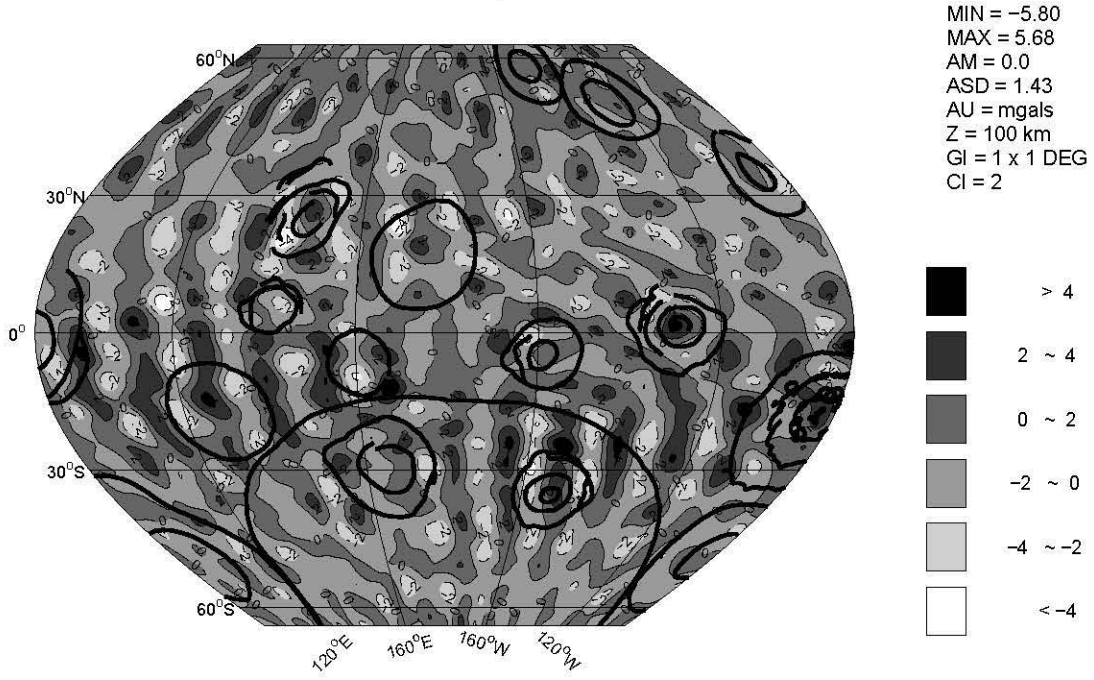

B) Farside

Figure 12: Inferred crustal components (*CTDFAGA*) of *TDFAGA* (Figure 7).

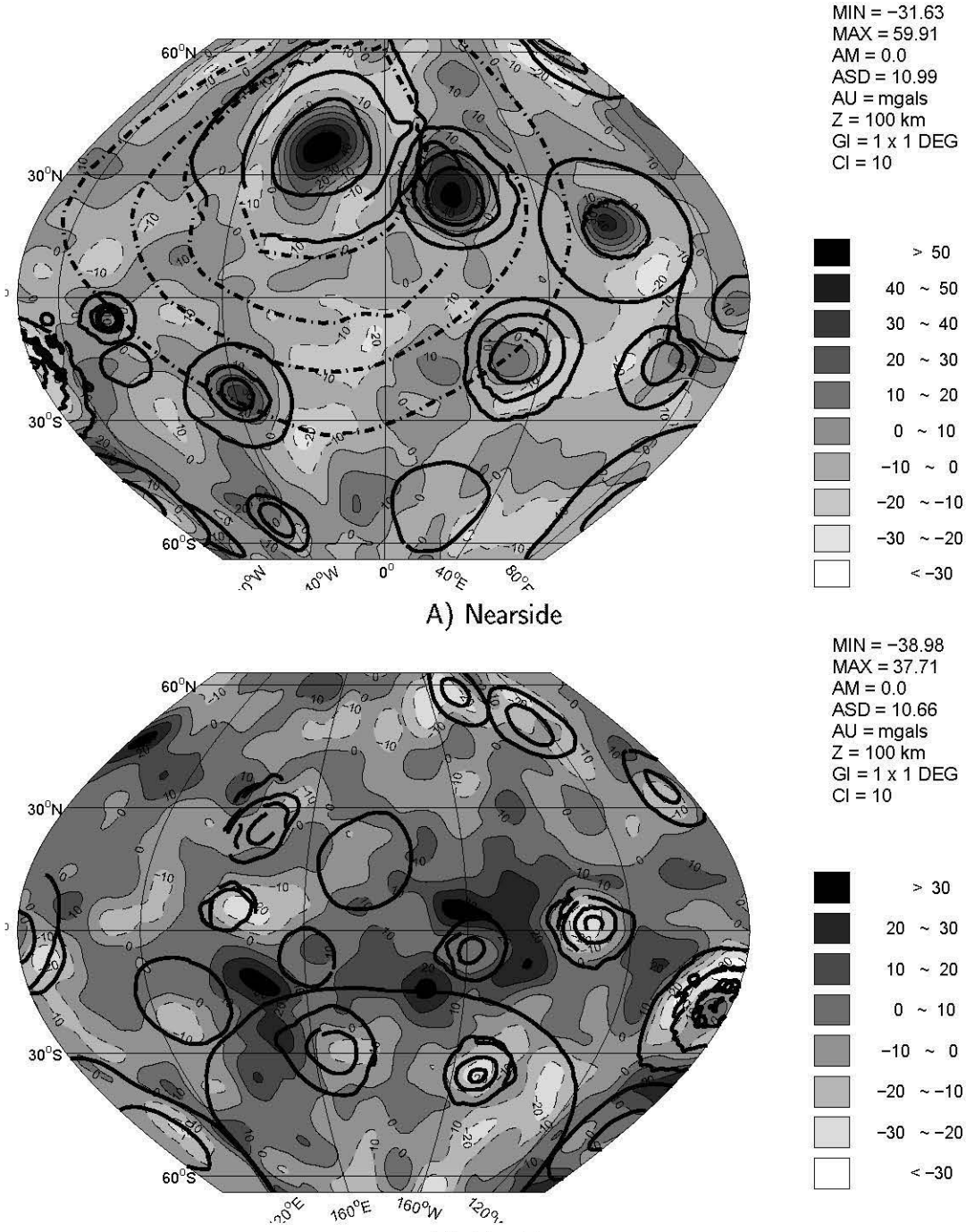

Figure 13: Inferred subcrustal components (*STDFAGA*) of *TDFAGA* (Figure 7).

Table 1 summarizes the various signals developed from the spectral correlation analysis between *TGE* and *FAGA*. The interpretation of the signals based on the decomposition of *FAGA* facilitate a comprehensive model for lunar mass variations.

2.4 Significance of the Crustal Modeling Results

Spectral correlation analysis of lunar free-air gravity anomalies (*FAGA*) as represented by LP75G and the gravity effects of the terrain (*TGE*) yielded the decomposition of *FAGA* into terrain-correlated (*TCFAGA*) and terrain-decorrelated (*TDFAGA*) components. Spectral correlation analysis between *FAGA* and *TDFAGA* also yielded estimates of the crustal (*CTDFAGA*) and subcrustal (*STDFAGA*) components of *TDFAGA*. In addition, the analysis estimated the compensated components of the terrain gravity effects (*CTGE*), as well as corresponding crustal thickness variations and their related *TCFAGA*-equilibriating adjustments. These results were mostly developed assuming isostatic compensation by thickness variations of the crust with a density contrast of -0.5 g/cm^3 relative to the mantle. They provide insight on the topographic, thickness, stress and strength dichotomies of the lunar crust, as well as the crustal attributes of the giant and major lunar basins that are considered below.

2.4.1 Crustal Dichotomies

The fundamental tectonic differentiation of the lunar crust into nearside and farside components is clearly evident in the topographic and crustal thickness data of Figures 3 and 9, respectively. For the nearside, lowland mare topography is dominant that is inversely correlated with the highland topography of the farside. To first order, half of the lunar topography is inversely correlated to the other half most strongly at the lag of 160^o E. The nearside topography ranges over 9.6 km with a standard deviation of 1.2 km that reflects a smoother topography than for the farside which ranges over 16 km with a standard deviation of 2.6 km. The gravity effects of the topography also reflect this nearside and farside dichotomy as shown in the Figure 4 where the range and statistics of *TGE* on the farside are more than twice those of the nearside.

The crustal thickness model produced in this study is also dichotomized between the near and far sides. An average global crustal thickness of 63 km was estimated by the wavenumber correlation analysis (WCA) that compares favorably with the 61-km average from Neumann et al. (1996) and the 60-km average of Wieczorek and Phillips (1998). However, the 13-km difference between farside and nearside crustal thicknesses in Figure 9 is much more consistent with the 12-km estimate of Neumann et al. (1996) than the 4-km value obtained by Wieczorek and Phillips (1998), which was based on a radially stratified crust that ignored possible lateral density variations. Also, the crustal thicknesses in Figure 9 for the farside were estimated to range over about 145 km with a standard deviation of roughly 21 km, whereas for the nearside the crustal thicknesses are dramatically reduced, only ranging over about 87 km with a standard deviation of roughly 11 km.

Signal	**Generated by**:	**Interpreted for**:
TGE	Visible topographic masses	Gravity effect of topographic masses
FAGA	Total density distribution of the Moon	Crustal and subcrustal mass variations
TCFAGA	Components of *FAGA* that correlate with *TGE*	Uncompensated crust that reflect • Isostatic properties of basin central mass anomalies • Residual stress field of crust resulting from impacts
TDFAGA	*FAGA* - *TCFAGA*	• Intracrustal density variations that may include mare fill, cryptomare, impact melt, crustal intrucion • Subcrustal mass distribution due to impacts and other effects
CTGE	*CTGE* = *TGE* - *TCFAGA*	Moho undulation
CTDFAGA	Short wavelength features of *TDFAGA*	Intracrustal mass anomalies that may include mare fill, impact melt, and cryptomare
STDFAGA	Long and intermediate wavelength features of *TDFAGA*	Subcrustal mass variations that may include the integrated effects of lateral density variation of the • core-mantle boundary • boundary undulations of the stratified mantle

Table 1: Interpretation of signals produced from correlation analysis of lunar terrain gravity effects (*TGE*) and free-air gravity anomalies (*FAGA*)

Viscous relaxation of the stresses generated by the topographic relief of large lunar impact basins has been suggested as a major factor for preserving impact basin topography (Solomon et al., 1982). For example, a model for the rebound of Mare Orientale by the deformation of a viscous layer of lower density overlain by a low-viscosity half-space of higher density suggests that an initial depth of 8 km would relax to the present value of 2 km through viscous deformation of a 50 km thick surface layer (Solomon et al., 1982). From the radial adjusment model of this study in Figure 10, the ASD for the farside crust is roughly 30% larger than it is for the nearside crust. This difference suggests that the farside crust may support substantially larger loads than the nearside crust. This strength dichotomy may reflect differences in the rheological and compositional properties of the crust and lithosphere at the time of basin formation. For example, it has been suggested that a dichotomy in density may have been generated by the asymetric crystalization of a primordial lunar core which preferrentially emplaced radiogenic elements toward the nearside mantle and thus may have contributed to center-of-mass and -figure offsets (Stevenson, 1980). Accordingly, the farside crust, being predominantly anorthosite (Wieczorek and Phillips, 1997) and deficient in radioactive elements, may have been more rigid than the nearside crust during bombardment times.

The inferred crustal properties of the farside also may reflect a much more brittle response to the impacts than may have been the case for the nearside crust. In fact, the strength dichotomy related to the possible compositional asymmetry of the lithosphere is consistent with the distribution of mostly non mascon-bearing impact basins on the farside while nearside basins nearly all tend to involve mascons. Topographic relaxation or smoothing of the Moho may have been attained by subcrustal flow from the added heat of the gravitational differentiation of the primordial core (Stevenson, 1980) and the pooling of radioactive heating elements in the region of Procellarum basin on the nearside (Korotev, 2000). More rapid subsequent cooling of the lunar farside may have resulted in minimal subsurface flows while the nearside crust may have cooled relatively slowly due to the asymetric compostion of the lithosphere.

This study suggests that the farside may have responded more rigidly to basin-forming impacts than the nearside. The lunar crust beneath the large basins was weakened by the impact-producing stresses and fractures (Arkani-Hamed, 1998). Hence, the mascon loads were largely decaying by the viscous deformation of the mantle in the early history of the Moon, but later were supported as the outer part of the Moon became more competent (Arkani-Hamed, 1998).

Analysis of the giant nearside Procellarum and farside South Pole-Aitken basins may demonstrate additional aspects of these first order crustal dichotomies.

2.4.2 Crustal Models of the Giant Basins

The giant 3200-km diameter, pre-Nectarian Procellarum basin (Figure 1) was initially postulated on the basis of the arcuate highland terrain that surrounds the lunar nearside mare (Whitaker, 1981; Wilhelms, 1987). However, the existence of this basin has been controversial with some investigators attributing it to an endogenic origin (e.g., Mason and Melson, 1970; Rukl, 1976), while others have denied its existence entirely (e.g., Spudis, 1993). In particular, it was argued that if this basin had an exogenic origin, then most of the pristine lunar crust in the Imbrium target area would have been

retained (Spudis, 1993). However, a study of the topography obtained from Clementine inferred a topographic low for Procellarum with a central crustal thickness of 47 km and a negative gravity anomaly near the center that may be interpreted in the context of an impact event (Zuber et al., 1994; Neumann et al., 1996).

The top and bottom panels of Figure 14 give NS and EW crustal cross-sections, respectively, through Procellarum. Lighter grey shading differentiates the inferred crust from the mantle that is denoted by the darker grey shading. The dashed-dot lines denote the equilibrium Moho that nullifies *TCFAGA*. It was obtained by adding the radial Moho adjustments estimated in Figure 10 to the Moho inferred from the compensating *TGE* (*-CTGE*) of Figure 8, which in Figure 14 is marked by the dashed lines. The surface topography has been exaggerated 5 times to emphasize its features better. The NS section shows relatively subdued Moho uplift beneath the ancient Nubium basin centered around 20^o S and a sharper mantle plug beneath the younger Imbrium basin centered roughly on 40^oN. The EW crustal cross-section shows the relatively pronounced mantle plug beneath Serenitatis at about 20^o E that is comparable in age to the Imbrium basin.

The crust beneath the superposed Nubium, Imbrium, and Serenitatis basins (Figure 14) shows distinct thinning that reflects their impact origins. Relative to the more ancient Nubium basin, the greater differences between present and equilibrated Moho for Imbrium and Serentatis may reflect the increase in lithospheric viscosity and strength with age. The Nubium basin, as well as Mare Tranquilitatis and Mare Fecunditatis, had been defined as pre-Nectarian nonmascon mare basins (Wilhelms, 1987). From the cross-section in Figure 14, the near coincidence of the Moho with the equilibrium Moho for the Nubium basin suggests that it may be essentially in isostatic equilibrium. Hence, the gravity effect of its relatively muted mantle plug is greatly diminished at 100 km altitude.

In general, the Procellarum basin appears to be underlain by a generally uniform slab roughly 60-km thick, which may consist almost entirely of relatively mafic, Th-rich material (Joliff et al., 2000). The "High-Th Oval Region" of Oceanus Procellarum (Haskin, 1998) has also been identified as the "Great Lunar Hotspot" (Korotev, 2000), where late stage liquids enriched in U and KREEP were presumably pooled from the asymmetric crystalization of a primordial lunar magma ocean (Stevenson, 1980). The apparent lack of a regionally uplifted Moho revealed by this study for Oceanus Procellarum is consistent with its inferred endogenic origin. By the time of the Imbrium impact at roughly 3.9 Byr, the "hotspot" was at least partially differentiated (Korotev, 2000), so that with the collapse of the Imbrium tansient crater radioactive elements were raised closer to the surface (Melosh, 1989). Accordingly, the Moho that was raised by meteorite impact may have greatly flattened over time by viscous relaxation (Solomon et al., 1982). Crustal relaxation may also have been significantly enhanced by a high thermal gradient due to the abundance of radioactive elements in the mantle and crust (Stevenson, 1980; Haskin, 1998; Korotev, 2000).

On the farside, the great South Pole-Aitken basin, being 13 km deep and 2600 km in diameter, is the largest known impact basin of the solar system (Spudis, 1993). The top and bottom panels of Figure 15 show the NS and EW crustal cross-sections, respectively, through the South Pole-Aitken basin. The surface topography in each panel is vertically exaggerated by a scale factor of 2. Other features in these panels are the same as previously described for Figure 14.

The inferred crustal structure suggests that the South Pole-Aitken basin may be overlain by a

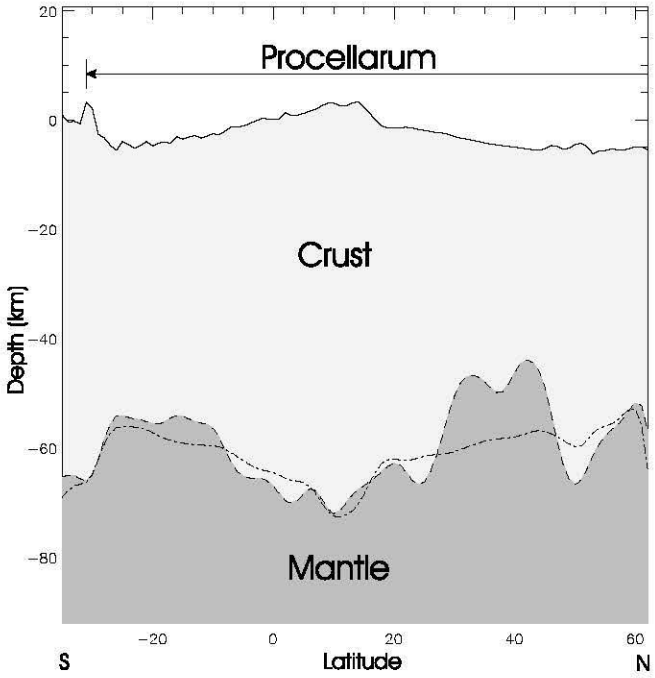

A) NS section along 25°W longitude.

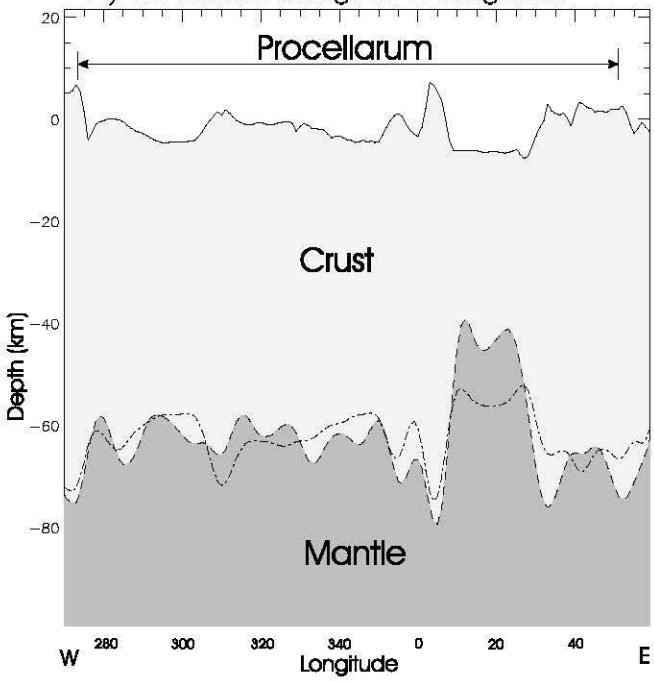

B) EW section along 25°N latitude.

Figure 14: Crustal cross-sections for Procellarum. The surface topography is vertically exaggerated by a factor of 5.

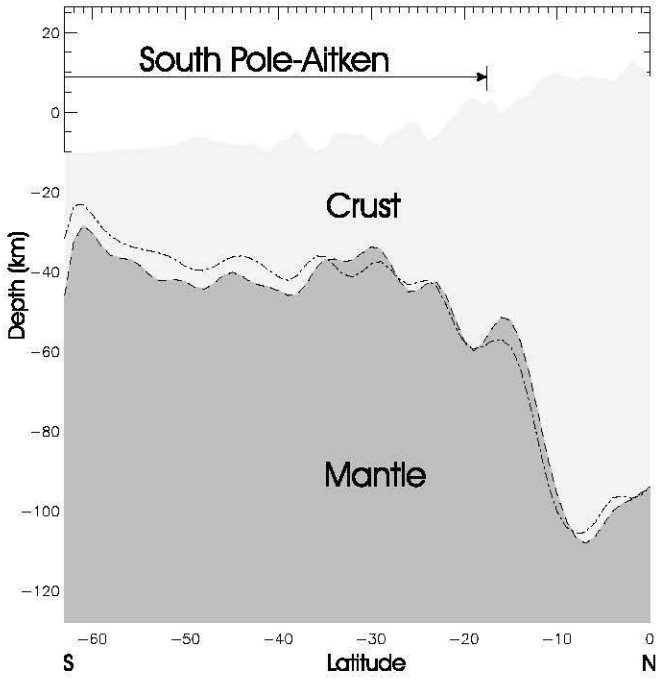

A) NS section along 170°W longitude.

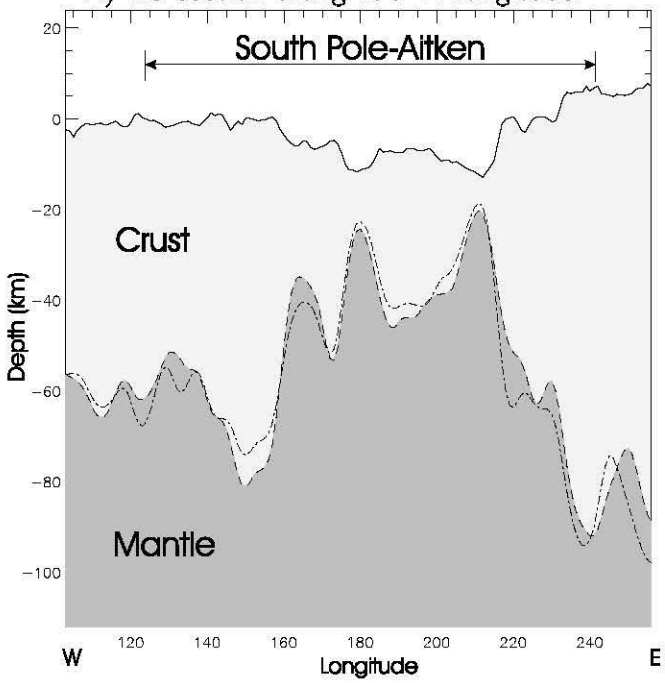

B) EW section along 40°S latitude.

Figure 15: Crustal cross-sections for the South Pole-Aitken basin. The surface topography is vertically exaggerated by a factor of 2.

relatively distinct regional mantle plug that is flanked by thicker-than-average crust. Elevated topography with a thickened crust that extends to the northeast may partly reflect the effects of an oblique impact by a large massive bollide (Neumann et al., 1996). Impacts of later age may have strongly modified the basin floor and obscured its original surface structures. These later impacts also appear to have modified the mantle plug that resulted from the original South Pole-Aitken impact. Examples of these modifications in Figure 15 include the Ingenii basin where the crust is thinnest in the top panel and at about 180°E in the bottom panel, as well as the thinned crust beneath the Apollo basin at about 210°E in the bottom panel. These later impacts occured after most of the primary structure had undergone viscous relaxation (Neumann et al., 1996). The near coincidence of the inferred present and equilibrated Moho suggests that the basin is mostly compensated, which is consistent with its muted gravity signal (Zuber et al., 1994).

The South Pole-Aitken basin was formed early in lunar history (Wilhelms, 1987) and undoubtedly had a great effect on the Moon's subsequent thermal evolution, especially on the crust and upper mantle in the vicinity of the impact. It occupies a broad topographic depression to a depth of about 13 km below the surrounding highlands. However, despite its extensive depth and crustal thinning to about 18 km, significant resurfacing by mare basalt did not occur (Neumann et al., 1996), which also is reflected by the related low-amplitude *CTDFAGA* of Figure 12. Inferred crustal thicknesses for this basin indicate that a significant amount of lower crustal material was not excavated, even though impact scaling laws predict that the impact should have excavated well into the mantle (Wieczorek and Phillips, 1999).

The apparent absence of a mantle plug for Procellarum may not only reflect an endogenic origin for the basin, but also the dichotomy of thermal and strength properties of the ancient lithosphere. Crustal viscosities on the farside of the Moon were at least an order of magnitude larger than the contemporaneous viscosities on the nearside (Solomon et al., 1982). Hence, the preservation of regional crustal features of the farside, such as the mantle plug beneath the South Pole-Aitken basin was probably enhanced greatly relative to the features of comparable age nearside basins such as Mutus-Vlacq and Balmer-Kapetyn that may be characterized by near-average crustal thicknesses.

Additional aspects of the dichotomized lunar crust may be inferred from analyses of the more local differentiations of the crust at the scales of its major basins.

2.4.3 Crustal Models of the Major Basins

Craters or topographic basins represent perhaps the most ubiquitious tectonic feature of the lunar crust. In this and the next three sections, the gravimetric and crustal attributes are compared for major lunar basins with diameters of roughly 300 km and greater.

The lunar crustal structure of the major lunar basins is generalized by the cross-sections through the 4 nearside (i.e., Humboltianum, Humorum, Nectaris, and Serenitatis) and farside (i.e., Hertzprung, Mendel-Rydberg, Moscovience, and Orientale) basins given in Figures 16 and 17, respectively. These 8 basins were selected because their crustal structures appear to have sustained minimal alteration from superposed or nearby impact events.

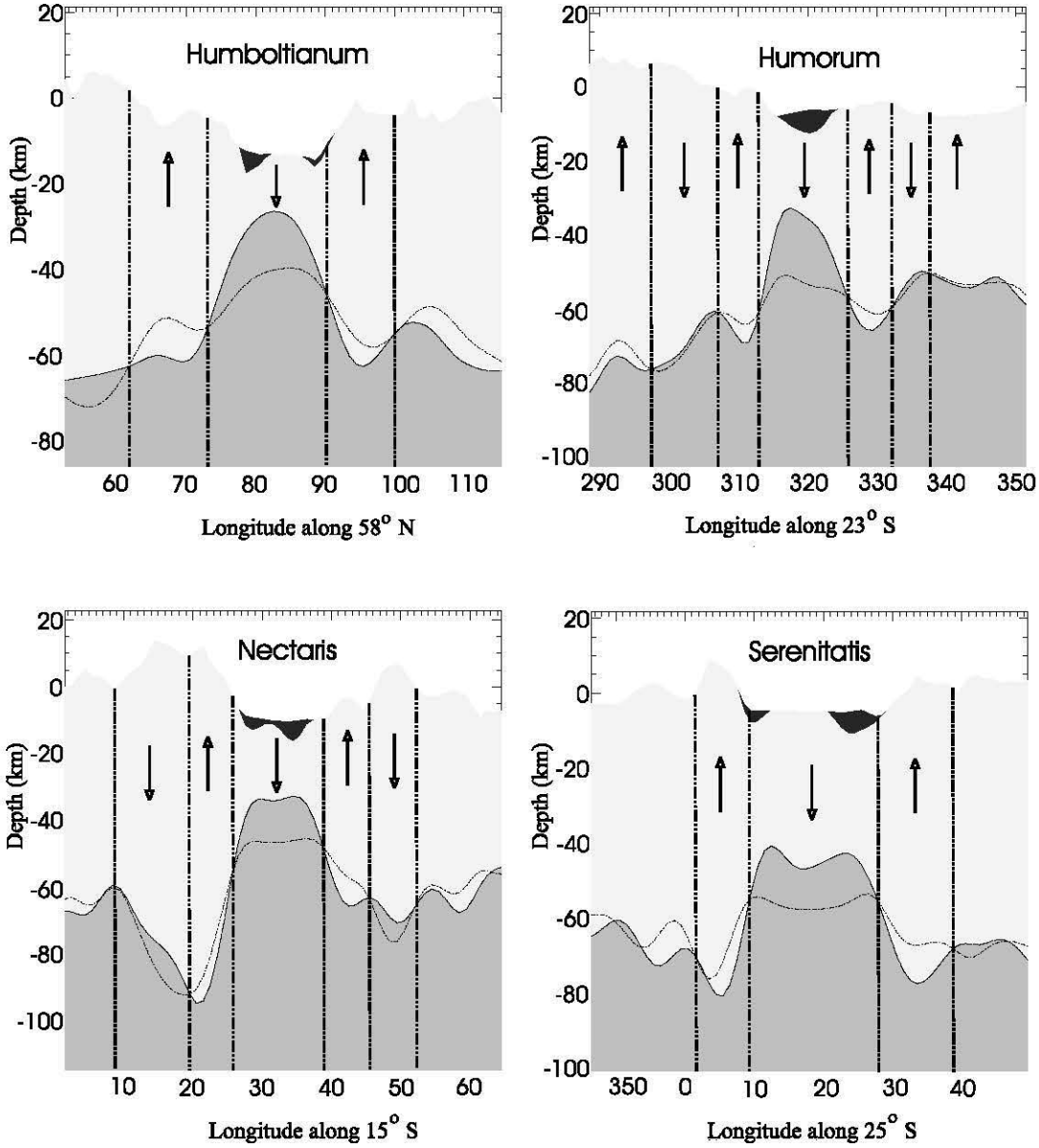

Figure 16: Crustal sections for the nearside Humboltianum, Humorum, Nectaris and Serenitatis basins. Each panel shows the crust and mantle in the lighter and darker grey shading, respectively, with black shading marking inferred distributions of mare fill. The dash-dot line represents the equilibrium Moho. Arrows indicate the direction of lithospheric thrusting that can nullify *TCFAGA*. A vertical exaggeration of 5:1 was used to represent the surface topography and mare fill.

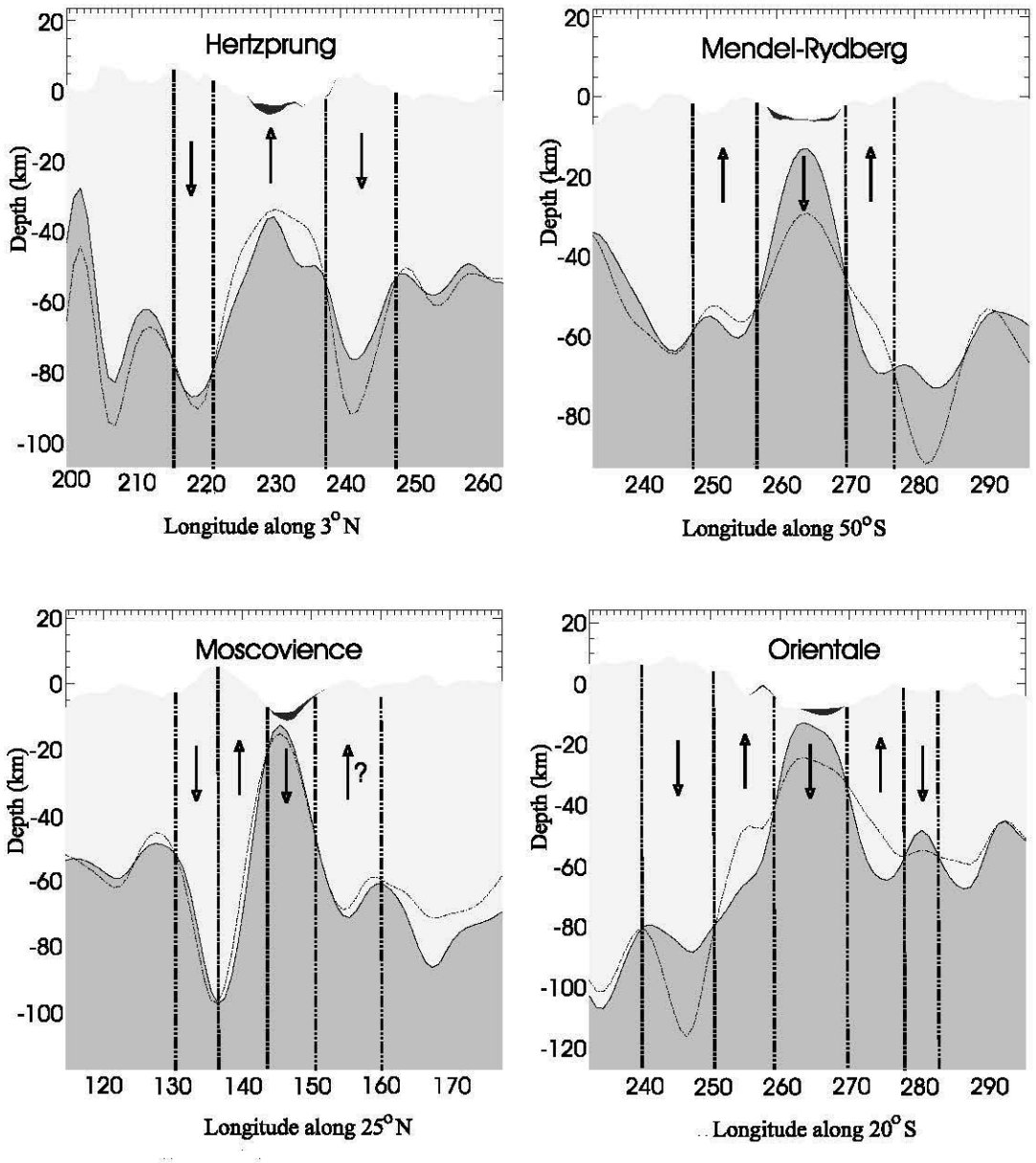

Figure 17: Crustal sections for the farside Hertzprung, Mendel-Rydberg, Moscovience and Orientale basins. Surface topography is at 2:1 vertical exaggeration.

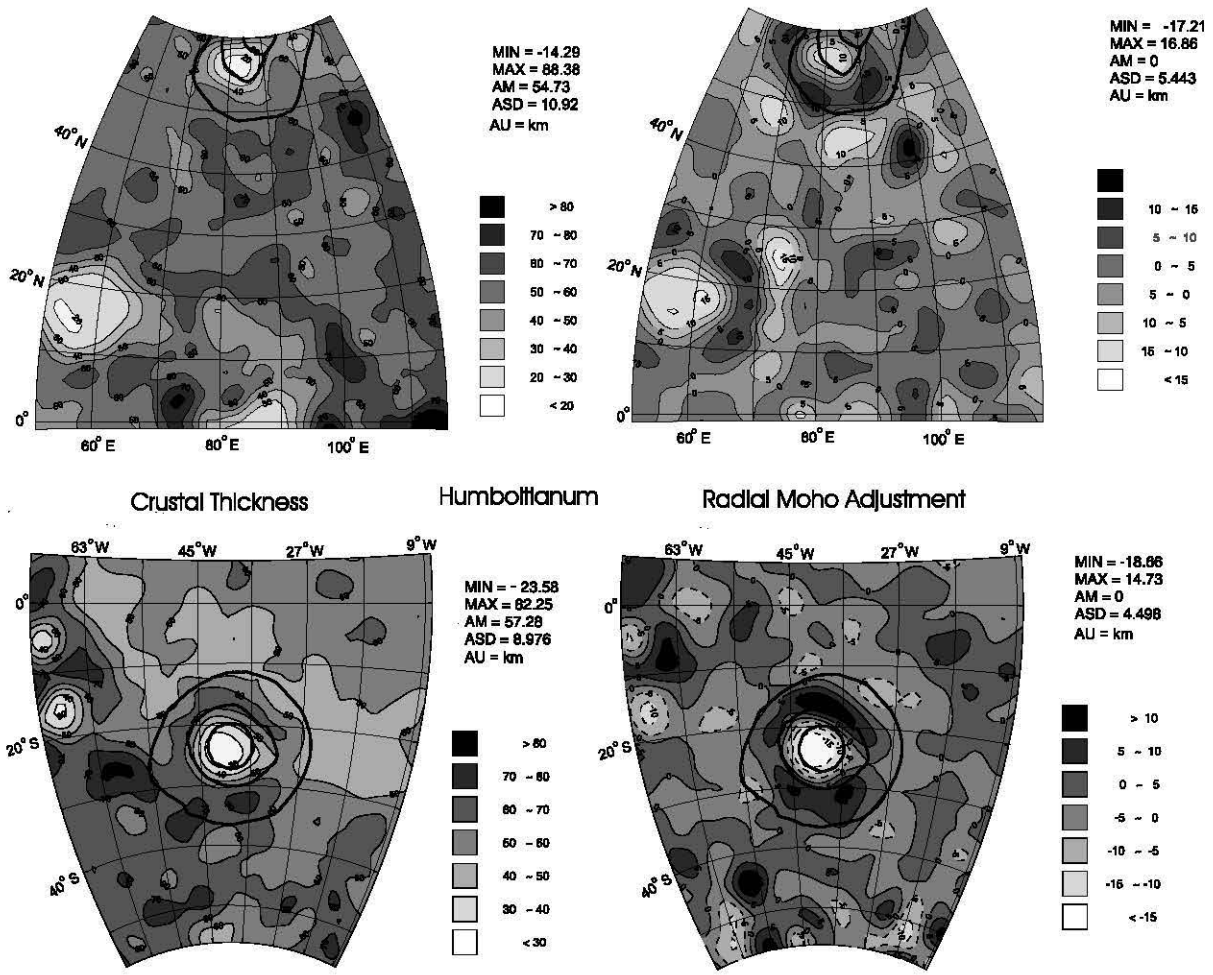

Figure 18: Crustal thickness variations (left panels) and equilibrating Moho adjustments (right panels) in km for the nearside Humboltianum (top) and Humorum (bottom) basins.

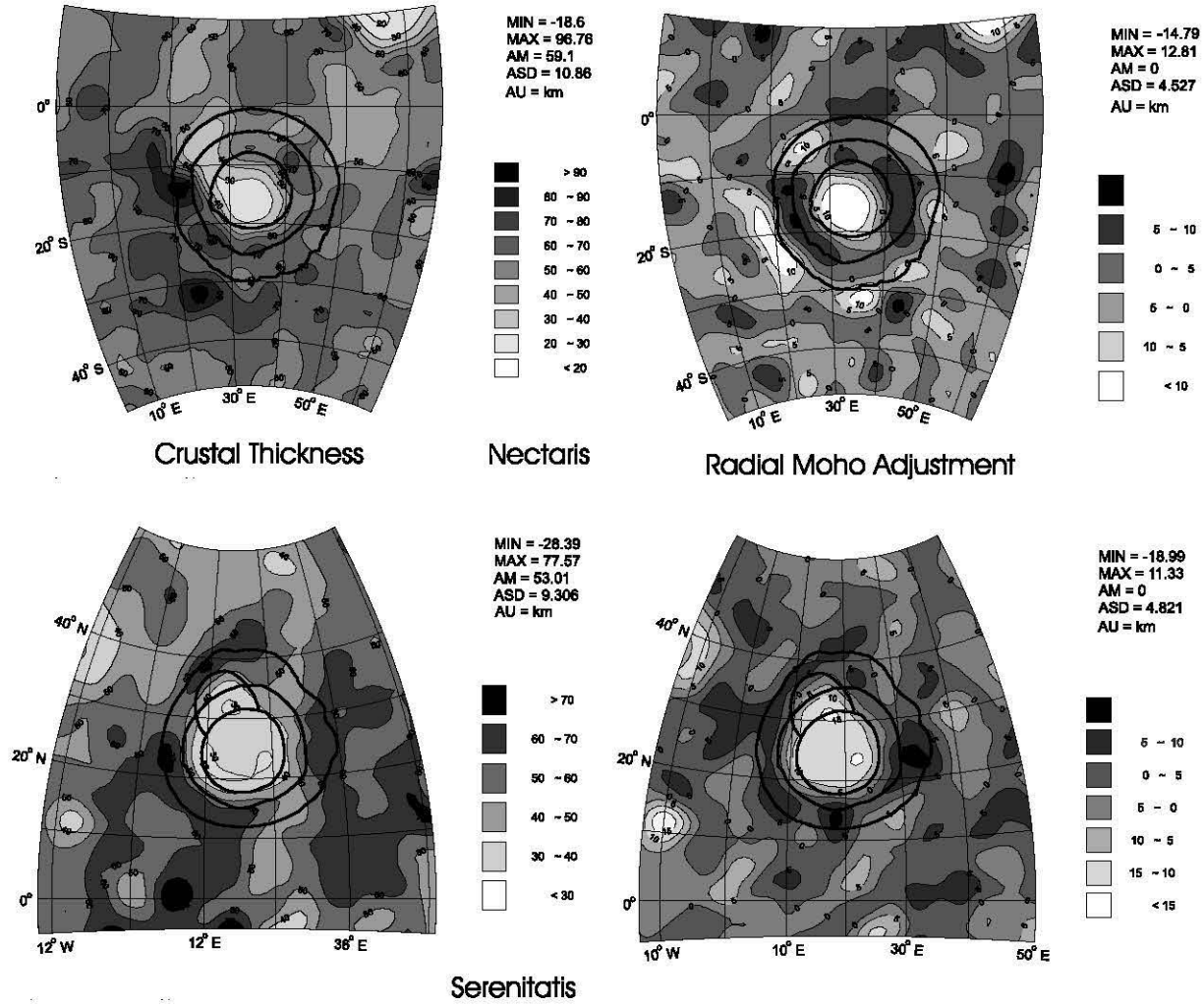

Figure 19: Crustal thickness variations (left panels) and equilibrating Moho adjustments (right panels) in km for the nearside Nectaris (top) and Serenitatis (bottom) basins.

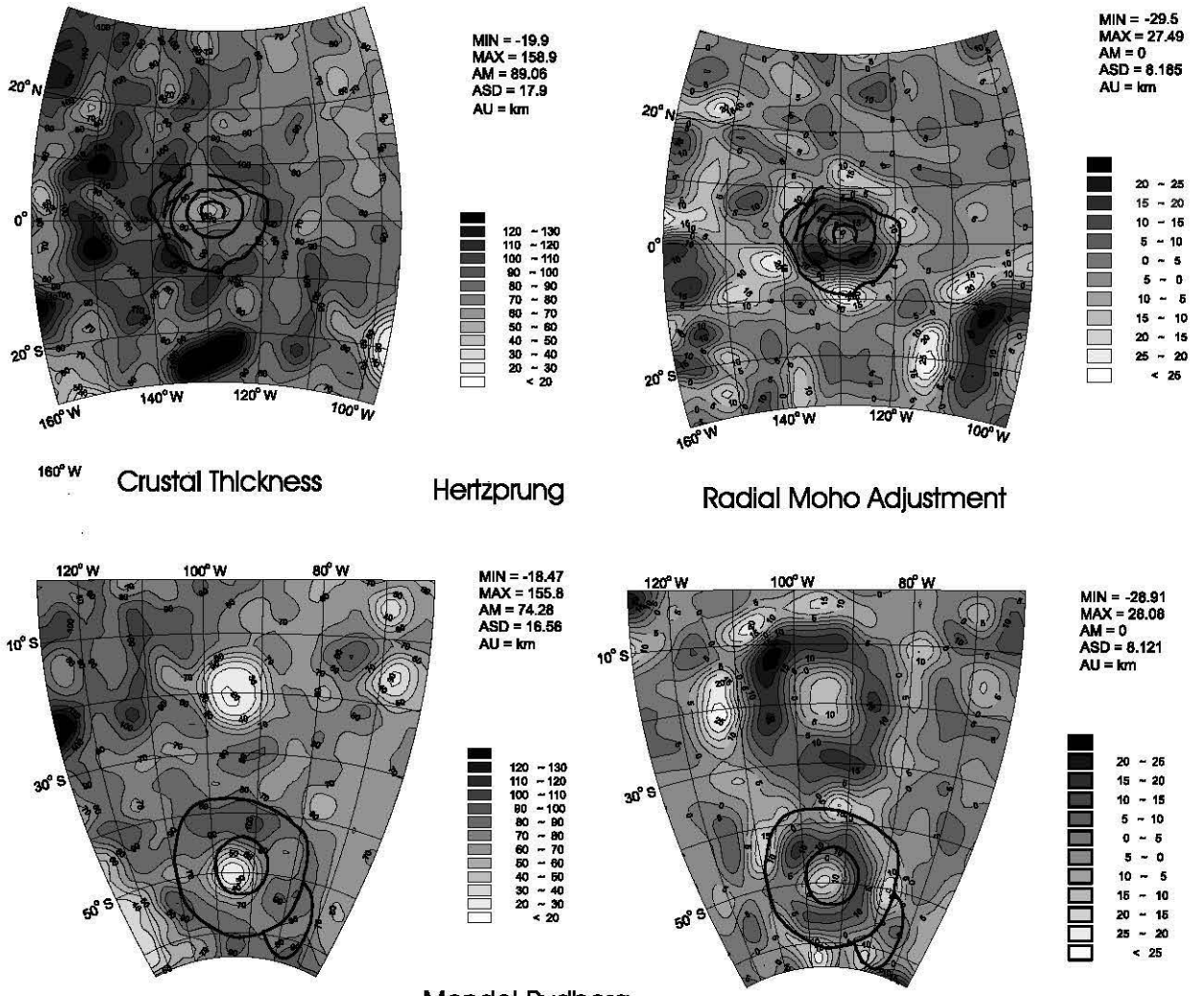

Figure 20: Crustal thickness variations (left panels) and equilibrating Moho adjustments (right panels) in km for the farside Hertzprung (top) and Mendel-Rydberg (bottom) basins.

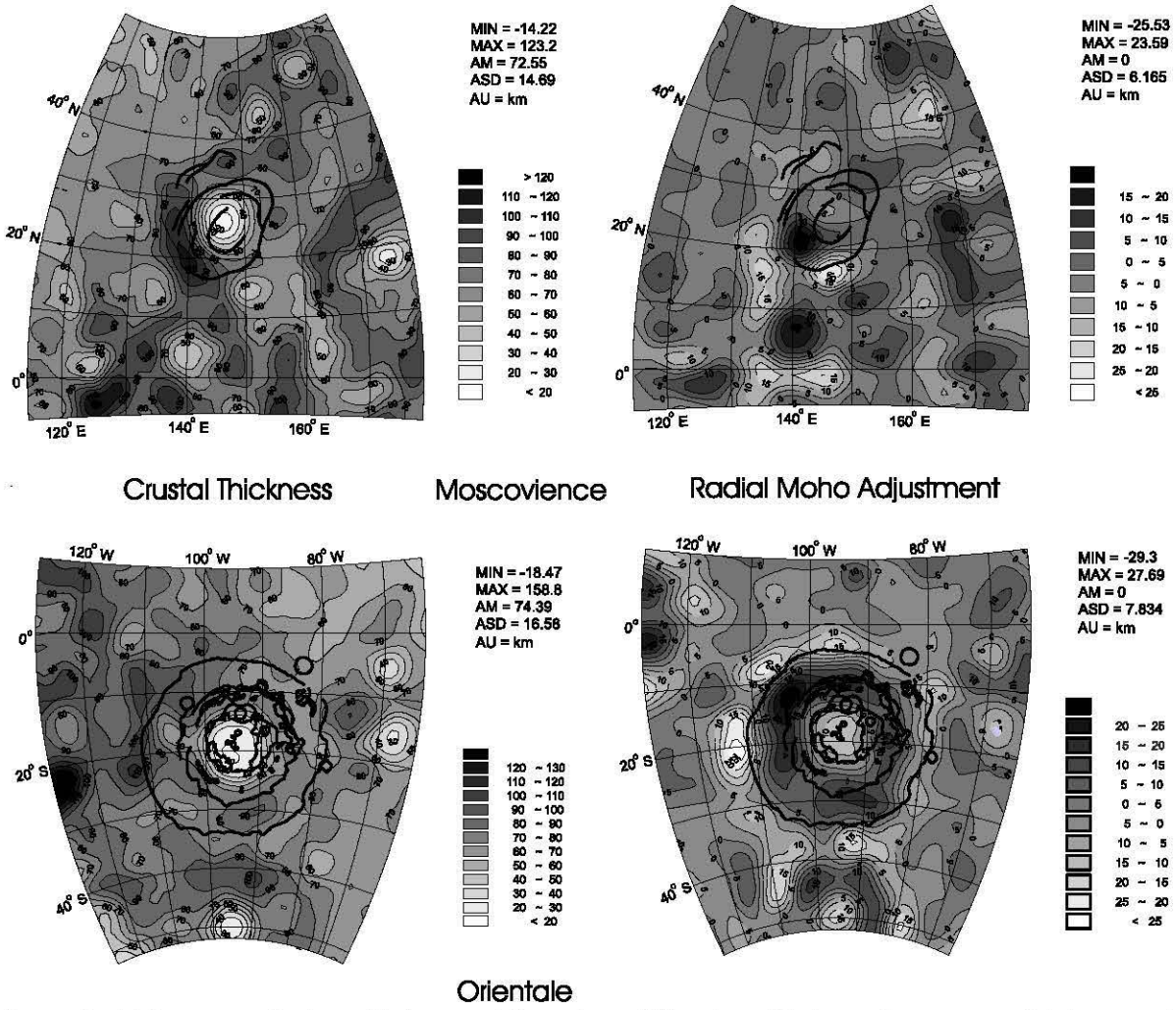

Figure 21: Crustal thickness variations (left panels) and equilibrating Moho adjustments (right panels) in km for the farside Moscovience (top) and Orientale (bottom) basins.

Maps that extend the inferred crustal thickness and isostatic attributes about a $64^o \times 64^o$ region centered on each of the 8 selected basins are given in Figures 18 - 21. The strong azimuthal symmetries of the mantle plugs in these maps reflect basins that may have been minimally altered by subsequent impacts. A more comprehensive catalogue of these maps and crustal cross-sections for all 27 basins of this study is given in Appendix E.

The features in the panels of Figures 16 and 17 are the same as described in Figure 14 except for the vertical lines drawn at the points where the differences between the inferred present Moho and equilibriated Moho boundaries are zero. These cross-over points correspond to where the zero contours of Figure 10 intersect the cross-sections. Between the cross-over points, the differences are either positive or negative with arrows indicating the relative motions of the crust that can nullify *TCFAGA* and bring the cross-section into isostatic equilibrium.

In general, all nearside basins and some farside basins (e.g., Coulomb-Sarton, Freundlich-Sharonov, Mendel-Rydberg, and Orientale) appear to involve mantle plugs that were uplifted beyond their isostatic positions and hence the stresses due to their loads may not have been completely relieved by viscous relaxation. However, the farside Hertzprung basin, which presumably occurred relatively late in lunar history (Wilhelms, 1987), may be characterized by an undercompensating mantle plug. Indeed, most of the farside basins (e.g., Birkoff, Lorentz, Keeler-Heaviside, Korolev, Mendeleev, and Tsiolkovskiy-Stark) appear to be associated with similar undercompensating mantle plugs. These subisostatic mantle plugs presumably were produced when the farside lithosphere had become significantly more rigid than the nearside lithosphere.

2.4.4 Crustal Thickness Estimates for the Major Basins

Table 2 contrasts the crustal thicknesses inferred for the major nearside and farside basins from SRB (Bratt et al., 1985), GAN (Neumann et al., 1996), JA-H (Arkani-Hamed, 1998) and the wavenumber correlation analysis (WCA) of this study. The acronymns SRB, GAN, and JA-H are the initials of the principal authors of the respective studies. Beneath the centers of many of the nearside basins, the crustal thickness estimates from GAN, JA-H, and WCA are remarkably consistent. This compatibility helps support the veracity of the new WCA approach for modeling the nearside lunar crust. However, the SRB estimates are significantly larger than the other three inferences, which probably reflects the use of lower quality data and considerably more regional crustal blocks in the inversion for crustal thickness. For the nearside Grimaldi and Humboltianum basins, as well as for many of the farside basins, quite large disparaties are also evident between the WCA and GAN estimates. These basins are located in regions of relatively rugged terrain where the disparate crustal thickness estimates may well reflect differences in accounting for the terrain gravity effects by the two studies.

2.4.5 Basaltic Fill Thickness Estimates for the Major Basins

The collapse of the transient crater after impact provides a topographic depression that was filled with mare basalt during the period of mare volcanism. Thicknesses for the basaltic fill have been estimated directly from the topographic signatures of the basins (e.g., Dehon, 1974: 1977; 1979;

Nearside Basins				
Study ⇒	SRB	GAN	JA-H	WCA
Balmer-Kapetyn (B-K)				47.6
Crisium* (Cri)	55	20.3	24.8	18.6
Cruger* (Cru)				29.8
Grimaldi* (Gri)		42.9		33.7
Humboltianum* (Humb)		34.8		14.3
Humorum* (Hum)	60	21.9	23.5	23.6
Imbrium * (Imb)		36.3	29.2	31.7
Mutus-vlacq (M-V)				44.6
Nectaris* (Nec)	60	24.7	17.5	23.2
Schiller-Zuchius* (S-Z)				42.3
Serenitatis* (Ser)	60	31.2	30.5	29.2
Smythii* (Smy)	65	26.3	23.5	23.0
Farside Basins				
Apollo (Apo)		55.0		15.3
Australe (Aus)		57.9		58.2
Birkhoff (Bir)				53.5
Coulomb-Sarton* (C-S)		48.2		28.6
Freundlich-Sharonov* (F-S)		45.3		25.0
Freundlich Sharonov*				61.1 51.8
Hertzprung* (Her)		71.7		52.2
Ingenii (Ing)				29.9
Keeler-Heaviside (K-H)				59.7
Korolev (Kor)		79.7		68.9
Lorentz (Lor)				55.4
Mendeleev (Men)		61.4		44.3
Mendel-Rydberg* (M-R)		51.1		20.3
Moscovience* (Mos)		39.8		14.2
Orientale* (Ori)	19	21.8	17.5	18.5
Tsiolkovskiy-Stark (T-S)				54.1

Table 2: Lunar crustal thickness estimates (km) for major basins from SRB (Bratt et al., 1985), GAN (Neumann et al., 1996), JA-H (Arkani-Hamed, 1998), and the WCA (wavenumber correlation analysis) of the present study. *⇒ reported mascon-bearing basins (e.g., Neumann et al., 1996; Konopliv et al., 1998). Abbreviated basin names are given in brackets.

Dehon and Waskom, 1976). However, the basaltic fill thicknesses obtained from these analyses may have been overestimated by a factor of two because the amount of degradation of the basins since their formation was not taken into account (Hörz, 1978). In addition, poor data coverage in these early studies may have limited estimates at the centers of the maria (Williams and Zuber, 1998).

Other approaches have also been used to estimate mare fill thicknesses. Pike (1974) suggested that the morphology of a crater may be defined by a power law relating its diameter and depth. Improved coverage provided by altimetric profiles from the Clementine LIDAR was used to estimate the mare thicknesses for 29 large craters and basins by this power law (Williams and Zuber, 1998). Mare basalt fill thickness estimates have also been indirectly estimated from modeling Bouguer gravity anomalies (e.g., Head, 1982; Bratt et al., 1985; Arkani-Hamed, 1998).

The WCA also was used to estimate the fill thickness for the Mare Orientale basin (von Frese et al., 1997b). More generally, at the satellite altitude (100 km) of the WCA, the longer wavelength *TGE* have extracted regional *TCFAGA* components that may be readily related to possible uncompensated components of the mantle plug as shown in Figure 10. However, the lack of shorter wavelength components in the *TGE* has resulted in the WCA passing the possible higher frequency effects of the mare basalts into the shorter wavelength components of *CTDFAGA* (Figure 12). Although the *CTDFAGA* are largely in the noise range of *FAGA*, many of the basins are systematically characterized by *CTDFAGA* maxima that may be readily interpreted for the gravity effects of mare fill (e.g., von Frese et al., 1997b).

Table 3 compares the WCA estimates of basaltic fill thicknesses for the major basins against the estimates from the other gravity-based studies (Bratt et al., 1985; Neumann et al., 1996; Arkani-Hamed, 1998), as well as analyses from photogeologic (Dehon, 1974; 1977; 1979; Dehon and Waskom, 1976) and crater morphology (Williams and Zuber, 1998) analyses. The WCA estimates were obtained for each basin by the inversion of *CTDFAGA* over a $64^o \times 64^o$ basin-centered region. *CTDFAGA* maxima over each basin were related by inversion to the thicknesses of mare basalt fill beneath the topographic surface. In particular, 1^o prism thicknesses beneath the topographic surface were estimated using GLQ integration and a 0.5 g/cm^3 density contrast of mare basalt fill relative to non-mare crust (e.g., Bowin et al., 1975; Bratt et al., 1985; Zuber et al., 1994; von Frese et al., 1997). For each of the basins considered in this study, the mismatch between the gravity effects predicted from the WCA estimates of basaltic fill thickness and the *CTDFAGA* is negligible.

The WCA thickness estimates for basaltic fill are significantly thinner than those obtained from the other gravity studies. The disparities clearly reflect differences in the gravity signals that the various studies have attributed to basaltic fill effects. Based on the correlations between *TGE* and *FAGA*, the WCA attributed most sources of lunar gravity anomalies to crustal thickness variations and related isostatic mass imbalances, as well as subcrustal mass differentials. Accordingly, only the residual *CTDFAGA* of relatively marginal gravity signals are available for constraining the effects of basaltic fill and other intracrustal mass variations. However, in contrast to the estimates from the other gravity studies, the WCA predictions of basaltic fill thickness appear to better match the non-gravity estimates, especially those from the photogeologic interpretations. This trend to thinner estimates also may hold for analyses of remote sensing data where, for example, an average basalt thickness of 0.8 km was recently obtained for the Humorum basin (Budney and Lucey, 1998).

Nearside Basins						
Study ⇒	PG	SRB	GAN	JA-H	CG	WCA
Balmer-Kapetyn						0.6
Crisium*	3-4	4.1	7.4	4.2	2.9	1.9
Cruger*						1.0
Grimaldi*	0.5		3.6		3.5	1.4
Humboltianum*						1.5
Humorum*	2.5	3.9	2.7	4.5	3.6	1.9
Imbrium *	1.5	2.2	9.2	3.9	5.2	1.1
Mutus-vlacq						
Nectaris*	2.3	4.5	4.5	5.5	0.8	1.2
Schiller-Zuchius*						0.9
Serenitatis*	3.5	4.5	8.5	3.3	4.3	1.3
Smythii*	0.5	1.8	4.9	4.7	1.3	1.2
Farside Basins						
Apollo						1.0
Australe						1.3
Birkhoff						0.5
C-Sarton*						1.2
F-Sharonov*						1.6
Hertzprung*						1.3
Ingenii						0.9
Keeler-Heaviside						0.3
Korolev						1.5
Lorentz						0.9
Mendeleev						1.0
Mendel-Rydberg*						0.6
Moscovience*						1.5
Orientale*	1-2	3.8	1.7	5.5	0.6	0.7
Tsiolkovskiy-Stark						1.1

Table 3: Basaltic fill thickness estimates (km) for major lunar basins from photogeologic (PG) interperation (Dehon 1974; 1977; 1979; Head, 1974; Greely, 1976; Waskom and DeHon, 1976), SRB (Bratt et al., 1985), GAN (Neumann et al., 1996 - as adapted from Solomon and Head (1980)), JA-H (Arkani-Hamed, 1998), crater morphology (CG) analysis (Williams and Zuber, 1998), and the WCA (wavenumber correlation analysis) of the present study. *⇒ reported mascon-bearing basins (e.g., Neumann et al., 1996; Konopliv et al., 1998).

This WCA suggests that the local results obtained for Mare Orientale by von Frese et al. (1997) may be extended in a straightforward manner for modeling the near-global properties of the lunar crust. Indeed, the main difference between the two studies in the vicinity of Mare Orientale is the way that *TDFAGA* were interpreted. On the $64^o \times 64^o$ scale of the Mare Orientale study, no evidence could be found for ascribing subcrustal mass variations to the *TDFAGA* (von Frese et al., 1997b). Hence, these *TDFAGA* were entirely attributed to upper crustal sources that included mare basalt fill extending about 4.0 km below the topographic surface. This thickness agrees strongly with photogeologic estimates, which indicate a thickness no greater than about 1 km (Head, 1974; Greeley, 1976) because submare topography appears to be exposed in the center of the basin. However, at the more global scale of the present WCA, significant components of *TDFAGA* may be attributed to subcrustal sources as suggested in Figure 11, so that surface and intracustal mass variations may now be related to a much smaller residual *CTDFAGA* component. Using these new *CTDFAGA* for Mare Orientale, a thickness estimate of about 0.7 km was obtained for the mare fill that is much better matched with the photogeologic estimates.

2.4.6 Major Basin Mascons and Maslites

The WCA results provide new insight on the possible crustal properties of the lunar basins. For example, the formation of lunar mascons invokes several controversial hypotheses (e.g., Konopliv et al., 1998). Mascons were originally identified by the presence of prominent positive free-air gravity anomalies that correlated negatively with the central topography of impact basins (Muller and Sjogren, 1968). After impact, extensive excavation of lunar material resulted in crater relaxation and the development of high crustal stresses (e.g., Melosh and McKinnon, 1978; Solomon et al., 1982; Bratt et al., 1985) and local melting (Spudis, 1993) within the crust. Accordingly, the Moho was uplifted by mantle rebound as a mantle "plug" into the heated and weakened crust (Wise and Yates, 1970; Bratt et al., 1985). A mascon anomaly, therefore, may reflect the combined higher density effects of the mantle plug and subsequent partial filling of the basin by mare basalt (Solomon and Head, 1979), although disparate views are held regarding the relative contributions of these components to the mascon anomaly (e.g., Wise and Yates, 1970; Phillips et al., 1972; Neumann et al., 1996; Arkani-Hamed, 1998).

A possible interpretation of the crustal attributes of the mascon anomaly is suggested by the WCA results. For example, a straightforward extension of the mascon anomaly completely in terms of its gravity attributes is possible by taking it as the positive free-air anomaly that is negatively correlated with the central terrain gravity effect of the impact basin. In this context, the mascon anomaly can involve positive components of *TCFAGA* and *CTDFAGA*.

In general, the gravity anomaly (GA) of the mascon for any basin may be readily estimated from the WCA results by

$$GA = TCFAGA + CTDFAGA. \tag{6}$$

Mascon gravity anomalies, being by definition the gravity effects of uncompensated central basin mass excesses, can only take on relatively positive or zero values of *TCFAGA* and *CTDFAGA*. The peak mascon gravity anomalies evaluated from the related peak *TCFAGA* and *CTDFAGA* values

are listed in Table 4 for the various basins considered in this study. Also listed are the percentages (%OC) of the GA that may be possibly related to overcompensating components of the mantle plugs. These percentages were calculated by

$$\% = [TCFAGA/GA] \times 100. \tag{7}$$

To the degree that the strength of the lithosphere may suspend overcompensating portions of the mantle in the crust to produce mascons, lithospheric strength may also suspend undercompensated portions of the crust in the mantle to produce mass difficiencies or "maslites." Possible examples of maslites are delineated by the central basin positive contours of Figure 10 which are predominantly found on the lunar farside.

Maslite gravity anomalies, being by definition the gravity effects of uncompensated central basin mass deficiencies, can only take on relatively negative or zero values of *TCFAGA* and *CTDFAGA*. For the various basins considered in this study, Table 4 lists the gravity anomalies (GA) of maslites evaluated from the superposition of related *TCFAGA* and *CTDFAGA* minima by equation 6. In addition, Table 4 gives the percentages (%UC) of the GA for maslites that may be attributed to the undercompensating effects of the mantle plugs by equation 7.

Also listed is the percentage of crustal thickness beneath each basin that is overcompensated (%CO) or undercompensated (%CU) by the mantle plug. These percentages were calculated by equation 7, but with *CTGE* in the denominator. The ratio in this modification of equation 7 is also equivalent to dividing the incipient radial adjustment value (Figure 10) by the crustal thickness (Figure 9) at the center of the basin.

Table 4 suggests quite a diversity of crustal properties for the major lunar basins. All the reported basins of the nearside having mascons, for example, appear to reflect a full complement of positive gravity contributions from an overcompensating mantle plug and basaltic fill. The five largest lunar mascon GA in descending order are affiliated with Serenitatis, Imbrium, Crisium, Nectaris, and Humorum. Table 4 also suggests that the mascon GA for nearly all the basins may be dominated by the positive gravity effects of the overcompensating mantle plugs.

On the farside, mascon GA are much smaller in amplitude and seem to reflect the predominantly positive gravity effects of the basaltic fill. Only the Coulomb-Sarton, Mendel-Rydberg, Moscovience, and Orientale basins appear to involve the full complement of positive gravity contributions from both the mantle plug and overlying basin mare fill. The Australe basin seems to exhibit only the positive effects of an overcompensating mantle plug. The rest of the farside basins appear to be dominated by central maslites that may reflect the negative effects of basin crust that is undercompensated by the mantle plug. The amplitudes of the central maslites generally range from -30 to -50 mGals. Many of these basins with prominent central maslites also appear to exhibit a small mascon GA that may be attributed to mare fill. On the nearside, a small-amplitude maslite GA may be attributed to the Balmer-Kapetyn basin.

In general, the WCA suggests that basins with central maslites may also exhibit mascon GA due to mare fill. In addition, the crustal compensating properties of the mantle plugs appear to be the dominant features that are reflected by the *FAGA*. However, the gravimetric properties of the basins can be complicated by data errors, as well as the effects of multiple impacts and other

Nearside Basins								
Gravimetric	*FAGA*		Mascon		Maslite		Crustal Effect	
Attributes ⇒	TC	CTD	GA	%OC	GA	%UC	%OC	%UC
Balmer-Kapetyn	-4	0?	0	0	-4	100		6
Crisium*	78	4	82	95	0	0	89	
Cruger*	24	3	27	89	0	0	45	
Grimaldi*	25	3	28	89	0	0	30	
Humboltianum*	22	4	26	85	0	0	94	
Humorum*	60	5	65	92	0	0	76	
Imbrium *	86	2	88	98	0	0	41	
Mutus-vlacq	0?	0?	0	0	0	0	0	0
Nectaris*	66	4	70	94	0	0	64	
Schiller-Zuchius*	6	8	14	43	0	0	21	
Serenitatis*	99	3	102	97	0	0	55	
Smythii*	40	3	43	93	0	0	35	
Farside Basins								
Apollo	-39	3	3	0	-39	100		20
Australe	30	0?	30	100	0	0	10	
Birkhoff	-40	1	1	0	-40	100		32
C-Sarton*	10	2	12	83	0	0	21	
F-Sharonov*	16?	3	19	84	0	0	64	
Freundlich	-45	-5			-50	90		18
Sharonov	-50	-3			-53	94		17
Hertzprung*	-45	4	4	0	-45	100		38
Ingenii	-36	2	2	0	-36	100		30
Keeler-Heaviside	-40	0	0	0	-40	100		34
Korolev	-30	2	2	0	-30	100		23
Lorentz	-33	2	2	0	-33	100		22
Mendeleev	-40	0	0	0	-40	100		45
Mendel-Rydberg*	30	1	31	97	0	0	84	
Moscovience*	4?	3?	7	57	0	0	42	
Orientale*	15	3	18	83	0	0	68	
Tsiolkovskiy-Stark	-51?	5?	5	0	-51	100		33

Table 4: Gravimetric attributes of the major lunar basins derived from the WCA include peak terrain-correlated (TC) and crustal terrain-decorrelated (CTD) *FAGA*, as well as the gravity anomalies (GA) for mascons and maslites in mGals. For each mascon or maslite, the percentage contribution of overcompensating (%OC) or undercompensating (%UC) mantle plug, respectively, is also inferred. The percentage of crustal thickness beneath each basin that is overcompensated (%OC) or undercompensated (%UC) by the central mantle plug is also listed. *⇒ reported mascon-bearing basins (e.g., Neumann et al., 1996; Konopliv et al., 1998); ?⇒ marginal estimates.

Isos	*TCFAGA*	*CTDFAGA*	CMA
OCMP	> 0	> 0	Mascon*
OCMP	> 0	0	Mascon
UCMP	< 0	0	Maslite*
UCMP	< 0	> 0	Mascon
EQ	0	0	pN
EQ	0	> 0	pN

Table 5: Gravimetric characterization of central basin mass anomalies. Isostatic conditions (Isos) include crustal equilibium (EQ), and overcompensating (OCMP), and undercompensating (UCMP) mantle plugs. Examples of central mass anomalies (CMA) include ancient pre-Nectarian (pN) basins, as well as mascons and maslites marked by asterisks that are typical nearside and farside basins, respectively.

basin-modifying tectonic factors. Complications such as these have produced entries in Table 4 with question marks denoting marginal estimates that may be poorly constrained by the data.

Table 5 summarizes the gravimetric characterizations of central basin mass anomalies inferred from the WCA. A mascon GA for typical nearside basins may be characterized by an overcompensating mantle plug plus mare fill. An unflooded basin exhibiting a mascon-like GA such as Cruger (Neumann et al., 1996), may be characterized by an overcompensating mantle plug. A mascon GA such as for Hertzprung basin may be characterized by mare fill although the inferred mantle plug is undercompensating. On the other hand, a typical unflooded farside basin exhibiting a negative gravity anomaly over a basin center may mark a subisostatic mantle plug. Ancient basins, flooded or unflooded, tend to exhibit flat *FAGA* that may reflect a state of near-isostatic equilibrium.

Considerable care must be taken in the use of the above results because interpretational complexities can occur for basins with complex tectonic histories. Consider for example the Freundlich-Sharonov basin on the lunar farside. This large basin, named for a series of impacts along its western margin, was newly identified as a mascon by the Lunar Prospector mission (Konopliv et al., 1998).

Figure 22 shows the inferred crustal cross-section and gravity profiles for the Freundlich-Sharonov basin. Based on relatively poor photography, the basin center was located at (19°N, 175°E) and a 600-km topographic ring inferred (Wilhelms, 1987) that were subsequently confirmed by the Clementine LIDAR data (Figure 3). The orthophoto maps of Moore (1981) clearly identified the individual Freundlich (25°N, 171°E) and Sharonov (13°N, 173°E) craters, while the Lunar Prospector satellite (Konopliv et al., 1998) revealed a well-defined gravity minimum over the Freundlich-Sharonov basin (Figure 2) that is roughly centered at (18°N, 175°E). However, the WCA also suggests that the effects of superposed craters may mask the effect of an earlier basin impact.

Ignoring data errors, the region of these impacts is characterized by a prominent maslite GA. The craters also are associated with small negative *CTDFAGA* that may reflect the effects of relatively unconsolidated deposits of ejecta and fractured and brecciated crust (e.g., von Frese et al., 1997b). However, the center of the basin appears to be characterized by an overcompensating mantle plug

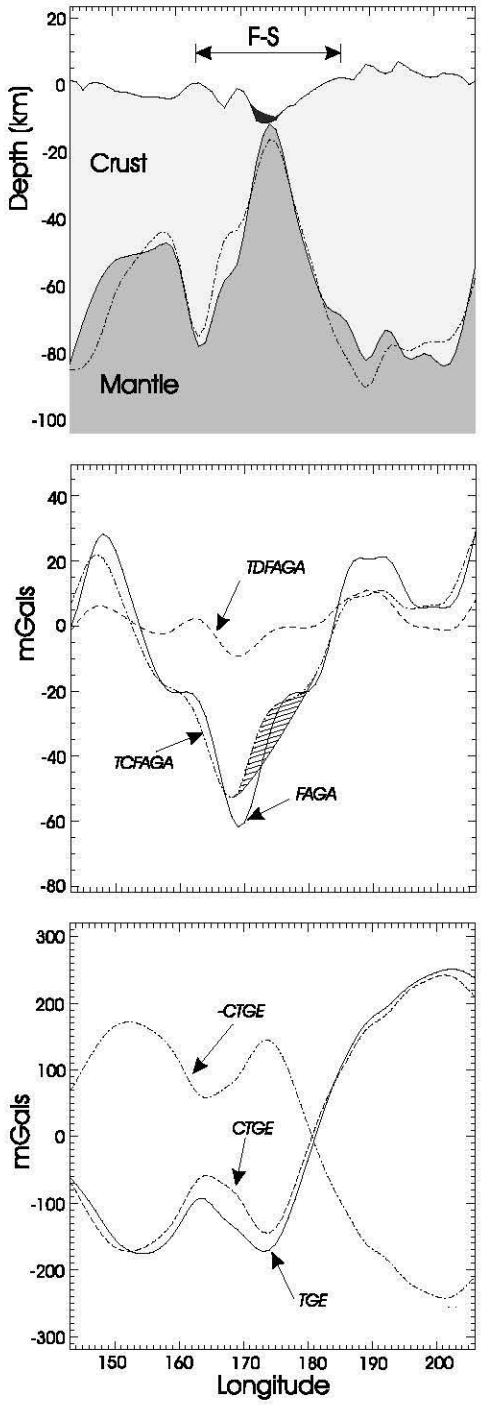

Figure 22: Freundlich-Sharonov (F-S) basin transects along 18°N include the inferred crustal cross-section (top panel), and related free-air gravity anomalies (middle panel), and terrain gravity effects (bottom panel). Surface topography and mare fill (black shading) are vertically exaggerated by a factor of 2.

that may mark the site of an earlier impact. The related mascon GA of 16 mGals, which is indicated by the shaded region of the *TCFAGA* profile in Figure 22, may be superposed on the larger maslite GA. Also centered on the basin is a marginally positive *CTDFAGA* that may reflect the effects of mare fill. Clearly, considerable interpretational complexity may be encountered when dealing with the gravity data of tectonically complicated basin sites.

The characterization of central mass anomalies inferred from this WCA may also provide additional perspective on their formation and evolution. The present topography of a lunar basin results from the cratering process (Melosh, 1989), so that gravity and topography were presumably positively correlated for the newly excavated basin. However, within a short period of time following the impact, the mantle rebounded isostatically and then slowly began to subside (Melosh, 1989). For the hot, viscous lithosphere of the nearside, the uplifted mantle may have subsided and become "frozen" at a superisostatic level by the strength of the lithosphere (Neumann et al., 1996). This situation would produce a mascon gravity anomaly due to the superisostatic component of the mantle plug resulting in negatively correlated gravity and topography. For the cooler, less viscous farside, on the other hand, insufficient mantle uplift during mantle rebound beneath a basin would produce a maslite gravity anomaly and positively correlated gravity and topography. The maslite GA may be ascribed to the subisostatic component of the mantle plug where enhanced lithospheric rigidity presumably inhibited flexure of the crust-mantle boundary at the time of impact (Solomon et al., 1982).

Mare flooding of the basins commenced nearly 100-800 Myr after the heavy bombardment period (Boyce, 1976). This event would have increased the mascon GA by contributing positive *CTDFAGA* that reflect the high-density effects of uncompensated mare basalt fill. For a maslite, by contrast, the superposition of a small mascon GA would result when the basin filled with mare basalt.

The notions of mascon and maslite have been used to characterize nonisostatic mass variations of the central basins only. This restiction seems quite artificial in view of the WCA, which suggests that basin rings may also involve nonisostatic crustal and upper mantle features. These features include the prominent gravity minima or "moats" (e.g., Neumann et al., 1996) around mascons, which for Mare Orientale were readily modeled as crustal displacements of the upper mantle (von Frese et al., 1997b). Hence, by the WCA, lunar nearside basins tend to be affiliated with central basin mascons that are flanked by alternating ring maslites and mascons, whereas central basin maslites with flanking ring mascons and maslites are the more characteristic features of farside basins.

2.5 Conclusions

New details on lunar subsurface mass variations that relate to the composition, structure, and isostatic and tectonic development of the crust were developed from a wavenumber correlation analysis between satellite-obtained free-air gravity (*FAGA*) and topography data. Contrasting crustal attributes of the lunar basins were also developed for insight on the evolution of the lunar lithosphere.

Accurate estimates for the terrain gravity effects (*TGE*) of the lunar topography were modeled in spherical coordinates at 100-km altitude by GLQ integration (von Frese et al., 1981; von Frese

et al., 1997b) using a 2.8 g/cm^3 density contrast of the terrain with the near-vacuum of space. The modeling procedure involved spherical prisms with flat tops and bottoms at the average altitudes provided by the GLTM-2 file of $1^o \times 1^o$ topographic estimates.

The wavenumber correlation analysis between *TGE* and *FAGA* isolated the terrain-correlated and -decorrelated components of *FAGA* and also decoupled the terrain-decorrelated free-air gravity anomalies (*TDFAGA*) and compensated terrain gravity effects (*CTGE*) that were obtained by subtracting the terrain-correlated free-air gravity anomalies (*TCFAGA*) from *TGE*.

Moho undulations and crustal thicknesses between $\pm 64^o$ selenodetic latitudes were estimated by least squares inversion of the compensating terrain gravity effects (-*CTGE*) using spherical prism modeling by GLQ integration with a density contrast of 0.5 g/cm^3 between the mantle and crust. The inversion yielded Moho undulations relative to a 64-km depth and an average near-global crustal thickness of roughly 63 km. The inferred crustal thickness of 54.6 km for the Apollo 12 and 14 landing sites is in good agreement with the reported seismic estimate of about 55 km.

A model for incipient radial adjustments of the inferred Moho was also estimated by the inversion of *TCFAGA*. These estimates may reflect the amount of subsidence and uplift that is required of the inferred Moho to equilibriate the lunar topography fully. They are strongly correlated with the basin rings, which suggests that these features may involve nonisostatic components. Hence, these adjustments may provide additional constraints on the stress regime of the crust that also includes superposed global stresses due to the thermal evolution of the Moon and the crustal stresses induced by the thickness variations of the crust.

The *TDFAGA* were separated into crustal and subcrustal components on the basis of their correlation spectrum with *FAGA*. The lower frequency components (n $<$ 24) of *TDFAGA* were interpreted for the longer wavelength effects of subcrustal mass variations. The higher frequency components (n $\geq$ 25), although largely in the noise range of *FAGA*, were interpreted for the gravity effects of mare fill because many of the basins appear to be systematically characterized by these anomaly maxima. Mare fill thicknesses were estimated from the inversion of the higher frequency *TDFAGA* components. They range from several hundred meters to a few kilometers only and are largely consistent with photogeologic estimates.

Dichotomies are clearly evident in terms of the crustal thickness and lithospheric stength properties that have been inferred by the WCA. For example, on the farside, the average crustal thickness ($\approx$ 70 km) is nearly 14 km thicker than the nearside average thickness ($\approx$ 57 km). A 50% increase in crustal thickness energy is evident on the farside relative to the nearside. These results may reflect the greater abundance of smooth mare floors for the nearside basins compared to the more rugged farside highlands.

A comparison of the inferred crustal structures of the giant Procellarum and South Pole-Aitken basins also supports the possible thermal, mechanical, and compositional dichotomies of the lithosphere. The Procellarum basin may be underlain by a roughly uniform 60-km thick crustal slab. Its apparent lack of Moho uplift may reflect considerable flattening over time by crustal viscous relaxation that was significantly enhanced by a high thermal gradient due to more abundant radioactive elements in the nearside mantle and crust. By contrast, the 13-km topographic depression of the SPA basin may be underlain by a prominent regional mantle plug. The preservation of the regional crustal

features of SPA compared to the muted features of Procellarum suggests that crustal viscosities on the lunar farside may have been at least an order of magnitude larger than the contemporaneous viscosities of the nearside crust (Solomon et al., 1982).

The dichotomy in lithospheric strength may also be reflected in the isostatic properties of the major impact basins as generalized by the 8 representative basins in Figures 16 - 21. In general, the farside crust seems to have responded more rigidly to impacts than the nearside crust. The nearside basins mostly reflect superisostatic mantle plugs, whereas most farside basins involve undercompensating or subisostatic mantle plugs. Nearside basins presumably were formed on a relatively thin, easily penetrated lithosphere that facilitated extensive post-impact modification. Farside basins by contrast, seem to have formed on thicker lithosphere that cooled rapidly and became rigid with limited opportunities for endogenic modification. Generally, nearly all nearside basins appear to be dominated by mass concentrations due to superisostatic mantle plugs plus mare basalt fill, whereas the farside basins appear to be dominated mostly by mass deficiencies resulting from subisostatic mantle plugs with marginal or no mare fill.

The WCA characterized central basin mass anomalies in terms of the *TCFAGA* and *CTDFAGA* components of *FAGA*. Basins with mascon anomalies can involve superisostatic mantle plugs with or without mare fill and subisostatic or equilibriated mantle plugs plus mare fill. Basins with maslite anomalies, on the other hand, involve mass deficiencies that are mostly due to their subisostatic mantle plugs.

However, interpreting *FAGA* for basins with complex tectonic histories can be complicated because gravity reflects the superposition of effects from all sources of mass variation. For the Freundlich-Sharonov basin, for example, the strong maslite anomaly due to younger impacts may be superposed on a weak mascon gravity anomaly from an earlier impact. Mascon and maslite anomalies also may offset each other to yield effectively zero *FAGA*.

These results are clearly limited by any errors in the data and assumptions used in the analysis and hence must be used with care. However, the analysis also indicates clearly that spectral correlation theory may be readily extended from the scale of a single basin like Mare Orientale (von Frese et al., 1997b) to a global model of the lunar crust. Further details on the lunar crust may result from considering the tracking data of the lowered Lunar Prospector satellite.

3 Lunar Basin Ring and Transient Cavity Attributes from Spectrally Correlated Free-air and Terrain Gravity Data

3.1 Introduction

A dominant feature of lunar impact basins is their multi-ringed structure. Basin rings consist of strongly expressed scarps with concentric patterns of rilles and ridges (e.g., Hartmann and Wood, 1971; Solomon and Head, 1980; Melosh, 1989; Spudis, 1993). Ring formation is the initial effect of the basin modification period that is followed by secondary effects of impact melting (Grieve and Cintala, 1997). However, this first order effect of bolloidal impact is poorly understood for its lithospheric processes. It is also difficult to appreciate the lithospheric significance of the spacing rule for the rings of impact basins on the terrestrial planets and the Moon, which for any given basin is given by $\sqrt{2}$D where D is the diameter of any one of the basin's rings (Spudis, 1993).

The origin of basin rings has been attributed to frozen tsunami-like wave effects (Baldwin, 1949; 1963; 1972; Van Dorn, 1968; 1969), interference between shear and compressional waves (Johnson et al., 1968), and standing wave effects (Chadderton et al., 1969) generated in the crust directly by the meteorite impact. Faulting at the time of impact or during subsequent tectonism along fractures formed by impact has also been proposed for the formation of basin rings (Hartmann and Kuiper, 1962; Hartmann and Wood, 1971; Head, 1974). In crater and ring development, the mechanical strength of the target material undoubtedly is a dominant factor that influences the forceful oscillatory dynamics of lithospheric uplift and collapse (Wilhelms, 1987). However, despite these insights, considerable uncertainty remains concerning the origin and evolution of lunar basins (Spudis, 1993).

In this study, a new approach using free-air and terrain gravity correlations is investigated for insights regarding the poorly understood tectonic development of basin rings. In particular, the *TCFAGA* that have been interpreted for incipient adjustments of the inferred Moho (Figure 10) reveal many remarkable associations with lunar basin rings that may help constrain ring formation processes. These results for Mare Orientale, for example, appear to accommodate the possible presence of shock-related residual stress fields that may have promoted the development of the topographic rings (von Frese et al., 1997b). Accordingly, the relationship between the photogeologically determined basin rings and the radial Moho adjustment model in Figure 10 will be investigated for further insight on the formation and evolution of basin rings.

The geometry of the transient cavity produced during the initial stage of impact yields valuable insight on basin formation and evolution. For example, estimates on transient cavity depths and diameters facilitate interpreting returned lunar samples for the compositional, structural, and physical properties of the lunar lithosphere affected by impacts (Bratt et al., 1985). Using the radial Moho adjustments in Figure 10, the dimensional relationship between the transient cavity diameter and viscosity (Melosh, 1982) will be investigated for insights on the lithospheric dichotomy in mechanical

properties between the near and far sides.

Reconstructions of transient cavities have been attempted from photogeologic interpretations of the distribution of exposed basement rocks (Floran and Dence, 1976), shock metamorphism in bedrock (Murtaugh, 1972), and preimpact landforms (Spudis et al., 1984). Reconstructions have also been inferred by proportional growth modeling that assumes a size-invariant shape for the cavity during impact (e.g., Croft, 1980; 1981; O'Keefe and Ahrens, 1993), and from estimates on the preimpact Moho position beneath basins (Wieczorek and Phillips, 1999). These techniques, however, yield disparate estimates that will be tested by the ring inferences interpreted from the radial Moho adjustment modeling in Figure 10.

In section 2, the cratering process and resulting basin morphologies are reviewed. In section 3, inferrences are developed on the possible origin of basin ring formation using the incipient radial adjustment model of Figure 10. In particular, estimates on ring diameters are derived and compared against photogeologic estimates. In section 4, these diameters are evaluated for inferences on the rheologic properties of the lithosphere and the depths of basin excavations. In section 5, the significance of these results is considered for modeling crater and ring formation processes. The conclusions are given in section 6.

3.2 Impact Cratering and Crater Morphology

The size of an impact basin is usually described in terms of the diameter of its main topographic rim (Wilhelms, 1987). Lunar impact basins range from simple craters with diameters no larger than about 20 km, to complex craters with diameters between 20 to 300 km, and multi-ring basins with diameters larger than 300 km (Wilhelms, 1987).

Figure 23 summarizes the various crater morphologies. The cratering process starts with the growing transient cavity (Figure 23A) that collapses into either a simple crater (Figure 23B), a complex crater (Figure 23C), or a multi-ring basin (Figure 23D). The final morphology depends on a range of factors including the gravity field of the planet, the physical properties of the substrate or target conditions and the atmosphere, as well as the projectile's size, speed, and trajectory (e.g., Wilhelms, 1987; Melosh, 1989). Hence, estimating the geometry of the tansient cavity from the several topographic morphologies that are possible from meteorite impact may provide valuable insight on basin formation and ring tectonism.

On impact, the shock wave expands and decays in strength as it progressively engulfs target material. Its decay in strength is due to energy spreading over a greater volume of material and irreversible energy losses. Moreover, the rapid passage of shock waves through the target sets the material behind it in motion. Once this excavation flow is fully developed, the cavity begins to grow. In particular, excavation flow initially opens an approximately hemispherical cavity comparable in size to the projectile's diameter. This cavity may also be lined with a thin sheet of impact melt (Melosh, 1989). The exacavation flow pattern pushes material radially outward into the evolving cavity wall. The cavity grows at a steadily decreasing rate while continuously ejecting material from the cavity until its maximum depth (d_{ex}) is attained (Figure 23A). Hence, the transient cavity (Figure 23A),

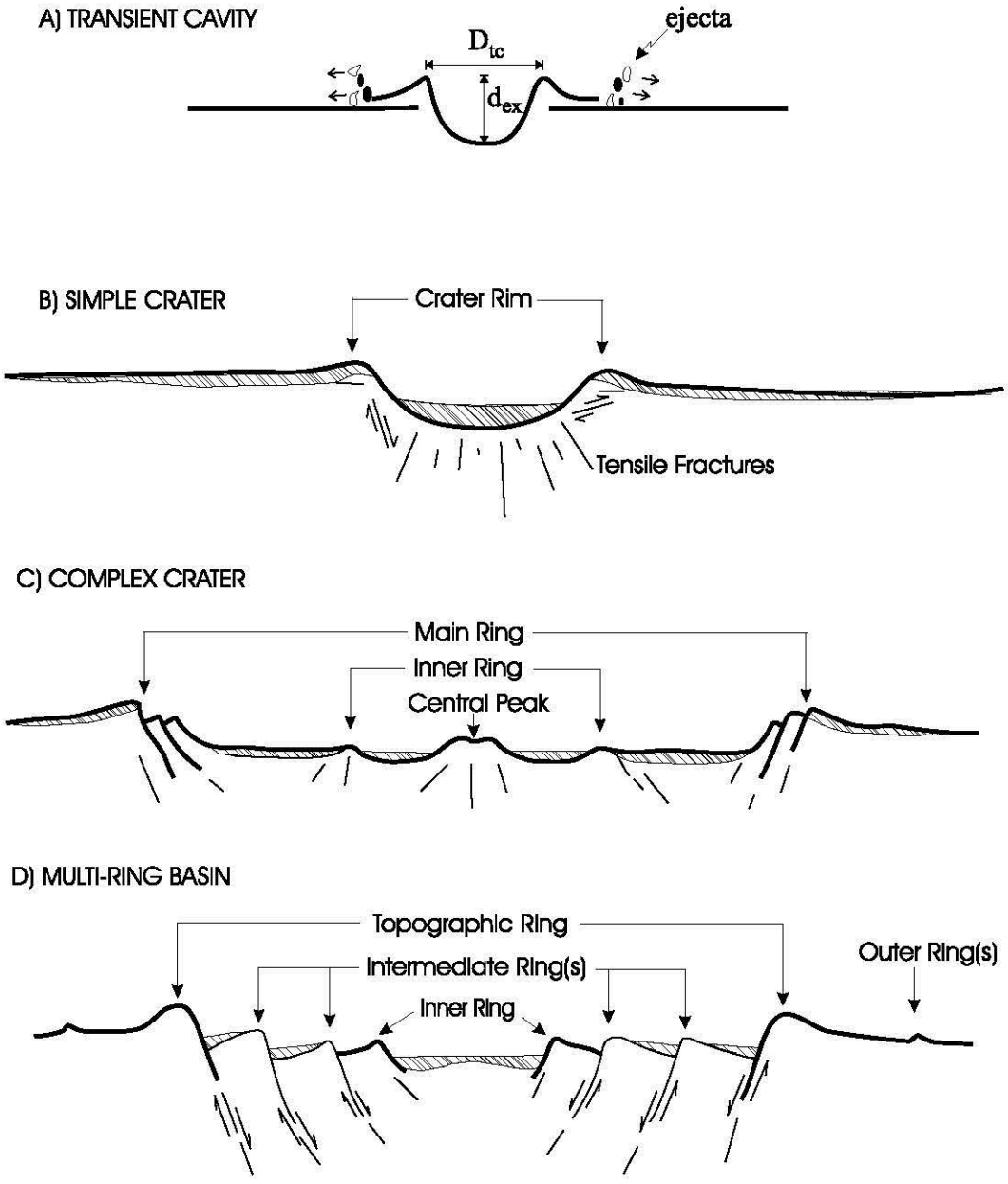

Figure 23: Generalized crater morphologies (adapted from Wilhelms (1987), Melosh (1989) and Spudis (1993)). The growth of A) the transient cavity (TC) facilitates basin excavation. The collapse of the transient cavity may result in B) a simple or C) complex crater, or D) a multi-ring basin. The final morphology depends strongly on the dimensions of the transient cavity. The simple crater has a raised rim wall, while the complex crater shows slumped walls with a central peak or inner ring. The horst-and-graben topography of the multi-ring basin suggests the possible involvement of faulting. Hatching represents possible distributions of the impact melt sheet.

defined by the interface between the vapour and melted or solid components of the cavity floor, grows in size and deforms in shape until excavation is halted (Melosh, 1989).

The identification of the diameter (D_{tc}) of the transient cavity is required for understanding the mechanism for basin formation, crustal volume displacement, lunar sample provenance and the origin of mascons (Spudis, 1993). Early studies relying on morphologic and stratigraphic relations seen in photographs related D_{tc} to the diameter of the innermost ring within the main basin rim (e.g., Head, 1974), while others suggested that the diameter of the main basin rim may be a suitable estimate for D_{tc} (e.g., Baldwin, 1974; Murray, 1980). However, these choices lead to disparate predictions of basin features such as excavation depth and ejecta volume (Head et al., 1975). For example, excavation depths have commonly been approximated by 0.1 D_{tc} (Pike, 1974). However, using the main rim diameter for D_{tc} usually yields excavation depths d_{ex} for basin-sized impacts that are excessive and generally not supported by remote sensing studies (Spudis et al., 1984). In the present study, the *TCFAGA* are investigated for developing reasonable estimates of D_{tc} and further insights on basin-forming processes.

The transient cavity (TC) starts as a small hemispherical feature that grows into parabolic shape and expands in size until excavation is halted. For smaller impacts, the collapse of the transient cavity may result in a simple crater (Figure 23B) that exhibits a smooth bowl-like interior profile and circular high rim or crest (Wilhelms, 1987; Spudis, 1993).

For larger impacts, the TC continues to grow laterally while the central cavity floor begins to rise as a complex crater (Figure 23C). The evolving cavity wall follows the parabolic shape of the TC while progressive unloading of the cavity center forces the TC to rise. Central uplift continues until the final stage of lateral extension when the TC collapses into a ring-shaped basin around the central rise (Henkel and Reimold, 1998). The final morphology of the complex cavity displays a central peak with blocks or slices of material slumped from its wall (Wilhelms, 1987; Spudis, 1993). The deepest position of the TC (i.e., the lowest point of the excavation) is reached at the time when collapse flow starts.

For the largest impacts yielding multi-ring basins (Figure 23D), the TC goes through similar stages of deformation as in the development of the complex crater. However, upon cavity collapse, the interface between vapour and the wall of melted and/or solid cavity materials becomes strongly deformed. As a consequence of wall collapse, the TC is pushed deeper into the cavity floor and material is dispersed over the evolving ring basin in response to the raising center (Henkel and Reimold, 1998).

For complex craters and multi-ring basins, the sequence of uplift and down-dropped terraces probably is formed through base failure (Grieve et al., 1977) by "push" and "pull" mechanisms (Wilhelms, 1987). In particular, the push-up phase may develop the central peak and uplifted terraces or horsts, while the pull-down or collapse of the cavity walls may produce grabens or down-dropped terraces (Wilhelms, 1987). The extent of collapse and the number of rings may be constrained by viscous damping because movement is halted when stresses induced by the maximum topography during any oscillation fall below the yield stress of the target material (Alexopoulos and McKinnon, 1994).

The WCA of free-air and terrain gravity anomalies may provide additional insights regarding the poorly understood tectonic development of basin rings. In particular, the interpretation of *TCFAGA*

in terms of incipient adjustments of the inferred Moho that is shown in Figure 10 reveals many remarkable associations with lunar basin rings that may help constrain ring formation processes

3.3 Basin Ring Inferences from Incipient Crustal Motions

In the cross-sections of the major basins (see Figures 16 - 17 and Appendix E) the equilibrium boundary of the crust was derived from adding the incipient radial adjustments of Figure 10 to the present Moho inferred from the inversion of the compensating terrain gravity effects (*-CTGE*) in Figure 8. The lunar crust may be working to achieve this equilibrium boundary, assuming that the Moon is evolving towards a minimum mean free-air gravity anomaly and constant crustal thickness. Accordingly, the radial adjustment model (RAM) of Figure 10 may reflect the incipient relative motions of the crust that it may be seeking for isostatic equilibrium (von Frese et al., 1997b). In particular, where the equilibrium boundary is above or below the inferred Moho, the crust may be under pressure to rise or sink, respectively.

In the basin cross-sections (Figures 16 - 17 and Appendix E), the vertical lines mark where the differences between the equilibrium and inferred Moho are zero, and hence where the zero contours of Figure 10 intersect the crustal cross-sections. Between these cross-over points are regions where the crust may be under pressure to rise or sink as suggested by the arrows in the cross-sections. These inferred incipient motions are consistent with the wave-like response of the crust to bollide impact where basin rings may have formed by oscillatory crustal uplift and subsidence (e.g., Baldwin, 1949; Grieve et al., 1980; Spudis, 1993).

The radial adjustment model (Figure 10) may be interpreted for *TCFAGA*-nullifying adjustments of the inferred Moho that the Moon may be seeking for equilibrium as a result of the crustal stresses produced by basin-forming events. The stress field of the crust may be considered as the global stress related to the thermal evolution of the Moon (Solomon and Head, 1980) with superimposed stresses due to crustal thickness variations and the loads represented by these Moho adjustments (von Frese et al., 1997b). The Moho adjustment model of Mare Orientale, for example, seems to reflect the possible presence of shock-related residual stress fields that may have promoted the development of the topographic rings (von Frese et al., 1997b). The radial adjustment model in Figure 10 suggests comparable associations for the other 26 major basins considered in this study. Hence, the possible extensions of the results for Mare Orientale to these other basins will be investigated for further insights on the formation and evolution of basin rings.

Rings originated and developed presumably during the basin modification phase (Melosh, 1989) and may be related to the incomplete isostatic adjustment of basin topography. However, the surface expressions of the rings of ancient pre-Nectarian basins such as Australe and Mutus-Vlacq may be largely muted due to viscous relaxation of the crust (Wilhelms, 1987; Melosh, 1989). In general, for basins with topographic features modified by viscous relaxation, ejecta from other impacts, and other surficial effects, new insight on the ring attributes may be provided by the radial Moho adjustments interpreted from *TCFAGA* .

3.3.1 Ring Diameter Estimates

Consideration of the radial adjustments in Figure 10 shows that the zero contours are commonly concentric about the centers of most of the impact basins. These zero contours represent "circles" that closely approximate basin "rings" as inferred from photogeologic interpretations (e.g., Solomon and Head, 1980; Wilhelms, 1987). For example, the cross-section for Mare Orientale in Figure 17 shows three circles represented by six vertical lines about the central basin. The spacings between the consecutive pairs of vertical lines represent circle diameters of 310, 660 and 1281 km about the basin center. These circle diameters are in good agreement with the photogeologically inferred ring diameters of 320, 620 and 1300 km, respectively (Spudis, 1993).

In addition to the zero radial adjustment, basin ring diameters also appear to correlate at maximum differences between the equilibrium and inferred Mohos. These regions of maximum difference may indicate concentric zones in the crust where maximum vertical stresses may be operating on the basin rings. For Mare Orientale, these maximum differences are represented by circle diameters of 512 and 968 km about the basin center that are in good agreement with the photogeologically determined ring diameters of 480 and 930 km, respectively (Spudis, 1993).

Interpretational examples are shown in Figures 24 - 25 for eight relatively isolated basins that appear to have sustained minimal structural modification from superposed or neighboring impacts. In these examples, dashed vertical lines connect the zero and maximum differences (lower panel) from the radial adjustment model (RAM) of Figure 10 with the inferred ring locations (upper panel) in the lunar topography of Figure 3. Here the separation between the inner pair of vertical lines may be taken to represent the diameter of the innermost ring, with the separation between the next flanking pair of vertical lines representing the diameter of the next larger adjacent ring, etc. Hence, starting from the basin center, the inner ring is located at the first cross-over, with the next ring occuring at the maximum difference, followed by another ring at the second cross-over, with another ring at the next maximum, etc.

Experience indicates that nearly every photogeologically identified basin ring is located at either a zero or maximum difference in the RAM data, however not all of these differences have been attributed to basin rings by photogeologic analysis. Figure 26 indicates the very strong correlation between the ring diameters inferred from photogeologic interpretations (PG) and the radial adjustment model (RAM) of the wavenumber correlation analysis (WCA). The photogeologic estimates from Solomon and Head (1980), Wilhelms (1987), and Spudis (1993) were used in this comparison. They included ring diameter estimates based on the $\sqrt{2}$D-spacing rule (Spudis, 1993).

A remarkable correlation of 0.99 between the RAM and photogeologically inferred basin ring diameters is evident in Figure 26. Accordingly, the radial adjustment model for a basin may reflect independent estimates on the size, location, and number of basin rings. The ring counts inferred by the WCA for the 27 multi-ring basins are summarized in Table 6.

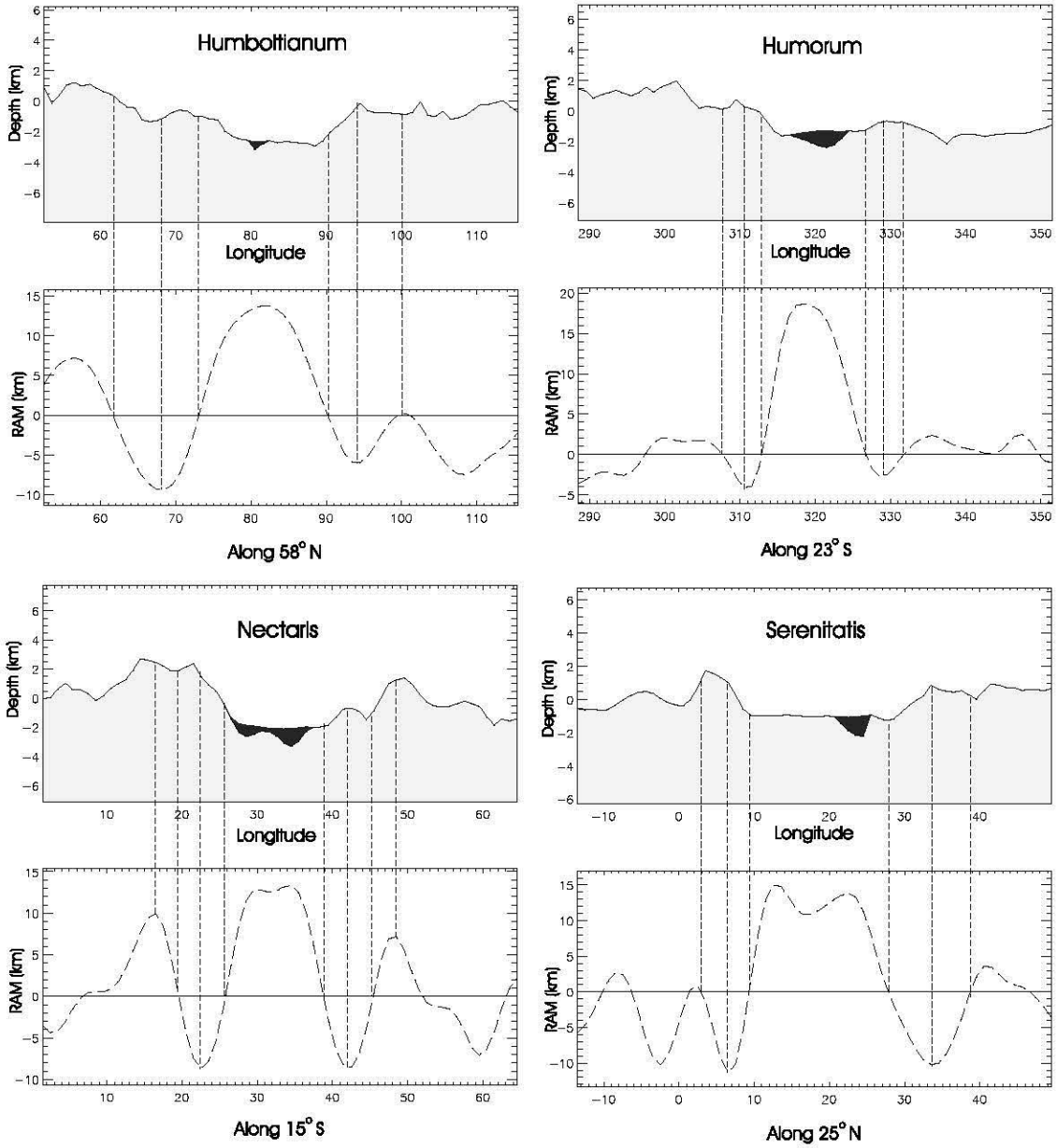

Figure 24: Crustal sections (top panel) and radial adjustment model (RAM) profiles (bottom panel) for the nearside Humboltianum, Humorum, Nectaris, and Serenitatis basins. Mare fill is shaded black. The dashed vertical lines are drawn from the critical points of the RAM profile to indicate possible ring locations at the surface.

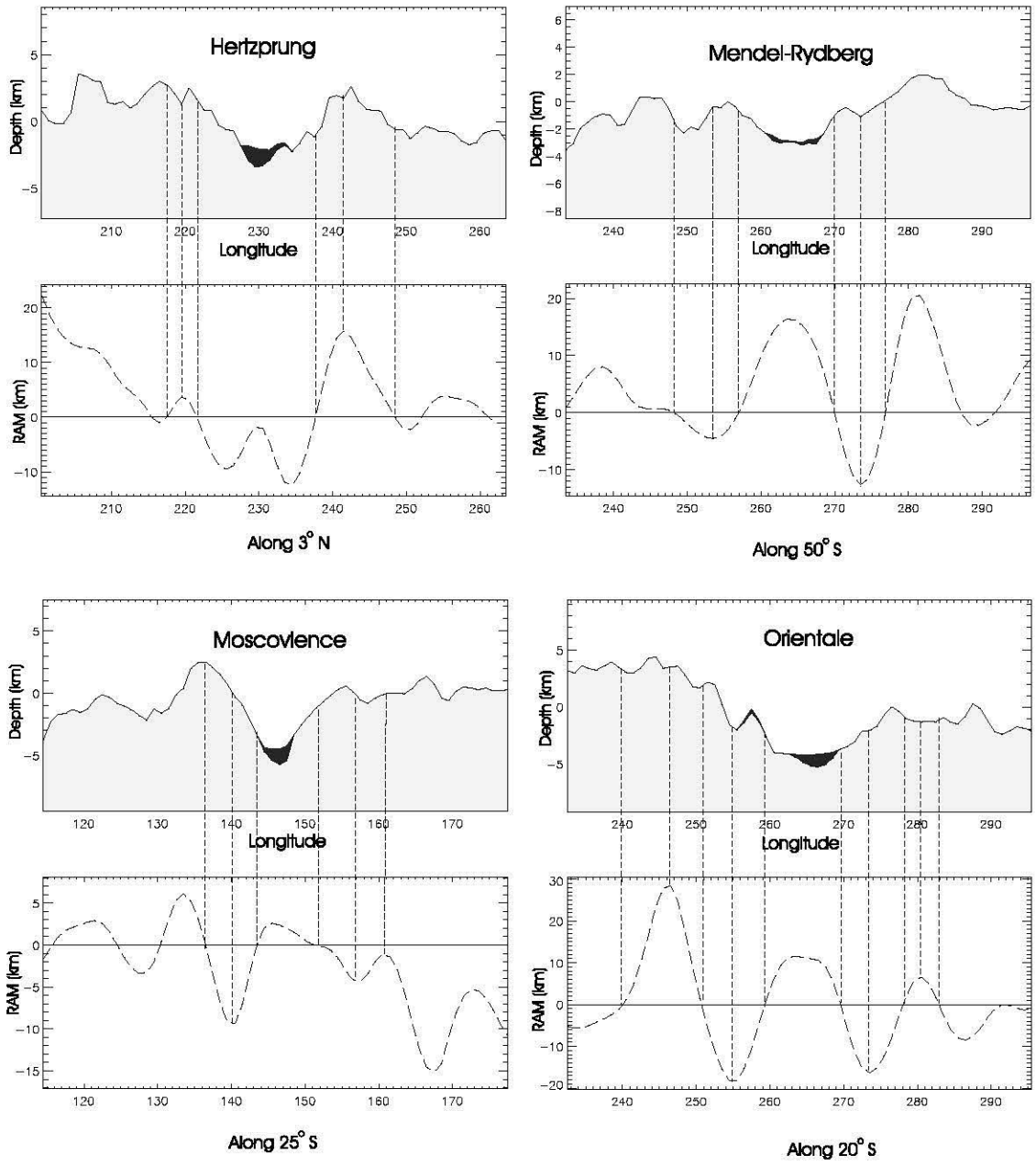

Figure 25: Crustal sections (top panel) and radial adjustment model(RAM) profiles (bottom panel) for the farside Hertzprung, Mendel-Rydberg, Moscovience, and Orientale basins. Mare fill is shaded black. The dashed vertical lines are drawn from the critical points of the RAM profile to indicate possible ring locations at the surface.

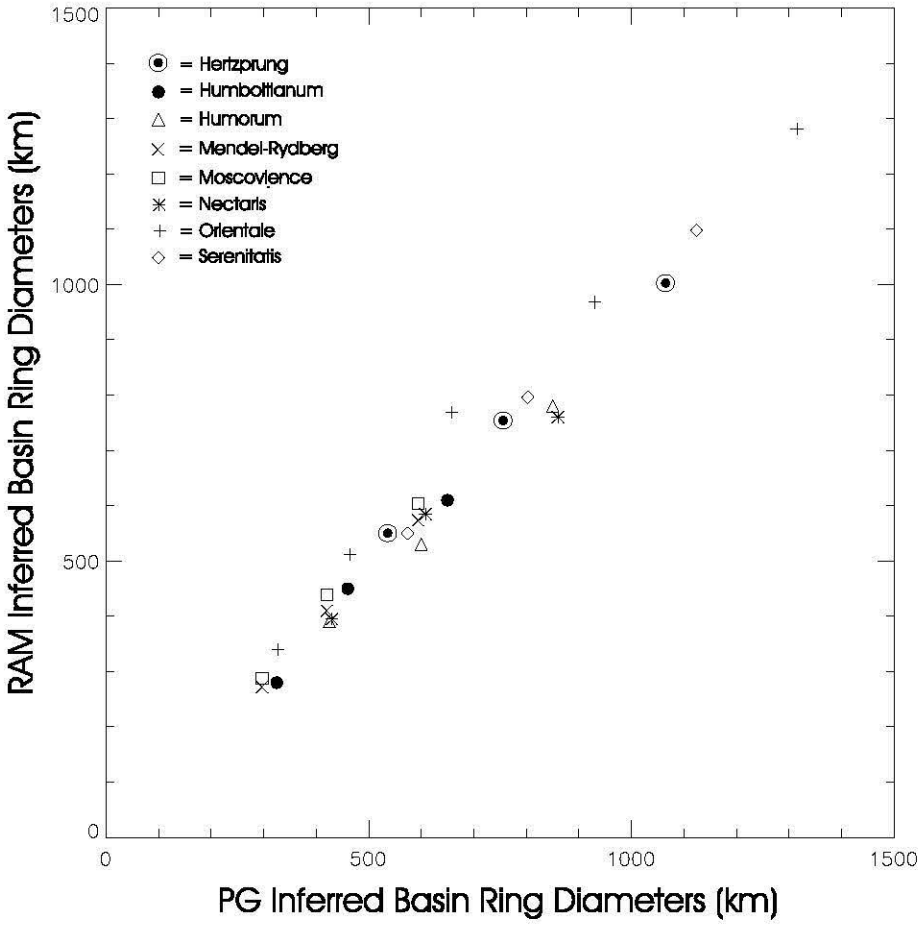

Figure 26: Comparison of basin ring diameters inferred from photogeological (PG) estimates (Solomon and Head, 1980; Wilhems, 1987; and Spudis, 1993) and the RAM estimates from Figures 24 and 25.

3.4 Reconstruction of Basin Transient Cavities

The dimensions of the transient cavity (TC) facilitate understanding basin-forming processes including the excavation depths of impacts that influence interpretations of the returned lunar samples (Bratt et al., 1985). They also provide insight on the mechanical properties of the lunar lithosphere as it responded to bollide impacts (Melosh, 1989), and the validity of the proportionality between excavation depth and transient cavity diameter (i.e., proportional scaling) in estimating the excavation cavity of a basin (Croft, 1980; Spudis, 1993).

Estimating the diameter D_{tc} of the transient cavity is problematic because it has been expressed by the diameters of both the main topographic rim (e.g., Wilhelms, 1987) and the inner ring (e.g., Floran and Dence, 1976). The transient cavity is an ephemeral feature formed during the excavation phase of basin formation, whereas the main topographic rim is a permanent feature formed during the basin modification (Spudis, 1993). Studies on terrestrial impact craters (Grieve, 1987) suggest that these two phases may be distinct (Spudis, 1993) and that D_{tc} is perhaps best associated with the inner ring diameter (Melosh, 1989).

The diameters of the transient cavity and main topographic rim may be related by the $\sqrt{2}$D-spacing rule (Hartmann and Wood, 1971) that the RAM data also apparently express as shown in Figure 26. For example, the WCA estimate of 980 km for the diameter of the main ring of Orientale (Spudis, 1993), which is the fourth ring visible from the center of the basin, is roughly $\sqrt{8}$ times the 340-km WCA estimate for the diameter of the inner ring. However, the inner ring diameter is probably the most effective estimate for the transient cavity diameter (D_{tc}) (e.g., Floran and Dence, 1976; Spudis et al., 1984). Hence, the related inferences from the radial adjustment model may have further utility in lunar basin studies that incorporate the attributes of transient cavities.

As shown in Figure 23, the size of the transient cavity, is commonly defined by its diameter (D_{tc}) and depth extent (d_{ex}) just prior to collapse and slumping of the cavity wall (Melosh, 1989). Accordingly, the dimensions of the transient cavity can provide estimates of the volume and depth of excavation (Pike, 1974). For major lunar basins, theoretical and experimental scale modeling studies of impact craters have attributed the (d_{ex}/D_{tc})-ratio to values ranging from 0.08 to 0.12 (e.g., Croft, 1981; Spudis et al., 1984; Wieczorek and Phillips, 1999). However, these estimates predict depths that would have excavated mantle material in contradiction to remote sensing studies which generally have inferred shallower excavation depths (e.g., Gaddis et al., 1995).

An alternate approach to estimating the dimensions of the transient cavity involves crustal reconstruction that relates a dual-layered crustal model to Bouguer gravity anomalies (Wieczorek and Phillips, 1999). Restoring the Moho to its preimpact position beneath these basins resulted in roughly parabolic depressions from which TC depths d_{ex} and diameters D_{tc} could be estimated. Geometric crustal reconstructions considered a stratified crust of anorthosite overlying norite with a density contrast of -0.3 g/cm^3, and yielded TC depths that are more in line with those from remote sensing studies. However, the results may be limited by the use of excessively thick mare fill components and not accounting for the gravity effects of the crustal topography and mantle undulations.

3.4.1 Transient Cavity Diameters

Transient cavity diameters have been previously estimated from photogeologic interpretations of topographic rim diameters (Wilhelms, 1987), inner ring morphology (e.g., Floran and Dence, 1976), the distribution of shock metamorphism in bedrock (e.g., Murtaugh, 1972), and preimpact landforms (Spudis et al., 1984), as well as by gravimetric crustal reconstruction (Wieczorek and Phillips, 1999). In general, the diameter of the inner ring may provide the better estimate of D_{tc} (e.g., Floran and Dence, 1976; Spudis et al., 1984; Melosh, 1989), but the location of the inner ring can be obscured by ejecta, lava flooding, and other blanketing effects from basin-forming processes (Melosh, 1989). The WCA, on the other hand, provides estimates of D_{tc} based on the gravity effects of basin subsurface features that may be useful for augmenting or testing the other results. As an example, transient cavity diameters for Mare Orientale of about 300 and 397 km were estimated photogeologically (Floran and Dence, 1976) and by gravimetric crustal reconstruction (Wieczorek and Phillips, 1999), respectively. These results are in good general agreement with the inner ring estimate of roughly 340 km from the radial adjustment model in Figure 10.

The transient cavity diameters from the radial adjustment model and crustal reconstruction are highly consistent for the 10 nearside lunar basins studied by Wieczorek and Phillips (1999). The comparison is given in Figure 27 where a strongly linear agreement is evident with a 0.98 coefficient of correlation. Hence, the two approaches provide remarkably similar D_{tc} estimates. In Table 6, the TC diameters inferred by the WCA are summarized and compared with the estimates from other approaches.

3.4.2 Transient Cavity Diameter and Crustal Thinning

The excavation of large quantities of crustal material presumably facilitated the uplift of the Moho beneath complex craters and multi-ring basins (Melosh, 1989). Neumann et al. (1996) estimated Moho uplift beneath basins and found a poor correlation with their topographic rim diameters (D_{tr}) as inferred by Wilhelms (1987). Crustal thinning due to crustal unloading and mantle uplift is related to basin formation whereas ring development is related to the basin modification phase (Melosh, 1989; Spudis, 1993). Accordingly, crustal thickness may be less correlated with the size of the basin's main rim than with the transient cavity diameter that developed during the basin excavation process.

Insights on the transient cavity diameter and its extensions by correlated parameters such as possibly crustal thickness may facilitate investigations of the mechanical properties of the lithosphere. For example, viscosity may be related directly to D_{tc} (Melosh, 1982), so that larger D_{tc} may be anticipated as viscosity presumably increased with time following the bombardment period when high near-surface temperatures associated with impact heating were prevalent (Solomon et al., 1982). Hence, the relationship between crustal thickness and D_{tc}, rather than D_{tr}, may be more fundamental for developing insight on basin lithospheric properties and processes. Basins involving mass distributions with contrasting isostatic properties may be especially useful for investigating the diverse mechanical properties of the lunar lithosphere.

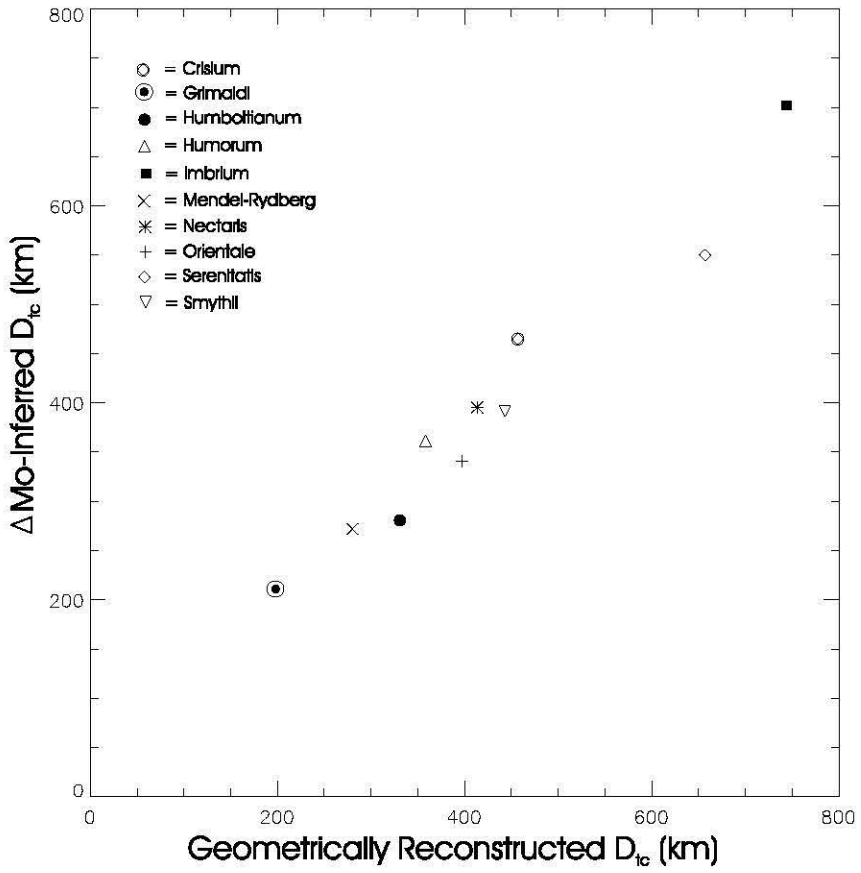

Figure 27: Comparison of transient cavity (TC) diameters determined by gravimetric crustal reconstruction (Wieckzorec and Phillips, 1999) and the radial adjustment model (RAM) in Figure 10.

Figure 28 shows scatter plots of crustal thicknesses (CT) versus transient cavity diameters (D_{tc}) as inferred from the WCA results in Tables 2 and 6, respectively, for the 24 basins with superisostatic (panel A) and subisostatic (panel B) mantle plugs. Several interesting patterns are evident in Figure 28 that may reflect lithospheric variations of composition and rheology during bombardment times, because the development of impact basins depends partly on the effective viscosity and yield strength of the target rocks (Melosh, 1982).

In Figure 28A, for example, the WCA results tend to indicate inverse correlations between crustal thickness variations and transient cavity diameters for both nearside and farside basins with overcompensating or superisostatic mantle plugs. Representative nearside basins, such as Crisium (Cri), Cruger (Cru), Grimaldi (Gri), Humorum (Hum), Nectaris (Nec), Shiller-Zuchius (S-Z), and Smythii (Smy) have crustal thicknesses (CT) in km that may be least squares modeled in terms of their inferred transient cavity diameters (D_{tc}) by

$$CT = 47.53 - 0.06 D_{tc}. \tag{8}$$

The representative equation 8 for nearside basins with superisostatic mantle plugs is plotted by the solid line in Figure 28A. Outliers to this equation may include the Humboltianum (Humb), Imbrium (Imb), and Serenitatis (Ser) basins. The crustal properties established for Humboltianum may be problematic in this analysis because the basin is located at high latitudes where topographic accuracies are poor (e.g., Neumann et al., 1996; Smith et al., 1997). Implementating the crustal properties for Serenitatis and Imbrium, on the other hand, is complicated because they are probably atypical of the nearside crust. These basins formed in largely resurfaced Procellarum KREEP terrane whose mafic petrogenesis may relate to the early differentiation of the Moon (Joliff et al., 2000; Haskin, 1998; Korotev, 2000).

Representative farside basins in Figure 28A, such as Coulomb-Sarton (C-S), Freundlich-Sharanov (F-S), Mendel-Rydberg (M-R), Moscovience (Mos) and Orientale (Ori), have crustal thicknesses that may be modeled by

$$CT = 38.29 - 0.07 D_{tc}. \tag{9}$$

This representative equation for farside basins with superisostatic mantle plugs is plotted by the dot-dashed line in Figure 28A.

In Figure 28B, the WCA results for the farside basins with undercompensating or subisostatic mantle plugs show no apparent correlations between variations of crustal thickness and transient cavity diameter. The average crustal thickness for these basins is 49.2 km, although possible outliers to this result may include the Apollo (Apo), Ingenii (Ing), and Korolev (Kor) basins. Apollo and Ingenii were formed on South Pole-Aitken terrane of mafic cryptomare and lower crustal and upper mantle materials (Joliff et al., 2000), which is atypical of the feldspathic terrane of the farside highlands. Korolev is an old pre-Nectarian basin (Greeley et al., 1993) located in anomalously thick crust (Neumann et al., 1996) with crustal properties that may have been modified by subsequent impacts (Bell and Hawke, 1984). However, removing these possible outlier values changes the mean thickness only to 53.9 km.

The average TC diameter for these farside basins with subisostatic mantle plugs is 419 km. However, a possible outlier to this value may be represented by the Birkhoff (Bir) basin, which is located at

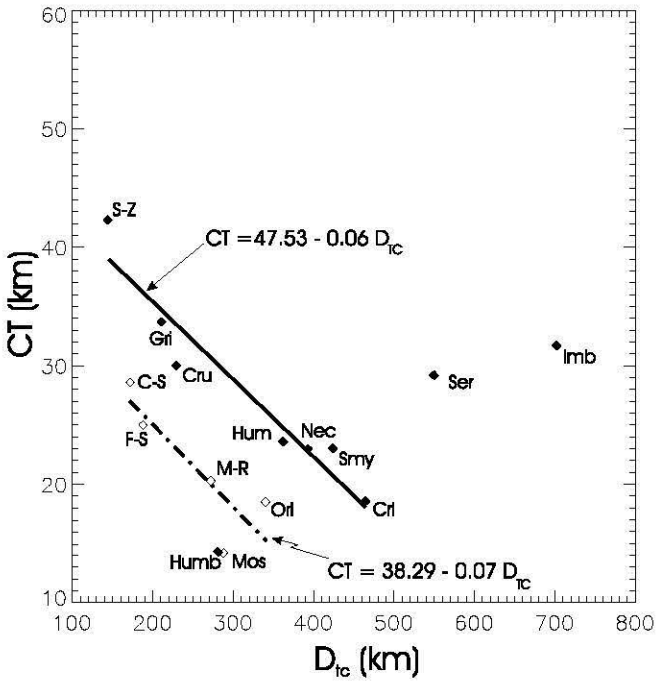

A) Basins with overcompensating mantle plugs.

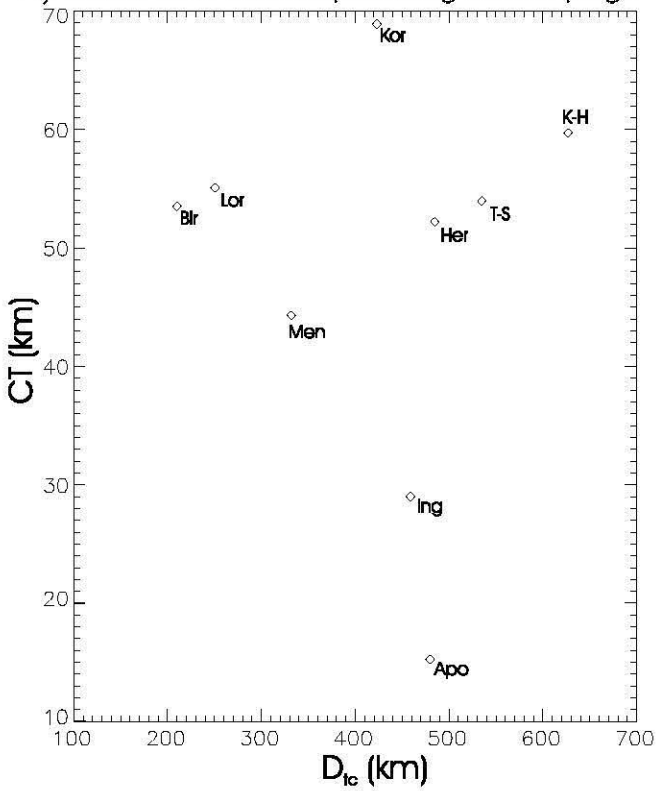

B) Basins with undercompensating mantle plugs.

Figure 28: Comparison of transient cavity diameters and crustal thicknesses for basins with A) superisostatic and B) subisostatic mantle plugs. The annotations for the basin names are listed in Table 6. Nearside and farside basins are marked by solid and open symbols, respectively.

high latitudes where topographic accuracies are poor so that its crustal properties also may be problematic for use in this analysis. Removing the possible outlier value increases the mean TC diameter for the farside basins to 445 km.

The TC diameters (D_{tc}) and the crustal thicknesses (CT) from the WCA used in Figure 28 are summarized in Tables 6 and 2 respectively. As discussed in section 3.5, these results tend to support the dichotomy in lithospheric properties between the lunar nearside and farside.

3.4.3 Transient Cavity Excavation Depths

Excavation depths (d_{ex}) of lunar basins have been inferred from multispectral data by applying the proportional scaling relation (d_{ex}/D_{tc}) for a dual-layered lunar crust with anorthosite overlying norite (Spudis, 1982, 1983; Spudis et al., 1984). The results of these studies on the nearside Crisium, Humorum, Nectaris, and Serenitatis basins and the farside Orientale basin concluded that (d_{ex}/D_{tc}) $\approx$ 0.1. This value of the proportional scaling has been applied to a wide range of transient cavity dimensions for the lunar multi-ring basins (Spudis, 1993), but with mixed results. For example, when applied to the photogeologically determined cavity diameter of 685 km for Imbrium, the result suggests that the impact may have sampled upper mantle material (Spudis, 1993), which is generally not supported by gravity (e.g., Bratt et al., 1985; Neumann et al., 1996) or remote sensing studies (e.g., Spudis, 1982; Spudis, 1983; Spudis et al., 1984).

A test of the scaling relation is to reconstruct the geometry of the transient cavity from gravity and topography by evaluating the mass balance between the uplifted mantle plug and excavated basin materials (Bratt et al., 1985). Basin excavation presumably created a parabollically shaped transient cavity due to crustal unloading that facilitated mantle uplift (e.g., Melosh and McKinnon, 1978). Accordingly, the mass lost by the crustal unloading was replaced by an ephemeral high-density mantle intrusion of the crust. Hence, the basin crustal models presented by the WCA may provide a simple, internally consistent framework in which to address the cavity dimensions and ejecta volumes, even though the crustal topography and relief of the high-density mantle plug may have been subsequently modified by the effects of ductile flow in the crust (Bratt et al., 1985). A first order measure of the volume of the preimpact crustal material may be inferred from the volume of the gravimetrically determined plug of uplifted mantle (Bratt et al., 1985).

Equating the mass of the uplifted mantle plug that would nullify *TCFAGA* to the mass of the excavated basin material yields a first order depth for the transient cavity (d_{ex}) given by

$$d_{ex} = \frac{2}{\pi} \frac{V_u}{R_{ex}^2} \frac{\varrho_m}{\varrho_c}, \tag{10}$$

where ϱ_c is the crustal density ($\approx$ 2.8 g/cm^3), and ϱ_m is the mantle density ($\approx$ 3.3 g/cm^3), R_{ex} is the radius of the transient cavity ($\approx$ 0.5 D_{tc}), and V_u is the volume of the mantle plug at the time of impact. This volume of the mantle uplifted during cavity collapse may be approximated by $V_u \approx 0.5\pi h_p R_p^2$ (Bratt et al., 1985), where the height of the plug h_p is estimated relative to the average depth of the equilibriated Moho, and R_p is the radius of the equilibriated mantle plug at $0.5h_p$.

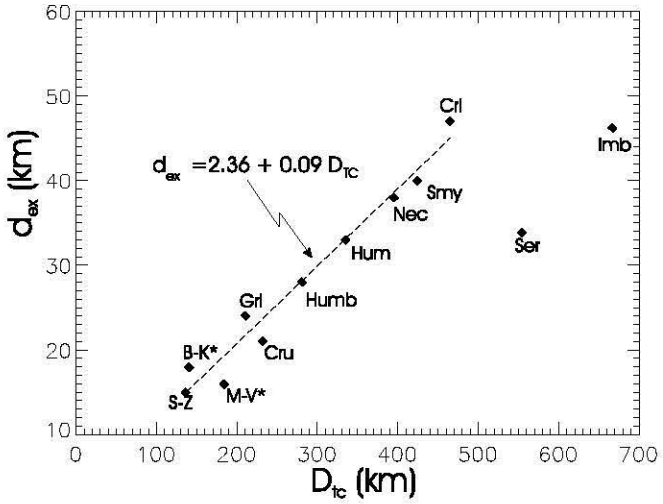

A) Nearside Basins.

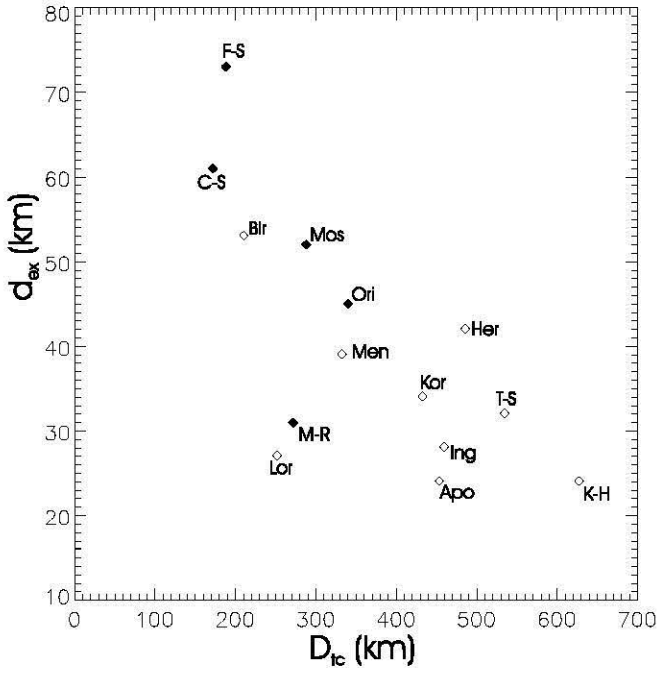

B) Farside Basins.

Figure 29: Comparison of transient cavity diameters and excavation depths for A) nearside and B) farside basins. Basins with superisostatic and subisostatic mantle plugs are marked by solid and open symbols, respectively, whereas those with mantle plugs in near isostatic equilibrium are marked by asterisks. The annotations for the basin names are listed in Table 6.

Figure 29 shows scatter plots of the TC excavation depths (d_{ex}) and diameters (D_{tc}) for 26 of the 27 nearside and farside basins considered in this study. The Australe basin was excluded because its mantle plug is poorly defined as shown by the cross-section in Figure 60. As an older basin, Australe's crust may have experienced considerable viscous relaxation, although clearly data and analysis errors also may have muted inferrences regarding its Moho undulations.

The WCA results in Figure 29A indicate a remarkable direct correlation between d_{ex} and D_{tc} for nearside basins with mantle plugs in both near-equilibrium and overcompensated isostatic states. Specifically, the TC excavation depths (d_{ex}) in km for Schiller-Zucchius (S-H), Balmer-Kapetyn (B-K), Mutus-Vlacq (M-V), Cruger (Crg), Grimaldi (Gri), Humboltianum (Humb), Humorum (Hum), Nectaris (Nec), Smythii, (Smy) and Crisium (Cri) may be modeled in terms of the TC diameter (D_{tc}) by

$$d_{ex} = 2.35 + 0.09 D_{tc}. \tag{11}$$

Outliers to this equation again appear to include the Serenitatis and Imbrium basins that probably involve atypical properties of the nearside crust.

Figure 29B, on the other hand, suggests that d_{ex} and D_{tc} may be largly independent for the farside basins when segregated by their isostatic properties. For example, the basins with superisostatic mantle plugs have a mean D_{tc} ranging between 252 and 243 km, respectively, with and without the possible outlier results from the Moscovience basin, while the corresponding mean d_{ex} range around 52 - 53 km. However, for the basins with subisostatic plugs, the mean D_{tc} range from 419 to 445 km, respectively, with and without the outlier results from the Birkhoff (Bir), Korolev (Kor), Ingenii (Ing), and Apollo (Apo) basins. Similarly, the mean d_{ex} for these basins range from roughly 34 to 33 km. A general inverse correlation in Figure 29B also may be suggested between d_{ex} and D_{tc} when the farside basins are lumped together and not segregated by their central basin isostatic properties. However, the lithospheric significance of this possible relationship is unclear at present.

Table 6 summarizes the TC diameters (D_{tc}) and excavation depths (d_{ex}) from the WCA used in Figure 29B. In general, these results are largely consistent with the lunar nearside and farside dichotomy in lithopsheric properties as discussed in the next section.

3.5 Discussion of Results

The main results of this study are summarized in Table 6, where the WCA estimates of the transient cavity diameters (D_{tc}) and depth of excavation (d_{ex}) are also compared with photogeologic (PG) predictions (Floran and Dence, 1976; Wilhelms, 1987; Spudis, 1993) and gravimetric crustal reconstruction (CR) estimates (Wieczorek and Phillips, 1999). The topographic basin rim diameters (D_{tr}) and the ring counts (# Rings) from photogeologic analysis (Wilhelms, 1987) and the WCA are also listed.

The ring counts from the WCA are generally larger than the PG-inferred number by an average of 1 or 2 more rings per basin. Hence, the relative number of basin rings from the WCA (Table 6) is consistent with photogeologic results, which suggest that nearside basins on average have more rings than farside basins (Solomon and Head, 1980; Wilhelms, 1987). This difference in ring counts supports the rheologic dichotomy of the lithosphere where a more rigid farside lithosphere may have inhibited basin modification so that fewer rings would form, whereas a weaker nearside lithosphere may have facilitated more extensive basin modification and ring development (Melosh, 1989).

Moreover, as shown in Figure 26, the spacing of the WCA ring estimates appears to follow the $\sqrt{2}$D-rule that has been noted for essentially all planetary impact basins (Spudis, 1993). Accordingly,

Nearside Basins									
	Diameter (D_{tc})			depth (d_{ex})			D_{tr}	# Rings	
Study ⇒	PG	CR	WCA	PG	CR	WCA	PG	PG	WCA
B-K			140			18	550?	2	5
Cri*	488	487	465	49	51	47	1060	4	5
Cru*			232			21			4
Gri*		198	211		26	24	440	3	6
Humb*		331	281		38	28	650	2	4
Hum*	380	358	335		45	33	425	3	5
Imb*	685	744	678	68	30	46	1160	4	5
M-V			183			16	690?	1	3
Nec*	540	414	395	54	45	38	860	4	5
S-Z*			136			15	321	2	4
Ser*	572	657	550	57	37	34	740	3	5
Smy*		443	424		40	40	840	2	5
Farside Basins									
Apo			453			24	480	2	3
Aus			641			?	880	1	3
Bir			210			53	330	2	3
C-S*			172			61	440	3	3
F-S*			188			73	600	2	3
Her*			485			42	570	1	3
Ing			459			28	315	2	3
K-H			627			24	500	1	3
Kor			423			34	440	2	3
Lor			251			27	360	2	3
Men			332			39	330	2	3?
M-R*		281	272		36	31	420	3	4
Mos*	230		288			52	420	2	3
Ori*	582	397	340	58	52	45	930	4	6
T-S			534			32	700?	1	3

Table 6: Summary of estimates in kilometers for the transient cavity diameters (D_{tc}) and excavation depths (d_{ex}) from photogeologic (PG) interpretation (Floran and Dence, 1976; Wilhelms,1987; Spudis, 1993), crustal reconstruction (CR) analysis (Wieczoreck and Phillips, 1999), and the WCA (wavenumber correlation analysis) of the present study. PG-inferred (Wilhelms, 1987) topographic basin rim diameters (D_{tr}) and basin ring numbers (# Rings), as well as the WCA ring counts are also listed. * = reported mascon-bearing basins (e.g., Neumann et al., 1996; Konopliv et al., 1998). Basin names are abbreviated. Refer to Table 2 for full names.

basin ring diameters recovered from the WCA may provide an important check on photogeologic estimates that can be limited by inherent subjective biases, the presence of masking cover from subsequent impacts, and other surficial distortions which can complicate photogeologic analyses. The WCA also suggests that the spacing rule may be dependent on the isostatic properties of the rings rather than those of the mantle plugs. The Mutus-Vlacq basin, for example, appears to have a mantle plug in near-isostatic equilibrium as well as rings with super- and subisostatic components.

The radial Moho adjustment model (Figure 10) inferred from *TCFAGA* yields effective global estimates of TC diameters (D_{tc}) that are very consistent with the limited number of estimates from gravimetric crustal reconstruction (Figure 27) and photogeologic analysis (Table 6). The D_{tc} estimate has special significance in the development of basins because it appears to be related to slope failure in which a segment of the rim of the bowl-shaped cavity slides into the cavity to produce a single terrace (Melosh, 1989). The viscosity of the substrate of a basin has also been related directly to $\sqrt{D_{tc}^3}$ so that variations of D_{tc} may provide insights on the viscosity variations of the lunar lithosphere during bombardment times (Melosh, 1982; Alexopoulos and McKinnon, 1994).

Testing the D_{tc} estimates from the WCA in Figure 28 revealed interesting relationships with crustal thicknesses beneath the central basins for characterizing the development and mechanical properties of the lunar lithosphere during bombardment time. For example, equations 8 and 9, respectively, for the representative nearside and farside basins with superisostatic mantle plugs have similar slopes but quite different intercepts. This offset between the two equations suggests that a much stronger lithosphere may have been involved with the formation of the farside basins than for the nearside basins. In particular, because of its greater strength, the thickness of the farside crust wherein superisostatic mantle plugs were produced was probably no greater than about 75% of the thickness of nearside crust in which these plugs were emplaced.

The negative slopes of these two equations are also consistent with the relative ages for the representative nearside and farside basins (Wilhelms, 1987). They may reflect thicker crust for the older basins due to enhanced subsidence of the uplifted Moho over time compared to more limited subsidence for the younger basins that formed when lithospheric viscosity was greater. A comparable age relationship for basins with subisostatic plugs is difficult to evaluate at present because these basins are mostly limited to the farside where the basin ages are poorly constrained (Head et al., 1993).

Figure 28 further indicates that the transient cavity diameters for basins with overcompensating mantle plugs are generally smaller than for basins with undercompensating mantle plugs. This supports the crustal dichotomy in viscosity between the nearside and farside because of the direct proportionality of viscosity with D_{tc} (Head, 1982; Melosh, 1982; Alexopoulos and McKinnon, 1994).

For the farside basins, Figure 28 also suggests that a critical crustal thickness of perhaps 30 km may have differentiated the production of superisostatic and subisostatic mantle plugs. The production of superisostatic mantle plugs was apparently limited to crustal thicknesses at or below this critical value, whereas in thicker crust the mantle plugs appear to have developed only to subisostatic levels.

Additional interesting associations for the TC diameters (D_{tc}) are given in Figure 29 in terms of the related excavation depths (d_{ex}) that were obtained from mass balance estimates on the WCA results. For example, the proportional scaling relation from photogeologic studies is strongly supported by

equation 11 for nearside basins with both overcompensating and essentially equilibriated mantle plugs. The intercept for this equation is only marginally different from zero given the uncertainties of the data and assumptions used in the WCA. Equation 26 also reflects the relative age relationships for the representative nearside basins that were inferred for equation 8

Figure 29A clearly portrays Serenitatis and Imbrium as possible outliers to equation 11. However, Imbrium and Serenitatis lie on a line of roughly the same slope as equation 11 but with an intercept difference of about 16 km. This offset suggests excavation depths for the outlier basins that may be about 28-37% shallower than the depths predicted by equation 11 for the representative basins with more typical nearside crustal properties.

Proportional scaling may not hold for farside basins as indicated by the results in Figure 29B. Apparently on the farside, excavation depths for basins with subisostatic plugs on average were only about 64% of the d_{ex} from basins with superisostatic plugs. The number of farside basins with superisostatic plugs is relatively small. However, the d_{ex} inferred for these basins are generally deeper than those of their nearside counterparts.

The shallowest d_{ex} have been inferred for the nearside Schiller-Zucchius (S-Z), Mutus-Vlacq (M-V), and Balmer-Kapetyn (B-K) basins that show minimal or no mare flooding (Konopliv et al., 1998). Hence, fractures for transporting magmas to the surface perhaps may not have reached sufficient depths to tap subsurface magma reservoirs. The shallow depths of excavation attributed to the farside basins with subisostatic plugs (Figure 29B) also may account for their apparent lack of mare flooding.

In general, the WCA results are consistent with the development of basin rings from impacts that created concentric faults (Wilhelms, 1987; Spudis, 1993) with further modification of the crustal surface and mantle topographies by viscous relaxation and sublithospheric flows (Melosh, 1989; Spudis, 1993). The ring and TC attributes inferred from the WCA support the dichotomy in lithospheric properties between the lunar nearside and farside. However, these interpretations are clearly simplistic and must be used with caution because basin site variations in local rheological properties, impactor attributes, and impact effects have not been taken fully into account.

3.6 Conclusions

The wavenumber correlation analysis (WCA) of lunar free-air gravity anomalies and terrain gravity effects was used to investigate basin ring and transient cavity attributes. In particular, the radial adjustment model (RAM) for the lunar Moho inferred from *TCFAGA* may provide insight on the number, distribution, and isostatic properties of the basin rings. Estimates on the location and size of basin rings were derived from the zero and maximum amplitudes in the RAM data that are concentric to basin centers. These estimates are strongly correlated with the results from photogeologic interpretations. Hence, the WCA estimates can complement and augment photogeologic analysis that may suffer inherent subjective biases and distortions of the basin surface due to ejecta blanketing from nearby or superposed impacts, mare flooding, and other masking effects.

The WCA-inferred basin rings follow the $\sqrt{2}$D-spacing rule that is observed for all multi-ring basins on the terrestrial planets and the Moon. Ring counts per basin on average are larger on the nearside than on the farside, suggesting that a more rigid farside lithosphere may have inhibited the development of basin rings (Melosh, 1989).

Basin rings probably originated from vertical crustal motions induced by the passage of the shock wave from bollide impact (Baldwin, 1949). The basin rings are consistent with forceful central uplift of the crust followed by circumjacent oscillatory zones of crustal collapse and uplift (Spudis, 1993). The large-scale wave-like deformation of the crust presumably produced mass variations that were sustained by the strength of the lithosphere (Baldwin, 1949; Melosh, 1989) and hence "frozen" in the lithosphere as incompletely compensated ring structures. The distribution of these features and their related incipient crustal motions may be inferred from adjustments of Figure 10 that the lunar lithosphere may be seeking for equilibrium.

The transient cavity diameter for a lunar basin may be estimated from the innermost basin-central zero contour in the RAM data. These diameters are generally larger for farside impact basins than for the nearside basins. Transient cavity diameters inferred for basins with superisostatic mantle plugs also tend to correlate directly with relative basin ages and generally are smaller than for basins with subisostatic mantle plugs. These results are consistent with the direct proportionality between transient cavity diameter and lithospheric rigidity variations that apparently characterizes the tectonic development of the lunar lithosphere.

For the farside, these results also suggest a critical crustal thickness of about 30 km that may have differentiated the development of superisostatic and subisostatic mantle plugs. Superisostatic mantle plugs presumably developed in crustal thicknesses below this critical value, whereas in thicker crust mantle plugs may have only developed to subisostatic levels. For all nearside basins, mass balance estimates of transient cavity excavation depths support the proportional scaling relation of roughly 0.1 D_{tc} that was obtained previously from photogeologic studies. However, for the Serenitatis and Imbrium basins with possibly atypical nearside crustal properties, this relation may overestimate excavation depths by 28-37%. For both nearside and farside basins, shallow excavation depths also may account for the apparent lack of mare flooding.

In general, the spectral correlations between lunar free-air anomalies and the gravity effects of the terrain reveal interesting insights regarding the mechanical properties of the lithosphere during bombardment times. However, caution is urged in using these results that may be complicated by local variations in basin rock properties and impact effects, as well as any errors in the data and assumptions of this study.

4 Lunar Subcrustal Differentiation from Spectral Free-Air and Terrain Gravity Correlations

4.1 Introduction

Lunar gravity anomalies are produced by subsurface density variations that also may reflect the internal dynamics of the Moon's evolution. In chapter 2, the free-air gravity anomalies (*FAGA*) of the Moon were separated into terrain-correlated (*TCFAGA*) and terrain-decorrelated (*TDFAGA*) components based on their spectral associations with the terrain gravity effects (*TGE*). From these correlations, crustal models of possible Moho variations and isostatic mass imbalances were developed that account for the *TGE* and *TCFAGA* components of lunar gravity field.

In the present chapter, the remaining *TDFAGA*-component is investigated for possible mass variations of the lunar core and mantle. Plausible models for the lunar subcrust are developed that are also constrained by studies of seismic data, normalized moments of inertia, and the gravitational differentiation and compressibility of lunar magmas. Residual *TDFAGA* are also estimated that include a minor crustal component and the small errors from subcrustal modeling.

In the next section, the *TDFAGA* spectrum is analyzed for components that may reflect major density discontinuities within the lunar core, mantle, and crust. A model of the radial densities of the Moon is synthesized in section 3 from geochemical studies and the Apollo seismic results to constrain the depths and magnitudes of possible mass discontinuities. In section 4, undulation models of the density interfaces are developed by least squares inversion of the gravity components as inferred from the *TDFAGA* spectrum. The significance of these results for developing enhanced models of lunar evolution are considered in section 5.

4.2 Spectral Decomposition of *TDFAGA*

Probing the Moon's interior to understand the stratigraphic properties of the core, mantle, and crust was initially attempted from seismic measurements taken during the Apollo era (e.g., Hood, 1986). These seismic studies were limited to a few stations on the nearside where seismicity turned out to be minimal yielding relatively marginal results (Nakamura, 1983). However, the seismic data provided a first order estimate of 56 km for the thickness of the crust at the Apollo landing sites (Toksöz et al., 1974; Nakamura et al., 1979; Goins et al., 1981; Nakamura, 1983). Hence, the existence of a lunar crust may well be complemented by additional stratification of fundamental density variations such as the subcrustal stratification that has been seismically inferred for the Earth (e.g., Morelli and Dziewonski, 1987).

Stratified distributions of lateral mass variations within planetary bodies can also be reflected in

gravity field observations. For example, variations of the Earth's core-mantle boundary have been commonly modelled from low degree and order spherical harmonic components of the gravity field (e.g., Hide and Malin, 1970; Dziewonski, 1984; Morelli and Dziewonski, 1987). Mantle convection in Mars has been related to the lower harmonics up to degree and order 10 of the gravity field (Kiefer et al., 1996). And in the gravity spectrum of Jupiter, a dramatic change in slope around degree 10 has been related to the rotation rate of Jupiter's deep metallic hydrogen interior while the higher zonal harmonics have been taken to reflect the redistribution of mass in its outer layers (Hubbard, 1999).

Slope changes in the amplitude spectrum of a data set are commonly used to explore for patterns of frequency components that may be related to major features of the data (e.g., Blakely, 1996; Naidu and Mathew, 1998). A spectral slope indicates the rate of change in energy over a bandwidth of frequencies. In gravity data from multi-depth sources, for example, spectral slope variations can help discriminate the effects from the different depths because the related frequencies vary inversely with depth. In general, the effects due to the relatively shallower sources are commonly reflected in the spectrum by a fairly broad bandwidth involving mostly the higher frequency components with a relatively flat rate of energy decay. The deepest sources, on the other hand, yield effects with severly attentuated higher frequencies that are characterized by a sharp slope over a relatively narrow bandwidth of the lower frequency components. The effects of the sources at intermediate depths will be expressed by intermediate slopes over bandwidths of the intermediate frequency components.

Unfortunately, not all slope variations in the gravity spectrum are uniquely diagnostic of the depth distribution of the sources because of the fundamental equivalent source ambiguity of potential field theory. However, these variations certainly can provide an interpretational context for testing the gravity data for the effects of subsurface sources from different depths.

For the Moon to first order, geological and geophysical evidence suggests that it may be stratified into crustal, mantle, and core components (e.g., Hood, 1986). The spectral properties of *FAGA* are largely consistent with the first order subdivision of the lunar interior. However, working out the relative contributions of these regions in *FAGA* is complicated by the considerable overlap in spectral properties that can occur between the related effects.

In chapter 2, for example, significant long and intermediate wavelength components of *FAGA* were attributed to the crust through the use of *TCFAGA*. Hence, to the degree that the crustal analysis was based on accurate data and assumptions, *TDFAGA* may yield enhanced estimates of the gravity effects of the mantle and core where the corrupting effects of the crust have been minimized. More generally, *TDFAGA* may be decomposed into crustal, mantle and core components for mass models that may be readily integrated by superposition with crustal models from the previous chapters to produce a comprehensive model for *FAGA*.

A possible separation of the crustal, mantle and core components in *TDFAGA* is suggested by its correlation spectrum with *FAGA* that is shown in Figure 30. The spectrum was obtained by computing correlation coefficients between spherical harmonic *FAGA* expansions (LP75G) up to degree 2, 3, 5, 7, 10, 12, 15, 20, 25, 30, 35, 40, 50, 60, 70 and 75 and the corresponding correlation-filtered *TDFAGA* components over the Moon between $\pm 64^{o}$ latitude. These *TDFAGA* correlate only partially with *FAGA* because they lack significant long, intermediate, and short wavelength

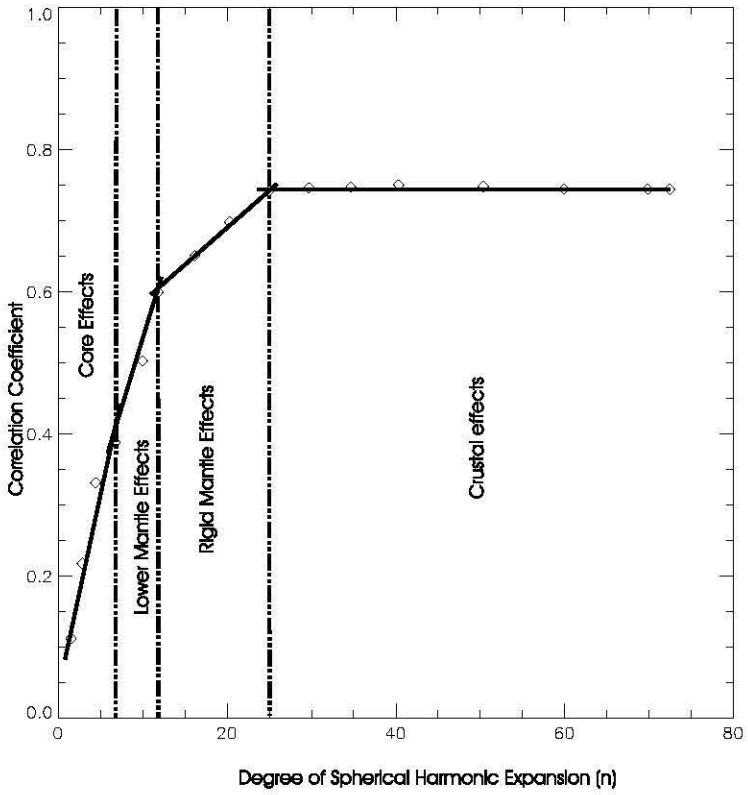

Figure 30: Correlation spectrum between *TDFAGA* and *FAGA* (LP75G). The spherical harmonic expansion of *FAGA* was evaluated at degree and order 2, 3, 5, 7, 10, 12, 15, 20, 25, 30, 35, 40, 50, 60, 70 and 75. The curve was interpreted for four slopes that may differentiate density variations due to lateral changes of the core-mantle ($n \leq 7$), lower mantle ($8 \leq n \leq 12$), and upper mantle ($13 \leq n \leq 24$) boundaries, as well as crustal properties ($25 \leq n \leq 75$).

components that have been attributed to the crust by the analysis in Chapter 2. However, the spectral properties of *FAGA*, by contrast, record among other things the effects from the multi-depth distribution of anomalous sources, so that the correlation spectrum may reflect the gross stratification of source effects in *TDFAGA*. As described below, this hypothesis can be readily tested against standard geological models of the lunar interior using the inversion procedures developed in Chapter 2.

Several branches seem to be apparent in the correlation spectrum for separating the *TDFAGA* into crustal, mantle, and core components. For example, a relatively flat branch corresponding to maximally correlated anomaly components above degree 25 may well be attributed to the higher frequency effects of the crust, which is a well-accepted constituent of the lunar interior. At the low-frequency end of the spectrum, on the other hand, another well-defined branch is evident with maximum slope through spherical harmonic degree 7 that may mostly reflect density variations in the core or across the core-mantle boundary. The existence of the lunar core was initially inferred from the paleomagnetic properties of the lunar rocks returned by the Apollo mission (Runcorn et al., 1970), and confirmed by the Doppler tracking of the spin-stablized Lunar Prospector satellite

(Konopliv et al., 1998). Finally, two additional branches with decreasing slopes were inferred for degrees 8 through 12 and 13 through 24, respectively, that may predominantly reflect the effects of lower and middle mantle density variations, respectively, in *TDFAGA*.

4.3 Standard Geologic Model for the Lunar Interior

Figure 31 gives a possible geologic context for interpreting the break down of *TDFAGA* that may be inferred from the correlation spectrum of Figure 30. This generalized model of radial lunar variations in compostion, density, and pressure is constrained by limited Apollo seismic data (e.g., Taylor, 1982; Hubbard, 1984) and studies of planetary differentiation processes (e.g., Delano, 1980; Circone and Agee, 1996; Agee, 1998). Its main structural features include the core, mantle, asthenosphere, lithosphere and crust that were possibly produced from an early magma ocean by differentiation (Agee, 1993).

Weakly paleomagnetic rock samples returned by the Apollo missions provided the initial evidence for the existence of a lunar core (e.g., Runcorn, 1996). However, improved estimates of the normalized polar moments of inertia from Doppler tracking of the Lunar Prospector satellite have confirmed an iron core roughly 220-450 km in radius for the Moon (Konopliv et al., 1998). For this study, a massive FeS core with a density of 7.9 g/cm^3, central pressure of 4.7 GPa, and a mean radius of 450 km was assumed.

Above the core is a complexly structured mantle possibly of pyroxene and olivine that to first order may include lower, middle, and upper components (Hood, 1986). Its solidification from the magma ocean was governed by many factors including various cooling rates, phase-density relations, rheologies, and thermal convection modes (Alley and Parmentier, 1998).

The lower mantle with a possible mean density of 3.7 g/cm^3 may extend from 650 km (Circone and Agee, 1996; Agee, 1998) to about 1288 km. It also may include a higher viscosity zone between 800 to 1000 km (Taylor, 1982; Hubbard, 1984) and an underlying lower viscosity zone from about 1000 km to 1288 km where density may increase dramatically by about 4.1 g/cm^3 into the core (Taylor, 1982; Hubbard, 1984; Alley and Parmentier, 1998). Hence, the lower mantle may include an elastically weak lunar asthenosphere around the metallic core that formed from a dense residual ilmenite cumulate of the magma ocean. At the time of bombardment before 3.5 Byr, the asthenosphere may have possibly extended to the top of the lower mantle providing magmas to lithospheric intrusive and extrusive processes (Hess, 1991; Spudis, 1993). Hence the topography of the lower mantle may reflect sublithospheric mass flow features due to meteorite impacts and other poorly understood lunar tectonic events.

The overlying middle mantle, with perhaps a mean density of 3.4 g/cm^3, may range from about 220 km to 650 km where density increases by perhaps 0.2 g/cm^3 (Binder, 1980; Hood and Jones, 1985; Bills and Rubincamp, 1995). It is overlain in turn by the upper mantle with a mean density of about 3.2 g/cm^3 that may extend from a mean depth of about 55 km to 220 km where the density may increase by 0.1 g/cm^3 (Binder, 1980; Hood and Jones, 1985; Hood and Jones, 1987). The 220-km boundary for the base of the upper mantle is a compromise of the mean 210-km estimates obtained

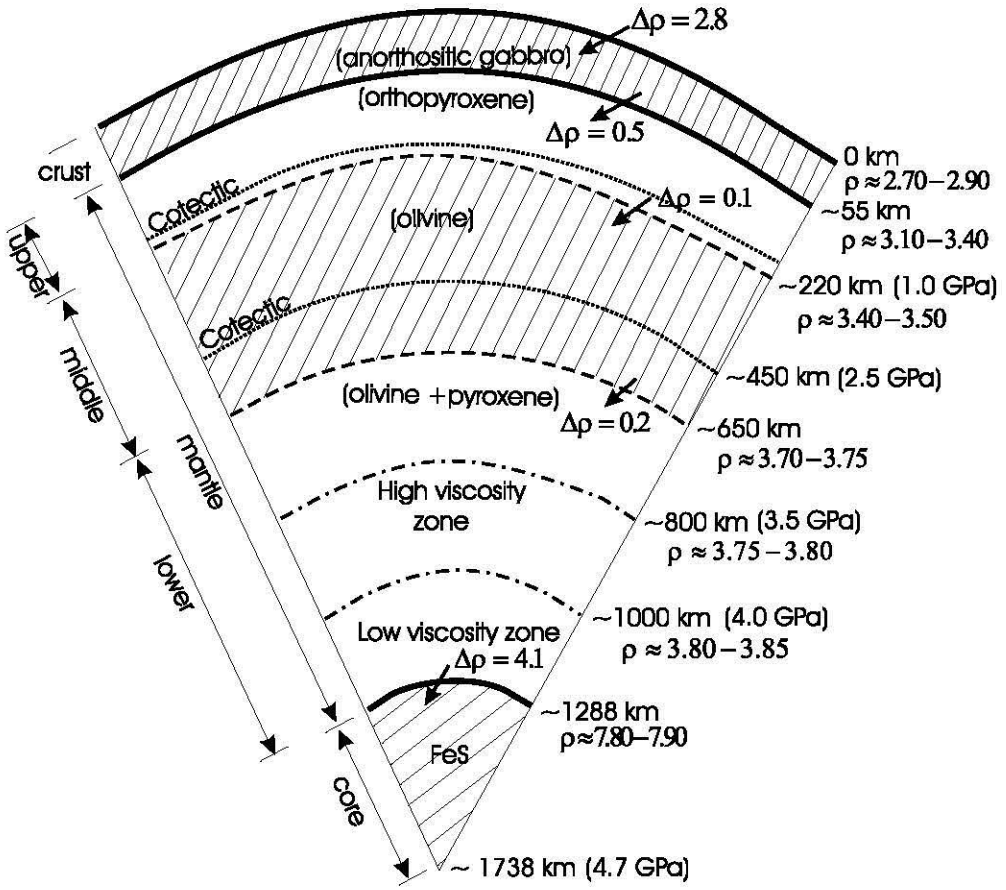

Figure 31: A generalized model of possible structural and compositional variations, as well as mean density (ϱ) and pressure gradients of the lunar interior (adapted from Taylor, 1982; Hubbard, 1984; Hood, 1986; Konrad and Spohn, 1997; Alley and Parmentier, 1998; Konopliv et al., 1998). The dotted lines represent cotectics for the density inversion between orthopyroxene and molten 'black glass' and olivine and 'black glass' at the average pressures of 1.0 and 2.5 GPa, respectively (Circone and Agee, 1996; Smith and Agee, 1997; Agee, 1998). Arrows indicate the density contrasts across the mass discontinuities assumed for this study. Boundary depths are not to scale.

by seismic analysis (Moore, 1981; Nakamura, 1983), a 220-km estimate from a combined analysis of seismic, geothermal, geochemical and moment of inertia results (Hood and Jones, 1987), and the 215-km estimate from the analysis of the lunar moments of inertia (Bills and Rubincamp, 1995).

The middle and upper mantle may also include cotectics that may help account for variations in mantle composition and the different mare basalts identified in the returned lunar samples. A cotectic represents the range of pressure wherein different elements can combine and form a magma with density that is different than the densities of the elements in their crystaline phases (e.g., Agee, 1998). With respect to orthopyroxene and olivine at liquidus conditions, for example, density increases can occur at 0.5-0.7 GPa and 2-2.5 GPa, respectively (Circone and Agee, 1996; Agee, 1998). These pressures roughly correspond to depths of 100 km and 400 km, respectively, in the lunar mantle where magmas may have been denser than the crystalline phases of orthopyroxene and olivine. Hence, lunar magmas may have originated at depths corresponding to olivine-pyroxene cotectics by the pressure-reducing effects of bolloidal impacts or other tectonic features.

In particular, melting of the olivine-pyroxene mantle may have formed the primary magmas for low-Ti mare basalt with green glass generated at the shallower depths corresponding to the pressure range of 0.5-1.5 GPa, whereas high-Ti mare basalt containing black glass may have originated at deeper depths corresponding to pressures of about 2.5 GPa (Delano, 1980; Circone and Agee, 1996; Agee, 1998). The depth of about 450 km from which green glass magma may have originated and risen is also the maximum depth for the bouyant rise of high-Ti basalt from its thermally equilibrated source (Smith and Agee, 1997; Agee, 1998), although the asthenosphere may also have been a source region of high-Ti magma (Hess, 1991).

Geochemical analyses suggest that olivine and pyroxene may coexist at depths greater than 500 km and hence the composition of the lower mantle may involve these minerals (Circone and Agee, 1996). The middle mantle may consist mostly of olivine up to possibly 500 km, while the composition of the upper mantle may involve mainly orthopyroxene and a relatively small amount of olivine. The crust appears to be rich in anorthositic gabrros, ilmenite, iron, and incompatible radioactive elements with crustal densities typically ranging between about 2.60 and 2.95 g/cm^3. (Hood, 1986; Hubbard, 1984).

The current lunar lithosphere then may consist of the upper and middle mantle and an anorthositic crust with a seismically inferred depth extent of about 1000 km (Taylor, 1982; Warren, 1993; Nakamura et al., 1982). During the first 2 Byr, the main effect of cooling was the growth of the lithosphere to a thickness of perhaps 600-700 km (Konrad and Spohn, 1997) while the lower mantle and core cooled relatively little due possibly to whole mantle convection (Alley and Parmentier, 1998).

The growth of the lithosphere was perhaps strongly influenced by whole mantle convection and conductive heat transfer through the anorthositic crust (Konrad and Spohn, 1997). Dense ilmenite cumulates, formed during the final solidification of the magma ocean, presumably sank to the Moon's center to form a core rich in U and Th that in turn started heating the overlying lower mantle. Hence, whole mantle convection may have resulted from the combined effects of cooling from above and heating from below (Alley and Parmentier, 1998). During the time of bolloidal impacts, the depth of the lithosphere was perhaps 650 km (Konrad and Spohn, 1997). Partial melts at pressures of about

2-2.5 GPa ($\approx$ 400-600 km) within the stratified mantle may have risen diapirically to the surface (Hess, 1991). In fact, heat was trapped in the lunar interior by the compositional stratification of the mantle, preventing the rapid formation of plumes capable of generating surface volcanism. Otherwise voluminous mare basalts would have appeared on the surface much earlier in lunar evolution than they are observed to occur (Alley and Parmentier, 1998).

The standard geological model of the lunar interior given in Figure 31 emphasizes the possible radial density gradients, which are most easily constrained by geophysical and geochemical arguments, over intralayer density variations that in general are poorly understood and constrained. Clearly, the undulations of these density boundaries may be principal sources of gravity anomalies by virtue of the lateral density variations that they define. These undulations also may well reflect ancient patterns of mass flow and hence provide new insight on the dynamic evolution of the lunar interior.

Accordingly, the interpretation of *TDFAGA* was focussed on inferring possible undulations related to major density contrasts of the lunar subcrust. Clearly, the largest of these occurs across the core-mantle boundary where density may increase by roughly 4.1 g/cm^3. These undulations may be mapped from the *TDFAGA* components up to degree 7 as inferred from the correlation spectrum of Figure 30. The next largest contrast may involve a 0.2 g/cm^3 increase across the middle-lower mantle boundary. The branch in Figure 30 corresponding to degree 8 through 12 components of *TDFAGA* has been inferred to reflect mostly the undulations of this boundary. In addition, the branch for the degree 13 through 24 components of *TDFAGA* has been taken to represent predominantly undulations of the boundary between the upper and middle mantle where a density increase of perhaps 0.1 g/cm^3 may occur within the subcrustal lithosphere.

The final branch in the correlation spectrum (Figure 30) corresponds to the degree 25 and higher components of *TDFAGA*. These components are perhaps the most appropriate free-air anomalies to relate to remote sensing imagery and other data sets that impose constraints on the poorly understood lunar crust.

4.4 Subcrustal Modeling of TDFAGA

In this section, the undulation models for the principal subcrustal density boundaries that have been inferred for the lunar interior will be developed. Specifically, undulations of the boundaries between the core and mantle, middle and lower mantle, and upper and middle mantle will be considered. Affiliated *TDFAGA* components will be estimated using spectral correlation filters developed between the various inferred *FAGA* components and *TDFAGA*. These anomaly estimates will then be used to model the various boundary undulations in the same way that the Moho was modelled in Chapter 2. In particular, GLQ integration will be used to relate the appropriate *TDFAGA* components to 1^o prism thicknesses at the appropriate reference depths and density contrasts.

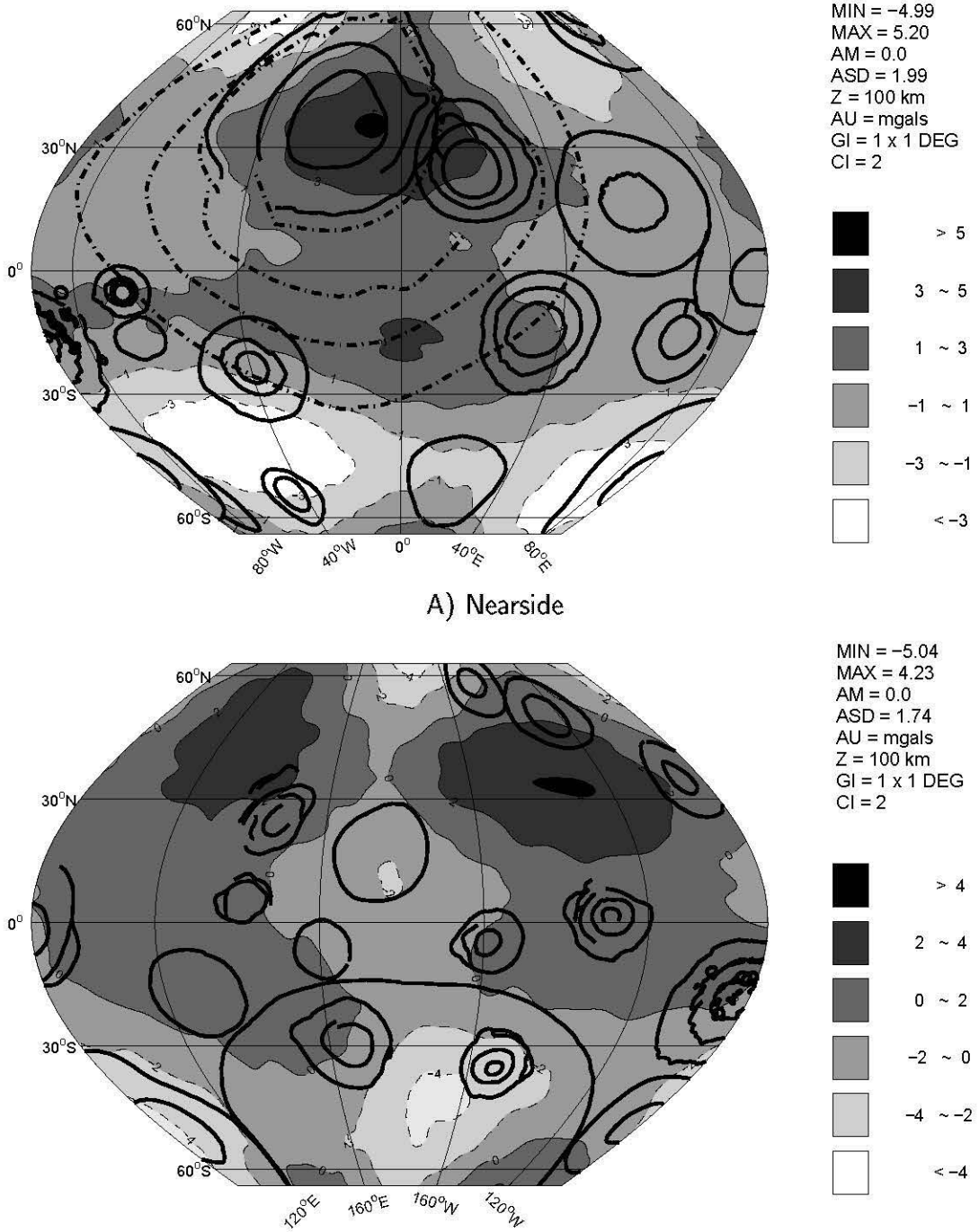

Figure 32: *TDFAGA* components estimated for possible lateral density variations of the core-mantle boundary.

4.4.1 Core Topography

Figure 32 shows the inferred core topography effects of *TDFAGA*. They were obtained by inversely transforming all the wavenumber components of *TDFAGA* (Figure 7) that are positively correlated with the wavenumber components of *FAGA* (LP75G) up to degree 7. While these amplitudes are marginal relative to the data errors, the anomalies are regionally systematic components of the best determined gravity field of the Moon currently available. Accordingly, testing these anomalies for the properties of the core and lower mantle, which are very poorly understood at present, may yield important new insight on lunar evolution.

Figure 33 shows the core topography that was inferred from the least squares inversion of the *TDFAGA* components of Figure 32. Thickness variations of 1^o spherical prisms modelled by GLQ integration were estimated assuming a heavy FeS-core with a radius of 450 km and a density contrast of 4.1 g/cm^3 across the core-mantle boundary. The inversion obtained core-mantle boundary undulations that produced gravity effects which matched more than 99% of the inferred *TDFAGA* core components (Figure 32) with 0.02-mGals standard error.

The results suggest a relatively subdued core topography with an amplitude standard deviation (ASD) of just under 4 km (Figure 33). Basin associations also appear to be relatively limited with possibly depressed core topography underlying the farside South Pole-Aitken, Australe and Freundlich-Sharonov basins and a broad raised region of the core beneath the nearside Imbrium and Serenitatis basins.

4.4.2 Differentiated Mantle Components

Estimates of the predominantly mantle components in *TDFAGA* are given in Figure 34. They were extracted from *TDFAGA* (Figure 7) using spectral correlation filters based on the degree 8 through 24 wavenumber components of *FAGA* (LP75G). These effects appear to indicate prominent density contrasts of the mantle that may reflect the deeper seated development of craters and other poorly understood tectonic features of the Moon. On the basis of the correlation spectrum in Figure 30, these mantle effects were subdivided further for the possible effects of lower and middle mantle topographic variations.

In particular, the *TDFAGA* components estimated for the effects of the lower mantle topography are shown in Figure 35. Again, these components were derived by spectral correlation filtering where all wavenumber components of *TDFAGA* were passed that correlated positively with the wavenumber components of the degree 8 through 12 *FAGA* as inferred in Figure 30. In general, many of the positive anomalies appear to be correlated with surface impact structures. Specifically, the nearside Imbrium, Serenitatis, Crisium and Humorum impacts may have resulted in disrupted and redistributed material at lower mantle depths. As described earlier, a possible source of these anomalies may involve variations of lower mantle topography. Hence, testing the anomalies for these undulations may yield insights on lower mantle mass flows and deformation in response to surface bolloidal impacts and other tectonic events.

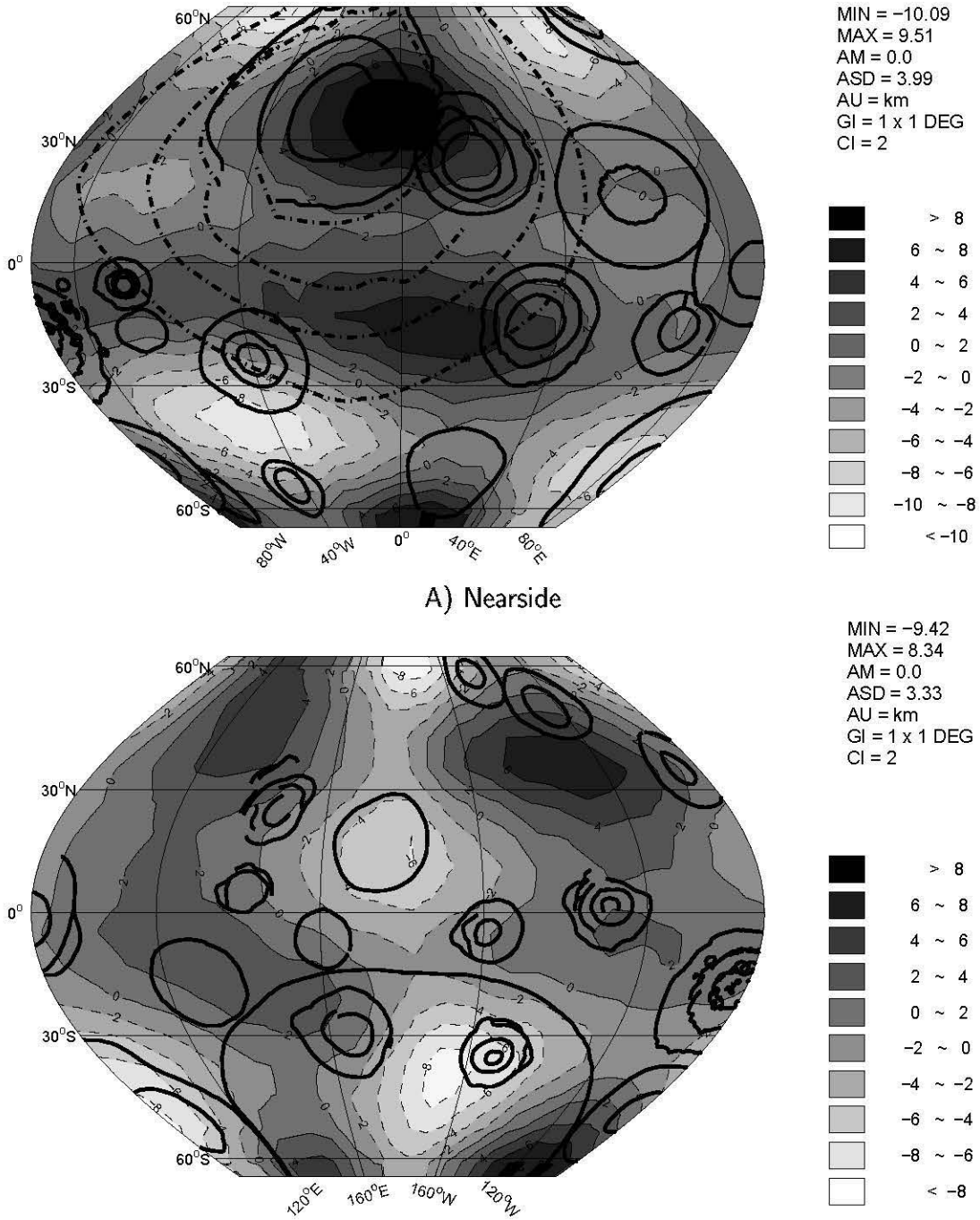

Figure 33: Inferred core topography relative to a mean core radius of 450 km and a density contrast of 4.1 g/cm^3.

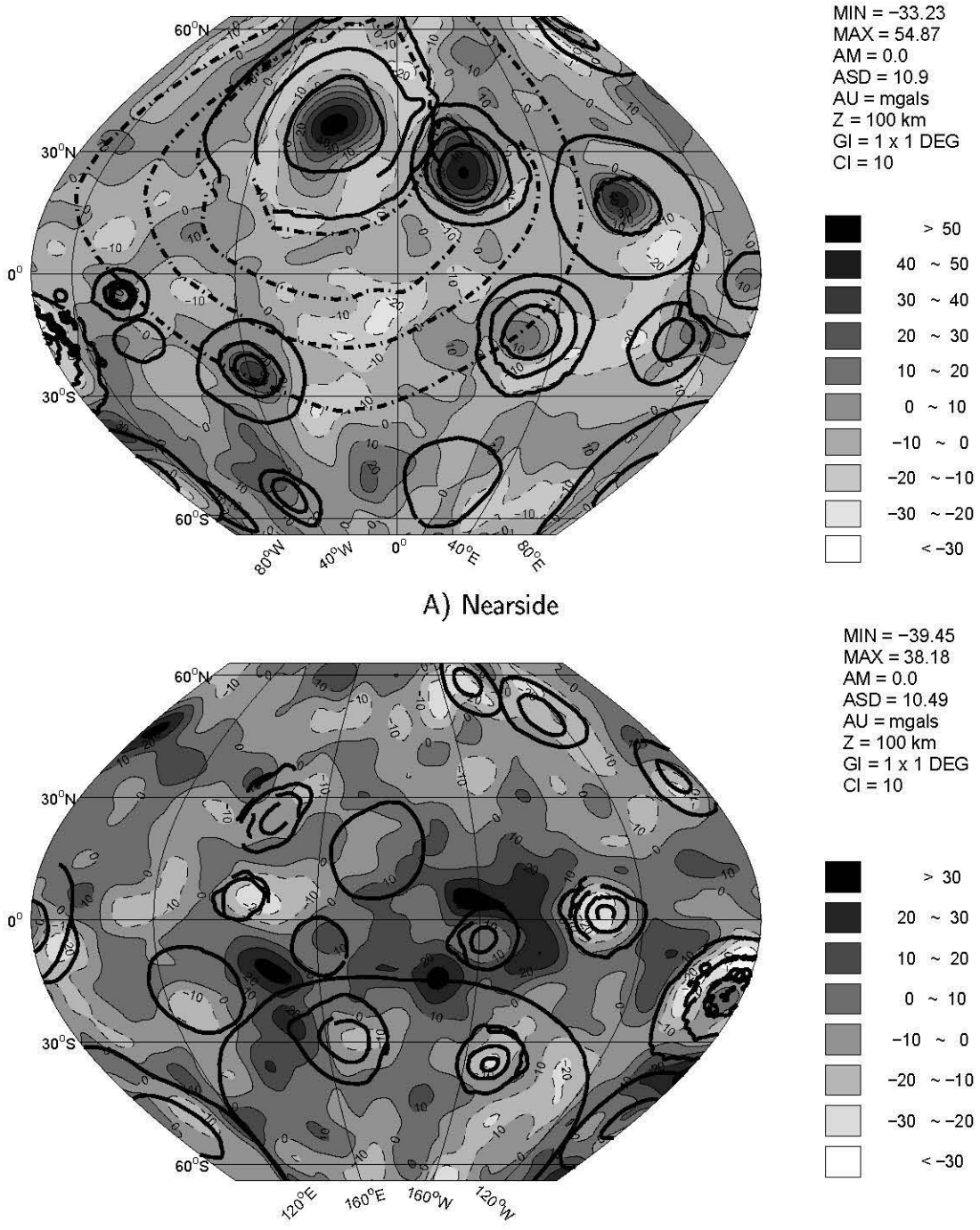

Figure 34: *TDFAGA* components estimated for possible lateral density variations of the mantle.

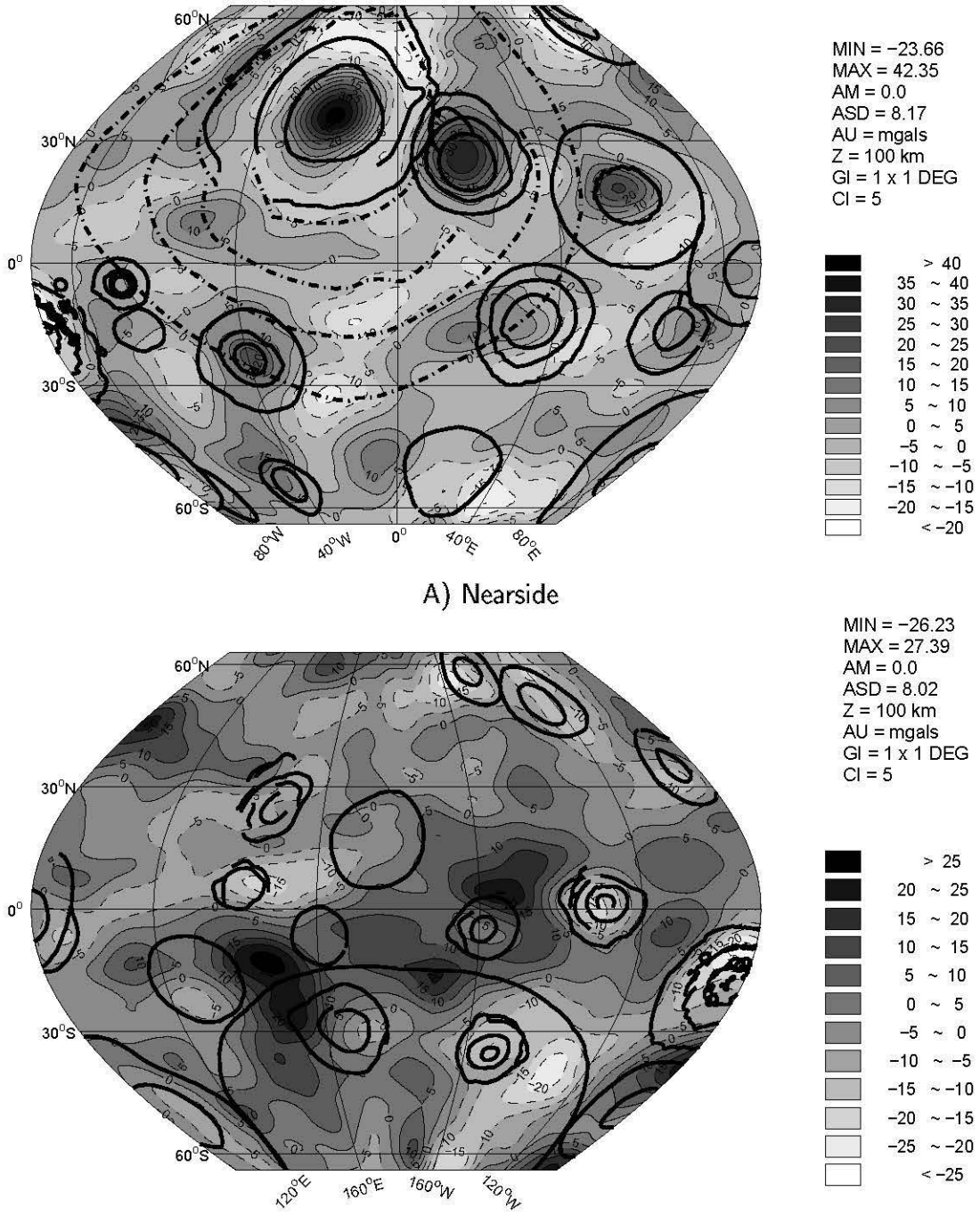

Figure 35: *TDFAGA* components estimated for possible lateral density variations of lower mantle topography.

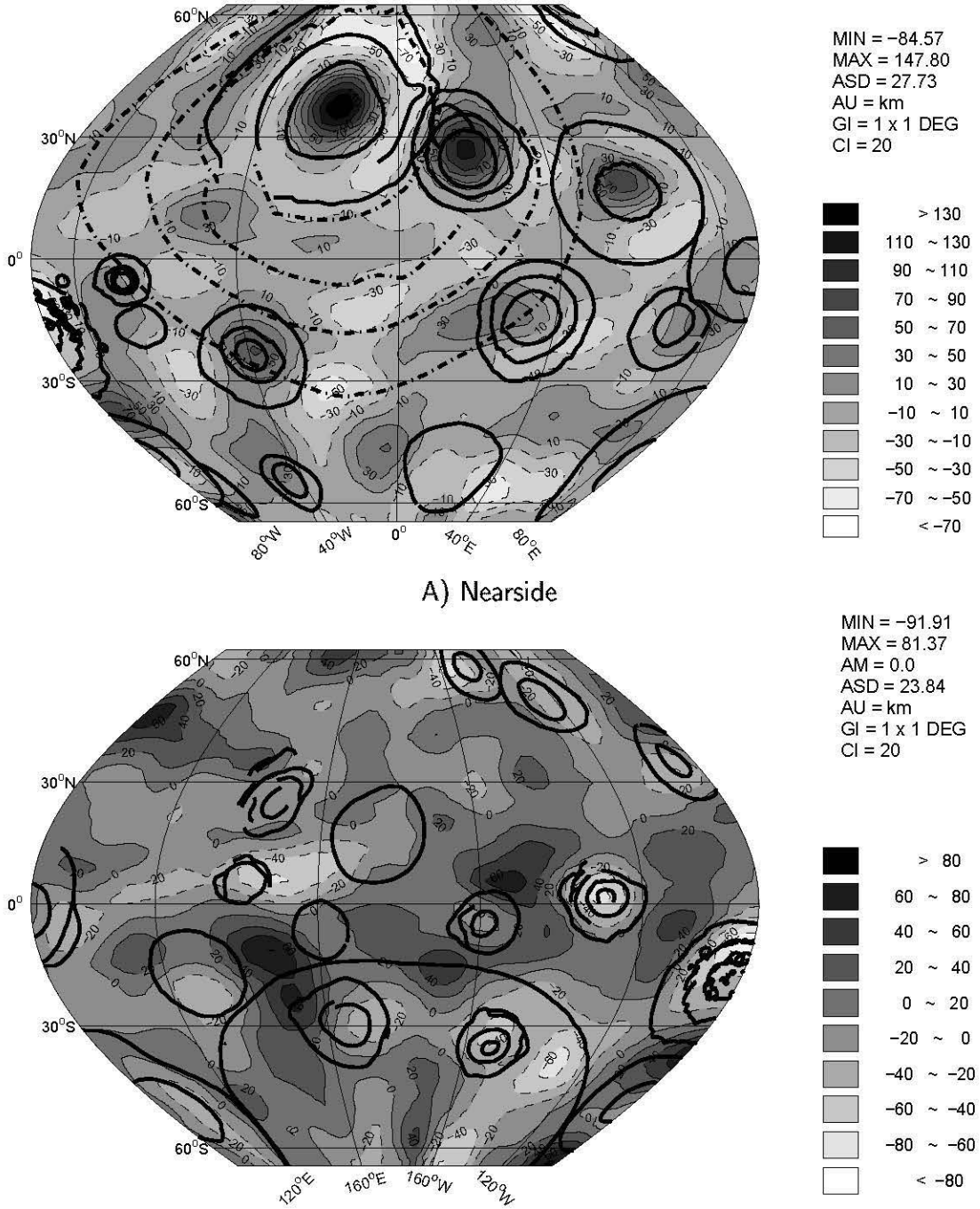

Figure 36: Inferred lower mantle topography relative to a mean depth of 650 km and a density contrast of 0.2 g/cm^3.

Figure 36 shows the lower mantle topography that was inferred from the least squares inversion of the *TDFAGA* in Figure 35 assuming a reference depth of 650 km where density may increase by 0.2 g/cm^3. The inversion based on GLQ modeling of 1^o spherical prisms obtained undulations with gravity effects that matched more than 99% of the *TDFAGA* in Figure 35 with a 0.03-mGals standard error.

The inferred topography of the lower mantle shows remarkable associations with the lunar basins. For example, on the nearside the lower mantle appears to be raised beneath the Imbrium, Serenitatis, Crisium, Nectaris and Humorum basins, whereas it is generally depressed under many of the farside basins. Assuming this boundary was also the lithospheric bottom during bombardment time suggests that the ancient lithosphere on the nearside may have been on average about 18 km thinner than its farside component. Also in this context, the energy of relief of this inferred boundary between the ancient lunar lithosphere and asthenosphere is about 16% greater for the nearside than the farside. This estimate, obtained by comparing the ASD's in Figure 35, is consistent with a lunar lithosphere that may have been hotter and less viscous on the nearside than the farside.

The *TDFAGA* components inferred for the effects of the middle mantle topography are given in Figure 37. Spectral correlation filtering was used to pass all wavenumber components of *TDFAGA* that were positively correlated with degree 13 through 24 *FAGA* components as estimated in Figure 30. These inferred effects of the topography of the middle mantle are substantially subdued relative to the previously estimated effects of the lower mantle topgraphy (Figure 36). However, their inversion for the possible topography of the middle mantle as shown in Figure 38 reveals numerous interesting affiliations with the lunar basins.

The results in Figure 38 were obtained as before by least squares inversion using GLQ modeling of 1^o prisms about a reference depth of 220 km where the density was presumed to increase by 0.1 g/cm^3. The gravity effects of the resultant undulations of Figure 38 matched more than 99% of the *TDFAGA* in Figure 37 with a 0.01-mGals standard error. For the most part, the inferred middle mantle topography and lunar basin relief for the near and far sides show negative and positive correlations, respectively.

4.4.3 Crustal and Other Residual Components

To this point, mass models have been inferred for the relief of the core and lower and middle mantle components that account for nearly all of the *TDFAGA* in Figure 7. The remaining *TDFAGA* components that have yet to be accounted for are shown in Figure 39. They include the crustal *TDFAGA* components of Figure 7 that are spectrally correlated with the degree 25 through 75 components of *FAGA* as suggested in Figure 30, as well as the small modeling errors from the subcrustal analysis.

The residual *TDFAGA* in Figure 39 are relatively higher frequency features with marginal amplitudes compared to the errors in *FAGA*. As pointed out in Chapter 2, many of these features appear to show systematic relationships with lunar basins that may be further modeled in terms of the positive effects of mare basalt fill, the negative effects of unconsolidated deposits of ejecta and fractured

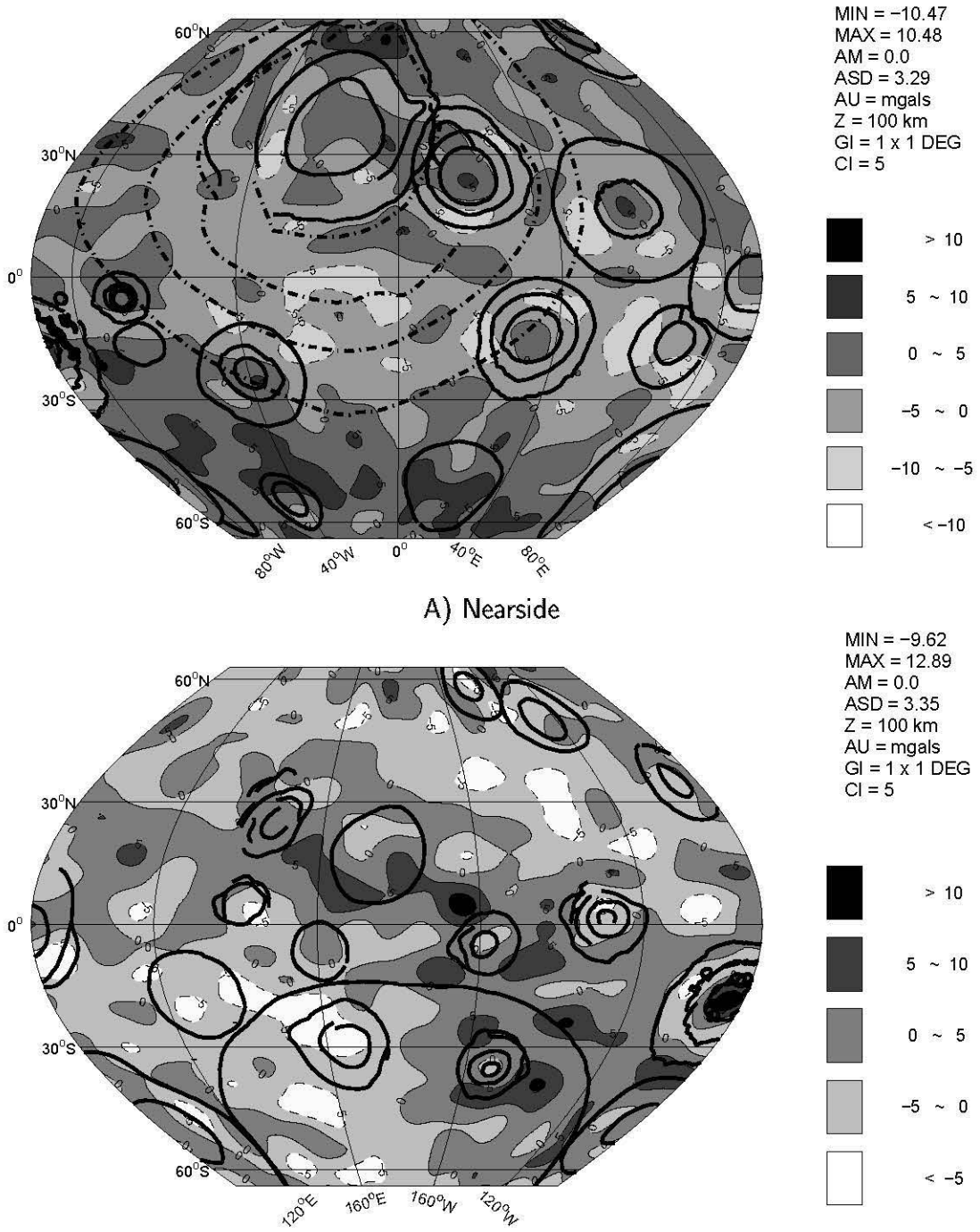

Figure 37: *TDFAGA* components estimated for possible lateral density variations of middle mantle topography.

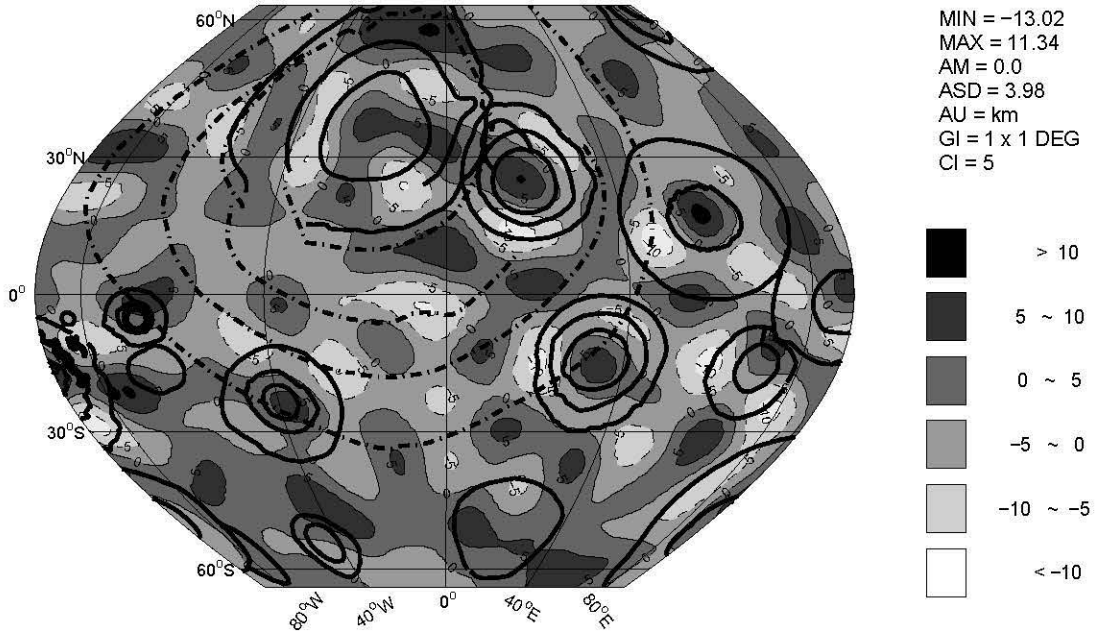

A) Nearside

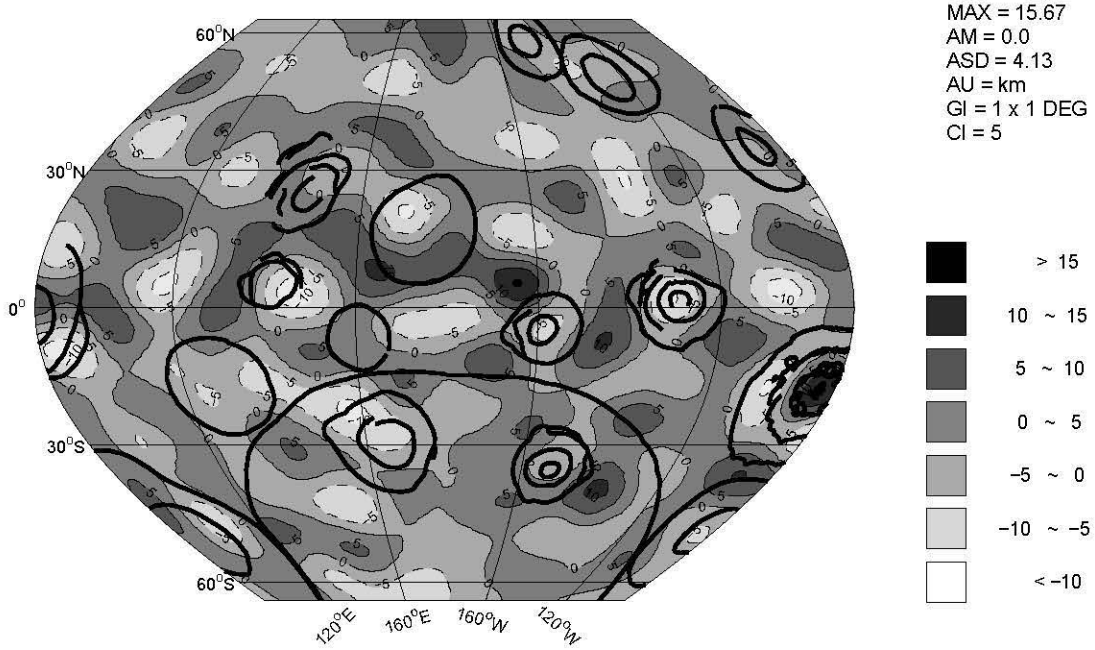

B) Farside

Figure 38: Inferred middle mantle topography relative to a mean depth of 220 km and a density contrast of 0.1 g/cm^3.

and brecciated crust, and other crustal effects. However, the residual anomalies in Figure 39 are quite marginal compared to *TDFAGA*, as well as *FAGA* and their related errors. Accordingly, for the purposes of this study, they will be taken to reflect mostly errors in *FAGA* and the subcrustal modeling. Hence, the consideration of their geological significance will be limited to the analysis presented in Chapter 2.

4.5 Geologic Significance of Results

The evolution of the interior of the Moon involved both exogenous (e.g., bolloidal impacts) and endogenous (e.g., mantle convection) events. Recent thermal evolution modeling of the Moon suggests that the core may have remained liquid or solid up to the present time, but that heat flow from the core probably decreased rapidly to shut off the magnetic dynamo by about 3.5 Byr, while the lower mantle remained relatively hot possibly at a temperatures of $1700^o\ K$ (Konrad and Spohn, 1997). Hence, heat supplied to the mantle could have ensured sublithospheric flow and deformation of mass discontinuities in response to bolloidal impacts. Accordingly, the above developed subcrustal lunar models are investigated below for insights on the possible internal properties and evolution of the near and far sides.

4.5.1 Core Topography Inferences

The lunar core probably formed by about 4.1 Byr, some 400 Myr after the formation of the Moon (Runcorn, 1996). If the Moon was initially cool, then its interior would have heated rapidly after accretion (Konrad and Spohn, 1997). Hence, inferences on core topography may provide valuable insights on the internal properties and evolution of the Moon.

For example, more radioactive elements may have been incorporated in the mantle and crust of the nearside than in the farside components (Stevenson, 1980). This compositional dichotomy undoubtedly contributed to the formation of the great lunar hotspot in the region of the Imbrium-Procellarum basin (Korotev, 2000). Differences in nearside and farside radiogenic heating may be related to the asymmetric crystallization of the primordial magma ocean (Stevenson, 1980). In particular, from the magma ocean at thicknesses of a few 100 km or more, iron droplets may have readily precipitated to form a thin layer on the surface of a cold undifferentiated primordial core. Maximum gravitational stability would be achieved if the iron accumulated on the farside surface of the core, forming perhaps a crescent-shaped region that displaced the primordial core towards the nearside when the Earth and Moon became tidally locked (Stevenson, 1980).

However, as core displacement developed, partially molten mantle material of magnesium-rich pyroxenes and olivine may have preferentially accumulated in the deeper part of the mantle. Subsequently, at about 4.2 Byr, when surface melting had largely ceased and an anorthosite crust was formed, light crystalittes of an unknown composition presumably rose beneath the farside crust during the initial crystallization stages of the magma ocean (Stevenson, 1980). However, these upwelling crystallites

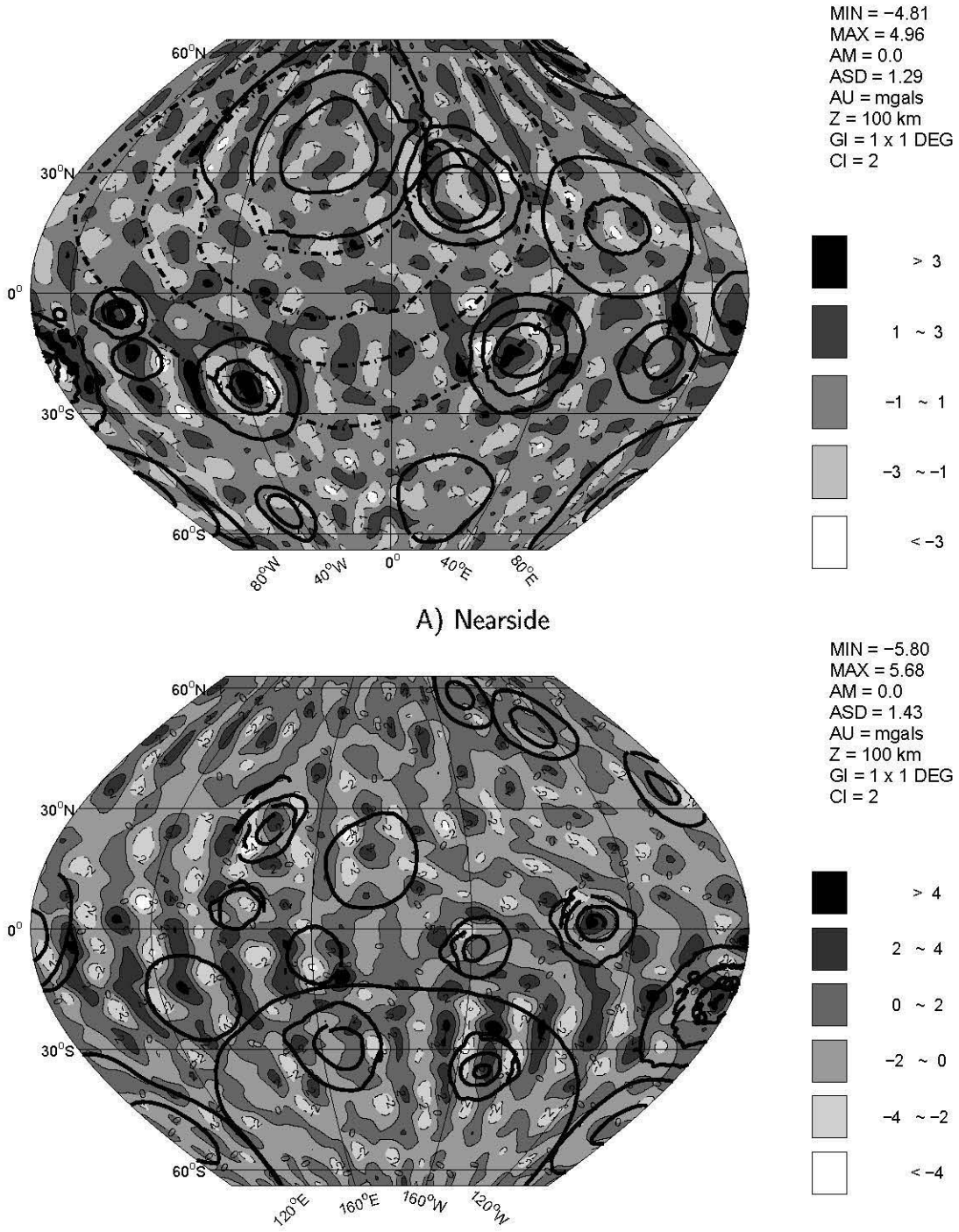

Figure 39: Residual *TDFAGA* components related possibly to crustal sources and subcrustal modeling errors.

may have swept around and concentrated partially molten material with enhanced concentrations of radioactive elements to the nearside (Stevenson, 1980). Accordingly, in the Imbrium-Procellarum region, KREEP elements may have been deposited presumably from these partial melts (Korotev, 2000). The hypothesis of a unique geochemical province in Oceanus Procellarum is supported by the predominance of primordial, more fusible material and greater radiogenic heating in the nearside mantle (Haskin, 1998).

The inferred core topography (Figure 33) also appears to be consistent with the evolution of the compositional asymmetry of the lunar mantle and crust. The high relief of the core beneath the Imbrium-Procellarum region suggests that the impactor which struck the "High-Th Oval Region" (Haskin, 1998) may have generated dikes and other conduits to great depths including possibly the ancient asthenosphere (Davies and Stephenson, 1977). These conduits facilitated possibly the upward flow of radioactive-rich magmas driven by hydrostatic pressure that resulted in multiple episodes of mare basalt flooding in the large Imbrium-Procellarum region (Davies and Stephenson, 1977; Solomon and Head, 1980). The release of pressure at depth may have raised core topography as mass flowed to compensate for the mass lost by extrusion of magma through the deep conduits to the lunar crust.

After the Imbrium impactor struck, the collapse of the transient cavity brought closer to the surface the underlying mafic material and magma ocean residuum carrying the compositional KREEP signature (Stevenson, 1980; Melosh, 1989; Korotev, 2000), thereby further enhancing the radiogenic content of an already unique geochemical province. Hence, the Imbrium impact probably contributed greatly to enhancing the radiogenic composition and heating of the nearside mantle and crust relative to the farside components.

In contrast to the Imbrium basin, the farside South Pole-Aitken basin appears to be associated with a depressed region of the core. This impactor apparently did not cause core intrusions into the overlying mantle. The collapse of its transient cavity brought minimal radiogenic elements toward the farside surface because of their low abundance in the farside subcrust. Furthermore, the raised topography inferred for the core beneath the Imbrium-Procellarum basin in Figure 33 may also have supported convective heat flow in the nearside mantle relative to the farside. Hence, the nearside lithosphere may have been less viscous than the farside lithosphere. Accordingly, the farside crust was probably cooled more rapidly than the crust of the nearside (Solomon et al., 1982).

Undulations of the lunar core may also provide insight on core flow patterns related to the ancient lunar magnetic main field. Similar undulations of the Earth's core-mantle boundary provide insight on the properties of the geomagnetic dynamo (e.g., Hide and Malin, 1970). The remanent magnetizations of lunar rocks suggest a 1 Tesla (T) field existed possibly by about 4.0 Byr that decreased to a few thousand nT by around 3.2 Byr (Cisowski and Fuller, 1986). Hence, models for a lunar core must be consistent with its sharply reduced capability of producing a magnetic field, as well as it being either completely liquid or solid (Konrad and Spohn, 1997).

Evidence for a lunar main field strongly supports a related molten or partially molten core where magnetic field-generating, Fe-laden core flows may have operated. In this case, core topography would have strongly constrained patterns of core flow, generally favoring flow in regions of raised relief around depressed relief where flow would have been constricted. Hence, the inferred topography of

Figure 33 might be useful for estimating properties of the ancient lunar main field that magnetized crustal features. However, further consideration of this issue is beyond the scope of the present study, especially as the crustal magnetic fields mapped by the Lunar Prospector at the study altitude of 100 km are quite weak with very small signal-to-noise ratio (M. H. Acuna, pers. comm., 1998) and hence very poorly known.

4.5.2 Lunar Tectonism

Thermal evolution studies of the Moon suggest that the main effect of cooling over the first 1.5-2.0 Byr was the growth of the lithopshere to an average thickness of about 650 km with relatively little cooling of the lower mantle and core (Konrad and Spohn, 1997). By this time, plate tectonism had ended because the lunar lithosphere was probably too thick (e.g., Morse, 1993; Warren, 1993). However, the remarkable associations between impact basins and undulations of the core, lower and middle mantle surfaces, as inferred from inversions of the related *TDFAGA* components, suggest that significant disturbances of subcrustal mass also may have resulted from the surface impacts of the raining bollides.

Basin-forming impacts clearly have played a major role in the crustal modification and thermal evolution of the Moon. In particular, the collision of large bollides with the lunar surface resulted in unloading large amounts of crustal material, followed by the rapid rebound of the transient cavity floor so that a mantle plug rose isostatically to compensate for the ejected mass of crustal material (Wilhelms, 1987; Melosh, 1989). Fluidization of the crater material resulted in the formation of a meltsheet presumably covering the crater floor. Large impacts also involved two major thermal effects. Firstly, the impact converted most of the kinetic energy of the projectile to heat. Secondly, the collapse of the transient crater increased the temperature beneath the crater. This second effect contributes to a net cooling of the planet because it brings hot material from depth closer to the surface (Melosh, 1989). However, the effects of surface impacts of large bollides may not be limited to the upper crust, but may also result in viscous flow in the mantle.

Figure 40 shows generalized cross-sections illustrating possible responses of the lunar nearside and farside interiors to bolloidal impacts. The upwarped ancient asthenosphere as depicted Figure in 40 (A) ensures mass excesses beneath the large nearside basins that are consistent with the overlying *TDFAGA* maxima. In addition to shock-induced rebound, the nearside asthenosphere may also have been uplifted further by the strong bouyancy forces of the melts. The asthenopshere presumably flowed inwards to compensate for the crustal material excavated from the basin cavity (Spudis, 1993).

For the farside basins, the ancient asthenosphere may have been downwarped as inferred in Figure 40 (B) to yield mass deficits which are consistent with related *TDFAGA* minima. The downwarped ancient asthenosphere constitutes deep-seated mass deficits beneath the farside impact basins that may reflect viscous entrainment of less dense material into deeper regions when viscous flow forces overcome bouyancy forces (Lenardic et al., 1993).

Entrainment is a macroscopic mixing of masses across a discontinuity where the viscosities of the

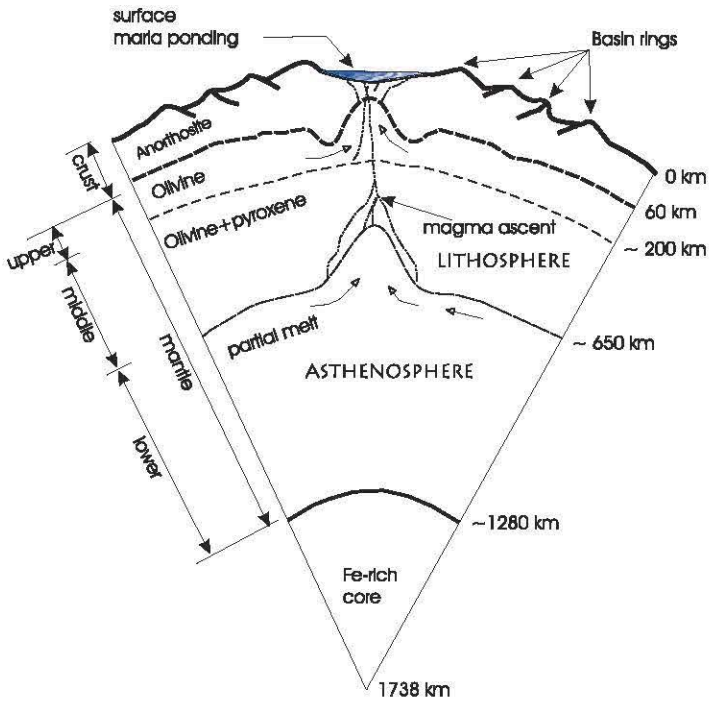

A) Nearside

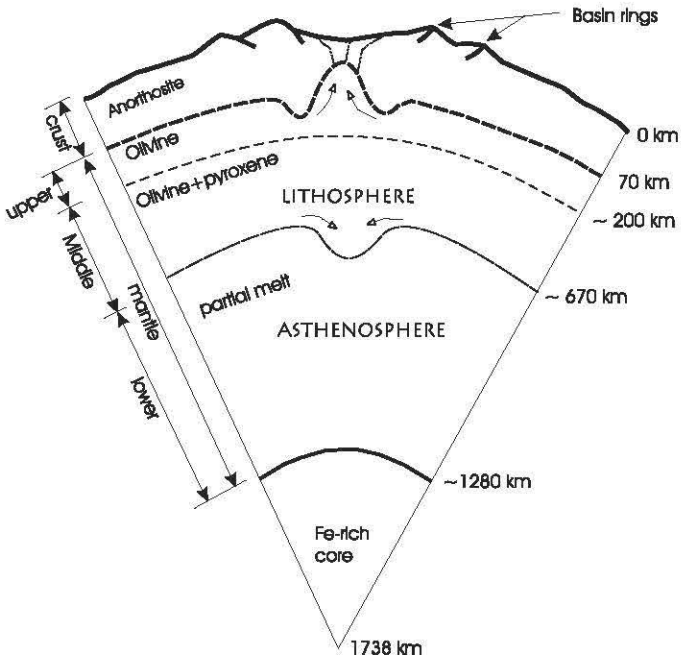

B) Farside

Figure 40: Generalized lunar cross-sections of the A) nearside and B) farside at the time of lunar bombardment. Arrows indicate possible directions of mass flow. None of the boundaries are to scale and the lunar surface topography is greatly exaggerated.

bounding layers facilitate significant coupling (Turner, 1986). Specifically, the overlying layer does not act as a rigid lid but rather is sufficiently viscous to allow horizontal flows along its boundary at the density discontinuity. When these conditions are met, convective downflows of the density discontinuity may occur because viscous flow forces overcome the stabilizing bouyancy forces and pull or entrain thin sheets of the lower density material into the underlying higher density layer (Lenardic et al., 1993).

For the Moon, the rheologic conditions necessary for entrainment may have occurred at the time of basin forming impacts, particularly on the farside. During this time, the farside lithosphere may have cooled relatively rapidly as cold plumes sank into the deep interior (Alley and Parmentier, 1998) while the collapse of the transient craters lifted temperature contours to the surface (Melosh, 1989). Furthermore, the farside crust, being relatively depleted of radioactive elements, may have lost heat fairly rapidly. Hence, at the time of basin-forming impacts, viscous entrainment may have facilitated horizontal mass transport of the lunar lithosphere (Spudis, 1993), downwarping the ancient asthenosphere beneath the farside impact basins as shown in Figure 40. Depressed asthenosphere also resulted in a lithosphere that is relatively thicker on the farside than the nearside as has been suggested by this study. Hence, viscous entrainment on the lunar farside in combination with rebound of a less viscous ancient asthenosphere on the nearside may have facilitated the development of the lithospheric thickness dichotomy.

This dichotomized lithospheric thickness also may have influenced the mass flow patterns in the asthenosphere and hence the unique tectonic development of lunar basin rings (Melosh, 1989; Spudis, 1993). In particular, lithospheric drag exerted by the inward flow of the asthenosphere, if strong enough, may have created extensional fractures in the lithosphere (Melosh, 1989). Basin ring features such as rilles, generally 1-2 km wide, and parallel-walled ridges may have formed as a result of horizontal extensional stresses up to a few hundred bars, compressive stresses of perhaps a kilobar, and the buckling of near-surface material (Solomon and Head, 1980; Spudis, 1993). On thicker, less viscous lithosphere, however, fewer rings would be formed (Melosh, 1989). Hence the number of rings associated with basins of the nearside would be larger than for the farside basins as was found in chapter 3.

4.5.3 Mare Basalt Volcanism

The dichotomies in composition, lithospheric thickness and sublithospheric mass flows may also have influenced basaltic flooding of the basins. Bollide impacts may have facilitated massive erruptions on the nearside through dikes that extended possibly from the core and lower mantle (Yingst and Head III, 1998). Thus, the Imbrium basin may have experienced significant contributions of magmas from the middle and lower mantle at around 3.9 Byr when volcanism was active (Solomon and Head, 1979).

During the first 2 Byr, hot upwelling plumes originating from the core released pressure and induced partial melting at depths ranging from about 400 to 600 km (Alley and Parmentier, 1998). Low density partial melts deep inside the mantle may have migrated and ponded in the deformed regions of the lithosphere (Spudis, 1993; Anderson, 1998). However, the ability of magma to reach the

surface from subcrustal reservoirs may have been related to the thickness of the crustal column (Yingst and Head III, 1998).

The nearside mascon basins are usually associated with multiple basalt flooding episodes in contrast to the farside impact basins that experienced minimal basalt flooding (Hartmann and Wood, 1971; Solomon and Head, 1980). The thinner nearside lithosphere and the upwarped asthenosphere may explain the large amounts of magma that could rise diapirically due to pressure release on the nearside (Yingst and Head III, 1998).

The entrainment of partial melts of the middle and lower mantle may explain the limited basalt flooding of farside basins. Ponded farside melts would have been entrained into the lower mantle so that high-Ti basalts that were generated at great depths most likely would not have reached the surface. Moveover, the thicker lithosphere beneath the farside impacts would also have inhibited the rise of melts to the surface. Accordingly, basalt flooding for most of the farside basins may have originated at shallower depths as suggested in Figure 40B. The absence of large quantities of mare basalt in the giant farside South Pole-Aitken basin may reflect the effects of a thicker, less viscous lithosphere with fewer radiogenic elements that promoted the viscous entrainment of magma.

4.6 Conclusions

The subcrustal interior of the Moon was investigated by analyzing the correlation spectrum between *TDFAGA* and *FAGA*. In particular, components of *TDFAGA* were obtained that could be plausibly related to first order subdivisions of lunar subcrustal mass. For example, the core components of *TDFAGA* were estimated by the wavenumber components that are positively correlated with the wavenumber components of the lunar gravity model (LP75G) up to degree 7. These core anomaly estimates (Figure 32) were used to model the core topography (Figure 33) for new insight on the poorly understood properties of the lunar core.

The mantle components of *TDFAGA* were also extracted, but with a spectral correlation filter based on the degree 8 through 24 wavenumber components of the lunar gravity model (LP75G). These anomaly components (Figure 34) suggest prominent density contrasts of the mantle that may reflect the subcrustal development of major craters and other poorly understood tectonic features of the Moon. They were interpreted for lateral density variations defined by the possible topography of the middle mantle at the mean depth of 220 km (Figure 38), and the relief of the lower mantle at a mean depth of 650 km (Figure 36) where the ancient asthenosphere may also have existed during bombardment time.

The residual *TDFAGA* (Figure 39) that are most strongly correlated with the degree 25 and higher wavenumber components of the lunar gravity model (LP75G) were attributed to crustal compenents and the small residual errors from modeling the relief of the core, and the lower and middle mantle surfaces. These residual components were relatively marginal in amplitude, but also showed many systematic associations with lunar basins that may be modeled in terms of possible mare fill thickness variations as described in Chapter 2. They are perhaps the most appropriate components of the free-air gravity anomaly field to relate to remote sensing imagery and other data sets that impose

constraints on the near-surface properties of the lunar crust.

The inferred core topography (Figure 33) is consistent with the development of "the great lunar hotspot" in the Imbrium-Procellarum region (Korotev, 2000). Asymmetric crystallization of the primordial magma ocean preferentially emplaced radiogenic heat sources in the upper nearside lithosphere. This compostional dichotomy may have been further enhanced by the Imbrium impact that also appears to have raised the core-mantle boundary. In particular, the elevated core topography may have sustained the upward flow of radioactive elements from great depths into the nearside region variously called the "High-Th Oval Region" (Haskin, 1998) or "Great Lunar Hotspot" (Korotev, 2000).

Ring tectonic development may have been affected by the viscosity variations of the lithosphere and asthenosphere during the time of bollide avalanche. A higher thermal gradient in the nearside mantle may have inhibited cold plumes from sinking deeply. Also, the nearside lithosphere was thinned by the flow patterns of sublithospheric mass transport in response to surface bombardment. On the farside however, a lower thermal gradient allowed cold plumes to sink to greater depths thereby facilitating viscous entrainment of mass into the lower mantle and the development of a thicker lithosphere. In general, for transient cavities of comparable size, more numerous rings are apparent for the nearside basins than for the farside basins. Relative to the farside, this development was apparently promoted in the nearside by a thinner lithosphere and mass transport in a hotter, less viscous sublithosphere.

Basin infilling of mare basalt also may have been affected by sublithospheric mass transport and the ponding of melts in the deformed regions of the ancient asthenosphere. Diapiric rise of magma probably facilitated massive flooding of the nearside basins while the viscous entrainment of melts may have minimized the flooding of farside basins. Basin fill on the nearside consists of both low- and high-Ti basalts. However, on the farside, basin fill presumably originated at shallower depths so that its composition may be mostly limited to low-Ti basalts.

The *TDFAGA* available for this study involved amplitudes comparable to the anomaly errors of the lunar gravity model (LP75G), and hence the results of this study must be used with care. Clearly, lunar gravity observations with improved accuracies will greatly enhance the determination of *TDFAGA* and their interpretation for crustal and subcrustal components.

However, despite the limitations of the currently available lunar gravity field, the analysis demonstrated the utility of *TDFAGA* to provide subcrustal and crustal information. These results significantly complement the crustal modeling of *TCFAGA* and *TGE* to yield a comprehensive model of lunar mass distribution that satisfies available terrain and gravity observations.

5 Inferences for the Shape of the Moon and Comparison of Planetary Gravity and Topography Spectra

5.1 Introduction

The shape of the Moon, as determined from the Apollo laser ranging and Clementine LIDAR observations, is pear-shaped with the long end of the pear directed away from the Earth (Sjogren and Wollenhaupt, 1973; Smith et al., 1997). One of the most striking physical discoveries of the Apollo mission was that the center of figure (COF) is displaced from the center of mass (COM) by about 1.9 km toward the farside (Lemoine et al., 1997; Smith et al., 1997). Hence, the COM/COF offset was interpreted in terms of a crustal thickness dichotomy that caused the equipotential surface to lie below the floors of farside basins (Head, 1976). In adddition, the departure from hydrostatic equilibrium has been attributed to thermal convection and lava flooding (Runcorn, 1974), processes relating to impacts, volcanism, rotation, and tides (Zuber et al., 1994), uncompensated density variations in the lunar interior (Kopal, 1972; Lemoine et al., 1997), and redistribution of crustal material from major impacts (Smith et al., 1997).

Lava flooding of nearside basins has been attributed to single cell convection. In particular, a single cell convection pattern likely produced the hemispherical crustal thickness difference of roughly 13 km (Figure 9) of an anorthosite shell about 4.4 Byr ago (Runcorn, 1996). The convection current in the early Moon, rising and falling at antipodal points now aligned along the Earth-Moon line, presumably assisted the upward movement of less dense anorthosite crystals and the downward migration of iron to the lunar center to form a core. The flow pattern presumably became unstable when the core radius became greater than 100 km and changed into a two cell pattern (Runcorn, 1996). The single cell convection pattern was presumably active when basalt flooded the nearside basins so that the smooth flooded surfaces would have taken up an equipotential surface (Runcorn, 1974). The general lack of volcanic fill of farside basins (Wilhelms, 1987) support this hypothesis.

That the present mare surfaces fit an equipotentail surface is still debated. For example, preliminary analysis of basin elevations determined from Apollo altimetry (Sjogren and Wollenhaupt, 1976) and radar soundings (Brown, 1974) suggested that nearside mare surfaces may constitute an equipotential surface, but the analysis was limited to the equatorial basins covered by the Apollo tracks. Recently, the Clementine altimeter data was analyzed and showed that all flooded basins follow a line parallel to the selenoid elevation but about 3 km below the average (Smith et al., 1997). Except for a few outliers, the study supported the equipotential hypothesis for mare surfaces (Smith et al., 1997). However, arguments rejecting this hypothesis suggested that the basin floors are not parallel to an equipotential surface (Arkani-Hamed, 1998). Arkani-Hamed (1998) argued that by plotting the elevation from -90° to +90°, the unflooded basins lie below the equipotential surface defined by floors of the flooded basins. Furthermore, the giant South Pole-Aitken basin, which is floored 1 km below all flooded basins, is unflooded.

A comparison of the selenoid undulation with mare floor elevations for the 27 major impact basins of this study may provide insight regarding the hypothesis that the lava surfaces constitutes an equipotential surface and that the fill contribute to the nonhydrostatic figure of the Moon.

The nonhydrostatic figure, which has been the subject of much controversy, presumably arose either from distortions produced in the early history of the moon and the shape was retained by the finite strength of the interior (Jeffreys, 1924), or due to present-day thermal convection (Runcorn, 1974). The theory that thermal convection was responsible for the nonhydrostatic figure of the moon was hypothesized on the differences in lunar moments of inertia (Bills, 1995). However, the Moon's departures from hydrostatic equilibrium may also be attributed to tides and internal mass distribution (e.g., Kopal, 1972; Lemoine et al., 1997; Burša, 1994; Zuber et al., 1994). Accordingly, tidal effects will be computed and internal mass models of the Moon will be compared to the selenoid for inference on the developement of the nonhydrostatic equilibrium figure.

The gross properties of a planet may be investigated from its topographic and gravity spectra. In particular, spherical harmonic gravity and topography models for the Moon, Earth, Venus and Mars are investigated. Hence, comparisons based on the roughness, slopes, and correlation between topography and gravity of the planets may provide insight on their diverse geologic evolution.

In the section 2, the physical parameters of the Moon will be considered for insight regarding the hydrostatic state of the Moon. In particular, shape distortions due to lava flooding, rotational and tidal effects, and internal mass distributions of the Moon will be investigated. In section 3, the hydrostatic configuration and the gravity and topographic spectra of the terrestrial planets will be compared. Conclusions are offered in section 4.

5.2 Physical Parameters of the Moon

In theories of figure of celestial bodies, an equipotential surface Γ of its external gravity potential, which best fits the outer boundary surface of a celestial body, may represent the body as a whole. Axes and flattening cannot be determined for such a general surface. A geometrically curved surface, e.g., an ellipsoid, may be used to approach the equipotential surface Γ. This means that both surfaces must satisfy the condition (Zhang, 1994)

$$\int\int_{\sigma}(r_{\Gamma}-r_{e})^{2}d\sigma = min. \tag{12}$$

where $r_{\Gamma}(\phi,\lambda)$ and $r_{e}(\phi,\lambda)$ are the planetocentric radius vector of the point on Γ and the ellipsoid, respectively.

For any celestial body, such as the Earth which is close to hydrostatic equilibrium, the rotational ellipsoidal surface can be used to represent its shape.

5.2.1 The Selenoid

The selenoid (Γ) is defined as the Moon's equipotential surface. The selenoid (lunar geoid) was computed using Bruns' equation (Heiskanen and Moritz, 1967) and the disturbing potential was computed from the LP75G coefficient model (Konopliv et al., 1998). The selenoid undulation of Figure 41 is defined as the height above (positive) or below (negative) the reference ellipsoid.

The selenoid over the study region has an amplitude range of -280 to 462 m. Most of the lunar basins including the large nearside Crisium, Humorum, Imbrium, Nectaris, and Serenitatis basins have prominent selenoid signatures. On the farside however, the impact basins are generally associated with selenoid lows although Orientale has a centrally raised selenoid with surrounding flanking lows. The giant South Pole-Aitken basin is characterized by a very prominent selenoid minimum of -280 m (e.g., Lemoine et al., 1997).

5.2.2 Departures from Hydrostatic Equilibrium

The hydrostatic equilibrium of a planet's can be deduced from the secular Love number k_s. The secular Love number k_s can be interpreted as a measure of a planet's yield to centrifugal deformation (Munk and MacDonald, 1960) and is given as

$$k_s = \frac{3GHC}{a^5\omega^2} \tag{13}$$

where $H = \frac{C-A}{C}$ is the precessional constant. Substituting for q, the ratio of centrifugal to gravitational acceleration (Bills, 1989) at the equator, as

$$q = \frac{\omega^2 a^3}{GM} \tag{14}$$

to get

$$k_s = 3\frac{H}{q}\frac{C}{Ma^2}. \tag{15}$$

where $\frac{C}{Ma^2} = \frac{2}{5}$ for a homogeneous spherical body, $\frac{C}{Ma^2} < \frac{2}{5}$ if the densities increase in the radial direction to the planetocenter, and $\frac{C}{Ma^2} = \frac{2}{3}$ for a spherical layer. For bodies in hydrostatic equilibrium, the parameter $k_s = \frac{3}{2}$ for a homogeneous model, and $k_s < \frac{3}{2}$ for models with increasing densities in the deep interior (Burša, 1994; Bills, 1995).

The precessional constant for the Earth and Moon is known. Hence, H/q is known for the Earth ($H = 3.273994 \times 10^{-3}, q = 3.461392 \times 10^{-3}$) and the Moon ($H = 519.3 \times 10^{-6}, q = 7.59 \times 10^{-6}$) and computes to 0.9 and 68.8, respectively. Values for k_s equal 1.1 and 82.6 for the Earth and Moon, respectively.

If the precessional constant is not known, such as in the case of Mars and Venus (Bills, 1989; Zhang, 1997), then the secular Love number k_s can be written as (e.g., Burša, 1984 ; Zhang, 1997)

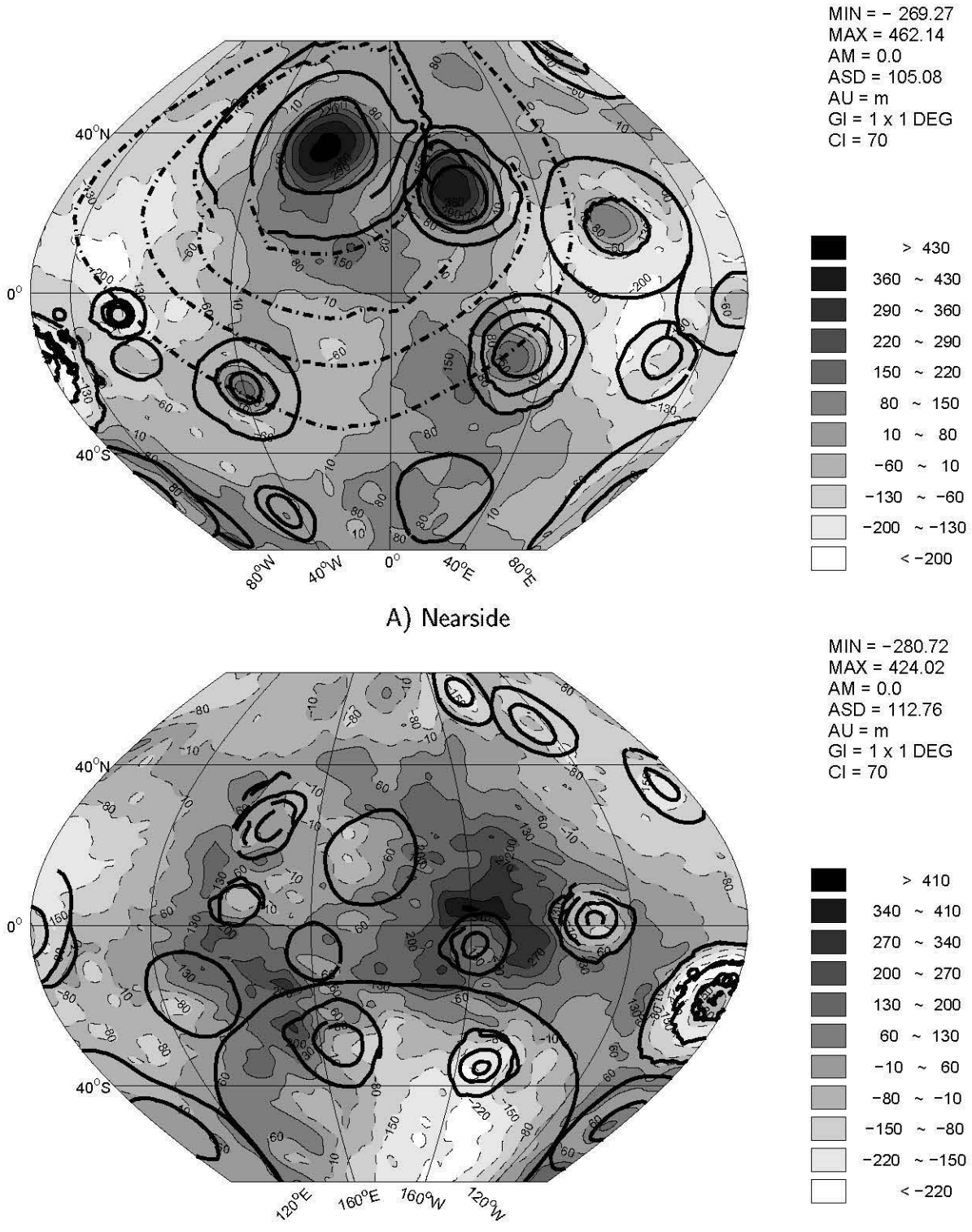

Figure 41: Selenoid computed from the LP75G gravity model with the J_2 term removed relative to the reference radius of 1738 km.

$$k_s = \frac{3J_2^{(o)}}{q} \tag{16}$$

where $J_2^{(o)}$ is the nonhydrostatic value of the second harmonic. This parameter can be obtained independent of an assumption of hydrostatic equilibrium. For example, the geometrical flattening f (Stacey, 1969) is given by

$$f = \frac{a-c}{a} = \frac{3}{2}\frac{C-A}{Ma^2} + \frac{1}{2}\frac{\omega^2 a^3}{GM} = -\frac{3}{2}J_2^{(o)} + \frac{1}{2}q \tag{17}$$

then

$$J_2^{(o)} = -\frac{2}{3}f + \frac{1}{3}q + \ldots. \tag{18}$$

is independent of the assumption of hydrostatic equilibrium.

The secular Love number k_s can be computed from equation 16. For the Earth and Moon, the geometrical flattening of their respective reference ellipsoids are equal to 3.352819×10^{-3} and 3.091257×10^{-4} (Zhang, 1997; Konopliv and Sjogren, 1994b). Using equations 16 and 18, the value of k_s equals 80.5 and 0.931 for the Moon and Earth, respectively. This means that while the Earth is close to equilibrium, the Moon is far from hydrostatic equilibrium.

5.2.3 Mare Surfaces

The Apollo altimetry measurements (Sjogren and Wollenhaupt, 1976) showed that basin mare surfaces tend to lie on an ellipsoidal surface. Accordingly, it was proposed that basaltic melt which presumably originated in the deep interior flooded the basins to an equipotential level (e.g., Runcorn, 1974; Solomon, 1975). The spatial and temporal characteristics of the lunar rilles and mare ridges for the Serenitatis basin led to the conclusion that the lunar interior expanded about 3.6 - 3.8 Byr ago and created tensile stresses which facilitated the transport of magma from the deep interior to the surface (Solomon and Head, 1979). Accordingly, the large nearside impact basins were favorable places for mare basalt to pond. The equipotential surface hypothesis was also used to explain the lack of pervasive flooding of farside basins. In particular, the offset of the center of mass of the Moon toward the Earth relative to its center of figure (Wollenhaupt et al., 1972) was interpreted in terms of a thicker farside crust, suggesting that the equipotential surface is about 2 km deeper on the farside than on the nearside (Solomon, 1975).

The equipotential surface hypothesis was later examined quantitatively by fitting an ellipsoidal surface to the mare floors (Sjogren, 1977). Although a single ellipsoidal surface did fit most mare surfaces, some basins floors such as Fecunditatis, Oceanus Procellarum and Tranquilitatis were above the surface by as much as 2 km.

Smith et al. (1997) re-examined the equipotential surface hypothesis using the Clementine topography data. By plotting mare surface elevations versus longitude from 0^o to 360^o it was claimed that these surfaces are almost parallel to the selenoid elevation. This led the authors to support the equipotential surface hypothesis. However, Arkani-Hamed (1998) argued that by plotting from

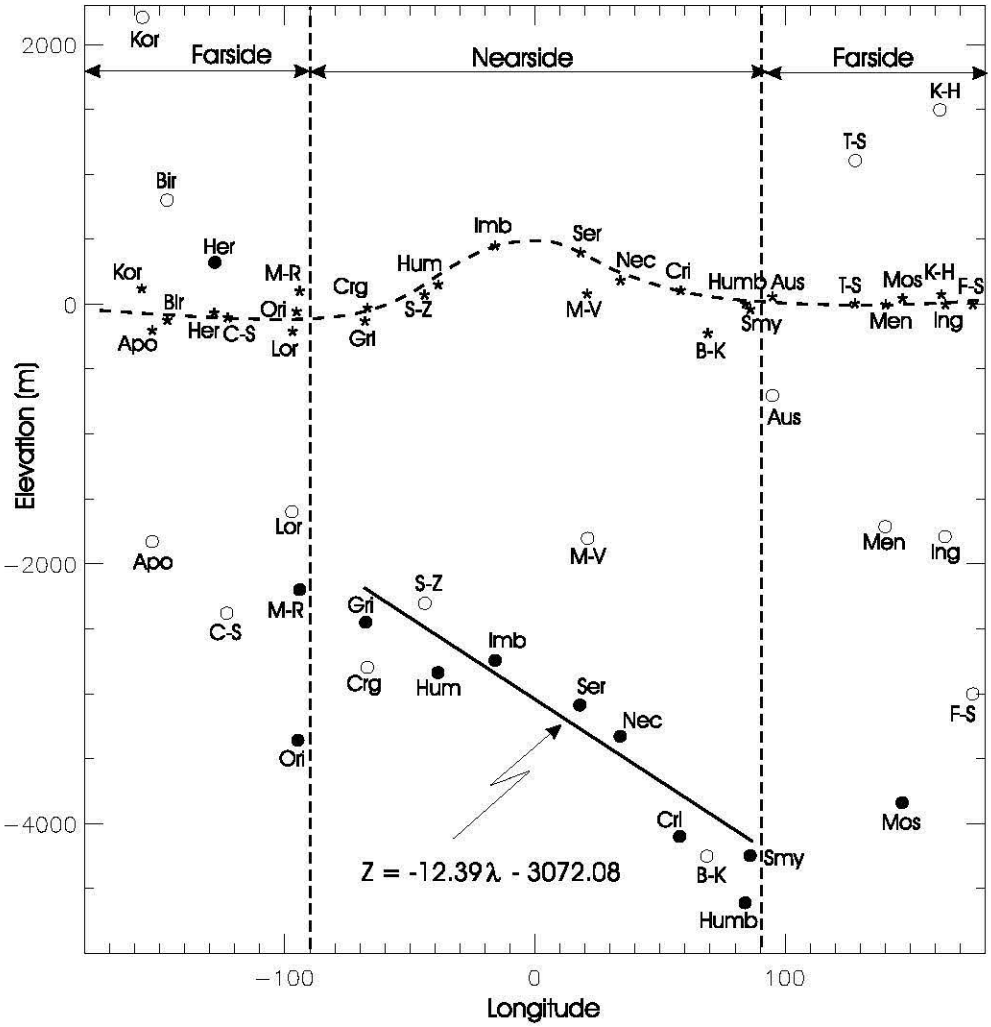

Figure 42: Comparison of selenoid undulation and basin surface elevations for nearside and farside basins. Surface elevation of mare flooded (solid circles) and unflooded (open circles) basins and selenoid heights at basin centers (asterisks) are relative to the ellipsoid with radius of 1738 km and flattening of 1/3234.93. The dashed curve shows the generalized trend of selenoid undulations and the solid line is the least squares fit for nearside basin surface elevations.

$+90^o$ to -90^o longitude rather than 0 to 360, a distinct slope of the mare floors from west to east compared to the selenoid is observed.

Using the Lunar Prospector gravity and Clementine topography data, Arkani-Hamed et al. (1999) showed the longitude dependence for ten nearside basins. The eastward deeping of the mare floors were attributed to postmare flow subsidence of the basins. In particular, the deepening of the nearside basins arose from the greater subsidence of the eastern basins under relatively larger mass loads of the mare fill. However, these mass loads were attributed to excessively large mare thicknesses that are generally not supported by recent studies on mare fill thickness estimates (e.g., Williams and Zuber, 1998; Budney and Lucey, 1998).

Figure 42 is a scatter plot of the surface elevations of flooded and unflooded basins as a function of longitude (λ), along with the corresponding selenoid heights (Figure 41) at basins centers. In this context, unflooded basins may included impact melt or cryptomare. The dashed curve represents the generalized trend of selenoid undulations.

Figure 42 shows that the shape of the selenoid tends to be maximally upwarped near the zero longitude in the direction of the Earth. The scatter of farside basin surface elevations are large compared to their nearside counterparts. All of the nearside basin surfaces lie below the selenoid. In contrast, several farside basins (Birkhoff, Hertzprung, Korolev, Keeler-Heaviside, and Tsiolkovskiy-Stark) lie above the selenoid. Lava surfaces of the farside basin Moscovience, Orientale, and Freundlich-Sharanov appear to lie below the floors of the nearside flooded Imbrium, Humorum and Grimaldi basins.

The nearside mare floors exhibit a definite slope of decreasing elevation from west to east and fit a linear function expressed as Z = -12.39 λ -3079.09. The slope of the line representing the mare surfaces appears to correlate with the gradient of the line in Figure 28A. This correlation may reflect the demise of mare flooding due to the growth of the lithosphere.

The depth/diameter ratio of the nearside basins (Figure 29A) appears inversely correlated with surface elevation which may also reflect that a more competent and rigid lithosphere may have inhibited endogenic processes. The inverse correlation however also suggests an eastward increase in basin excavation depth.

This study shows that mare surfaces of the nearside basins do not lie on a common equipotential surface and that basin subsidence under the mare loads did not significantly contribute to their eastward deeping. In fact, fill thicknesses listed in Table 3 range over a few kilometers and was presumably supported by a rigid lithosphere. Moreover, mare fill may not have significantly contributed to the lunar figure distortion (Kopal, 1972). However, the eastward deepening of the mare floors may be attributed to the greater depths of excavation.

5.2.4 Figure Distortion due to Earth

In this section, the effect of the rotational and tidal distortions on the Moon's figure parameters is investigated. The Earth-Moon system should reflect tidal distortions as regards orbital elements and the figures of both the Earth and Moon. However, only the effects on the Moon will be considered below.

The second zonal and the second sectorial Stokes parameters of the Moon's gravitational field may explain the tidal distortions due to the Earth (Burša, 1994). The gravity potential W of the Moon can be written (Zhang, 1994) as

$$W = V + \Phi + V_t \tag{19}$$

where the gravitational potential is

$$V(r,\theta,\lambda) = \frac{GM}{r}\Big[1 + \sum_{n=2}^{\infty}(\frac{a}{r})^n \sum_{m=0}^{n}(C_{nm}cos(m\lambda) + S_{nm}sin(m\lambda)P_{nm}(cos\theta)\Big]; \tag{20}$$

the centrifugal potential is

$$\Phi = \frac{1}{3}\frac{GM}{r}q\left(\frac{r}{a}\right)^2[1 - P_{20}(cos\theta)] \tag{21}$$

and the averaged value of tidal potential due to Earth is

$$V_t = \frac{1}{2}\frac{GM_\oplus}{a}\left(\frac{a}{d}\right)^3\left[1 - P_{20}(cos\theta) + \frac{1}{2}P_{22}(sin\theta)cos2\lambda\right] \tag{22}$$

where GM is the product of gravitational constant and mass of the Moon, $GM_\oplus$ is the geocentric gravitational constant, r is the selenocentric radius, θ is the latitude, λ is the longitude, $[C_{nm}, S_{nm}]$ are the fully normalized potential coefficients of degree n and order m, P_{nm} are the associated fully normalized Legendre functions, a is the scaling parameter associated with potential coefficients (Kaula, 1966), and d is the distance of the Moon's and Earth's mass centers.

The deforming potential at the surface of the Moon (Burša, 1994; Zhang, 1994) is given by

$$\delta\Phi = \Phi - \frac{1}{3}\omega^2 r^2 = -\frac{1}{3}\frac{GM}{r}q\left(\frac{r}{a}\right)^2 P_{20}(cos\theta) \tag{23}$$

and due to tides

$$\delta V_t = \frac{1}{2}\frac{GM_\oplus}{a}\left(\frac{a}{d}\right)^3\left[P_{20}(cos\theta) + \frac{1}{2}P_{22}(sin\theta)cos2\lambda\right] \tag{24}$$

The parameter q, in the potential of centrifugal force (Burša, 1994), is

$$q = \frac{\omega^2 a^3}{GM} = \frac{G(M_\oplus + M)}{GM}\left(\frac{a}{d}\right)^3 = 9.08 \times 10^{-6} \tag{25}$$

using a = 1738 km, GM= 4902.8003 $\times 10^9$ m^{3}s^{-2} (Konopliv et al., 1998), ω = 2.661699 $\times 10^{-6}$ rad s^{-1}, and d = 384400 km (Kopal, 1972).

Assuming the Figure distortion of the synchronously rotating Moon (Lambeck and Pullan, 1980) developed when it was closer to the Earth, then the orbital distance d and period T can be estimated from

$$\frac{GM_\oplus}{GM}\left(\frac{a}{d}\right)^3 = \frac{\overline{\omega}^2 a^3}{GM} = \frac{4J_{22}}{k_s} = \frac{8.958 \times 10^{-5}}{k_s} \tag{26}$$

where the Earth-Moon mass ratio = 81.300566 (Konopliv et al., 1998) and $J_{22} = (C_{22}^2 + S_{22}^2)^{\frac{1}{2}}$ but $S_{22}^2 = 0$ and $C_{22} = 22.395 \times 10^{-6}$ (Konopliv et al., 1998). Hence, the orbital parameters are estimated as

$$d = (168271.5km)\sqrt[3]{k_s}$$

$$\overline{n} = 9.144 \times 10^{-6}\sqrt{k_s};\quad T/\sqrt{k_s} = 7.97days$$

By considering the Earth and Moon as a binary system (Kopal, 1978), Burša (1994) estimated the average time of maximum deformation at 1.6 Byr with direct tidal effect of 154.95 m and the present direct tidal effect of 13.03 m, respectively.

In the next subsection, possible figure distortion from internal mass distribution will be inferred from correlations between the selenoid and density boundaries.

Correlation Coefficient		
	Selenoid	
Undulations	Nearside	Farside
DEM	-0.13	0.01
CT	0.04	0.66
Moho	-0.13	-0.52
Eq. Moho	-0.08	-0.63
RAM	-0.44	-0.45
MMT	0.19	0.13
LMT	0.37	0.51
CMB	0.37	0.13
Gravity Components		
TGE	-0.03	0.67
CTGE	-0.18	0.62
TCFAGA	0.77	0.79
TDFAGA	0.53	0.65
CTDFAGA	0.03	0.09
STDFAGA	0.47	0.61

Table 7: Summary of correlation coefficients between the Selenoid and undulation models and gravity components. The undulation models include the lunar topography (DEM), crustal thickness (CT), radial adjustment model (RAM), middle mantle topography (MMT) at depth of 220 km, lower mantle topography (LMT) at depth of 650 km, and the core mantle boundary (CMB).

5.2.5 Correlations between the Selenoid and Undulation Surfaces

The attributes of the selenoid may be compared with the mass models derived in the previous chapters. In particular, correlation coefficients were computed for the selenoid height and subcrustal undulation models of the core-mantle, lithosphere-asthenospehere, and middle-upper mantle boundary, respectively. It is expected that the selenoid will have higher correlation with long wavelength mass anomalies (Bowin, 1994).

Table 7 summarizes the correlations coefficient estimates for the various surfaces and gravity components. Low correlations appear to be associated with the short wavelength features of the topographic surface and the boundary of the middle mantle topography (Figure 38). The Moho and the equilibrium Moho have higher negative correlation on the farside compared to the nearside. This may reflect that the higher frequency terrain gravity effects are better determined on the nearside due to direct line of sight measurements compared to the farside. Selenoid anomalies appear to have higher correlation with the longer wavelengths features such as the mass anomalies at the core-mantle boundary and the lower mantle topography (Figure 36), and for the RAM data (Figure 10).

Point data corresponding to the basin centers were also extracted for selenoid heights, RAM data,

lower mantle topography, and the core-mantle boundary. The point data were averaged over $4^0 \times 4^0$ regions centered on the basins.

Figure 43 shows the comparison of basin centered point data for the selenoid, RAM data, lower mantle topography, and the core-mantle boundary. The selenoid (panel A) correlates with the RAM data (panel B) at -0.52, with lower mantle topography (panel C) at 0.81, and with the core-mantle boundary at -0.51, respectively.

Internal mass distribution of the Moon, in response to bollide impacts, may also have contributed to the departure from hydrostatic equilibium. In fact, it was suggested that the source of the Moon's departure from equilibrium may be sought in a regions in its interior (Kopal, 1972). The highest correlation with the selenoid is the lower mantle topography (Figure 36). It appears that the lithosphere should be primarily responsible for the bulk of the lunar momonts of inertia (Kopal, 1972). However, further analysis is required to verify this claim.

If the lunar core is a spherically symmetric inviscid fluid, then it would contribute nothing to the lateral variations in the gravity field, nor would it participate in the librations of the mantle and crust (Bills, 1995). However, these results suggest that the asymmetric core-mantle boundary is highly correlated with the selenoid. Hence, the lunar core may contribute to libration of the lunar mantle.

In this section, inferrences for the shape of the Moon were investigated from lava flooding, tidal effects and internal mass distributions. Lava flooding commenced about 3.6 - 3.8 Byr (Solomon and Head, 1979) about 200 Myr after bollide impacts. However, the nearside basin mare surfaces are not parallel with the selenoid. Mare fill thicknesses are not excessive so that localized lava flooding of lunar basins may have had little influence on the large-scale distribution of mass responsible for the momenta (Kopal, 1972). Moreover, the lunar bulge may have formed about 1.6 Byr or about 2 Byr after the mare flooding seized. Hence, the change from a first to second order harmonic convection pattern would have taken some time (Runcorn, 1996).

Subsurface density boundaries deformed in response to bollide impacts. Hence, the deformed boundaries, particularly the lithosphere-asthenosphere boundary, may have altered the convection flow pattern. In particular, this boundary may have aided the change from a single cell convection pattern to include a second harmonic degree component that in turn presumably was responsible for the development of the lunar bulge (Runcorn, 1974; 1996).

5.3 Comparing the Moon to the Terrestrial Planets

In this section, the 4 terrestrial planets, Earth, Moon, Venus, and Mars will be compared for their hydrostatic configuration and their gravity and topography spectra.

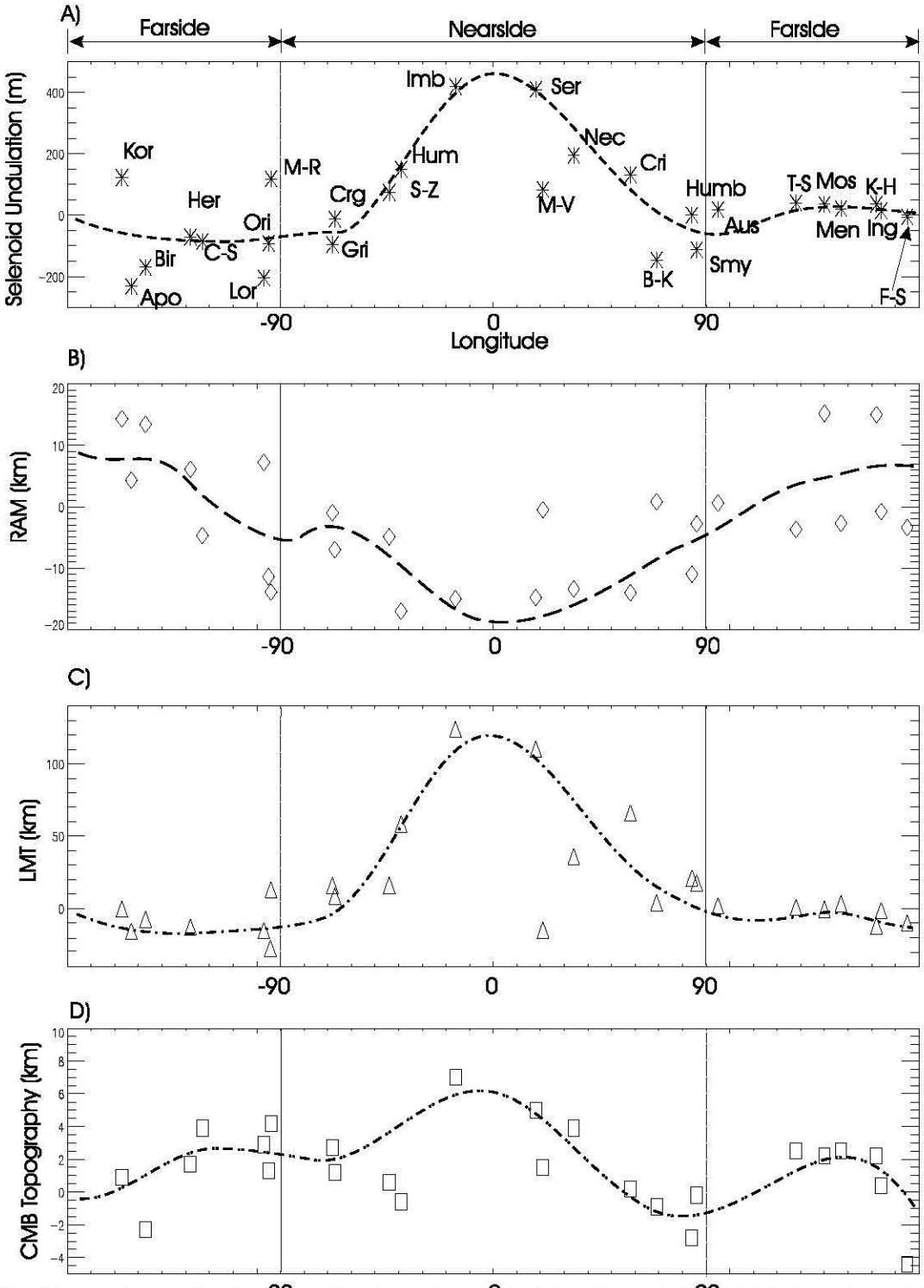

Figure 43: Comparison of point data for the selenoid heights (panel A), RAM data (panel B), lower mantle topography (panel C) and the core-mantle boundary (panel D) centered over the basins. In each panel, a generalized curve shows the trend in the data.

Planet	Planetary Constants and Derived Values					
	GM $[10^9 m^3 s^{-2}]$	ω $10^{-7}[rads^{-1}]$	f^{-1} $[10^{-6}]$	q $[10^{-6}]$	$J_2^{(o)}$ $[10^{-6}]$	k_s $[10^{-6}]$
Moon	4 902.8	2.662	3234.9	7.586	-203.56	80.5
Earth	398 600.4	729.2115	299.3	3461.39	-1073.62	0.9
Venus	324 858.6	2.993	587110.0	0.0612	-1.12	18.5
Mars	42 828.4	7.088	155.1	4599.2	-2765.23	1.8

Table 8: Comparision of hydrostatic state of the terrestrial planets. The equatorial radius in kilometers for the Moon, Earth, Venus, and Mars is 1738.30, 6378.14, 6053.84, and 3397.15 respectively. Flattening for Venus was taken from model calculation of Zhang (1997).

5.3.1 Comparison of Physical Parameters of the Terrestrial Planets

Table 8 shows the comparison of the secular Love number computed for the terrestrial planets as explained in section 5.2.2. The results indicate that while the Earth and Mars are close to hydrsotatic equilibrium, Venus and the Moon are far from hydrostatic equilibrium. In addition, the 742-m selenoid undulation range compares to a total range of 200 m for the Earth, 2000 m for Mars and 225 m for Venus, respectively. The large value for Mars' geoid is due to Tharsis and Olympus Mons (Esposito et al., 1992).

5.3.2 Comparison of Terrestrial Planetary Gravities and Topographies

In this section, a comparison will be made of the geophysical properties of the terrestrial planets only to first order. In particular, the comparison will focus on the variances spectra for gravity and topography, correlation and the spectral slope (Kaula, 1993). Variance provides a convenient measures of variability (or roughness) versus wavelength (Bills et al., 1987) and the spectral slope (or decay) describes its global behaviour i.e., a steep slope indicates higher viscosites and smaller temperature gradients (Kaula, 1993).

The 4 terrestrial planets have evolved under diverse geologic processes. Their topographic features provide important clues on the endogenic (i.e., internal processes like convection in the core or mantle) and exogenic (i.e., processes that originate at or near the surface such as volcanism, weathering, cratering etc.,) processes which shaped their surfaces and subsequently modified their interiors. For example, the history for the Earth is not well preserved due to erosion and the action of plate tectonics with plates that are the thermal boundary layers of mantle convection cells (Head and Solomon, 1981). Venus, on the other hand, experienced global resurfacing as a result of episodic global volcanism due either to episodic mantle convection or temperature increase during geologically long periods of lithospheric thickening (Head and Solomon, 1981). The Moon experienced diverse processes from impact cratering to basalt flooding into surface basins. The surface evolution of Mars is associated with the complexities of a volcanic shield construction and aeolian erosion (Turcotte, 1996).

5.3.3 Data Descriptions

Datasets of radiometric tracking of the Magellan and Pioneer Venus Orbiter satellites were combined to produce a 60th degree and order spherical harmonic gravity field of Venus (Konopliv and Sjogren, 1994b). The spherical harmonic topography model was produced by a complete set of Magellan altimeter data augmented by Pioneer Venus and Venera data (Rappaport and Plaut, 1994).

A 50th degree and order spherical harmonic gravity model for Mars was produced from doppler tracking from orbiting spacecraft (Smith et al., 1993). The spherical harmonic topography model for Mars was based on the digital elevation models compiled from data sets comprising Earth-based radar ranges, Mariner 9 occultation timing, photogrammetry and spectrographic atmospheric soundings (Bills and Nerem, 1995).

The complete 360th degree and order spherical harmonic gravity for Earth was computed from a combination of satellite tracking data, satellite altimetry and surface gravimetry (Rapp and Pavlis, 1990). The topography of the Earth, however is unique among the planets due to two different physical surfaces namely surface (i.e., land topography and ocean surface) or the rock-liquid interface (i.e., land topography and ocean bottom bathymetry). I will use the "equivalent rock topography" model of Pavlis and Rapp (1990) which consists of partial filling in the ocean basins with a column of crustal rock of mass equal to the oceanic water column.

5.3.4 Harmonic Analysis of the Terrestrial Planets

The gravitational potential of a planet is commonly represented in a spherical harmonic series as given by equation 20. Estimates of the potential coefficients can be derived from analysis of satellite observations for Venus, Moon and Mars (e.g., Konopliv and Sjogren, 1994b; Konopliv et al., 1998; Bills and Nerem, 1995) as described above. For the Earth, terrestrial gravity data have been combined with satellite observations (Rapp, 1994).

The topography of a planet can be represented in a surface spherical harmonic expansion

$$H(\theta,\lambda) = R\sum_{n=2}^{\infty}\sum_{m=0}^{n}\Big[A_{nm}cos(m\lambda) + B_{nm}sin(m\lambda)\Big]P_{nm}(cos\theta) \tag{27}$$

where $[A_{nm}, B_{nm}]$ are fully normalized spherical harmonic coefficients of the topography, R is a scaling parameter associated with the elevation coefficients (usually the mean radius of the planet).

5.3.5 Variance and Correlation Spectra

The power spectrum of the observed gravitational potential (G) and topography (H) can be expressed as (Kaula, 1993)

$$V_n(G) = \sum_{m=0}^{n}\Big[C_{nm}^2 + S_{nm}^2\Big] \tag{28}$$

$$V_n(H) = \sum_{m=0}^{n} \left[A_{nm}^2 + B_{nm}^2 \right] \tag{29}$$

In addition to the variance spectrum the co-variance spectrum of gravity and topography per degree n may be defined (Bills and Kobrick, 1985) as

$$V_n(G,H) = \sum_{n=0}^{max} \sum_{m=0}^{n} \left[C_{nm}A_{nm} + S_{nm}B_{nm} \right] \tag{30}$$

where max is the maximum degree of the coefficient model. Thus, the correlation between the gravity and the topography (Bills and Kobrick, 1985) may be obtained by

$$\beta_n(G,H) = \frac{V_n(G,H)}{\sqrt{V_n(G)}\sqrt{V_n(H)}} \tag{31}$$

For comparison with the observed variances, model variance curves are included. In particular, the model gravity spectrum has the form (e.g., Kaula, 1966; Rapp, 1989)

$$\frac{(2n+1)A}{n^4} \tag{32}$$

and the topography spectrum has the form (e.g., Bills and Kobrick, 1985; Rapp, 1989)

$$\frac{B}{n(n+1)} \tag{33}$$

Figures 44 showing the gravity and topography spectra has two panels. The top figure shows the amplitude spectra for the Earth's topography and gravity fields plotted with their expected power laws for gravity and topography for comparison with the observed spectra. The irregular dash-dot line is the topography spectrum and the irregular solid line is the gravity spectrum. The smooth dotted curve represents the expected power law for gravity and topography. The bottom panel shows the correlation per degree n between gravity and topography. The top panel shows the variance for the gravity and topography and the bottom panel shows the correlation spectrum between gravity and topography.

The variance spectra of the gravity and topography are quite close to the expected forms, with the conventional values of $A = 10^{-10}$ and $B = 2 \times 10^{-7}$. The largest departure is the topographic deficit at harmonic degrees 1-5. The correlation between topography and gravity on the Earth is rather poor at the longest wavelengths, but beyond harmonic degree 11, the correlation is consistently and significantly positive.

The variance spectra of gravity and topography for Venus are presented in Figure 45. Both spectra adhere remarkably close to the expected forms. The topography spectrum follows the Vening-Meinesz form very well, with scale factor $B = 5.0 \times 10^{-8}$, except at degree 1 and 2. The degree 1 topography variance reflects the displacement of center-of-figure from the center-of-mass (Bills and Kobrick, 1985). The degree 2 topography variance is below the expected trend. The gravity

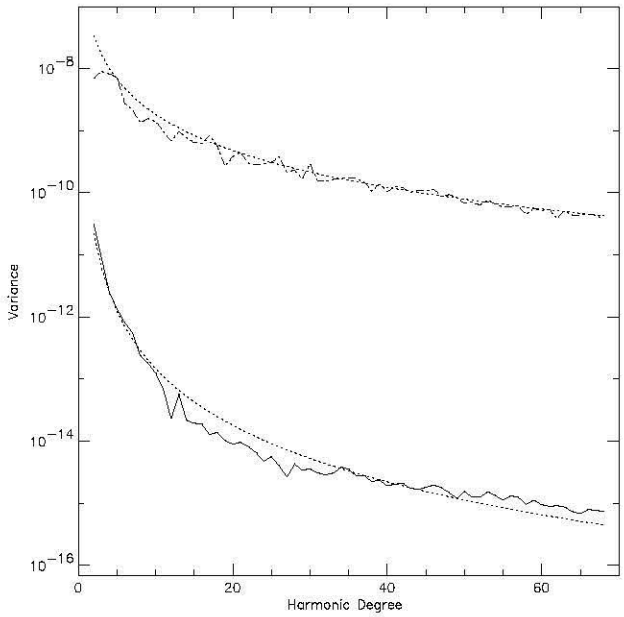

Earth: Degree variance for gravity and topography

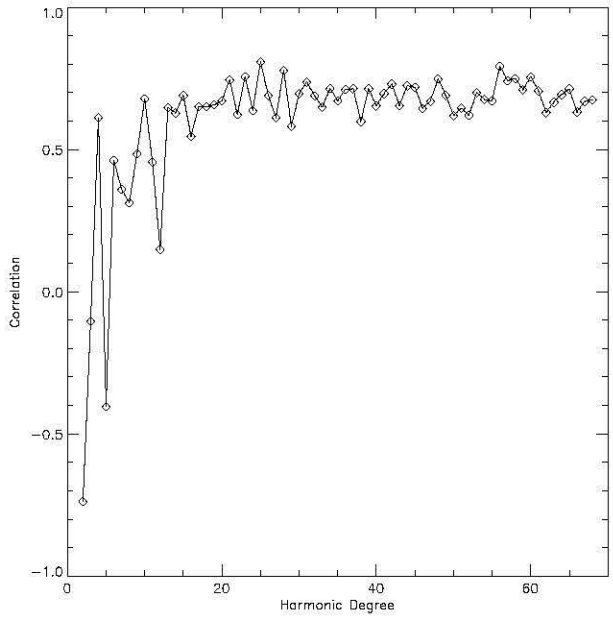

Figure 44: Gravity and topography spectra for Earth. The top figure shows the amplitude topography spectrum as an irregular dash-dot line and gravity spectrum as an irregular solid line. The smooth dotted curves represents the expected power law for gravity and topography respectively. The bottom panel shows the correlation per degree n between gravity and topography.

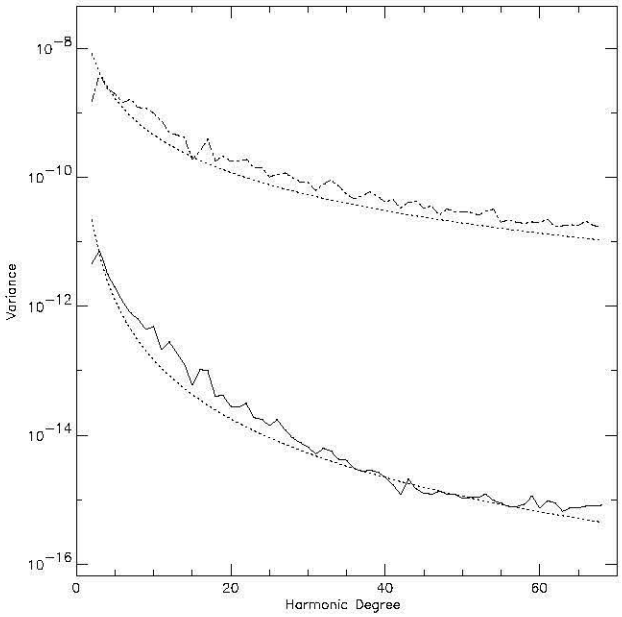

Venus: Degree variance for gravity and topography

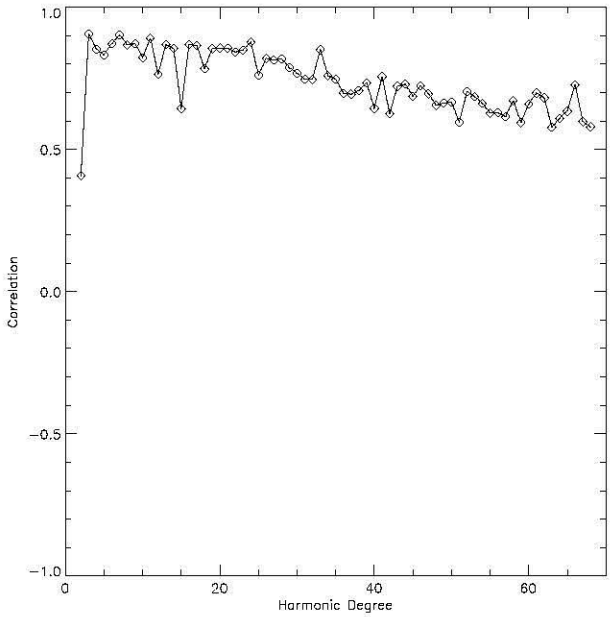

Figure 45: Gravity and topography spectra of Venus.

Correlation

spectrum follows the Kaula form with scale factor $A = 1.0 \times 10^{-10}$ with most notable deficit at degree two. The correlation spectrum for gravity and topography (bottom panel in Figure 45) is consistently positive, with the notable exception of degree 2. The high correlation starts at degree two whereas the high correlation for Earth starts at degree six. The low correlation at degree two seem to be part of the perculiar convective style (Kiefer et al., 1986).

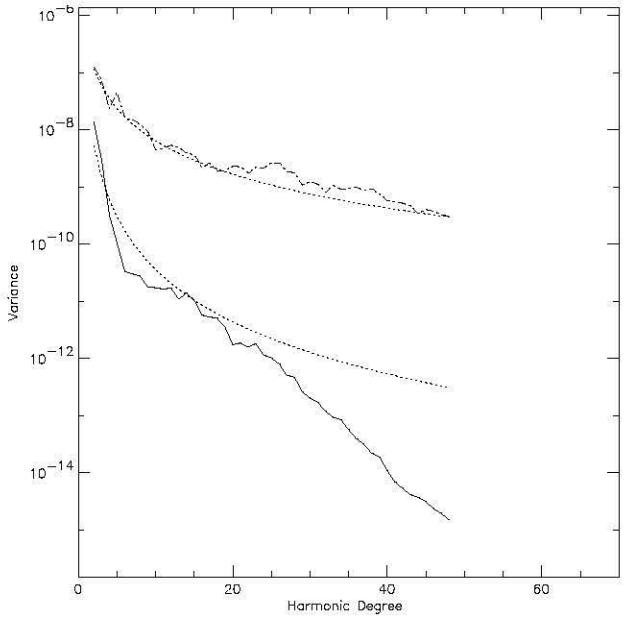

Mars: degree variance for gravity and topography

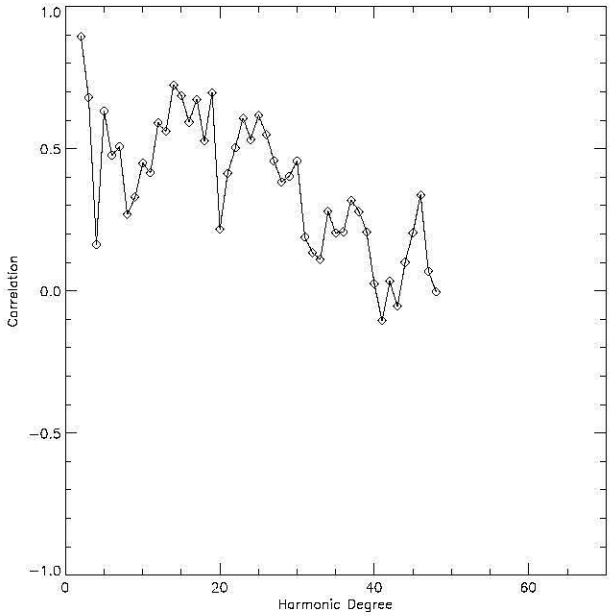

Figure 46: Gravity and topography spectra of Mars.

Figure 46 illustrates the gravitational and topographic variance spectra for Mars, and compares them to the Kaula and Vening-Meinesz spectral forms. The topography spectrum has a scale factor $B = 7.0 \times 10^{-7}$ and follow the expected Vening-Meinesz shape across the entire observed frequency range. The gravitational spectrum, with scale factor $A = 1.7 \times 10^{-8}$, has two regions of modest departure from the expected Kaula form. The low degree anomaly itself has two parts. At the lowest degree, $2 \leq n \leq 6$, the spectrum decays more rapidly than expected, then over the range $6 \leq n \leq 10$ the spectrum is nearly flat. This feature appears to be a genuine feature of the gravity field of Mars (Bills and Lemoine, 1995). The high degree anomaly ($40 \leq n \leq 50$) represent a model deficit in variance which may only be an artifact. The correlation spectrum between gravity and topography on Mars shows that degree 4 is unsual, in that it exhibits very low correlation. The correlations in the spectral region $6 \leq n \leq 12$ are all significantly positive, but are still below the level obtained at high spatial frequencies. Over the frequency range $12 \leq n \leq 50$ the drops off.

The variance spectra of gravity and topography for the Moon are presented in Figure 47. The topography spectra very nearly follows the Vening-Meinesz form, with the value of the scale factor $B = 1.6 \times 10^{-6}$ clear across the entire range of observed spatial frequencies. Contrary to the Earth, there is no low degree deficit. The gravity spectrum, deviates somewhat from the Kaula spectrum, with scale factor $A = 2.0 \times 10^{-8}$, with the largest departures occuring beyond degree 40. This high degree deficit is likely an artifact, due to the use of a smoothing constraint in the solution algorithm (Konopliv et al., 1998).

The correlation spectrum suggests several discrete patterns. For example, degree 2 shows unusually low correlation due to the long wavelength complexities associated with SPA basin (Konopliv et al., 1998). Degrees 3-9 exhibit strong positive correlation. Degrees 10-20 show negative correlation which may be due in part to the five principal mascon basins (Konopliv et al., 1998). The low positive correlation improves above degree 27 to a low positive peak at degree 47 and drops off, but remains positive.

By comparing the spectra for the four planets, it appears that Venus fits the expected form better than Mars and Moon. The fact that the correlation is better for Venus than Earth may simply reflect differences in the relative strength of the coherent and incoherent parts (i.e., the part that does not correlate with topography (Dorman and Lewis, 1970)) of the gravitational field and may be due to the greater effective depth of isostatic compensation (Bills and Kobrick, 1985). The discrete patterns in the correlation spectra for Mars and the Moon exhibit similar trends. The lowest correlation occur around degrees 4 and 11 for Mars and the Moon respectively. The correlation spectra become more positive and reach respective peaks around degrees 15 and 45 for Mars and the Moon, respectively, after which the correlations drop off although never below zero.

5.3.6 Comparison of the Decay of the Spectra

The degree power spectral density (PSD) for the spherical harmonic series is defined as

$$P_n(k_n) = C(k_n) n^{-\alpha} \tag{34}$$

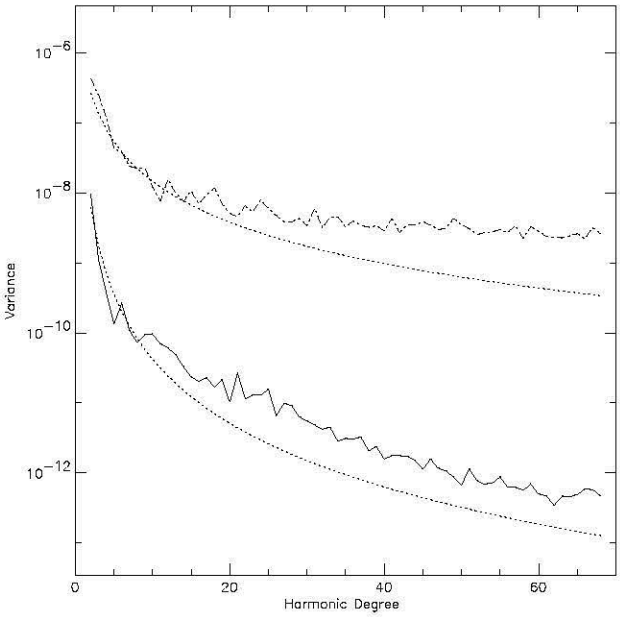

Moon: Degree variance gravity and topography

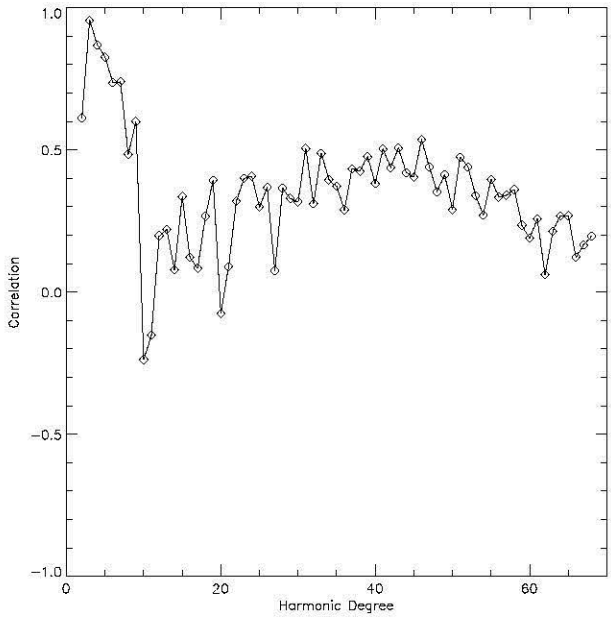

Correlation

Figure 47: The Moon's gravity and topography spectra.

Spectral Decay		
Planet	α	$10^6 C$
Gravity		
Earth	1.9	6.0
Moon	1.83	120.0
Mars	2.87	628.0
Venus	2.08	14.1
Topography		
Earth	1.38	269.0
Moon	1.13	785.0
Mars	1.37	510.0
Venus	1.41	116.0

Table 9: Results of linear fits for slope α and intercept.

for $\alpha > 0$ and C is a constant. Since the data are given on a sphere, the linear wavelength λ_0 is $2\pi R$ and the wavenumber k depends on degree n (Kucinskas and Turcotte, 1994)as

$$k_n = \frac{n}{2\pi R} \tag{35}$$

More commonly used than the degree variance is the rms magnitude of coefficients by degree (Kaula, 1993) or PSD as

$$\sqrt{\frac{V_n(G)}{(2n+1)}} \approx C/n^{\alpha} \tag{36}$$

with a magnitude C and slope α. The decay of the PSD spectra for each of the planets were modeled as C/n^{α} by performing a least sqaures fit of the log-log spectrum over ranges $75 \leq n \leq 2$ for Earth, Venus and Moon and $50 \leq n \leq 2$ for Mars. Results of the fits namely the slope α and the intercept C are given in Table 9.

Table 9 lists the slope and intercepts for the planets. Over the respective degree intervals, Mars' gravity signal have much steeper slope than the larger planets Venus and Earth. The spectral decay of potential of about 1.9 is similar for the Earth and Moon but about 2.1 for Venus.

The spectral decay of topography is similar for Earth, Venus and Mars, being around 1.4, whereas a flatter slope of 1.1 is suggested for the Moon.

For the two planets further from hydrostatic equilibrium, their gravity spectra indicate that the Moon has the lower temperature gradient and the Mars has the highest viscosity.

5.4 Conclusion

The departure from hydrostatic equilibrium of the Moon may be atrributed to internal mass distribution (Kopal, 1972). In particular, the lithosphere may be primarily responsible for the bulk of the lunar moments of inertia and the the asymmetric core-mantle boundary may contribute to libration of the lunar mantle. Localized lava flooding of lunar basins, however, may have had little influence on the large-scale distribution of mass responsible for the momenta (Kopal, 1972).

The eastward deepening of the nearside basin mare surfaces can be attributed to their greater depths of excavation.

Comparison of the measured spectra of the terrestrial planets suggest that the Moon has the lowest temperature gradient and is the furthest from hydrostatic equilibrium.

6 Conlusions and Recommendations

6.1 Introduction

Lunar Prospector's gravity and Clementine's topographic data were subjected on a nearly global basis to spectral correlation analysis for the crustal and subcrustal properties of lunar maria, highlands and impact basins. The analysis yielded a crustal thickness model and fundamental constraints on the residual stress field of the crust. Subcrustal models were also inferred for the relief of the core-mantle boundary, as well as the surfaces for the lower and middle mantle. These results were investigated for new insights on the properties and tectonic evolution of the lunar crust, mantle and core. The selenoid and hydrostatic components in the lunar figure parameters were computed and the results were investigated for inferences on effects of mass distribution on shape distortions and to test the hypothesis that mare surfaces constitute an equipotential surface. The secular Love number k_s and the measured gravity and topography spectra of the terrestrial planets were also compared.

6.2 Data and Modeling

Lunar free-air gravity and topography observations from the Lunar Prospector, Clementine, and earlier satellite missions were analyzed at 100-km altitude for a comprehensive model of crustal and subcrustal mass variations. Terrain gravity effects (*TGE*) were computed in spherical coordinates from 1^0 topography (GLTM-2) by Gauss-Legendre quadrature (GLQ) integration using a terrain density of 2.8 g/cm^3. Corresponding free-air gravity anomalies (*FAGA*) were evaluated from the lunar gravity model LP75G. The correlation spectrum between the independent *TGE* and *FAGA* estimates was used to isolate the terrain-correlated (*TCFAGA*) and -decorrelated (*TDFAGA*) components.

The *TCFAGA* were interpreted to reflect isostatically imbalanced crust assuming the crust was mainly compensated by its thickness variations. Subtracting *TCFAGA* from *TGE* inferred the compensated *TGE* (*CTGE*) that are poorly represented in *FAGA*. Accordingly, the annihilating *TGE* (*-CTGE*) were used to estimate the lunar Moho and related crustal thickness variations. These estimates were obtained from *-CTGE* by least squares inversions using spherical prisms represented by GLQ integration to model undulations of the Moho about a reference depth of 64 km with a density increase of 0.5 g/cm^3 into the mantle. These inversion procedures also were used on *TCFAGA* to obtain radial adjustments of the inferred Moho that may fully compensate the lunar topography.

The *TDFAGA* were separated into crustal (*CTDFAGA*) and subcrustal (*STDFAGA*) components based on their correlation spectrum with *FAGA*. Least squares inversions of *STDFAGA* by GLQ integration inferred boundary undulations for the core-mantle, asthenosphere-lithosphere, and middle-upper mantle during bombardment time. Inversion assumptions included, respectively, a mean core surface at 1288 km with a 4.1 g/cm^3 density increase, an asthenosphere-lithosphere reference depth of 650 km with a 0.2 g/cm^3 density increase, and a middle-upper mantle reference depth of 220 km with a density increase of 0.1 g/cm^3. In addition, basin mare thicknesses were estimated from

CTDFAGA by inversion using GLQ integration assuming a density increase of 0.5 g/cm^3 for the mare fill relative to nonmare crust.

The lunar selenoid was computed from spherical harmonic coefficients of the LP75G model (Konopliv et al., 1998) and the state of hydrostatic equilibrium was inferred from the estimates of the secular Love number k_s. The second zonal harmonic in the gravitational potential of the planets was computed from the geometrical flattening of the reference ellipsoid and rotational parameter q. Correlations of the selenoid with surface and subsurface topographic surface as well as point data, centered on the basins, were computed for inference on the shape distortions of the Moon.

Coefficient models for the Earth, Venus, and Mars were obtained from analyses of satellite tracking data. Hence, the variance, correlation of gravity and topography, spectral slopes, and the secular Love number k_s of the planets were compared.

6.3 Analysis of Results

New details on mass variations that relate to the composition, structure, and isostatic and tectonic development of the lunar crust, mantle, and core were developed from a spectral correlation analysis between the satellite-measured free-air gravity and topography data. In addition, mare surfaces are not parallel to the selenoid and compared to the terrestrial planets, the Moon is farthest from hydrostatic equilibrium and has the lowest temperature gradient.

6.3.1 Crustal Attributes

Nearside and farside dichotomies in Moho, crustal thickness and strength variations are clearly evident in the modeling results. For example, relative to nearside crustal thicknesses, farside thicknesses average about 14 km greater and show a 50% energy increase. These dichotomies may also be reflected in the disparate crustal properties inferred for the giant nearside Procellarum and farside South-Pole Aitken basin. The muted topography and apparent lack of Moho uplift beneath Procellarum relative to the 13-km topographic depression and distinct regional mantle plug of the South Pole-Aitken (SPA) basin infer crustal viscosities on the farside of the Moon that may have been at least an order of magnitude larger than the contemporaneous viscosities on the nearside (Solomon et al., 1982).

Mare fill thicknesses estimates from *CTDFAGA* ranging from several hundred meters to only a few kilometers and are consistent with photogeologic and remote sensing estimates.

Isostatic properties of the basins were interpreted from *TCFAGA* RAM data. Although all impact basins show centrally uplifted Moho, uplifted Moho is mostly emplaced superisostatically on the nearside and subisostatically on the farside. Hence, a strength dichotomy is reflected by a consistent distribution of nearside basins having mostly superisostatic mantle plugs in contrast to farside basins involving mostly subisostatic mantle plugs. A higher nearside thermal gradient due to abundance of

radioactive elements in the nearside mantle and crust relative to the farside may also have contributed to these strength variations.

Characterization of basin central mass anomalies were inferred from *TCFAGA* and *CTDFAGA* components. Mascon anomalies reflect mostly the effects of superisostatic mantle plugs or mare fill or both or a subisostatic mantle plug plus mare fill. A maslite anomaly involve a mass deficit that may be attributed to a subisostatic mantle plug. These effects can sometimes be offset by small positive effects of mare fill.

Basins having no mascons may be characterized by a mantle plug in near-isostatic equilibrium. However, for tectonically complex basins, a mascon gravity anomaly may be delineated by a local positive *TCFAGA* superposed on a general negative *TCFAGA*.

6.3.2 Basin Ring and Transient Cavity Attributes

RAM data were analyzed for correlations with photo-geologically inferred basin basin rings. Reconstruction of the basin transient cavity (TC) geometries also provided insight on the lithospheric evolution during bollide bombardment times.

The origin of basin rings appear to be compatible with large-scale wave-like deformation of the crust, induced by the passage of the shock wave from bollide impact, presumably produced mass variations. These mass variations were apparently sustained by the strength of the lithosphere as incompletely compensated ring structures (Baldwin, 1949; Melosh, 1989).

The WCA-inferred basin rings follow the $\sqrt{2}$D-spacing rule and the ring counts per basin are on average larger on the nearside than on the farside. The results suggest that a more rigid farside lithosphere may have inhibited the development of basin rings.

The geometry of the basin TC appear to support the 0.1 proportional scaling relation. The depth/diameter ratio of 0.09 is consistent with previous estimates for all nearside basins. For the larger nearside Serenitatis and Imbrium basins, the proportionality relation may overestimate the excavation depths by 28-37% due possibly to their atypical crustal properties.

The inner zero contour of the RAM data provide good estimates on lunar basin transient cavity diameters. The sizes of transient cavity diameters are consistent with lithospheric rigidity variations that presumably characterize the tectonic development of the lunar lithosphere. On the nearside, transient cavity diameters tend to correlate directly with relative basin ages.

Development of isostatic properties of central basin mass anomalies may be constrained by crustal thickness. A critical crustal thickness of about 30 km may have differentiated the development of superisostatic and subisostatic mantle plugs on the farside. In particular, superisostatic mantle plugs presumably developed in crustal thicknesses below this critical value, whereas in thicker crust mantle plugs may have only developed to subisostatic levels.

For both nearside and farside basins, shallow excavation depths also may account for the apparent lack of mare flooding.

6.3.3 Subcrustal Attributes

Subcrustal undulation boundaries provided insight regarding the tectonic evolution of the Moon. For example, the elevated core-mantle boundary beneath the Procellarum-Imbrium basins is consistent witht uplifting effects of the Imbrium impact that presumably facilitated the development of the "Great Lunar Hotspot".

Inferred topographic undulations for the lower and middle mantle also may reflect lithospheric responses to surface bollide impacts. On the nearside a higher thermal gradient probably expedited the development of a thinner lithosphere by mantle convection (Zuber et al., 1994). A lower thermal gradient on the farside may have promoted viscous entrainment of lower density mass into the lower mantle and the development of a thicker lithosphere. Nearside mantle convection presumably facilitated diapiric rise of magma and subsequent flooding of the nearside basins, whereas the viscous entrainment of melts may have limited opportunities for basalt flooding of the farside basins.

Basin fill on the nearside consists of low and high-Ti basalts possibly because conduits may have extended to greater depths where the olivine-rich magma reservoirs were formed. Mare fill in farside basins presumably originated at relatively shallow depths where its composition was constrained mostly to low-Ti basalts.

6.3.4 Shape Attributes

The shape distortion of the Moon may be attributed to internal mass distributions while localized lava flooding of lunar basins may have limited influence on the large-scale distribution of mass responsible for the momenta.

Mare surfaces of the nearside basins generally decrease in elevation basins from West to East and are strongly out-of-phase to the selenoid. Hence, the hypothesis that mare floors describe a lunar equipotential surface is not supported by this study. However, the eastward deepening of the nearside mare surfaces may to be related to the greater depth of excavation of the respective basins.

By comparing the measured spectra of the planets, it appears that the Moon has the lowest temperature gradient and is farthest from hydrostatic equilibrium compared with the other terrestrial planets.

6.4 Recommendations

The veracity of the models derived in this study may be tested by the analysis of higher resolution gravity data. In particular, improved understanding on the evolution of the Moon may be gained from analyzing the geologic significance of high frequency terrain decorrelated free-air gravity anomalies in the context of available remote sensing multi-spectral data from Clementine (Nozette et al., 1996) and Lunar Prospector electron reflectometer and magnetometer data.

Improved lunar gravity data may provide new insights on the poorly understood structure of the lunar Megaregolith and crust. For example, preliminary investigations suggest that positive feature associations between these anomalies and crustal variations of iron as may be reflected in the lunar maps of Fe- and Ti concentrations (Lucey et al., 1995; Blewett et al., 1995). Concentrations of anorthosite in the Earth's crust tend to be characterized by gravity and magnetic minima (eg., Lucius and von Frese, 1988) so that one would anticipate negative feature associations between crustal potential field anomalies and compositional diversity of the lunar crust as interpreted from remote sensing studies (e.g., Pieters et al., 1993; 1996). Anticipated results of the feature association with gravity and remote sensing data may facilitate insight on the differentiation of the lunar crust into geologically unique lunar provinces such as the mafic province of Procellram KREEP Terraine (PKT), Felsphatic Highlands Terrane (FHT), and the South Pole-Aitken Terrane (SPAT) (Joliff et al., 2000).

Improved details of the surface reflectance properties and the mineral composition of the surface from band ratio images should yield better understanding of the lunar surface when combined with gravity or magnetic models. In addition, new insights on the tectonic development of the crust may be suggested by the correlations between *CTDFAGA* and textural variations in the remote sensing data that may reflect zones of fracture or brecciation within the upper crust, including the surface topogaphy.

The static components of the orbital magnetometer data may be used to identify possible magnetic anomalies and related magnetization properties of the lunar geology and to test for their geologic affinities at various orbital altitudes of the Lunar Prospector mission.

The farside gravity anomalies are generally poorly determined because no direct line-of-sight observations were available. High resolution gravity data from the Lunar Prospector satellite lowered to 25 km may still be limited for the more detailed understanding of mass variations on the farside. Accordingly, a lunar mission that support satellite-to-satellite Doppler tracking of a low-altitude lunar orbiter by means of a high-altitude relay satellite (Matsumoto et al., 1999) can provide improved gravity data over the farside.

With the availability of higher resolution gravity and elevation models, improved terrain gravity effect modeling capabilities should be developed. For example, the 1^o prism model in the present GLQ modelling should be replaced with a TIN model to represent terrain.

Modeling capabilities developed with this study can readily be extended to studies of other planetary bodies involving satellite potential field, topographic, and remote sensing observations.

A Selenodesy

The determination of the gravity field of the Moon is one of the fundamental goals of selenodesy. Knowledge of the gravity field is important for applications such as the determination of selenoid heights (i.e., similar to geoid heights for the Earth) and other selenophysical phenomena.

The determination of the lunar gravity field was estimated from the analysis of the motions of orbiting satellites (Konopliv et al., 1998). In particular, potential coefficients are determined from the analysis of trajectories of lunar orbiting satellites. A convenient way of representing the gravitational potential of the Moon is through a spherical harmonic series (Ferrari et al., 1980).

In this study, inferred mass distribution models were derived from the analysis of correlations between lunar gravity and topography. The terrain gravity effects (*TGE*) were modeled in spherical coordinates by Gauss-Legendre Quadrature integration.

In the first section, the gravimetric definitions are described for representing the gravity field, and the spherical approximations and the spherical harmonic representation of the gravity anomalies are given. In section 2, the determination of the selenoid is described. In section 3, the computation for the gravity effect of the lunar topography is described.

A.1 Definitions

In 1945, Molodensky proposed that the surface of a planet such as Earth's can be gravimetrically determined (Heiskanen and Moritz, 1967). In particular, the Molodensky boundary value problem (BVP) introduces an approximation for a planet's surface by a known closed surface called the telluroid and denoted Σ. Hence, the gravimetric quantities relating to the Moon's gravity field can be described in terms of the Molodenksy BVP.

The Moon's surface S can be approximated by a known surface Σ called the telluroid and the Moon's actual gravity potential W can be approximated by the gravity potential U of a reference ellipsoid of revolution. The rotating ellipsoid usually involves the same mass and rotation as the Moon (Heiskanen and Moritz, 1967) so that U is equal to a gravitational potential (V) plus the centrifugal potential (Φ).

Figure 48 shows the geometry of the problem. P and Q are points on the surface and telluroid, respectively, and P_0 is a point on the equipotential surface, called the selenoid (Γ), and Q_0 lies on the reference ellipsoid. The distance QP is called the height anomaly (ζ), Q_0P_0 is the selenoid height (N), and Q_0Q is the normal height (H^*) of point P.

The potential anomaly is defined as

$$\Delta W = W_P - U_Q \tag{37}$$

and the disturbing potential at point P as

$$T_P = W_P - U_P, \tag{38}$$

respectively (Moritz, 1989).

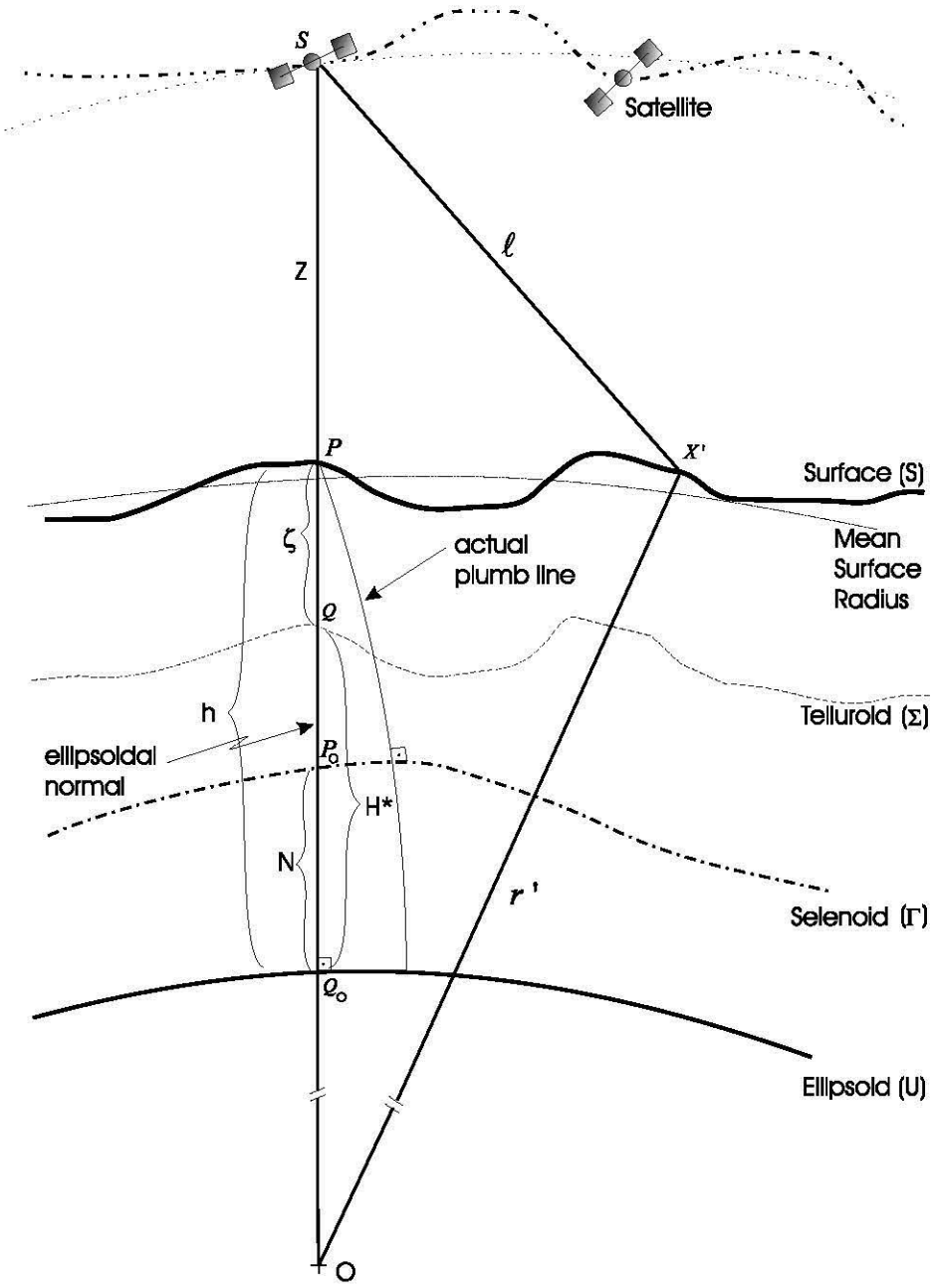

Figure 48: Geometry of the surfaces for the Moon. S is satellite observation point, P is the corresponding sub-satellite point and the origin O is located at the center of mass. Z is the mean satellite altitude, h is ellipsoidal height, r' is the selenocentric radius to the source point (X'), and ℓ is the slant range from S to X'. The mean surface radius (thin line) is 1738 km.

A.1.1 The Boundary Condition for Solving Laplace's Equation

Choosing the telluroid (Σ) as the surface of points Q on the ellipsoid normal from the points P such that

$$W_P = U_Q \Leftrightarrow \Delta W = 0, \tag{39}$$

the Molodensky problem consists of solving the Laplace's equation

$$\nabla^2 T = \frac{\partial^2 T}{\partial x^2} + \frac{\partial^2 T}{\partial y^2} + \frac{\partial^2 T}{\partial z^2} = 0, \tag{40}$$

under the following boundary condition on the telluroid (Moritz, 1989)

$$\frac{\partial T}{\partial \tau} + \frac{1}{\gamma}\frac{\partial \gamma}{\tau} T + \Delta g = 0 \tag{41}$$

where $\frac{\partial}{\partial \tau}$ represent a derivative along the isozenithals (i.e., lines along which the normal gravity vectors are parallel).

The gravity anomaly Δg (Moritz, 1989) is the difference between the magnitude of the actual gravity acceleration at the surface point P minus the magnitude of the normal gravity acceleration at the corresponding telluroid point Q, i.e.,

$$\Delta g = |g_P| - |\gamma_Q| \tag{42}$$

where gravity g and normal gravity γ are the negative vertical gradients of W and U, respectively.

A.1.2 Spherical Approximation

The shape of the Moon can be described by a best fitting ellipsoid with semi-axes a (=1738.056 km) and b (= 1737.843 km) (Smith et al., 1997) for a flattening of 1/3234.93 (Zuber et al., 1994). A spherical approximation of this reference ellipsoid, therefore, is very good, with an error of about 0.03%, so that errors of this order of magnitude in the equations relating quantities of the anomalous gravity field in the boundary conditions can be tolerated (Moritz, 1989).

For a spherical approximation, the radius R of the sphere may be related to the axes (a, b) as (Moritz, 1989)

$$R = \sqrt[3]{a^2 b} = 1737.985 \tag{43}$$

which is close to the mean radius (1738.00 km) and the normal gravity in the boundary condition (41) is approximated as

$$\gamma = \frac{GM}{r^2}, \tag{44}$$

where $r = R + h$. The plumb lines, as well as the isozenithals, approximately coincide with the spherical radii (Moritz, 1989) so that

$$\frac{\partial}{\partial \tau} = \frac{\partial}{\partial r}, \tag{45}$$

where $\frac{\partial}{\partial r}$ represent a radial derivative. Using 44 we can write

$$\frac{1}{\gamma}\frac{\partial \gamma}{\partial r} = -\frac{2}{r}. \tag{46}$$

Hence, the Molodensky solution consists of solving the Laplace's eqation $\nabla T = 0$ under the boundary condition

$$\left(\frac{\partial T}{\partial r}\right)_Q + \frac{2}{r_Q} T_Q + \Delta g = 0 \tag{47}$$

on the telluroid.

A.1.3 Height Anomalies

From Figure 48 it is easy to see that

$$U_P = U_Q + \frac{\partial U}{\partial r}\zeta = U_Q - \gamma_Q \zeta. \tag{48}$$

Substituting equation (38) the disturbing potential can be written as

$$T_P = W_P - U_Q + \gamma_Q \zeta \tag{49}$$

and the height anomaly ζ given by Bruns' formula

$$\zeta = \frac{T_P}{\gamma_Q} \tag{50}$$

The normal gravity γ_Q at the telluroid point Q is computed from the normal gravity at the ellipsoid γ_0 by the normal free-air reduction applied upwards. An elementary approach is possible through formal analytical continuation by means of a Taylor series expansion (Heiskanen and Moritz, 1967; Moritz, 1989)

$$\gamma_Q = \gamma_0 + \frac{\partial \gamma}{\partial h} H^* + \frac{1}{2}\frac{\partial \gamma}{\partial h} H^{*2} + \ldots \tag{51}$$

where γ_0 corresponds to normal gravity on the ellipsoid and the normal gravity vector $\vec{\gamma}_0 = \text{grad}\ U_0$. The normal gravity gradient $\frac{\partial \gamma}{\partial h}$ is approximately 0.1864 mgals/m (for the Earth $\frac{\partial g}{\partial h} = 0.3086$ mgals/m). The normal height H^* is given by equation (4-44) of Heiskanen and Moritz, 1967 and is independent of density. The ζ-values can now be plotted above the telluroid, yielding the physical surface of the Moon.

The ellipsoidal height h of P is given by

$$h = N + H = \zeta + H^*. \tag{52}$$

A.2 Gravity Anomalies and Selenopotential Coefficients

During the space age, methods were developed to estimate potential coefficients from satellite orbital analysis. For the Moon, a convenient way of representing the Moon's gravitational potential is through spherical harmonic representation (e.g.,Ferrari et al., 1980; Bills et al., 1987).

A spherical harmonic representation of the Moon's gravitational potential V on the surface is defined as (Ferrari et al., 1980) from potential coefficients of the LP75G gravity model (Konopliv et al., 1998)

$$V(r,\theta,\lambda) = \frac{GM}{r}\left[1 + \sum_{n=2}^{\infty}(\frac{a}{r})^n \sum_{m=0}^{n}[C_{nm}cos(m\lambda) + S_{nm}sin(m\lambda)]P_{nm}(cos\theta)\right] \tag{53}$$

where GM is the product of gravitational constant and mass of the planet, r is the geocentric radius, θ is the latitude, λ is the longitude, $[C_{nm}, S_{nm}]$ are the fully normalized potential coefficients of degree n and order m, P_{nm} are the associated fully normalized Legendre functions (Heiskanen and Moritz, 1967) and a (= 1738.056 the equatorial radius of an adopted mean Moon ellipsoid) is the scaling parameter associated with potential coefficients (Kaula, 1966). Selenocentricity of the coordinates system enforces the absence of the first-degree harmonics in (53).

The disturbing potential T at a point $P(r,\theta,\lambda)$ is

$$T(r,\theta,\lambda) = \frac{GM}{r}\sum_{n=2}^{\infty}(\frac{a}{r})^n \sum_{m=0}^{n}[C'_{nm}cos(m\lambda) + S_{nm}sin(m\lambda)]P_{nm}(cos\theta) \tag{54}$$

where, the zero-degree term in (54) has been set to zero, assuming equality for the actual mass of the Moon and the reference ellipsoid, and the free-air gravity anomaly (*FAGA*), denoted by the usual Δg symbol, is

$$\Delta g(r,\theta,\lambda) = \frac{GM}{r^2}\sum_{n=2}^{\infty}(n-1)(\frac{a}{r})^n \sum_{m=0}^{n}[C'_{nm}cos(m\lambda) + S_{nm}sin(m\lambda)]P_{nm}(cos\theta) \tag{55}$$

A.3 The Selenoid

The selenoid height of P is the distance Q_0P_0 and is given by Bruns' formula

$$N = \frac{T_{P_0}}{\gamma_{Q_0}} \tag{56}$$

The theoretical estimability of the selenoid undulation is quite complex and conceptually not perfectly possible because of a lack of knowledge of the density distribution of the Moon. Since no masses are allowed outside Γ the topography must be eliminated mathematically (Moritz, 1989).

The conversion of the height anomaly to the geoid undulation can be done with the following expression (Rapp, 1994)

$$N = \zeta + \Delta g_B H \tag{57}$$

where the Bouguer gravity anomaly (Δg_B) is given by (Heiskanen and Moritz, 1967) and H is the orthometric height. Accordingly, the selenoid can be computed from potential coefficients by substituting T from Equation (54) into Equation (50) and then using Equation (57)

$$N = \frac{GM}{r_P \gamma_P} \sum_{n=2}^{\infty} (\frac{a}{r_P})^n \sum_{m=-n}^{n} [C'_{nm} cos(m\lambda) + S_{nm} sin(m\lambda)] P_{nm}(cos\theta) + \Delta g_B H \qquad (58)$$

The orthometric height is given by the distance from the selenoid to the surface i.e., by $H = h - N$. For the Earth, orthometric heights are obtained from spirit leveling. On the Moon, however, ellipsoidal heights were estimated from LIDAR data and the selenoid undulation was computed from the spherical harmonic coefficients of the GLGM-2 gravity model (Smith et al., 1997).

A.4 Terrain Gravity effects

Figure 48 shows the geometry for gravitational modeling in spherical coordinates of a source point X'. In particular, the gravitational effect δg_r, due to a mass anomaly referred to a geocentric coordinate system as shown in Figure 48 is given by

$$\delta g_r = -\left[G \frac{\partial}{\partial \ell} \left(\frac{1}{\ell} \right) \frac{\partial \ell}{\partial r} \Delta m \right] \qquad (59)$$

where G is the gravitational constant, ℓ is the distance between the source point and the observation point, and Δm is the mass contrast of the mass anomaly.

Consideration of equation (59) shows that the incremental gravitational effect due to a point source located a distance ℓ from the observation point can be generalized according to the relation (von Frese et al., 1981)

$$q(\ell) \Delta \sigma \qquad (60)$$

where $q(\ell)$ is the geometrical point source function which describes the inverse distance between the observation point and the source point, and $\Delta \sigma$ is the density contrast of the point source.

An anomalous body may be considered as being composed of a source volume distribution of gravity point poles. Hence, to estimate the gravitational effect at an observation point, it is necessary to evaluate and sum the anomalous values due to each point source at the observation point (von Frese et al., 1981). To determine the total field effect it is necessary to evaluate at each observation point (r, ϕ, λ) the volume integral given by

$$\int_{\lambda'_a}^{\lambda'_b} \int_{\phi'_a}^{\phi'_b} \int_{r'_a}^{r'_b} (q(r, \phi, \lambda; r', \phi', \lambda') \Delta \sigma) dr d\phi' d\lambda' \qquad (61)$$

where the primed variables refer to the coordinates of the anomalous body and (λ'_a, λ'_b), (ϕ'_a, ϕ'_b), and (r'_a, r'_b) are the longitudinal, latitudinal, and radial limits of the source volume.

The numerical evaluation of the integral of equation (61) can be obtained by Gaussian quadrature formulae. In particular, by extending the standard Gauss-Legendre quadrature procedure for a volume integral, equation (59) can be written as (von Frese et al., 1981)

$$\begin{aligned} \delta g_r &= \int_{\lambda'_a}^{\lambda'_b}\int_{\phi'_a}^{\phi'_b}\int_{r'_a}^{r'_b}(q(r,\phi,\lambda;r',\phi',\lambda')\Delta\sigma)dr d\phi' d\lambda' \\ &\approx \Delta\phi'_k\sum_k\{\Delta\lambda'_j[\sum_j\Delta r'_i(\sum_i(q(r'_i,\lambda'_j,\phi'_k)\Delta\sigma)A_i]A_j\}A_k \end{aligned} \tag{62}$$

where the source point coordinates are (primed) and the observation point coordinates (unprimed), r is the radial distance vector between the center of mass of the Moon and the observation point coordinates, and (A_i, A_j, A_k) are the Gauss-Legendre quadrature weights (Stroud and Secrest 1966). In addition, $\Delta\phi'_k = [\frac{\Delta\phi'_{ka}-\Delta\phi'_{kb}}{2}]$, $\Delta\lambda'_j = [\frac{\Delta\lambda'_{ja}-\Delta\lambda'_{jb}}{2}]$ and $\Delta r'_i = [\frac{\Delta r'_{ia}-\Delta r'_{ib}}{2}]$ and (ϕ'_{ka}, ϕ'_{kb}), $(\lambda'_{ja}, \lambda'_{jb})$ and (r'_{ia}, r'_{ib}) are the lower a and upper b volume limits of the body, respectively, in the k-th coordinate of co-latitude (ϕ), the j-th coordinate of the longitude (λ), and the i-th radial coordinate of (r).

However, the integration limits for a uniformly shaped body such as a prism, are easy to specify. For a prism, the integration limits are $(r'_{ia}, r'_{ib}) = (r'_a, r'_b)$, $(\phi'_{ia}, \phi'_{ib}) = (\phi'_a, \phi'_b)$, and $(\lambda'_{ia}, \lambda'_{ib}) = (\lambda'_a, \lambda'_b)$

The lunar topography can be represented by spherical prisms of varying radial dimensions relative to the mean radius. However, approximation improves with sufficiently small $\delta\phi$ and $\delta\lambda$ prism dimensions. In this study, the lunar topography was represented by $1^0 \times 1^0$ flat-top and flat-bottom spherical prisms.

Accordingly, the radial gravitational effect δg_r in spherical coordinates (ϕ, λ, r) of the lunar topography as represented by these spherical prisms and uniform density contrast $(\Delta\sigma)$ with free space, may be estimated by

$$\delta g_r(\phi,\lambda,r) \approx \Delta\phi'_k\sum_k\{\Delta\lambda'_j[\sum_j\Delta r'_i(\sum_i(q(r'_i,\lambda'_j,\phi'_k)\Delta\sigma)A_i]A_j\}A_k \tag{63}$$

In particular, the lunar terrain gravity effect *TGE* was modeled by equation (63) and assuming a density contrast of 2.8 g/cm^3 with the vacuum of space.

B Attributes of the Satellite Gravity and Topography Data Sets

Mapping and sampling during the Apollo and Luna landing missions identified the major lunar terranes, ages, and rock types as well as providing a first glimpse of the farside of the moon although the data resolution was low and coverage at higher latitudes was poor. Higher resolution data became available from the Clementine mission which produced global gravity, and topography data as well as hinting that the polar regions may be harboring ice (Binder, 1998). Further refinements and improved magnetic, gravity and compositional data were sought with the latest Lunar Prospector (LP) mission equipped with a magnetometer and gamma-ray spectrometer. The goal of the Lunar Prospector was to test and extend the Clementine results by obtaining higher resolution gravity, magnetic and compositional data (Binder, 1998).

The purpose of this appendix is to provide a brief description of the satellite observed gravity and topography data models used in this study as well as attributes of the terrain gravity effects of the Moon.

B.1 Attributes of the Lunar Prospector Satellite Gravity Model (LP75G)

The gravity model LP75G is the most recent model obtained from Doppler tracking of the Lunar Prospector (LP) satellite. The gravity information comes from tracking the spacecraft in its circular polar orbit of 100 km altitude with the Deep Space Network (DSN), by measuring the line-of-sight velocity from the Doppler shifts to an accuracy of 0.2 mm s^{-1} (Binder, 1998).

In developing the global gravity model, several datasets from earlier lunar missions were combined. In particular, continuous tracking data of LP were combined with the data from Lunar Orbiter, Apollo and Clementine to produce a 75 degree spherical harmonic gravity model (LP75G). Clementine data, obtained from tracking the spacecraft in its elliptical orbit with periapsis altitude of 400 km improved the low degree (n=2,3) and sectorial terms (to degree 20) of the gravity field. Less than 16% of the Clementine observations were at spacecraft altitudes of less than 1,000 km, so that the Clementine dataset represents the principal constraint on the low-frequency properties of the gravity field (Zuber et al., 1994).

The major improvements of the LP75G model over previous missions that mapped the gravity field of the Moon, revealed three new large mass concentrations or mascons (Muller and Sjogren, 1968) beneath the nearside impact basins Mare Humboltianum, Mendel-Rydberg and Schiller-Zucchius. Four mascons on the farside that were previously suggested from the Clementine mission (Zuber et al., 1994) have been resolved with the LP75G model. In particular, these farside mascons are located in the Coulomb-Sarton, Freundlich-Sharanov, Hertzprung, and Moscovience basins (Konopliv et al., 1998).

An estimate on the accuracy of the gravity model is required to constrain the interpretations for the results that were obtained in this study. In particular, the gravity anomaly models derived in this study were evaluated at a satellite altitude of 100 km above the mean radius of the Moon.

The anomaly degree variances can be evaluated from the potential coefficients on a sphere (Torge, 1989; Rapp and Pavlis, 1990) of radius R by

$$C_n = \gamma^2 (n-1)^2 \left(\frac{R}{R+100} \right)^{2n} \sum_{m=-n}^{n} (C_{nm}^2 + S_{nm}^2) \tag{64}$$

where $\gamma = GM/R^2$ and (C_{nm}, S_{nm}) are the fully normalized potential coefficient set resulting from the adjustment solution (Konopliv et al., 1998).

The anomaly error degree variance was computed at 100 km above the mean surface radius of 1738 using a modified equation 64

$$\varepsilon C_n = \gamma^2 (n-1)^2 \left(\frac{R}{R+100} \right)^{2n} \sum_{m=-n}^{n} (\sigma_{C_{nm}}^2 + \sigma_{S_{nm}}^2) \tag{65}$$

where $(\sigma_{C_{nm}}, \sigma_{S_{nm}})$ are the coefficient standard errors obtained from the error covariance of the gravity solution.

Figure 49 shows the anomaly degree variance and the error anomaly degree variance computed at 100 km above the mean radius of 1738 km. The total estimated error variance of the gravity field at 100 km above the mean radius is about 12.3 mGals^2. The large errors are attributed to the lack of direct-line-of-sight tracking on the farside (Konopliv et al., 1998).

The gravity model can support resolution of up to 50 km and about 200 km for the nearside and farside, respectively (Konopliv et al., 1998).

B.2 Attributes of the Clementine Satellite Lunar Topography Model (GMLT-2)

The polar orbiting Clementine spacecraft (Nozette et al., 1996) carried a laser ranging instrument (LIDAR) which measured the slant range from the spacecraft to most of the lunar surface from 78^0 S to 78^0 N, covering the known or hypothesized major lunar basin structures (Wilhelms, 1987) and confirming several probable basins (Spudis, 1993). Clementine measured a 16-km range in topography which is over 30 % greater than previously mapped by Apollo satellites. The most pronounced topographic feature of the Moon is the farside South Pole-Aitken basin with a diameter of 2500 km and a maximum depth of 8.2 km below the reference ellipsoid (Zuber et al., 1994).

To produce a global topographic model from LIDAR data, a precise orbit was subtracted from the range profiles. In particular, by interpolating the spacecraft orbital trajectory to coincide with the time of the laser pulse, the arrival time of the laser pulse at the lunar surface was converted to

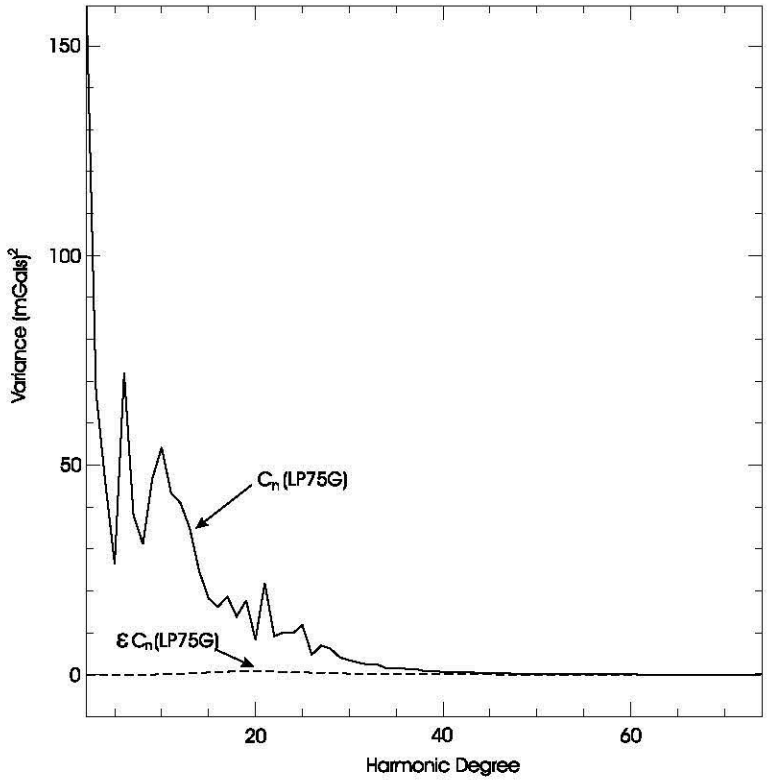

Figure 49: Anomaly degree variance (C_n) and the error variance (εC_n) of the LP75G potential coefficient model at 100 km altitude.

selenocentric coordinates (Zuber et al., 1994). The observed range from the spacecraft to the surface was transformed into a radius, measured in a lunar center-of-mass reference frame (Zuber et al., 1994). While the altimetry along-track data is fairly dense, the east-west coverage was limited by the 2.8^0 spacing of the ground tracks, repeating every 132 revolutions. Hence, cross-track and polar latitude regions were filled by minimum-curvature interpolation (Smith and Wessel, 1990) to produce a 72 degree spherical harmonic expansion model. The elevations of the Goddard Lunar Topographic Model 2 (GLTM-2) were referenced to an ellipsoid with an equatorial radius of 1738 km and flattening of 1/3234.94 (Smith et al., 1997).

A fundamental characteristic of the lunar shape is the bimodal distribution of its topography. The difference between the nearside and farside of the study region (Figure 3) is easily seen from the distribution histogram shown in Figure 50.

The relief shown in Figure 3 ranges over 16 km with the greatest topographic excursion occuring in the farside highlands. The nearside has a gentle topography with amplitude range (AR) = [-5.54 km ; 4.19 km] and amplitude standard deviation (ASD) of 1.2 km while the farside shows a much larger variation with AR = [-7.95 km ; 8.13 km] and ASD of 2.6 km. The sharpness of the nearside

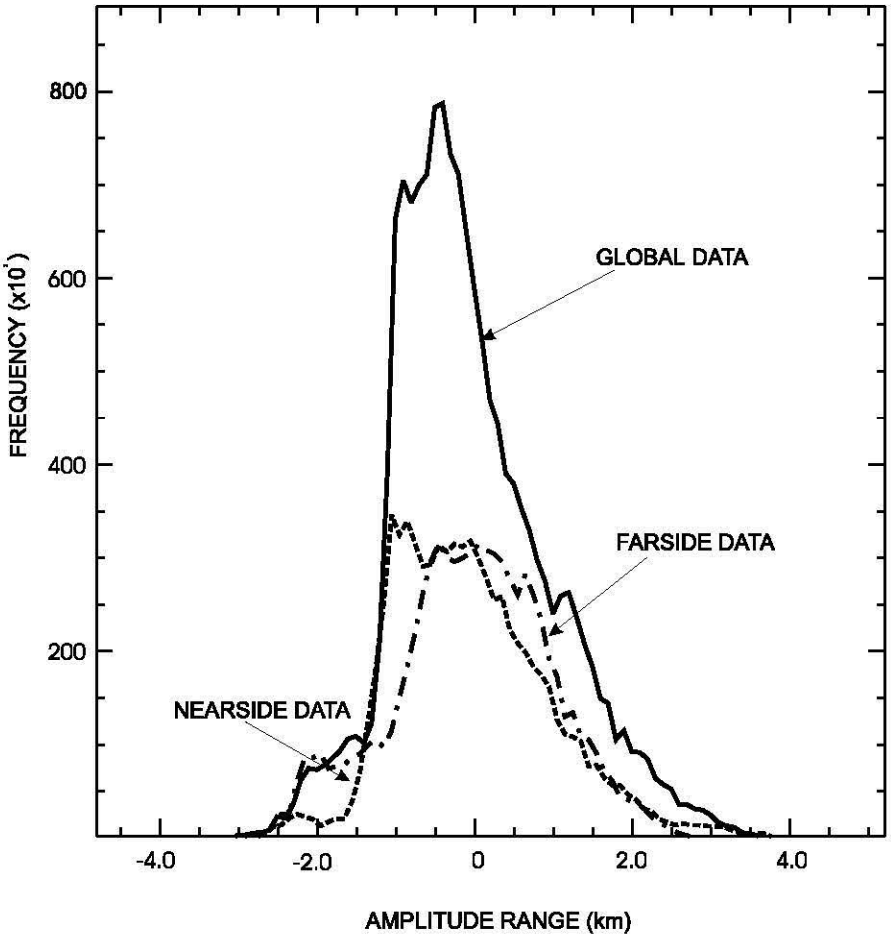

Figure 50: Histogram of ellipsoidal heights of the near-global lunar topography of Figure 3 (thick solid line), nearside topography (dashed line) and farside topography (dash-dot line).

histogram is due to the flat maria situated around the mid-latitude and equatorial regions whereas the rugged highlands of the farside have a symmetic distribution (Smith et al., 1997). Many of the regions with low topography are large impact basins and most basins have been filled by mare basalts (Hartmann and Wood, 1971). An exception is the South Pole-Aitken basin with the lowest depression but very little basaltic fill.

B.3 Attributes of Lunar Terrain Gravity Effects

For efficient calculation of the terrain gravity at 100 km above the mean surface radius, the topography was characterized by spherical prismatic elements with flat tops at the average altitude provided by the GLTM-2 file of $1^0 \times 1^0$ topographic data.

The gravity effect of the topography of Figure 3, shown in Figure 4, was modelled according to equation 63 in lunar spherical coordinates assuming a topographic density 2.8 g/cm^3 (e.g., Zuber et al., 1994). The range of more than 1000 mGals is significant with large positive values due mostly to the farside highlands. The negative values are mostly associated with the large South Pole-Aitken basin and the nearside mare basins of Imbrium, Serenitatis, Crisium, Nectaris and Humurom.

System	Age (Aeons)	Remarks
pre-Nectarian	4.5 to 3.9 4.2 4.2 to 4.1 4.1 to 3.9	- Early formation - Crustal solidification cratering including - Heavy impacts including the formation of Procellarum and Aitken Basin - Impacts forming smaller basins of 500 km diameter on average.
Nectarian	3.92 to 3.85	- period named "cataclysm" because heavy bombardment during 0.1 aeon.
Imbrium -Early Imbrium -Late Imbrium	3.85 to 3.2 3.85 to 3.72 3.72 to 3.2	- Most maria, some Basins, degraded craters. - Impacts forming Imbrium and Orientale basins and significant impact cratering. - Subordinate number of cratering events. and no basin impacts - Greatest period of volcanic activity. - Formation of most maria.
Eratosthenian	3.2 to 1.2	- Includes both slightly degraded craters such as Eratosthenes crater and some maria.
Copernican	1.2 to present	- Marked by fresh and rayed craters such as Copernicus crater.

Table 10: Time-stratigraphy of Lunar Geology.

C Lunar Geologic History

The relative lunar stratigraphy involves the identification of material in craters, basins, and maria (Wilhelms, 1987). The purpose of this Appendix is to briefly describe the chronological events of the Moon that pertain to this study.

C.1 Relative Basins Ages

Radiometric dating of returned Apollo samples indicates that the Moon was formed about 4.5 Byr ago. After accretion, a period of bollide avalanche caused lunar basin excavations. Basin excavation, 3.92 - 3.85 Byr was followed by mare lava emplacement dated around 3.84 - 3.17 Byr years ago and finally, superposed craters caused surface degradation of the younger lunar basins (Wilhelms, 1987).

Table 10 lists the major lunar chronological events for the Moon (Wilhelms 1987). Three major events divide the time-stratigraphy into four major sequences. In particular, laterally extensive

deposits of the Nectarian, Imbrium and Orientale basins divide the lunar stratigraphy into 4 major sequences as: pre-Nectarian, Nectarian, Lower Imbrian, and Upper Imbrian through the Copernican system. The Nectarian System comprise 10 basin impacts, and the Imbrium System comprise two basin impact events, respectively. The Eratosthenian and Copernican Systems are characterized by superposed cratering events.

The lunar pre-Nectarian epoch (pN) (4.2 Byr - 3.92 Byr) provides the clearest look at the early Solar System. The barrage of cosmic bodies that must have affected all moons and planets is richly recorded by pre-Nectarian basins and large craters. By definition, all materials formed since the origin of the Moon until the formation of the Nectarian basin are pre-Nectarian.

The Nectarian (N) epoch (3.92 Byr - 3.85 Byr), includes all materials of the Nectarian basin and all younger lunar materials emplaced before the deposition of the Imbrium basin material. The Nectarian epoch is also referred to as the "cataclysm", because of the heavy bombardment over only 0.1 aeon (Wilhelms, 1987).

The Imbrium epoch (Im) defined between 3.92 Byr - 3.2 Byr is divided into two separate systems namely the Lower and Upper Imbrium. The lower Imbrium epoch is associated with the Imbrium and Orientale impact events. the Imbrium basin dominates the lunar surface that is visible from Earth. The Orientale basin is the youngest impact basin on the Moon and it's deposits dominate the terrae on both sides of $90^{o}W$. The Orientale basin also serves as a prototype lunar basin (Spudis, 1993).

The Upper Imbrium System is mainly associated with mare volcanism, maria formation, and subordinate crater materials. The maria, of only a few kilometers thick, presumably resulted from basalt emplacement and ponding in the low-lying regions of the large basins after an eruption of overpressurized subcrustal magma reservoirs. Subsequent superposed cratering events presumably facilitated lateral mass redistribution and basin degradation. Some craters (size 10-30 km) may have fractures the basin floor and facilitated the formation of laccoliths which in turn raised the crater floor (Wichman and Schultz 1995). No basin forming events are associated with this epoch.

The Eratosthenian and Copernican Systems are associated with the Moon's youngest time-stratigraphic systems. In fact, the Eratosthenian and to a lesser extent, the Copernican Systems continue the geologic style of the Upper Imbrian Series. In particular, the ejecta of the Eratosthenes impact is superposed on nearby mare material, whereas rays from Copernicus are superposed on Eratosthenes. The Eratosthenian and Copernican units serve as models for interpreting the older mare units due to their freshness and clear stratigraphic relations. In particular, crater topography for these crater are less eroded and minimal mixing of ejecta material with the substrate ocurred (Wilhelms, 1987).

C.2 Major Lunar Basins

Table 11 lists the major basins for the Moon in alphabetical order. The basin radius (in km) refers to the main topographic basin rim (Wilhelms, 1987), the relative age refers to the time-stratigraphy of Table 10, the elevation (H_z) of the basin floor relative to the mean radius of 1738 km (Smith

Basin	Center	Radius(km)	H_z(km)	N (m)	Rel. Age
Apollo	$36^oS; 153^oW$	250	-1.83	-194.5	pN-17
Australe	$51^oS; 95^oE$	440	-0.75	+44.9	pN-4
Balmer-Kapetyn	$15^oS; 69^oE$	275	-4.25	+85.4	pN-2
Birkhoff	$59^oN; 147^oW$	165	+0.8	-120.0	pN-14
Coulomb-Sarton	$52^oN; 123^oW$	265	-2.38	-100.0	pN-10
Crisium	$17^oN; 58^oE$	530	-4.10	120.4	N-8
Cruger	$17^oS; 67^oW$	150?	-2.80	-10.0	(?)
Freundlich-Sharanov	$18^oN; 175^oE$	300	-3.00	+11.0	pN-15
(Fucenditatis)	$4^oS; 52^oE$	490	-2.13	-37.0	pN-3
Grimaldi	$5^oS; 68^oW$	215	-2.45	-118.0	pN-16
Hertzprung	$3^oN; 128^oW$	285	0.32	-64.0	N-10
Humboldtianum	$58^oN; 84^oE$	600	-4.61	+14.0	N-6
Humorum	$24^oS; 39^oW$	410	-2.84	+171.0	N-7
Imbrium	$33^oN; 16^oW$	900	-2.74	+465.0	Im-1
Ingenii	$35^oS; 164^oE$	280	-1.79	+10.0	pN-8
Keeler-Heaviside	$10^oS; 162^oE$	390	+1.50	+80.0	pN-9
Korolev	$4.5^oS; 157^oW$	440	2.21	125.0	N-4
Lorentz	$34^oN; 97^oW$	180	-1.60	-204.0	pN-12
Mendeleev	$5^oN; 140^oE$	165	-1.71	+5.0	N-5
Mendel-Rydberg	$50^oS; 94^oW$	320	-2.20	+102.0	N-2
Moscovience	$26^oN; 147^oE$	275	-3.84	+45.0	N-3
Mutus-Vlacq	$51^oS; 21^oE$	345	-1.80	+95.0	pN-6
Nectaris	$16^oS; 34^oE$	430	-3.33	201.4	N-1
(Nubium)	$21^oS; 17^oW$	345	-2.91		pN-7
Orientale	$20^oS; 95^oW$	650	-3.36	-52.0	Im-2
(Procellarum)	$26^oN; 15^oW$	2568	-2.65		pN-00
Schiller-Zuchius	$56^oS; 44^oW$	165	-2.30	+92.0	pN-13
Serenitatis	$27^oN; 18^oE$	450	-3.08	420.4	N-9
Smythii	$3^oS; 86^oE$	480	-4.25	-15.0	pN-11
S. Pole-Aitken	$56^oS; 180^oW$	1250	-4.71		pN-01
(Tranquilitatis)	$7^oN; 32^oE$	400	-1.46		pN-5
Tsiolkovskiy-Stark	$15^oS; 128^oE$	350	+1.10	+10.0	pN-1

Table 11: Selenodetic coordinates, radius (Wilhelms, 1987), surface elevation (H_z) (Smith et al., 1997), and selenoid heights (N) at the centers of the major lunar basins. Relative basin ages relate to primary geologic events of the Moon such as the pN=Pre-Nectarian, N=Nectarian and Im=Imbrium, Systems, respectively (Wilhelms, 1987).

et al., 1997), and the selenoid height (N).

Relative ages of the basins are taken from the description by Wilhelms (1987) and described in

terms of the major lunar chronological events as listed in Table 10. The tabulated relative ages refer to the chronological sequence of the basin impacts as suggested by Wilhelms (1987). For example, the Korolev basin presumably was the fourth impact after the Nectaris impact basin was formed. Accordingly, this basin's relative age is denoted as N-4 in Table 11. However, discrepancies exist regarding the chronological sequence of farside basins as inferred from radiometric dating and remote sensing data (e.g., Greeley et al., 1993).

D Least Squares Inversion by Gauss-Legendre Quadrature Integration

D.1 Introduction

Undulations of a density boundary may be obtained from an inversion of gravity anomaly data. Undulations of the core, lower, and middle mantle surfaces of the Moon may provide insight on possible internal mass distributions from surface basin-size bollide impacts. A least squares inversion procedure based on modeling spherical prisms by Gauss-Legendre quadrature (GLQ) integration is developed and tested on a $64^0 \times 64^0$ region centered on the Mare Orientale basin.

D.2 Observation Equation

The forward problem was described in section 3 of Appendix A where the terrain gravity effect was computed from equation 63 given the radial dimension of the spherical prisms. In the forward problem, the surface topography was represented by flat-top-flat-bottom spherical prisms. Accordingly, the inverse problem consists of estimating the radial dimension for each flat-top-flat-bottom spherical prism for a given gravity anomaly field.

Figure 51 shows the geometry of the problem for estimating the Moho undulation. A source grid, comprising flat-top-flat-bottom spherical prisms, is located at a reference depth R_D and the observation grid is located at an elevation R^0 above the mean surface radius.

Assuming that each prism dimension has 2 nodes, then equation 63 can be written as

$$\Delta g_r(\phi,\lambda,r) \approx \Delta\phi'_k \sum_{k=1}^{2}\{\Delta\lambda'_j[\sum_{j=1}^{2}\Delta r'_i(\sum_{i=1}^{2}(q(r'_i,\lambda'_j,\phi'_k)\Delta\varrho)A_i]A_j\}A_k \tag{66}$$

The summation given by equation (66) for one observation point and one source prism can be written as

$$\begin{aligned}\Delta g_r(\phi,\lambda,r) \;=\; & \frac{1}{2}\Delta\lambda\Delta\phi\Delta r(Q_{111}A_1^rA_1^\lambda A_1^\phi + Q_{211}A_2^rA_1^\lambda A_1^\phi + \\ & Q_{121}A_1^rA_2^\lambda A_1^\phi + Q_{221}A_2^rA_2^\lambda A_1^\phi + Q_{112}A_1^rA_1^\lambda A_2^\phi + \\ & Q_{212}A_2^rA_1^\lambda A_2^\phi + Q_{122}A_1^rA_2^\lambda A_2^\phi + Q_{222}A_2^rA_2^\lambda A_2^\phi)\end{aligned} \tag{67}$$

where the subcripts (i,j,k) denote the node indexes and $A_{i,j,k}^{r,\phi,\lambda}$ are the weights associated with the nodes in each dimension. In addition, the parameter Q_{111} denotes the function $q(r'_1,\lambda'_1,\phi'_1)\Delta\varrho$, and Q_{112} denotes $q(r'_1,\lambda'_1,\phi'_2)\Delta\varrho$, and so on. Equation 67 is the general model that relates the observations to the parameters.

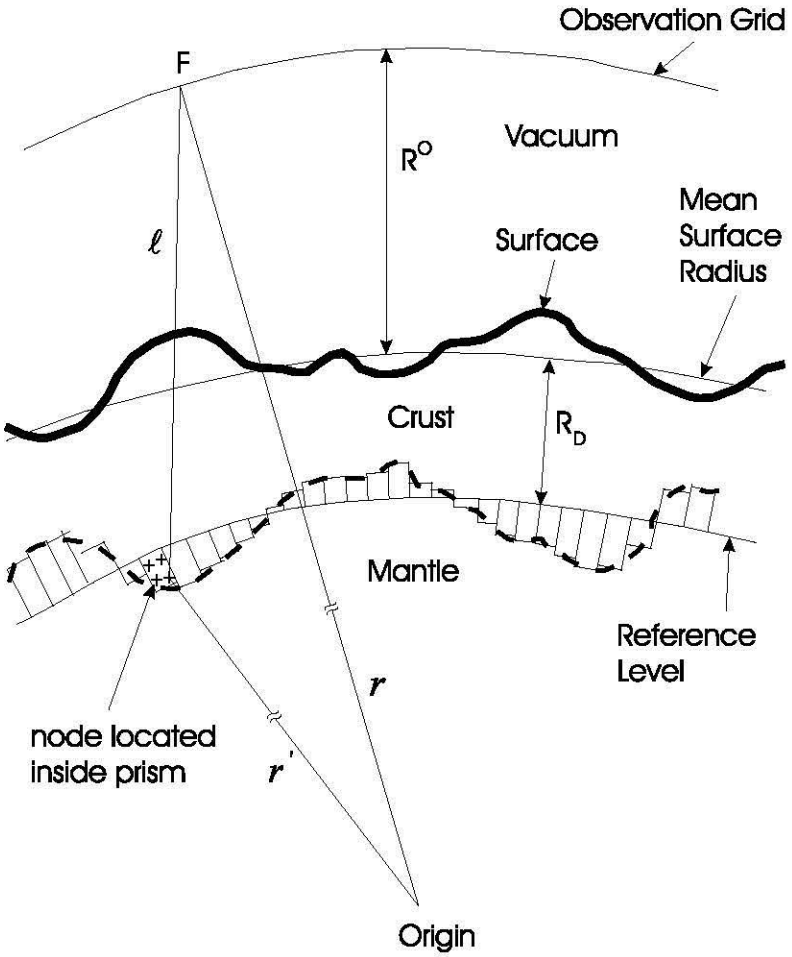

Figure 51: Section showing the geometry of the inverse problem for modeling spherical prisms by GLQ integration. The spherical prism tops approximate the Moho undulation and the bottoms are located at the reference level at a depth R_D below the mean surface radius. The major density boundaries shown are the surface (solid thick line) and the Moho boundary (dashed line).

D.2.1 The Gauss-Markov Model (GMM)

The Gauss-Markov Model (GMM) is used in a least squares adjustment procedure for observation equations and defined as (Koch, 1987)

$$\Delta y_{n\times 1} = y^o_{n\times 1} - y^c_{n\times 1} = \mathbf{A}_{n\times u}\Delta\xi_{n\times 1} + e_{n\times 1} \tag{68}$$

where $y^o_{n\times 1}$ is the vector of the observed anomaly field, $y^c_{n\times 1}$ is the calculated anomaly field, vector $\Delta\xi_{u\times 1}$ contains increment estimates of the radial dimension for each prism, $e_{n\times 1}$ is the error vector that contains inaccuracies of the observations and modeling errors, n is the total number of observations, and u is the total number of unknowns. The subscripts denote the array dimension. The coefficients of $\mathbf{A}$ are completely determined from the known geometry of the observation point and mass nodes. The dispersion matrix $D\{y_{n\times n}\} = \sigma_0^2\mathbf{P}^{-1}_{n\times n}$, where $\mathbf{P}$ is the weight matrix and σ_0^2 is unknown (Koch, 1987). For this study, the dispersion matrix is set to $\mathbf{I}_{n\times n}$.

The GLQ model given by equation 67 is non-linear in radial dimension of the spherical prisms. In particular, the node locations are dependent on the distance ℓ. Furthermore, the GMM assumes that the observations are represented by a linear combination of the parameters. However, the problem can be linearized by a Taylor series expansion around the initial (approximate) model parameter vector ξ^0 and ignoring higher order terms (Mikhail and Ackerman, 1976), as follows

$$F(\xi^0) + \frac{\partial F(\xi)}{\partial \xi}\Big|_{\xi=\xi^0}\Delta\xi = 0 \tag{69}$$

where $F(\xi)$ denote the non-linear function given by equation (67) and ξ is the vector of unknowns and $\Delta\xi$ is the parameter incremental vector.

The coefficient matrix $\mathbf{A}$ contains partial derivatives that are computed by differentiating $F(\xi)$ with respect to the model parameters. However, the analytical differentiation of equation (67) with respect to the prism node locations yields lengthy expressions. Hence, the Jacobian can be calculated simply by using prisms of unit thickness. The initial values of the model parameters are then improved iteratively based on the differences between observed and calculated anomaly fields (Mikhail and Ackerman, 1976).

The unknown parameters in the GMM can be estimated by the method of least squares so that the sum of squares of the residuals is minimized. The target function (Koch, 1987) can be written as (and omitting subscripts)

$$\Phi(\Delta\xi) = (\Delta y - \mathbf{A}\Delta\xi)^T(\Delta y - \mathbf{A}\Delta\xi) \doteq min_{\Delta\xi} \tag{70}$$

with Euler-Lagrange necessary Conditions as

$$\frac{1}{2}\frac{\partial\Phi}{\partial\Delta\xi} = -(\mathbf{A}^T\Sigma_y^{-1}\mathbf{A})\Delta\xi + \mathbf{A}^T\Delta y \doteq 0 \tag{71}$$

and proof of Sufficiency as

$$\frac{1}{2}\frac{\partial^2\Phi}{\partial^2\Delta\xi} = \mathbf{A}^T\mathbf{A} \Rightarrow pos.def \tag{72}$$

so that the estimated parameters are given by the normal equations

$$\mathbf{A}^T\mathbf{A}\Delta\hat{\xi} = \mathbf{A}^T\Delta y \tag{73}$$

and the error variance co-variance matrix for the estimated parameters is

$$\Sigma_{\Delta\hat{\xi}} = (\mathbf{A}^T\mathbf{A})^{-1}. \tag{74}$$

The solution of the normal equations can be obtained by the Choleski algorithm. In theory, $\left(\mathbf{A}^T\mathbf{A}\right)_{u\times u}$ is a positive, definite symmetric matrix and by replacing the matrix $\left(\mathbf{A}^T\mathbf{A}\right)_{u\times u}$ by its Choleski factorization $\left(\mathbf{R}^T\mathbf{R}\right)_{u\times u}$ permits rapid and efficient processing of the systems of equations for the least squares estimate of $\Delta\xi$. The matrix $\mathbf{R}$ is an upper triangular matrix so that $\left(\mathbf{A}^T\mathbf{A}\right)_{u\times u} = \left(\mathbf{R}^T\mathbf{R}\right)_{u\times u}$ (Lawson and Hanson, 1974).

D.2.2 Adjustment with Special Constraints

Without changing the expected value of the observations, the unknown parameters can undergo a scale change by shifting the observation grid or the reference level. To overcome this datum defect of the free adjustment, the observation grid and the source grid are fixed at an elevation R^0 (typically at 100-km altitude for lunar studies) above the mean surface radius and at a depth R_D below the mean surface radius, respectively. R_D is a calibrated reference depth that is based on seismic data and a global crustal thickness model (Zuber et al., 1994).

In theory, the linear systems can be singular only if the source points and observation points are specified at the same locations whereas in practice, singularity or near-singularity may be introduced by various factors including errors in specifying the variables used to compute the coefficients in $\mathbf{A}$, or improper scaling of these computations where the significant figures of the variables are only partially accounted for within the computer's working precision (von Frese et al., 1988). The model given by equation (67) is under-determined. In particular, the coefficient matrix $\mathbf{A}_{n\times u}$ has rank $q < u$. Each observation requires two node locations.

The parameters in the under-deterimed model (i.e., model not of full rank) are not estimable without bias. Hence, a linear transformation of parameters into estimable functions is called reparameterization or projection (Koch, 1987). The relation between the original parameters and the projected parameters is related by means of constraints. A linear transformation of parameters $\Delta\xi$ into an estimable function (Koch, 1987) is given by

$$\Delta\xi_p = (\mathbf{A}^T\mathbf{A})^-\mathbf{A}^T\mathbf{A}\Delta\xi \tag{75}$$

and the best linear unbiased estimator $\Delta\hat{\xi}_p$ of $\Delta\xi_p$ is obtained by

$$\Delta\hat{\xi}_p = (\mathbf{A}^T\mathbf{A})^-\mathbf{A}^T\mathbf{A}(\mathbf{A}^T\mathbf{A})^-\mathbf{A}^T\Delta y = (\mathbf{A}^T\mathbf{A})^-\mathbf{A}^T\Delta y \tag{76}$$

where $(\mathbf{A}^T\mathbf{A})^-$ is a generalized inverse of $\mathbf{A}^T\mathbf{A}$ and the covariance matrix is given by $\Sigma_{\Delta\hat{\xi}_p} = \sigma_0^2(\mathbf{A}^T\mathbf{A})^-\mathbf{A}^T\mathbf{A}((\mathbf{A}^T\mathbf{A})^-)^T$.

By introducing

$$(\mathbf{A}^T\mathbf{A})^-_{rs} = (\mathbf{A}^T\mathbf{A})^-\mathbf{A}^T\mathbf{A}((\mathbf{A}^T\mathbf{A})^-)^T \tag{77}$$

as a symmetrical reflexive generalized inverse of $\mathbf{A}^T\mathbf{A}$ (Koch, 1987), the best linear unbiased estimate of the parameters is obtained by

$$\Delta\xi_p = (\mathbf{A}^T\mathbf{A})^-_{rs}\mathbf{A}^T\Delta\xi. \tag{78}$$

The matrix $(\mathbf{A}^T\mathbf{A})^-\mathbf{A}^T\mathbf{A}$ of equation 75 is a projection operator. Hence the projections of equation 78 are $u-q$ constraints that facilitate an unbiased estimation of the parameters (Koch, 1987).

The generalized inverse is not unique, however, and arbitrarily many projections can be introduced to define the estimable function. Rank deficiencies can be overcome by introducing constraints on the parameters that take the general form of

$$\mathbf{K}\Delta\xi = z_0 \quad , \quad with \;\; e \sim (0, \sigma_0^2 P^{-1}) \tag{79}$$

where e is the noise vector and z_0 is the vector containing the pseudo observations.

Introducing the target function as

$$\Phi(\Delta\xi, \lambda) = (\Delta y - \mathbf{A}\Delta\xi)^T(\Delta y - \mathbf{A}\Delta\xi) + 2\lambda^T\mathbf{K}\Delta\xi \doteq min_{\Delta\xi} \tag{80}$$

with Euler-Lagrange necessary conditions as

$$\frac{1}{2}\frac{\partial\Phi}{\partial\Delta\xi} = -\mathbf{A}^T(y - \mathbf{A}\Delta\xi) + \mathbf{K}^T\lambda \doteq 0 \tag{81}$$

$$\frac{1}{2}\frac{\partial\Phi}{\partial\lambda} = \mathbf{K}\Delta\xi \doteq 0 \tag{82}$$

and proof of Sufficiency as

$$\frac{1}{2}\frac{\partial^2\Phi}{\partial^2\Delta\xi} = \mathbf{A}^T\mathbf{A} \Rightarrow pos.def, \tag{83}$$

the estimated parameters are given by the normal equations

$$(\mathbf{A}^T\mathbf{A} + \mathbf{K}^\mathbf{T}\mathbf{K})_{u\times u}\Delta\hat{\xi}_{u\times 1} = (\mathbf{A}^T\Delta y)_{n\times 1}. \tag{84}$$

where $\mathbf{K}_{(u-q)\times u}$ is the matrix of special constraints. There are infinitely many choices of constraints so that $\mathbf{K}$ can take any form (Koch, 1987). The suitable choice of constraints will be investigated in the next section by sensitivity analysis.

D.2.3 Sensitivity Analysis and Performance

In lithospheric applications in general, a myriad of singularity parameters related to the inverse distance function between sources and anomaly observation may combine to influence the stability of

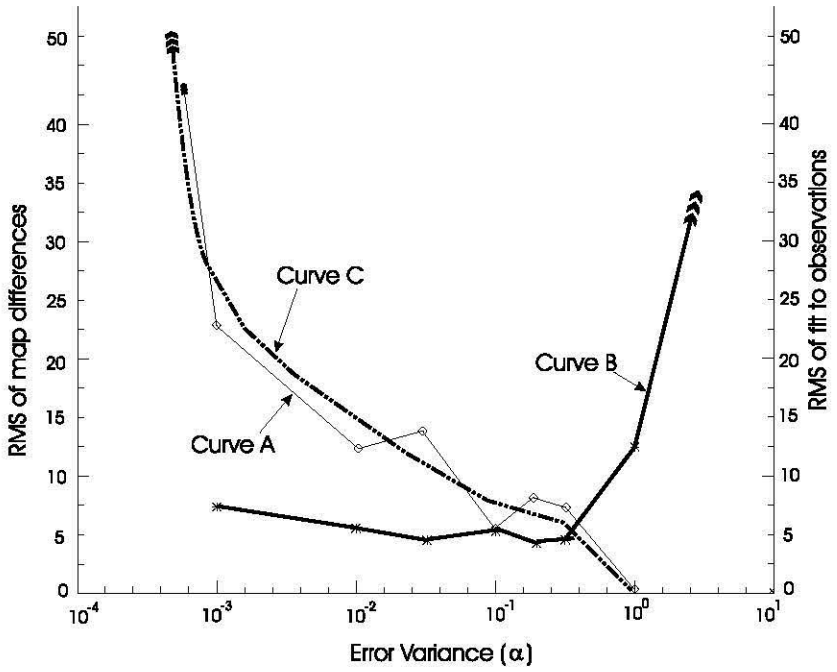

Figure 52: Error variance (α) spectra derived from the solution of gravity anomalies over Mare Orientale produced by the inversion.

the inversion so that by imposing a constraint whereby retaining the smaller, problematic eigenvalues and weighting them by the addition of a small positive constant, obtains a solution which satisfies the data. In this way the variance of the solution is reduced and the estimation is stabilized (von Frese et al., 1988). Re-writing equation (84) for a constraint (damped) least-squares solution (von Frese et al., 1988) as follows;

$$\Delta\xi = (\mathbf{A}^T\mathbf{A} + \alpha\mathbf{I})^{-1}\mathbf{A}^T\delta y \tag{85}$$

where the error variance or damping factor (α) is a scalar and $\mathbf{I}_{u\times u}$ is the identity matrix. A straightforward procedure is to estimate the optimal value of the error variance (α) as a function of the rms of the misfit. Sensitivity analysis will be performed on a $64\,\mathrm{deg}\times 64\,\mathrm{deg}$ region centered over the Mare Orientale basin. The basin was selected because its was extensively studied for its crustal properties (e.g., Neumann et al., 1996; von Frese et al., 1997b; Arkani-Hamed, 1998).

The observation vector y contains the annihilating gravity anomalies (*CTGE*) evaluated at 100 km above the mean surface radius, the vector ξ $(= \xi^o + \Delta\xi)$ contains estimates of the Moho undulation, and assuming a crust-mantle density contrast of 0.5 g/cm^3 and a depth of 64 km (eg., Zuber et al., 1994).

Figure 52 shows the error variance (α) spectra from inversion. The left ordinate axis shows the rms of map differences and the right ordinate axis shows the rms fit of the observation given by

Curve A of Figure 52 gives the behaviour of the sum of squared residuals (SSR) between the predicted gravity anomalies at $\alpha = 1.0$ and the anomaly maps from solutions obtained using smaller positive values of the error variance. This curve exhibits relatively good definition of the range of error

variance for which the solutions are underdamped.

Curve B represents the variation of the sum of squared residuals (SSR) between the observations and the models of the data predicted by various nonzero values of α. As the error variance is increased, the predictions become unstable so that the sharp rise in the curve for all $\alpha > 10^0$ provides a fairly straightforward indicator of the range of error variance for which the solutions are overdamped.

Curve C is a best fit curve through the points of Curve A. After the initial sharp gradient of Curve C, the flattened gradient between 10^{-1} and 10^0 is an indicator of the range of error variance which may be required to stabilize the underdamped solution.

The results of Curves A, B and C suggests an optimal range of error variance (1×10^{-1} to 6×10^{-1}) for obtaining gravity anomalies by equivalent point source inversion. The suitability of the inversion to produce a Moho undulation model is investigated in the next subsection.

D.2.4 Estimating Surface Undulation

Starting with initial prisms of unit thicknesses, each iteration performs corrections to the radial dimension of the spherical prisms. Using the improved estimates for prism thicknesses, an updated anomaly field (y^c) is computed by the forward model according to equation (67). The inversion scheme iteratively improves on an initial estimate until the solution convergences. The process is repeated until convergence is reached i.e., when the correlation between the y^c and y^o and the observed data approaches 1.0 and the rms fit is less than the error limit of the data.

Figure (53) shows the Moho prediction based on the least squares inversion with $\alpha = 0.1$. The gravity effects of the estimated Moho matched more than 99 % of the annihilating anomalies with 0.04 mGals standard error where the standard error (Davis, 1986) is

$$S_e = \sqrt{\frac{\sigma^2}{n}}. \tag{86}$$

The crustal thickness is obtained by subtracting the Moho undulation (i.e., Figure 53A) from the elevation data for the Orientale basin given by the GLTM-2 dataset (Smith et al., 1997). The crustal thickness has an amplitude range (AR) of [17.5 km - 127.4 km]. The 17.5 km crustal thickness for the basin center compares favorably with 21.8 km (20.1 km plus 1.7 km basalt thickness) result of Neumann et al. (1996) and $\sim$ 18 km thickness estimate of Arkani-Hamed (1998).

D.3 CPU requirement for a high resolution output

Computer limitations may influence the efficacy of inversions. For example, the scale of inversion may be simply too large for in-core procedures. For many geologic applications large-scale inversions can only be accomplished by "boot-strapping" procedures; i.e. piecing together a series of adjoining

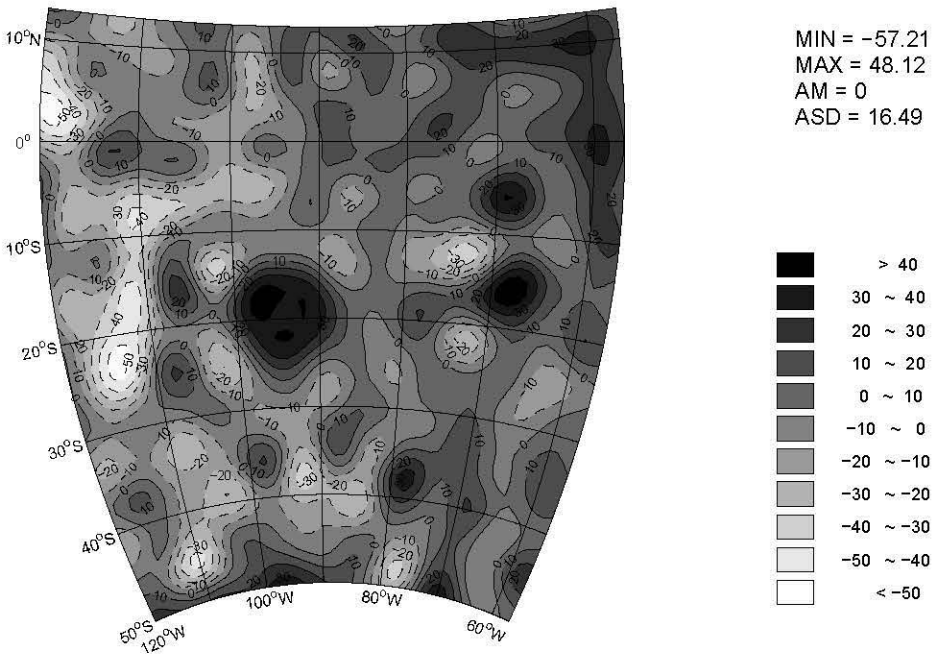

A) Moho topography for Orientale.

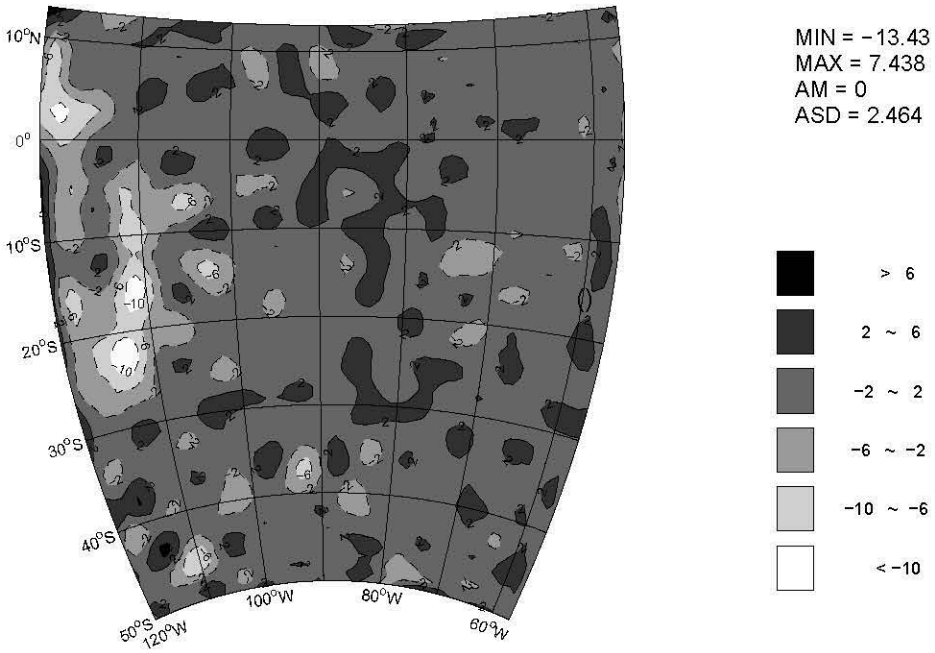

B) Residuals of least squares fit of A.

Figure 53: Results from least squares inversion based on spherical prism modeling by GLQ-integration.

or overlapping inversions on smaller regional scales (e.g., Langel et al., 1984; Ridgway and Hinze, 1986) or out-of-core procedures.

For an in-core solution on the T94 supercomputer, the upper limit for a vector length is 67108864. The formula $u \times (u+1)/2$ (von Frese et al., 1988), where u is the number of model parameters, shows that u must be 11584 or smaller. This means that the maximum dimension of the source grid can be a 107×107, 256×45, or a 128×90 grid, respectively. A near-global solution of $1\,\mathrm{deg} \times 1\,\mathrm{deg}$ source grid over a latitude range of $\pm 64^o$, requires a source grid of 128×360. This problem is too large to run an in-core solution on the Cray computer. Hence, special routines for out-of-core techniques are required.

The Cray Research Scientific Library out-of-core routines for linear algebra lets one solve problems for which it is not possible to store all the data in main memory during program execution. The central concept is based on the idea of virtual matrices stored outside the main memory and referenced through a Fortran I/O unit number.

CPU requirements for high resolution (i.e., $1\,\mathrm{deg} \times 1\,\mathrm{deg}$) inversions, based on the modeling spherical prisms by GLQ integration, for a global solution requiring out-of-core routines, are excessive. However, for lower resolution solutions, the cell size can be increased because the sources are further away (i.e., deeper) from the observation point. Hence, the number of unknowns and the CPU requirements are significantly reduced.

E Cross-sections, Gravity Profiles, and Crustal Maps

F Introduction

This Appendix shows the crustal cross-sections, gravity profiles and maps of crustal thickness and radial adjutments for the 27 basins listed in Table 2. The cross-sections and maps complement the discussions in Chapters 2 and 3 on the details of the WCA-inferred structure of the lunar crust.

The crustal cross-sections and gravity profiles are give in section F.1 and maps of crustal thickness and radial adjustment are given in section F.2.

F.1 Cross-section and Profiles

Crustal cross-sections and gravity profiles are shown in Figures 54 - 67. In each Figure, the WCA-results are plotted for two of the basins in the order that they are listed in Table 2. In each figure, features for the two basins with their corresponding subsurface cross-sections (top panels), *FAGA* components (middle panels), and *TGE* components (bottom panels) are given. For each basin, the top panel shows the crust (shaded light grey), the mantle (dark shade) and the crustal cross-section including surface topography (top solid line), Moho (dashed line) and equilibrium Moho (dot-dash line). The middle panel gives the *FAGA* (solid line), *TCFAGA* (dot-dash) and *TDFAGA*(dash) components. The bottom panel shows the *TGE* (solid), compensated TGE (dot-dash) and related compensating *TGE* (dash) components. The topography for the nearside basin and mare fill thickness are at vertical scale 5:1 and the farside basin topography and mare fill at vertical scale of 2:1.

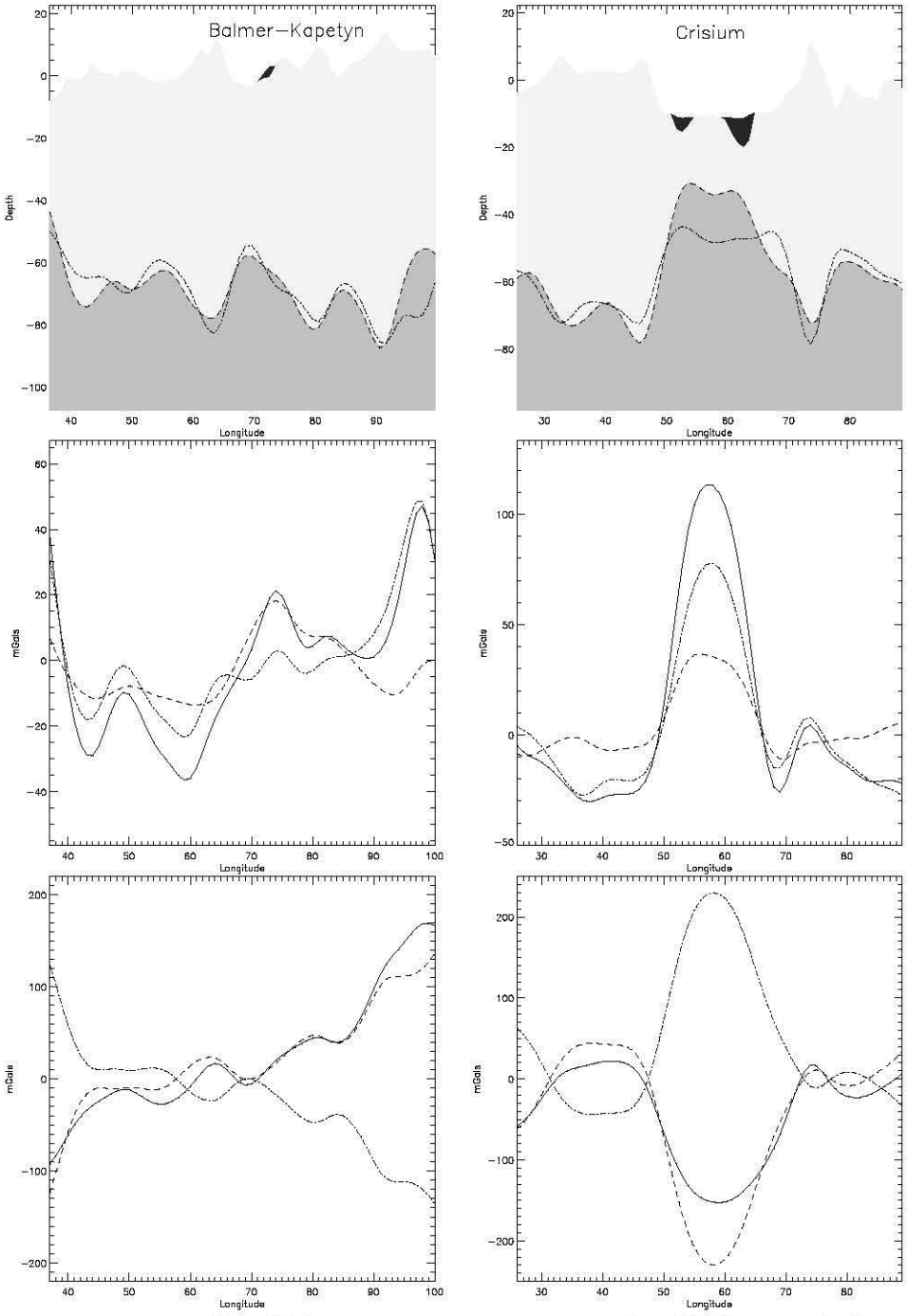

Figure 54: Crustal and gravity profiles across the nearside basins Balmer-Kapetyn (left panels) and Crisium (right panels). Vertical scale for topography and mare fill is 5:1.

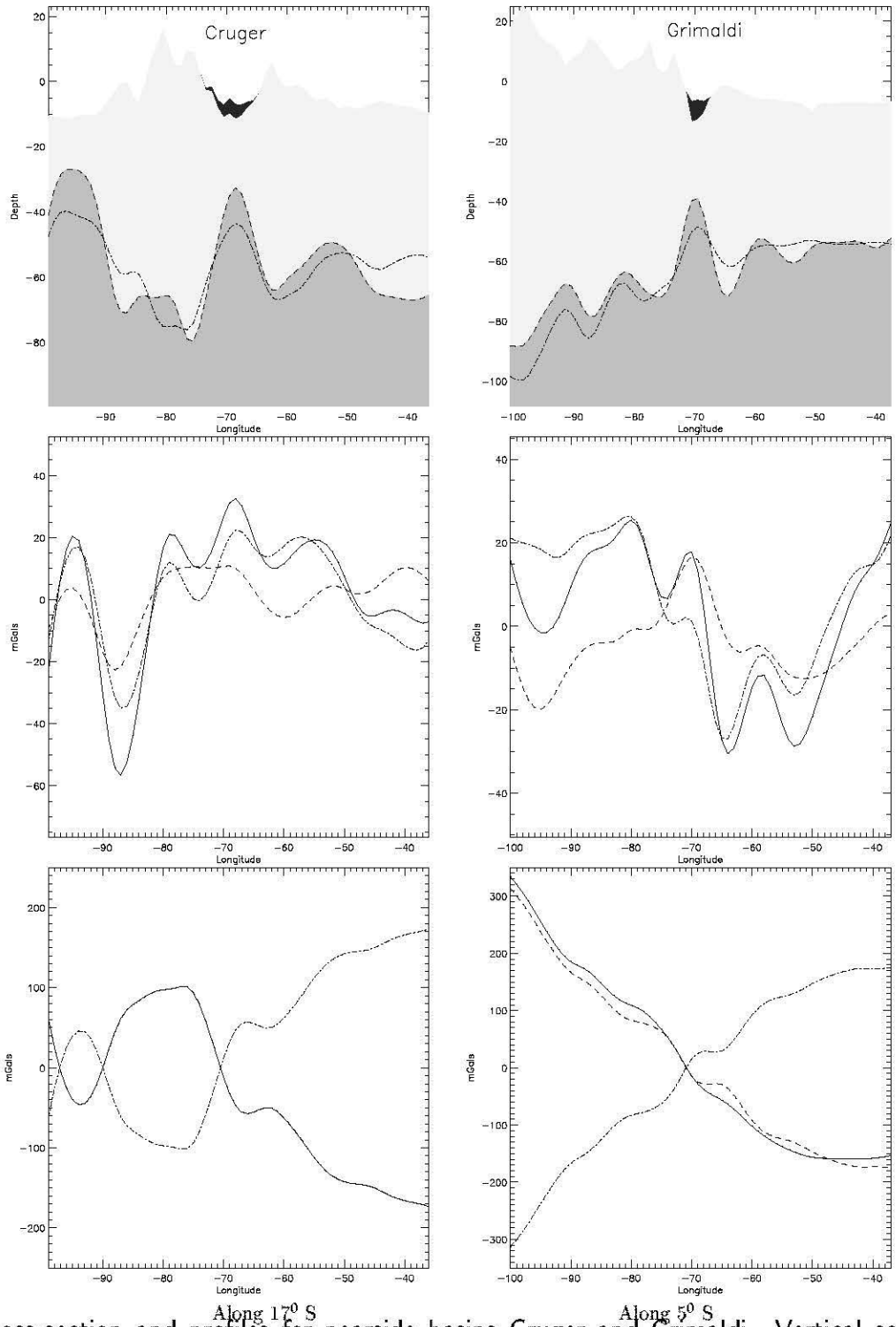

Figure 55: Cross-section and profiles for nearside basins Cruger and Grimaldi. Vertical scale for topography and mare fill is 5:1.

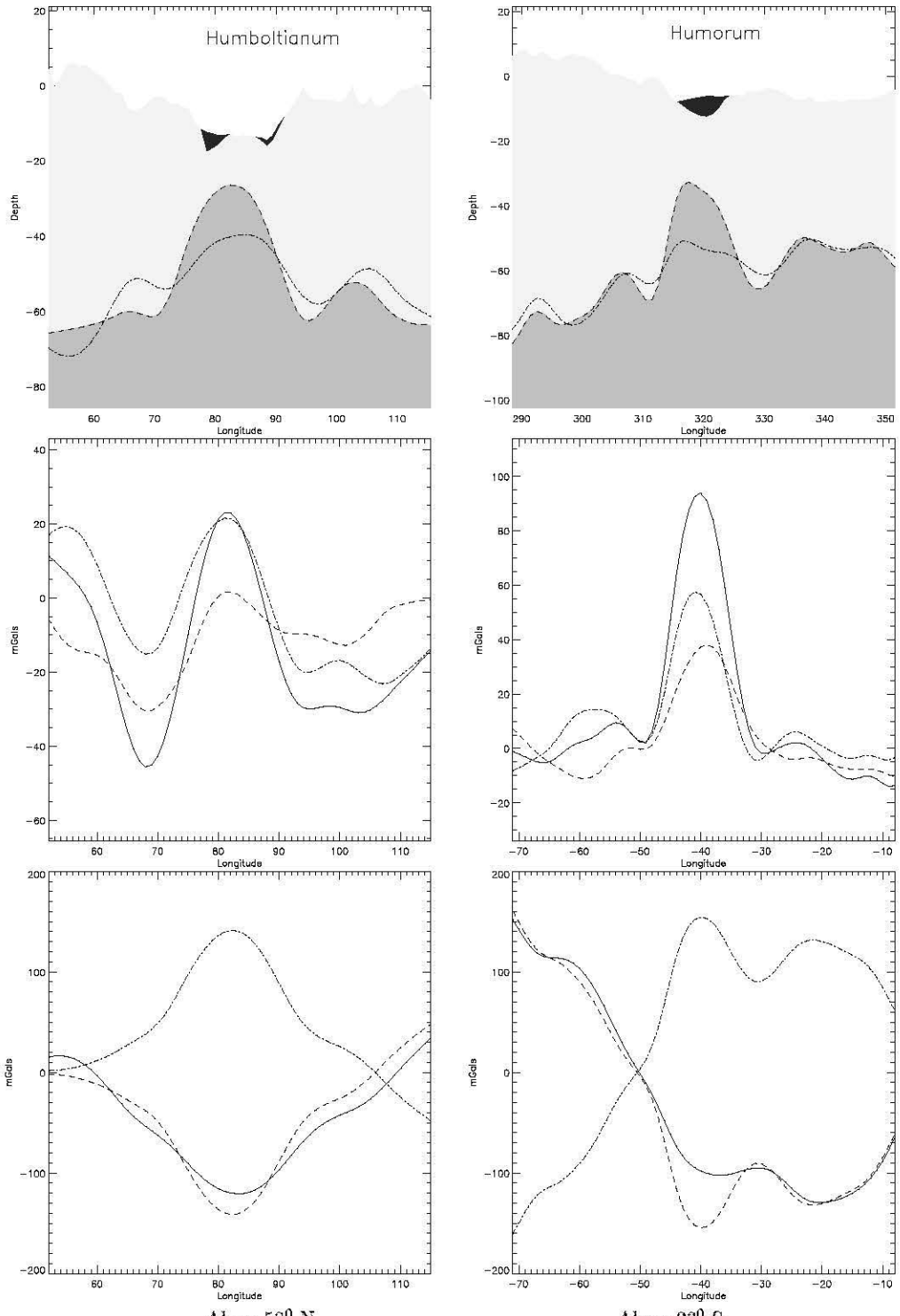

Figure 56: Cross-section and profiles for nearside basins Humboltianum and Humorum. Vertical scale for topography and mare fill is 5:1.

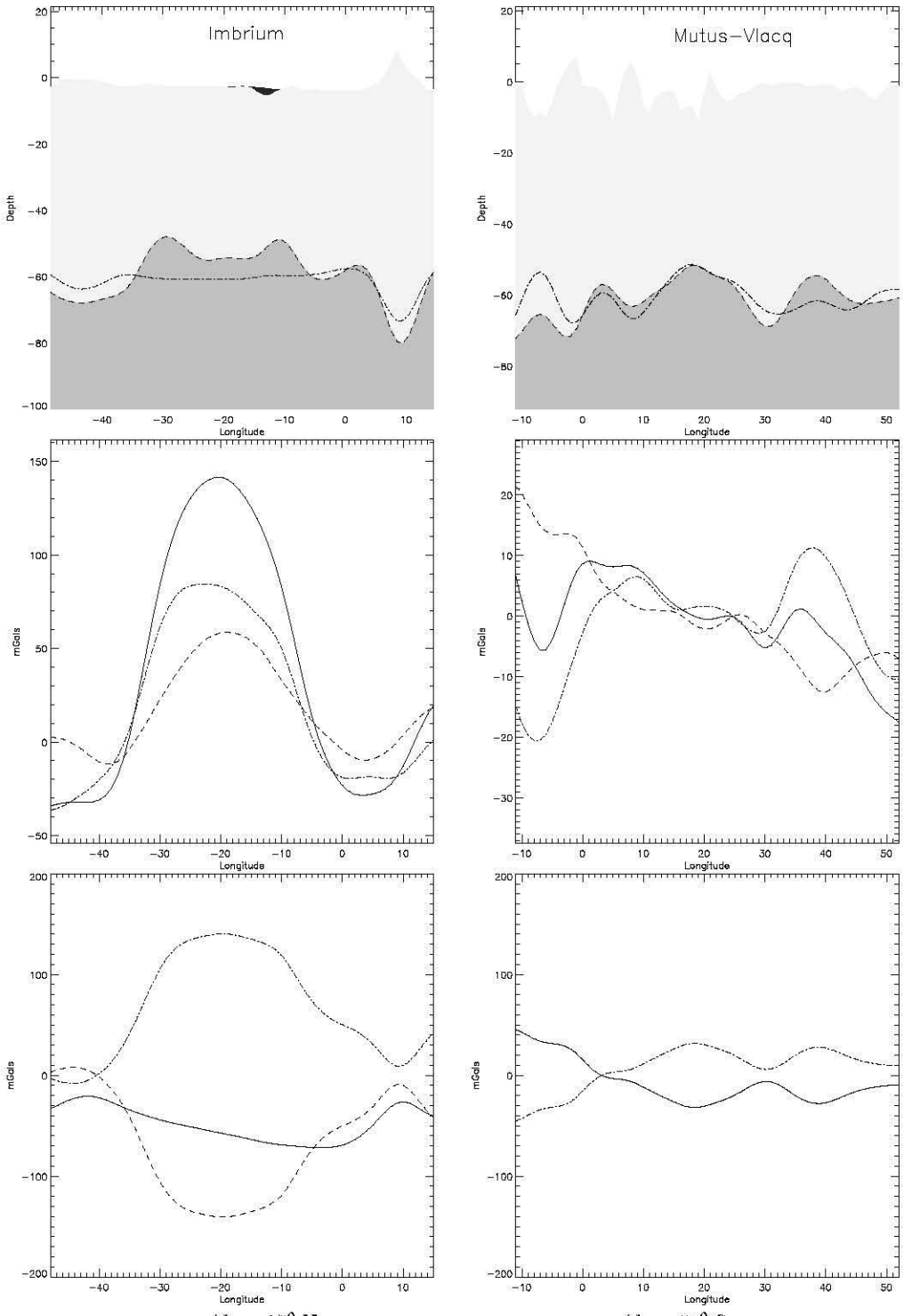

Figure 57: Cross-section and profiles for nearside basins Imbrium and Mutus-Vlacq. Vertical scale for topography and mare fill is 5:1.

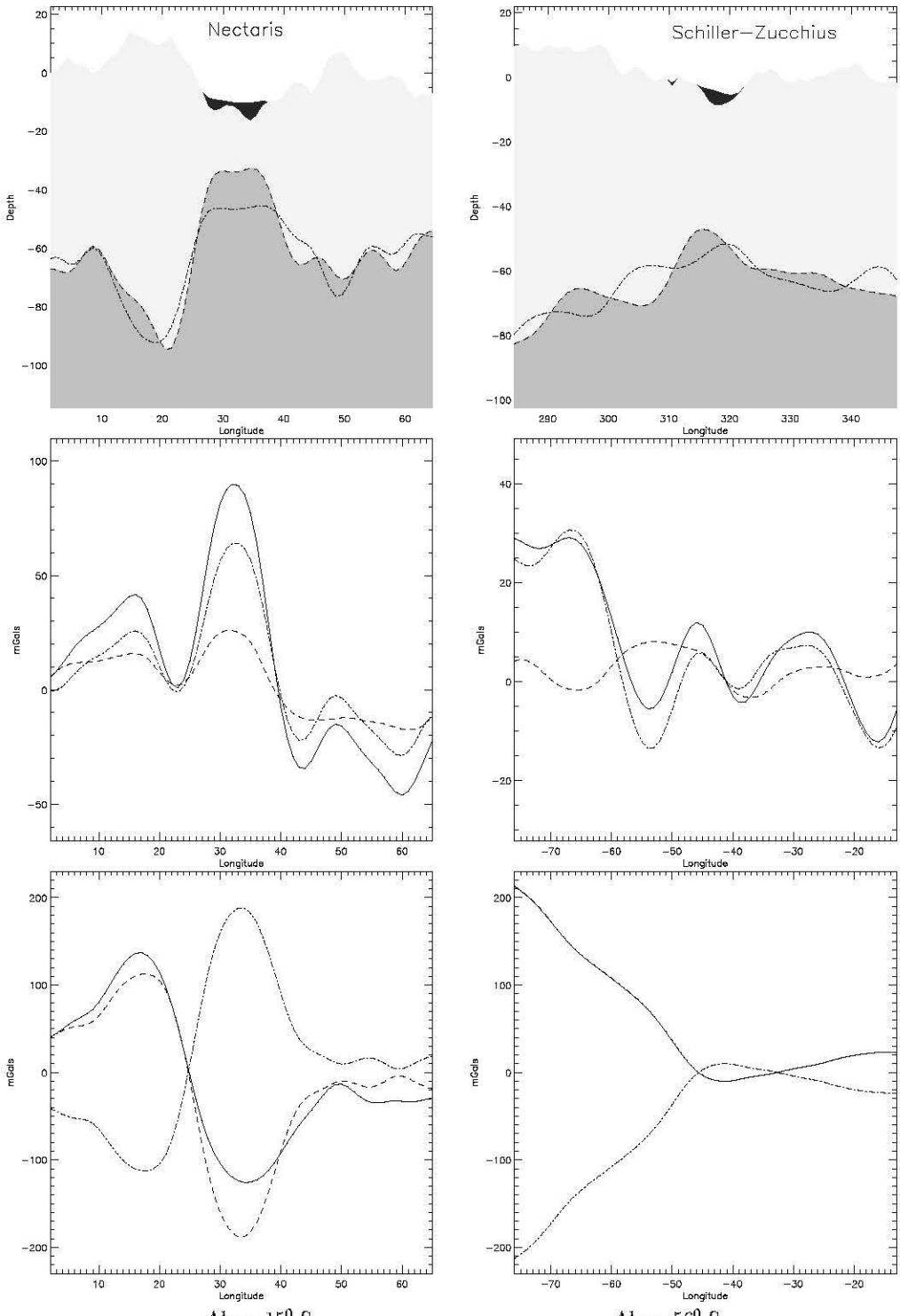

Figure 58: Cross-section and profiles for nearside basins Nectaris and Schiller-Zuchius. Vertical scale for topography and mare fill is 5:1.

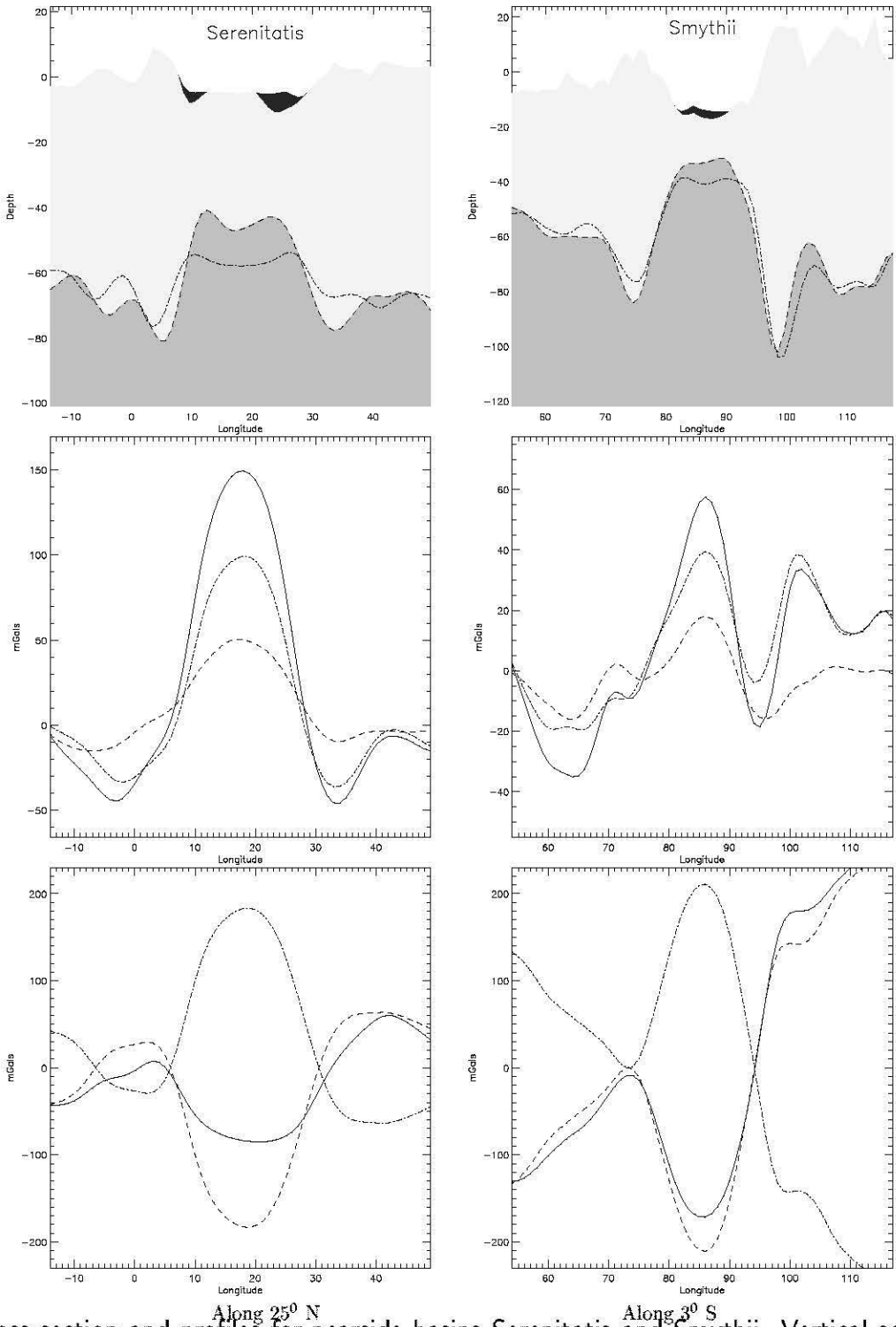

Figure 59: Cross-section and profiles for nearside basins Serenitatis and Smythii. Vertical scale for topography and mare fill is 5:1.

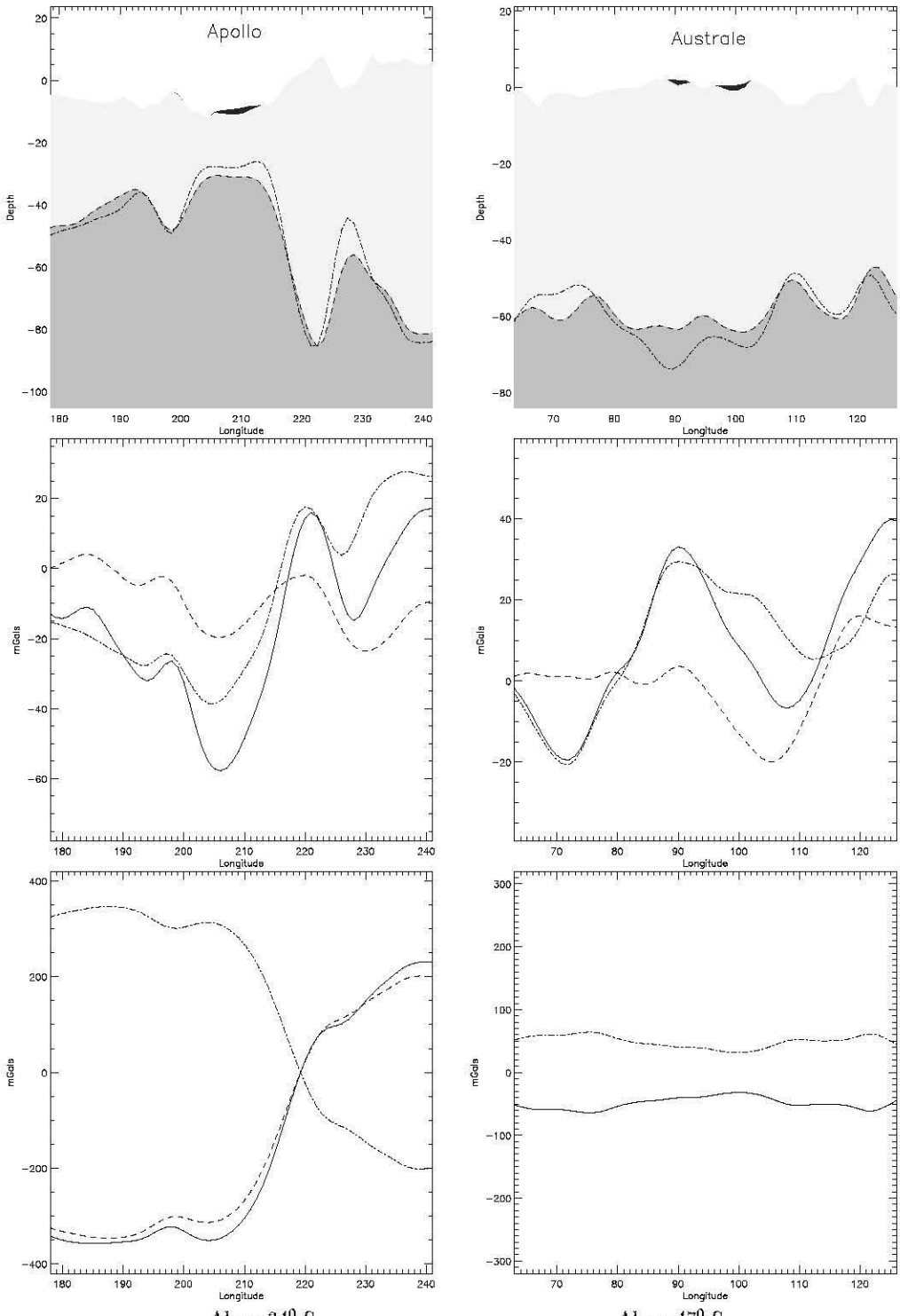

Figure 60: Cross-section and profiles for farside basins Apollo and Australe. Vertical scale for topography and mare fill is 2:1.

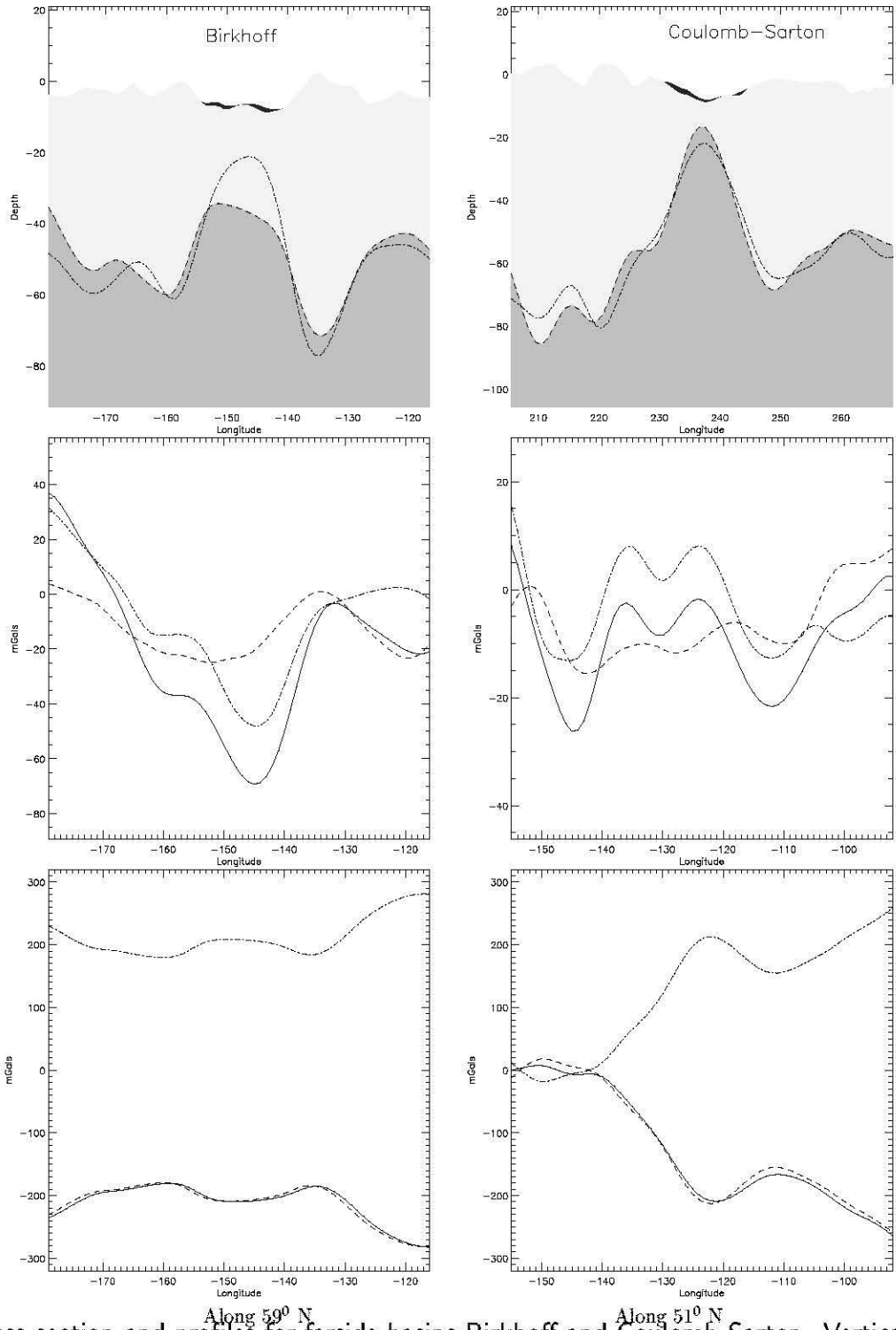

Figure 61: Cross-section and profiles for farside basins Birkhoff and Coulomb-Sarton. Vertical scale for topography and mare fill is 2:1.

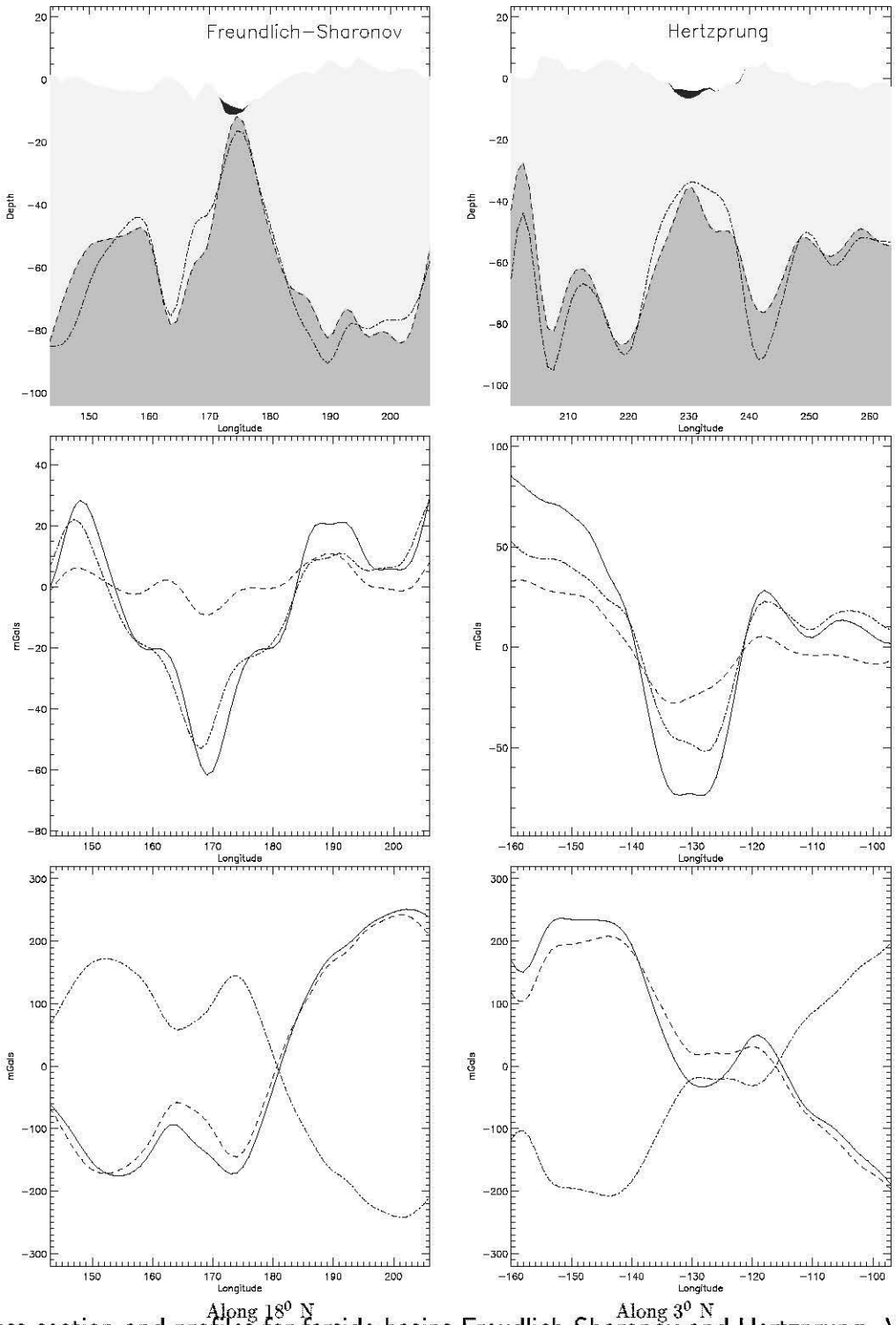

Figure 62: Cross-section and profiles for farside basins Freudlich-Sharonov and Hertzprung. Vertical scale for topography and mare fill is 2:1.

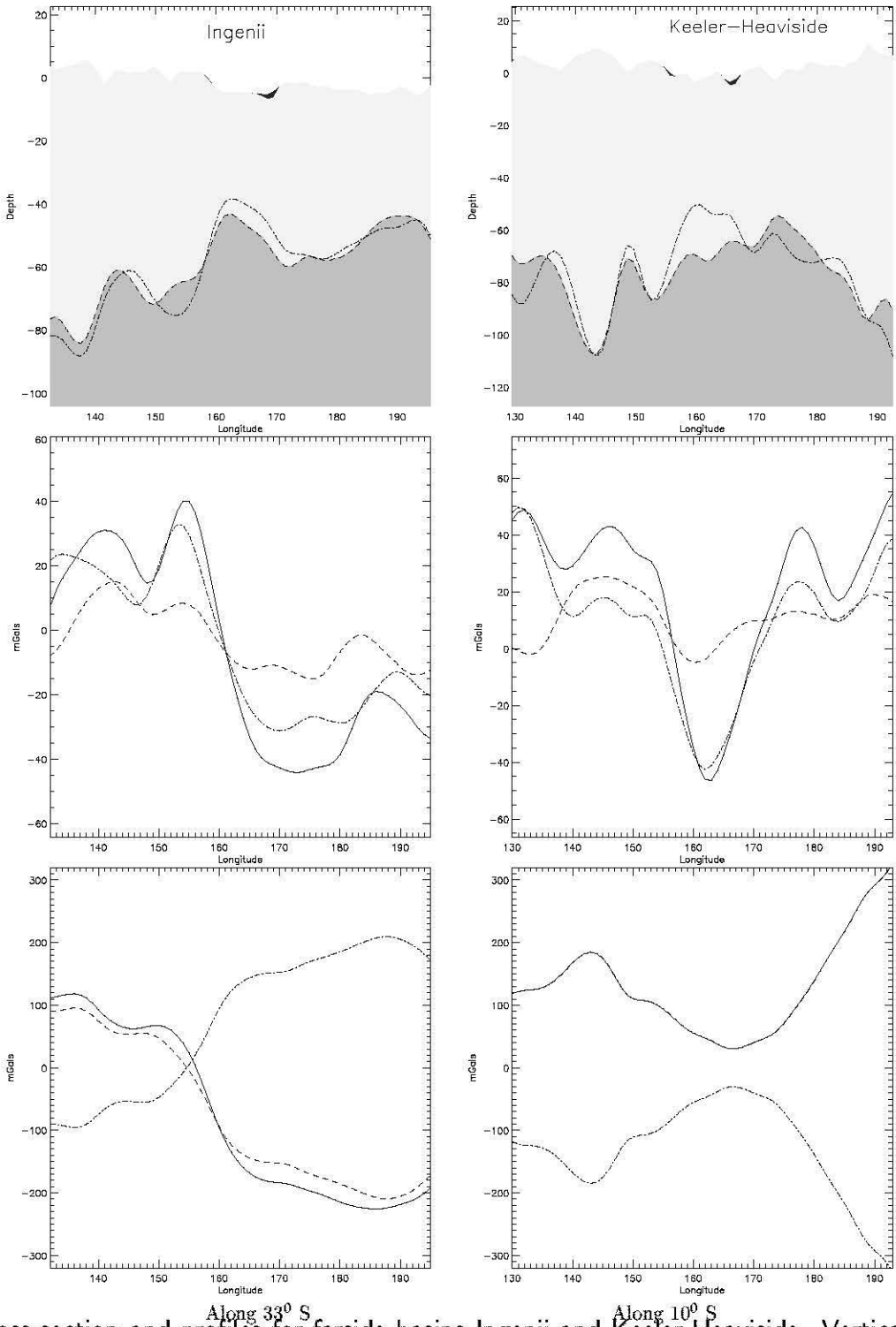

Figure 63: Cross-section and profiles for farside basins Ingenii and Keeler-Heaviside. Vertical scale for topography and mare fill is 2:1.

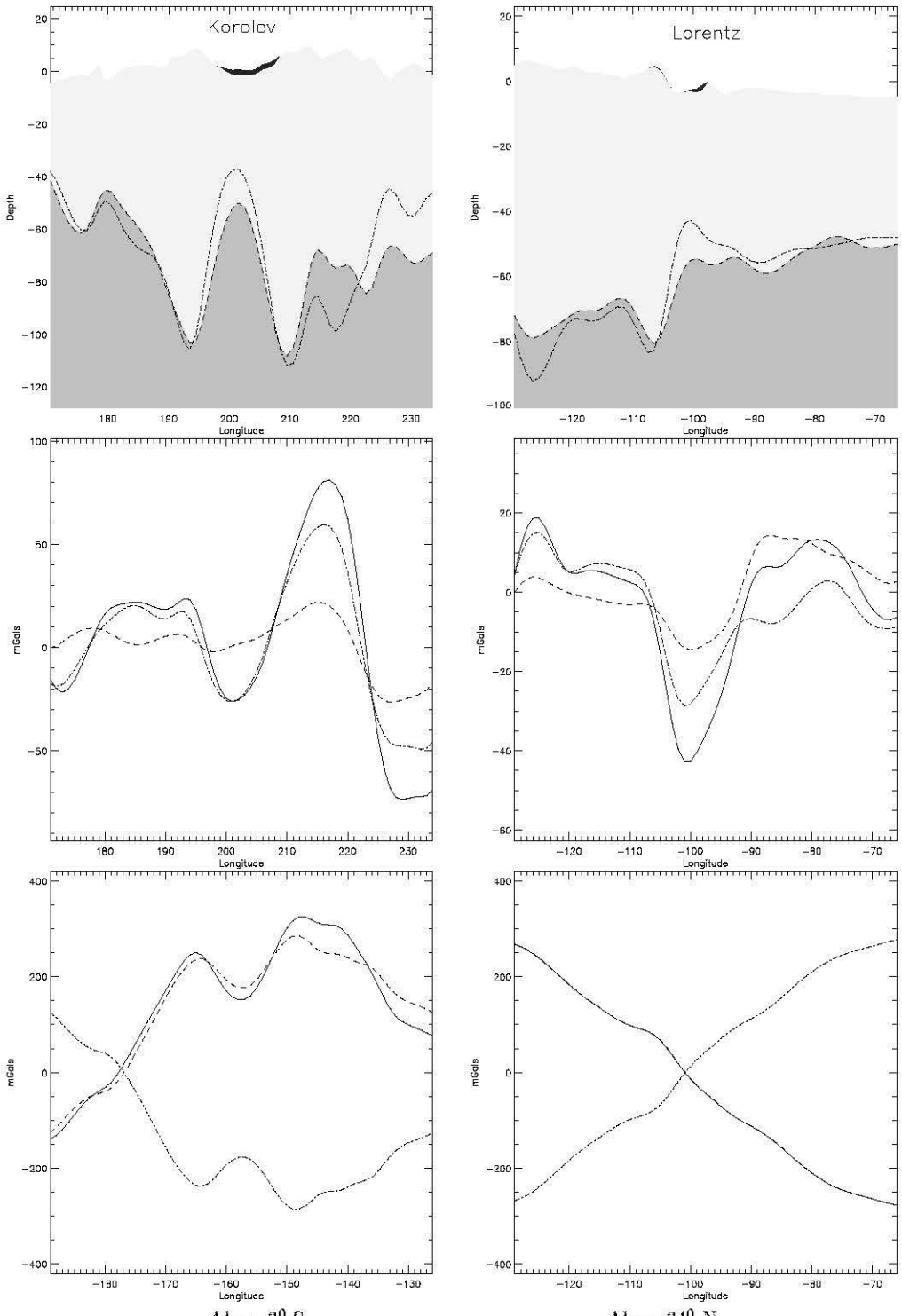

Figure 64: Cross-section and profiles for farside basins Korolev and Lorenz. Vertical scale for topography and mare fill is 2:1.

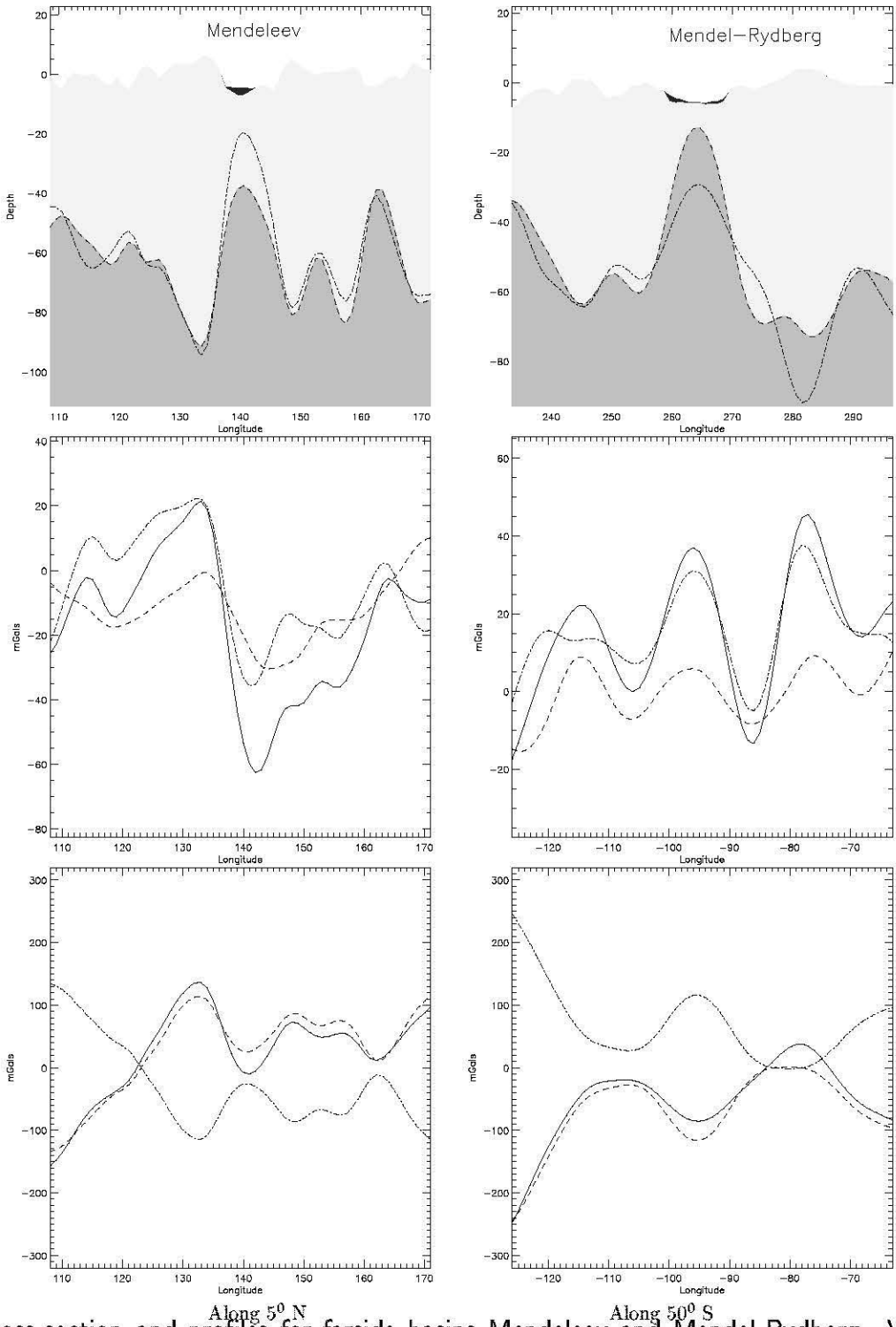

Figure 65: Cross-section and profiles for farside basins Mendeleev and Mendel-Rydberg. Vertical scale for topography and mare fill is 2:1.

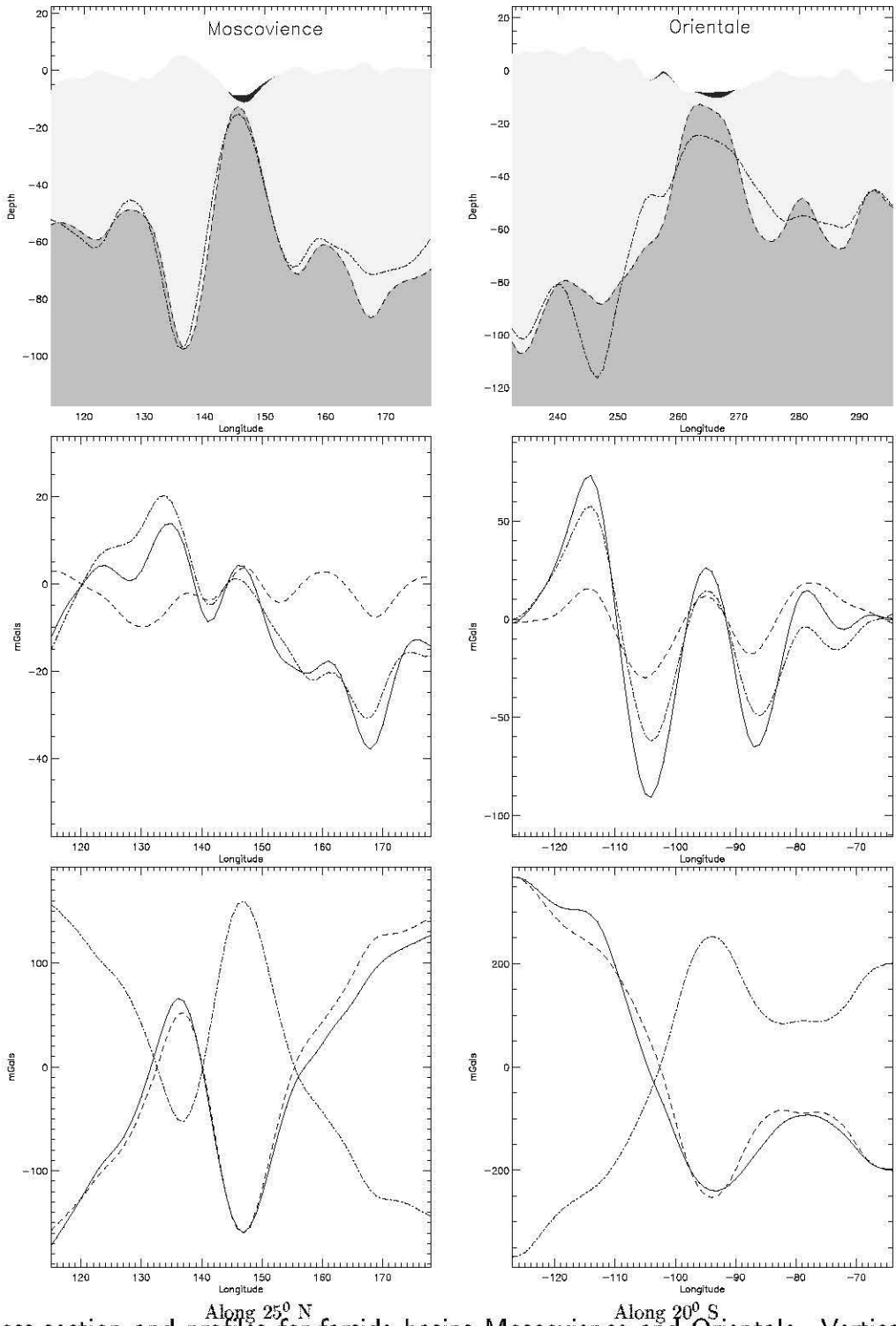

Figure 66: Cross-section and profiles for farside basins Moscovience and Orientale. Vertical scale for topography and mare fill is 2:1.

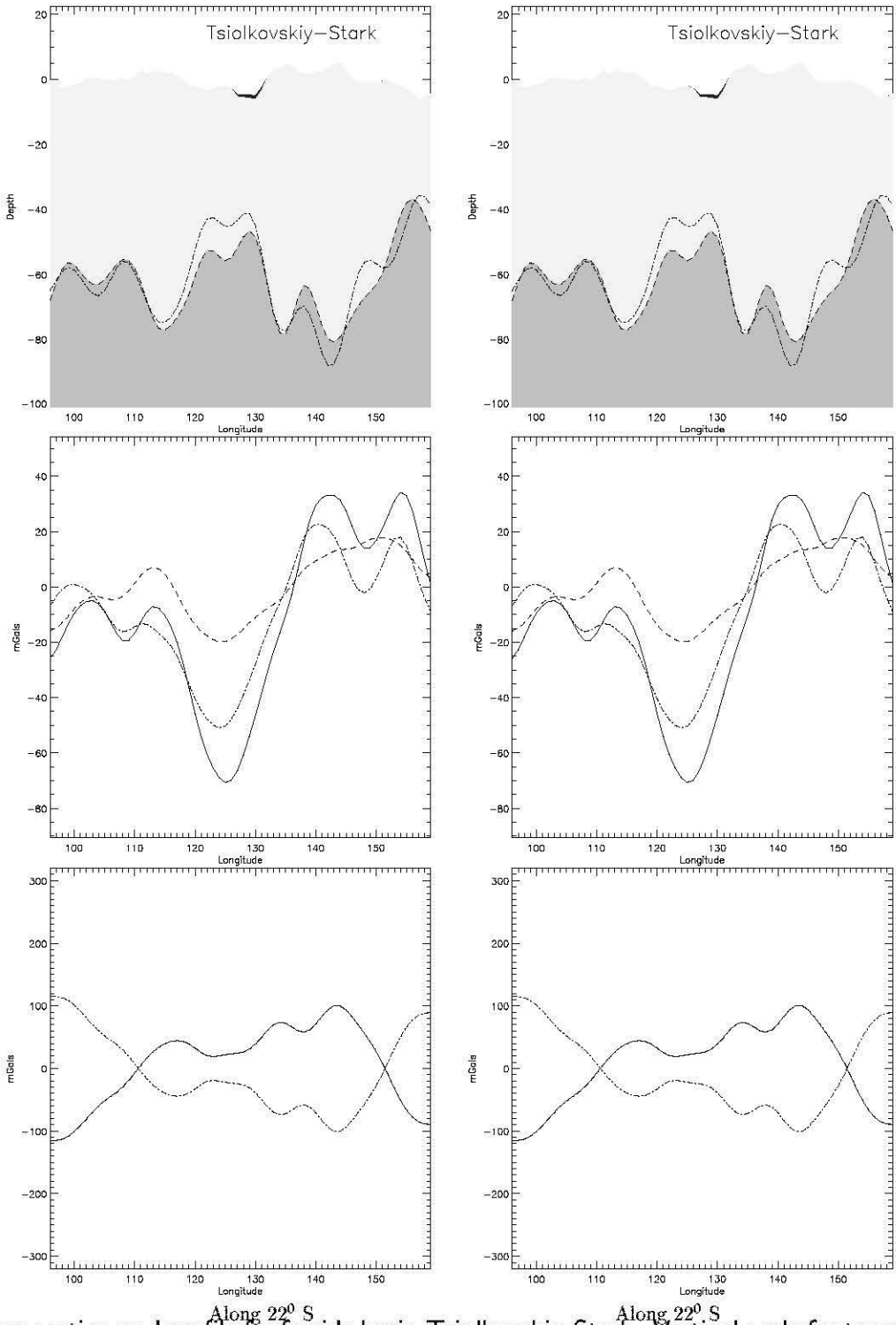

Figure 67: Cross-section and profile for farside basin Tsiolkovskiy-Stark. Vertical scale for topography and mare fill is 2:1.

F.2 Crustal Thickness and Radial Adjustment Models

Regional $64^0 \times 64^0$ maps of crustal thickness and radial adjustment for all 27 basins listed in Table 2, are given below. Each figure gives the crustal thickness models (left panels) and the radial equilibriating adjustments (right panels) for two basins. The photogeologically inferred basin rings (e.g., Solomon and Head, 1980; Wilhelms, 1987) are also shown.

A tradition established early in basin studies was to associate one of the observed rings with its excavation cavity. The excavation cavity is a feature from which material is ejected during basin formation (Spudis, 1993). However, some believe that the excavation cavity of basins which corresponds to the excavation cavity of simple craters is approximately the present basin itself, that is, the depression (Wilhelms, 1987). For example, the 900-km diameter topographic rim for Orientale is Cordillera which bounds the excavation (Wilhelms, 1987). The WCA results, supported by others, show that the original cavity may be identified with one of the interior rings. In general, the location of the topographic rim of the 27 basins of this study as defined by (Wilhelms, 1987) is not consistent when the $\sqrt{2}$D-spacing rule is applied to its WCA-estimated excavation cavity diameter.

The crustal structure of the basins appear to be azimuthally symmetric about a centrally thinned impact basin although subsequent impacts may have sligthly modified its original symmetry. All basins exhibit a centrally uplifted mantle with a flanking ring of thickened crust. The majority of this thickened crust lies within the diameter of the main topographic ring. For Serenitatis, however, the bulk of thickened crustal ring lies well beyond its 920-km topographic ring (Neumann et al., 1996).

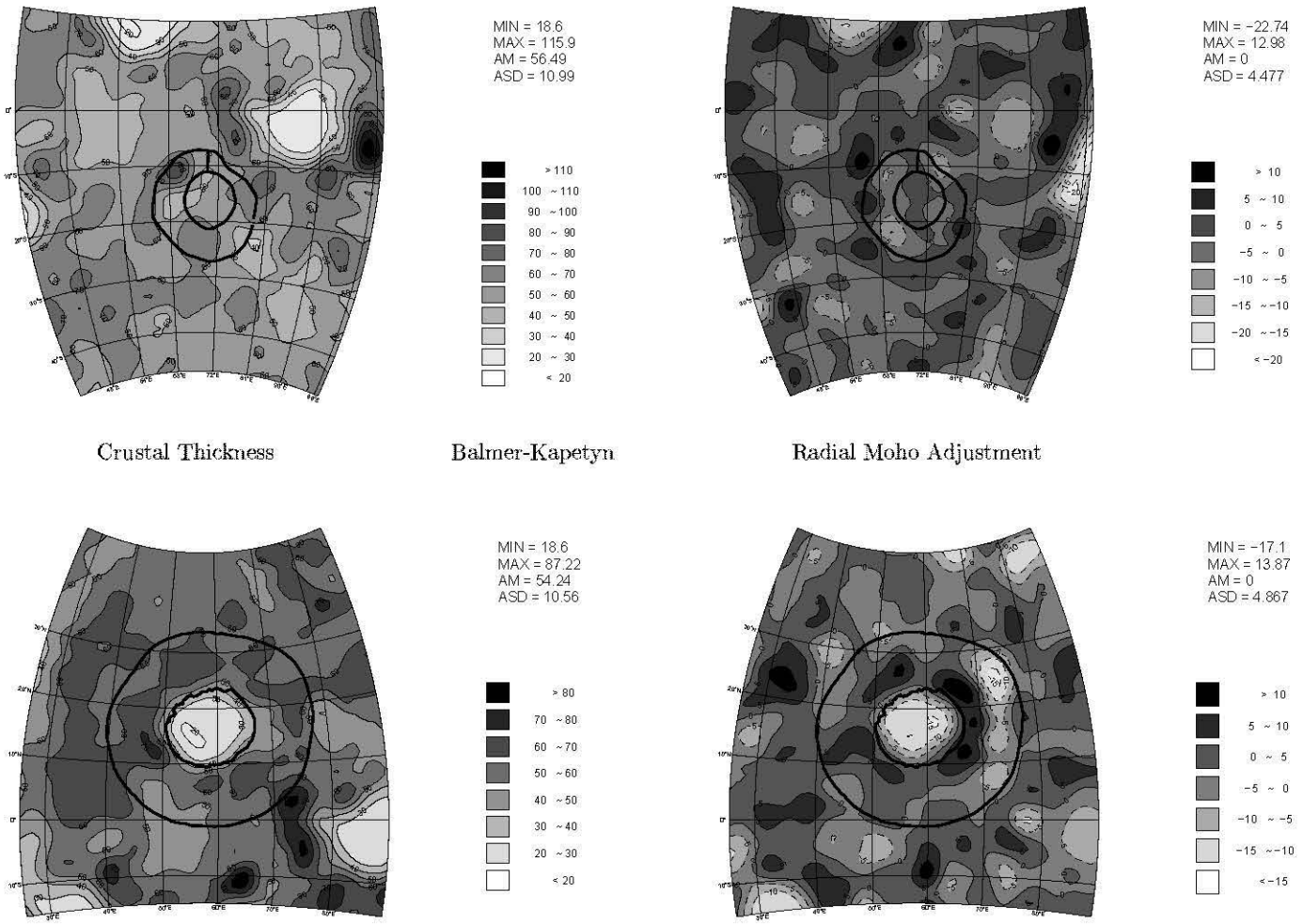

Figure 68: Crustal thickness variations (left panels) and equilibrating Moho adjustments (right panels) for the nearside basins Balmer-Kapetyn (top) and Crisium (bottom).

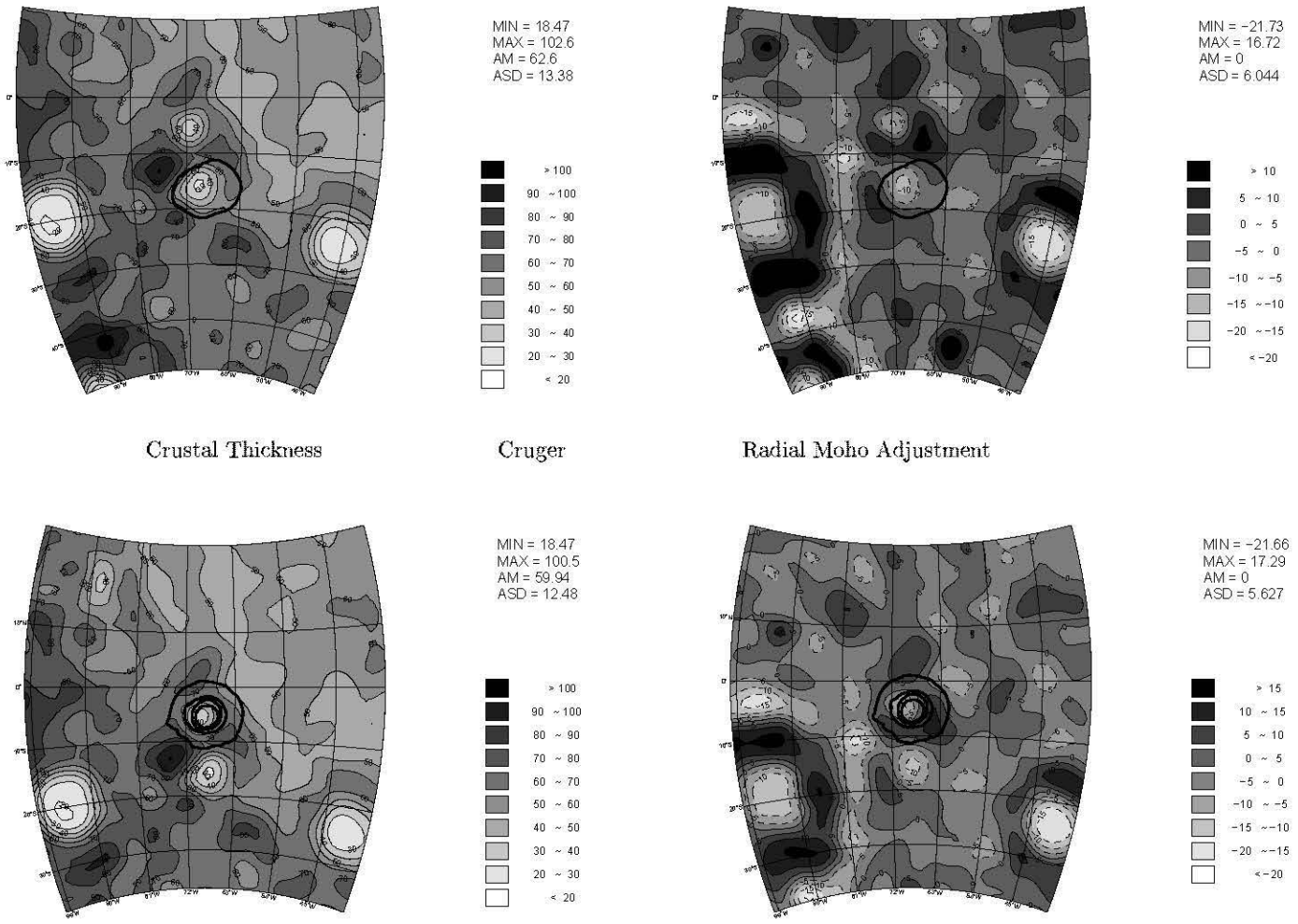

Figure 69: Crustal thickness variations (left panels) and equilibrating Moho adjustments (right panels) for the nearside basins Cruger (top) and Grimaldi (bottom).

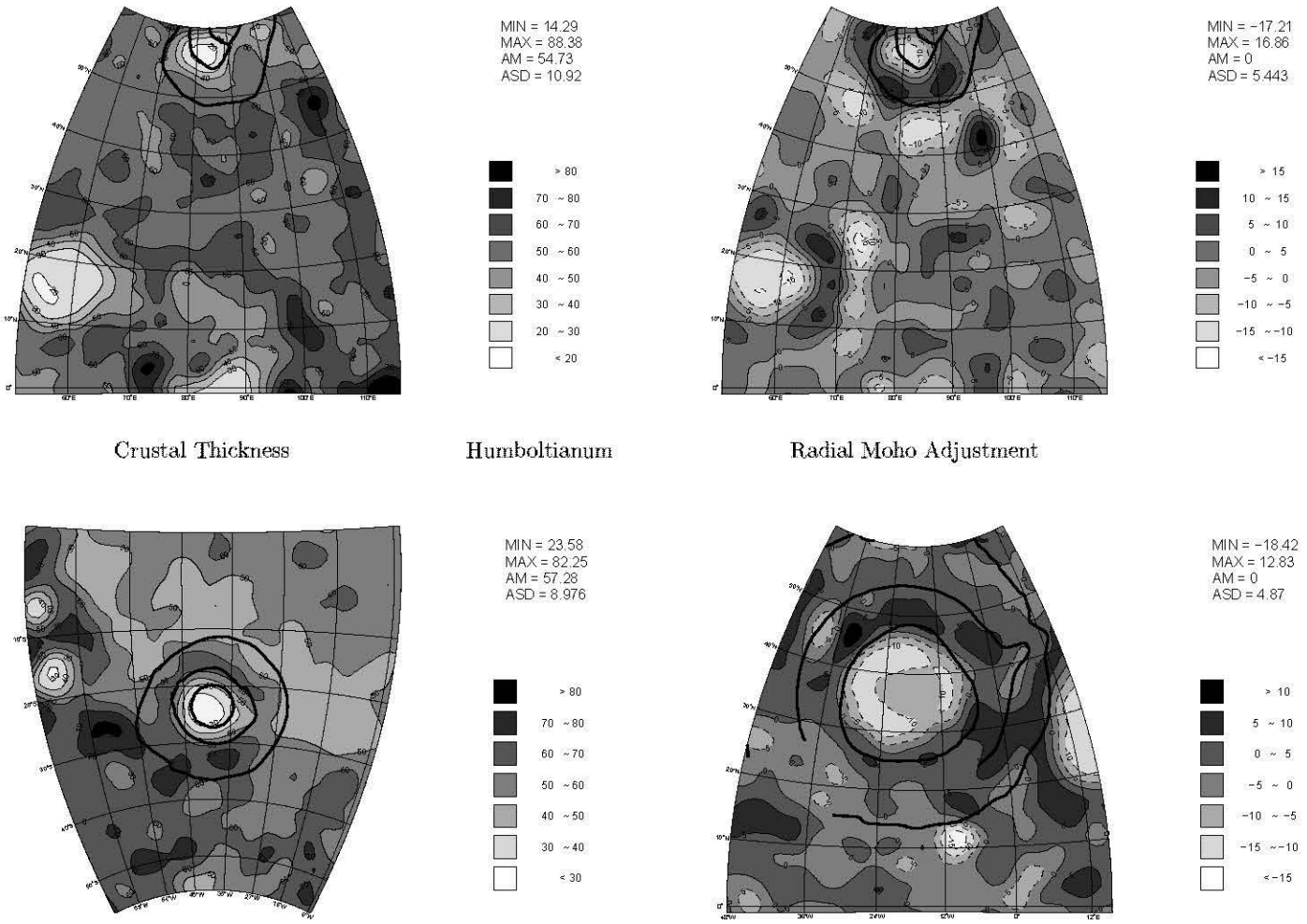

Figure 70: Crustal thickness variations (left panels) and equilibrating Moho adjustments (right panels) for the nearside basins Humboltianum (top) and Humorum (bottom).

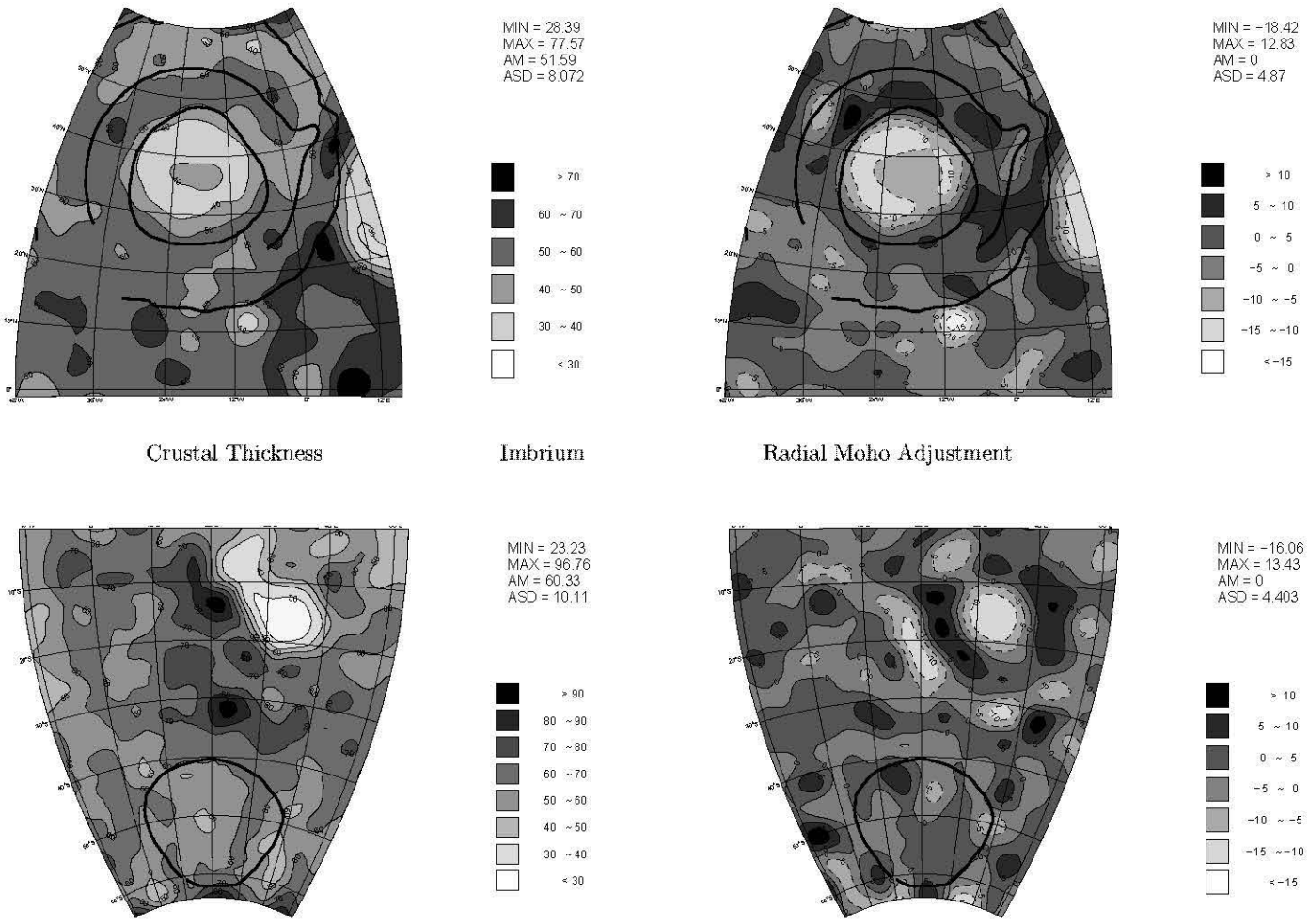

Figure 71: Crustal thickness variations (left panels) and equilibrating Moho adjustments (right panels) for the nearside basins Imbrium (top) and Mutus-Vlacq (bottom).

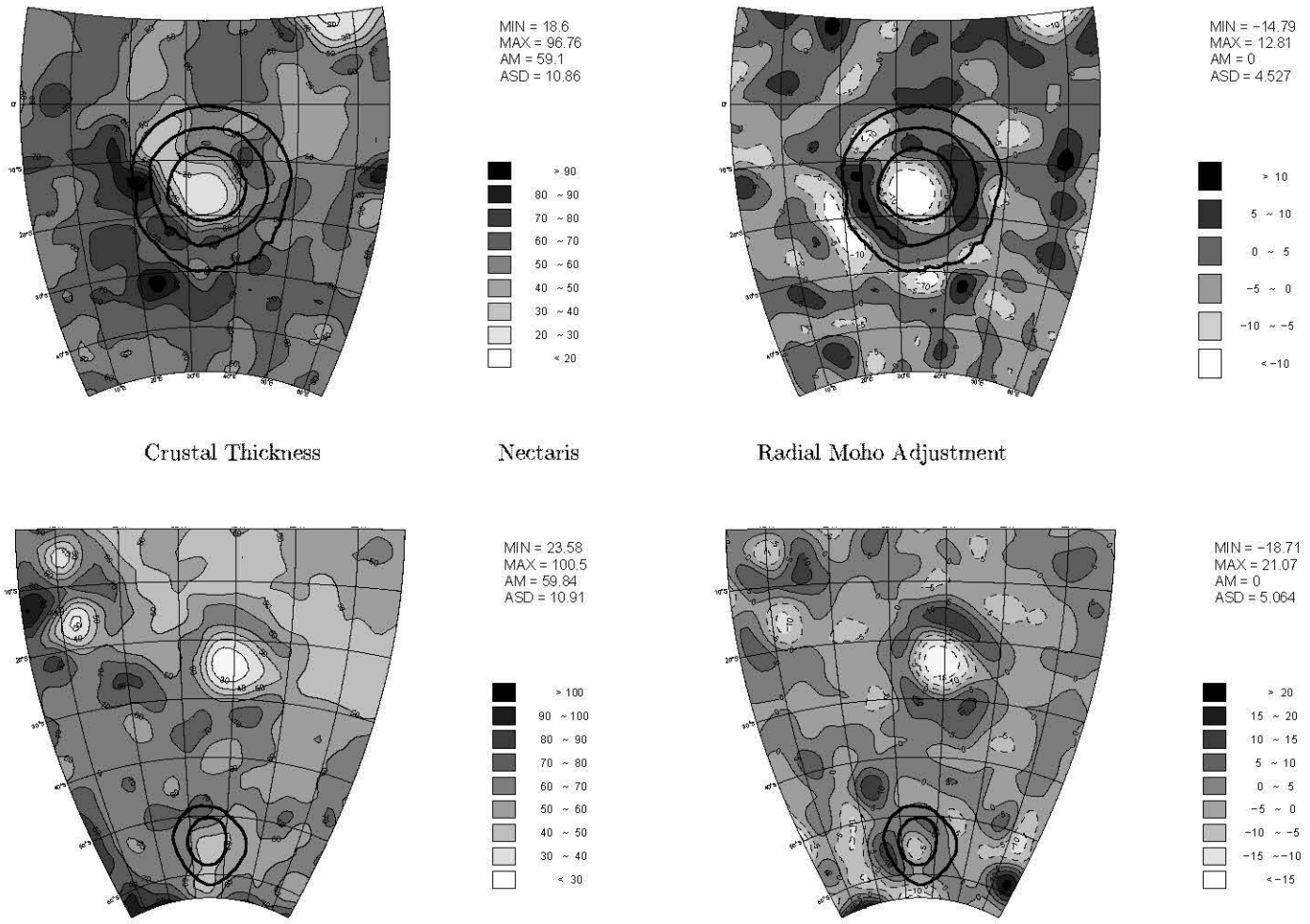

Figure 72: Crustal thickness variations (left panels) and equilibrating Moho adjustments (right panels) for the nearside basins Nectaris (top) and Schiller-Zucchius (bottom).

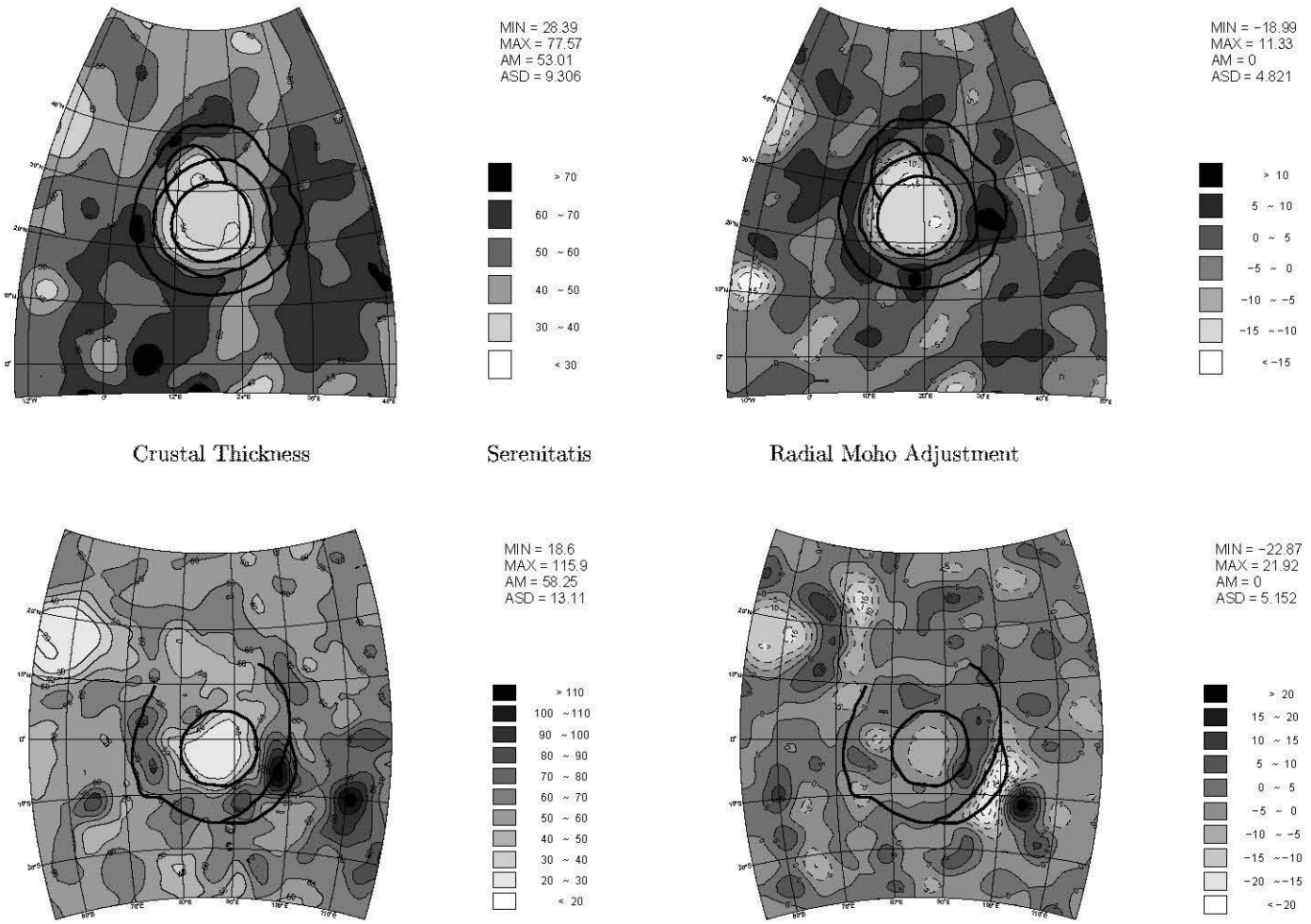

Figure 73: Crustal thickness variations (left panels) and equilibrating Moho adjustments (right panels) for the nearside basins [ ] (top) and [ ] (bottom).Nearside basins Serenitatis and Smythii.

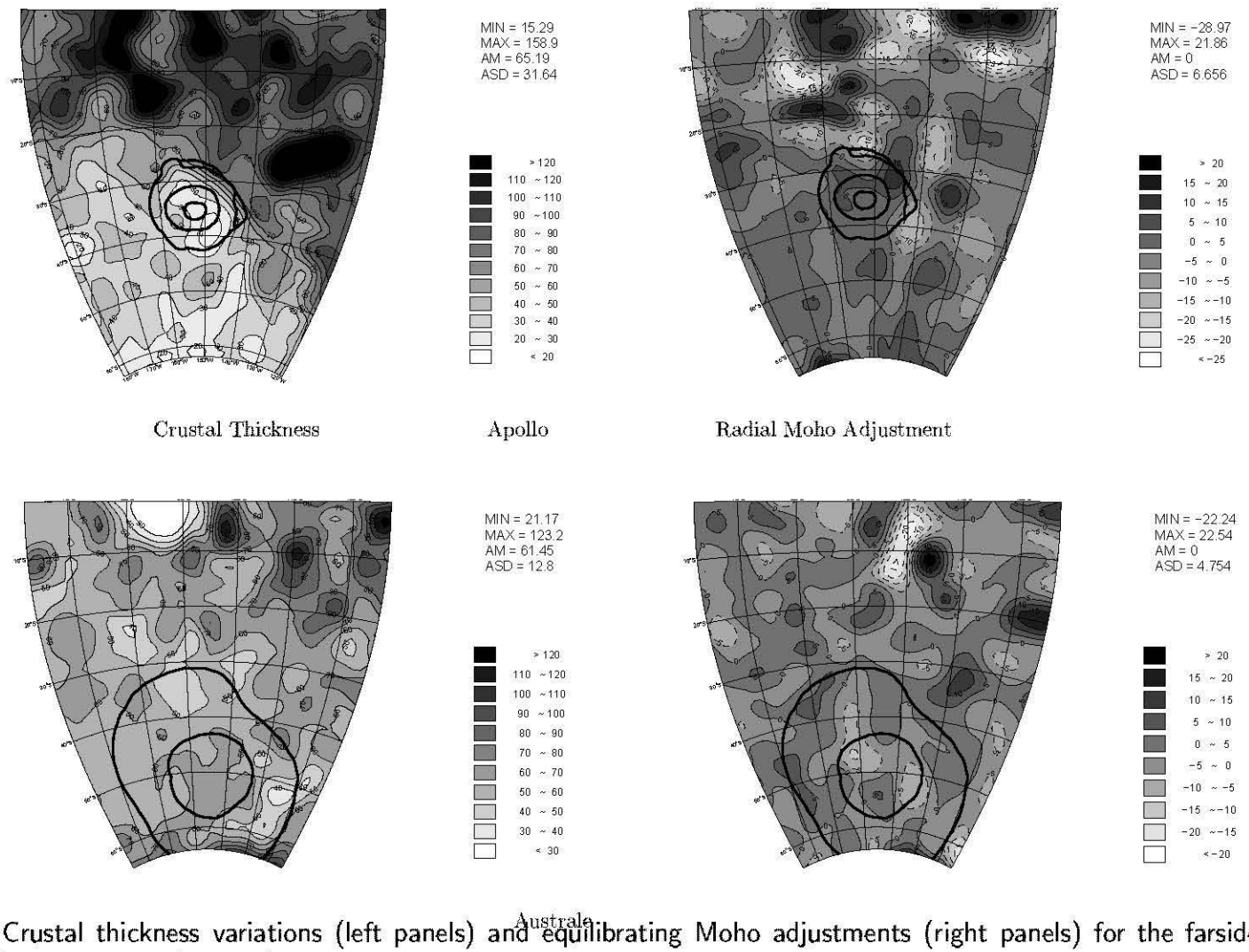

Figure 74: Crustal thickness variations (left panels) and equilibrating Moho adjustments (right panels) for the farside basins Apollo (top) and Australe (bottom).

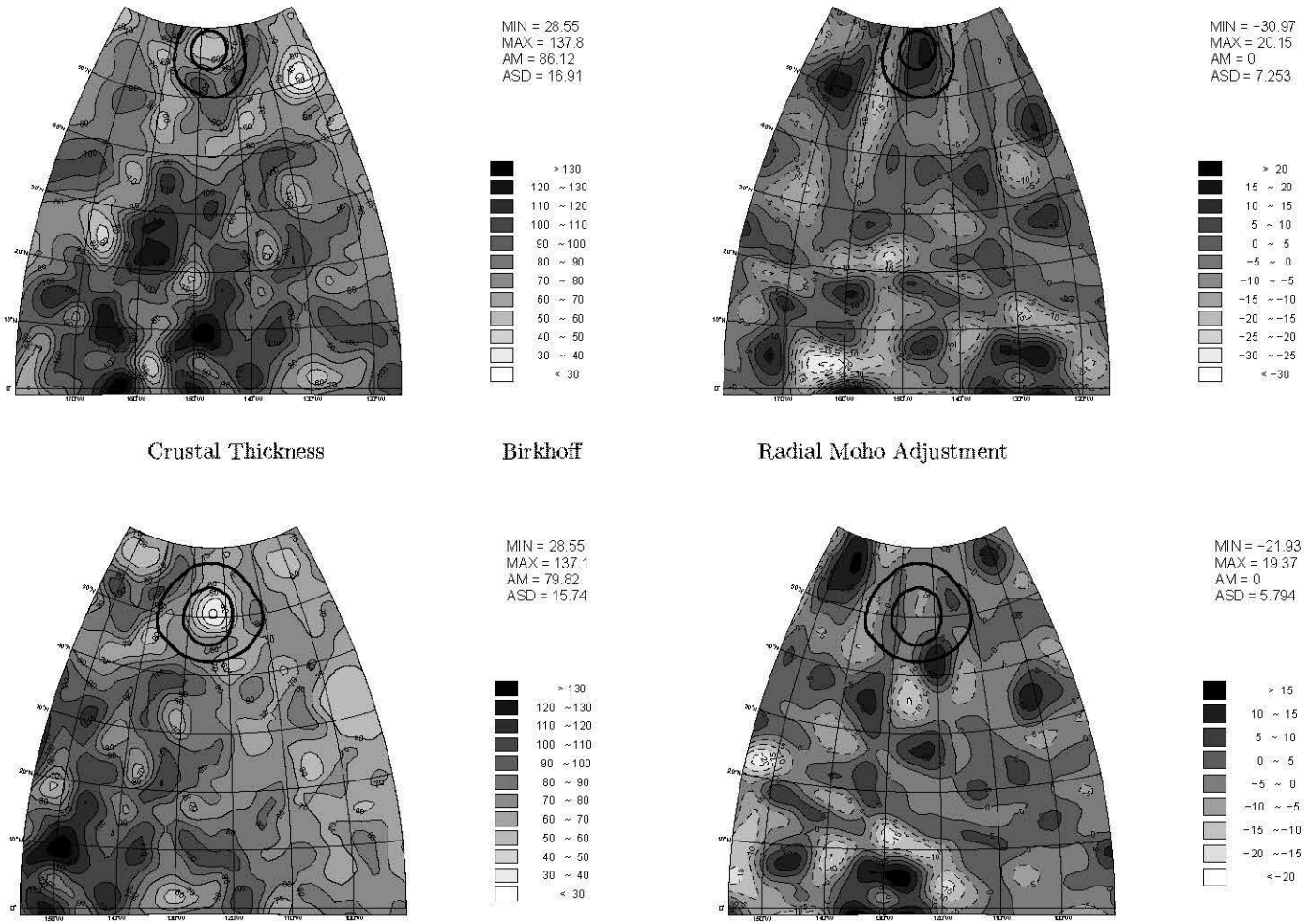

Figure 75: Crustal thickness variations (left panels) and equilibrating Moho adjustments (right panels) for the farside basins Birkhoff (top) and Coulomb-Sarton (bottom).

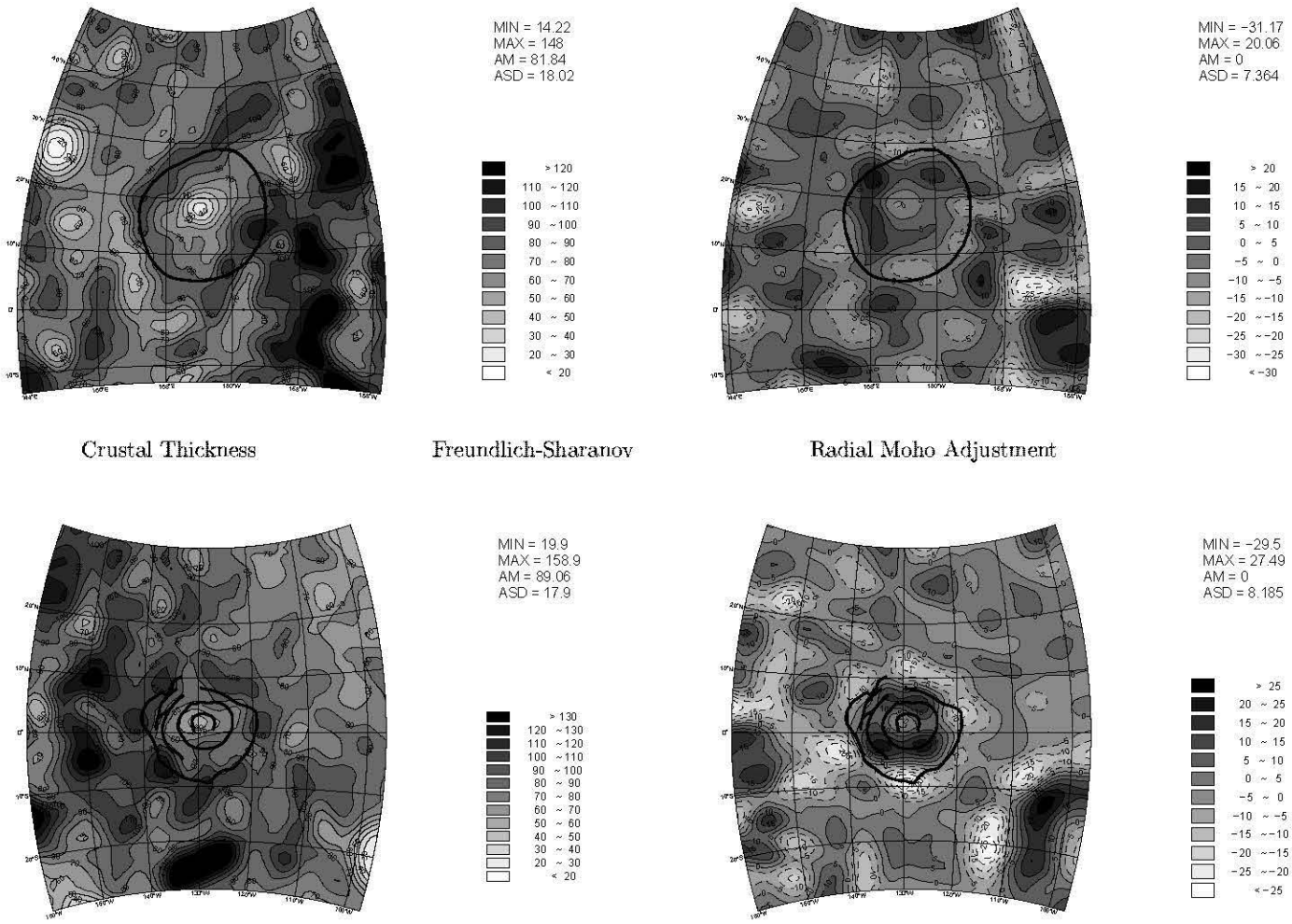

Figure 76: Crustal thickness variations (left panels) and equilibrating Moho adjustments (right panels) for the farside basins Freudlich-Sharonov (top) and Hertzprung (bottom).

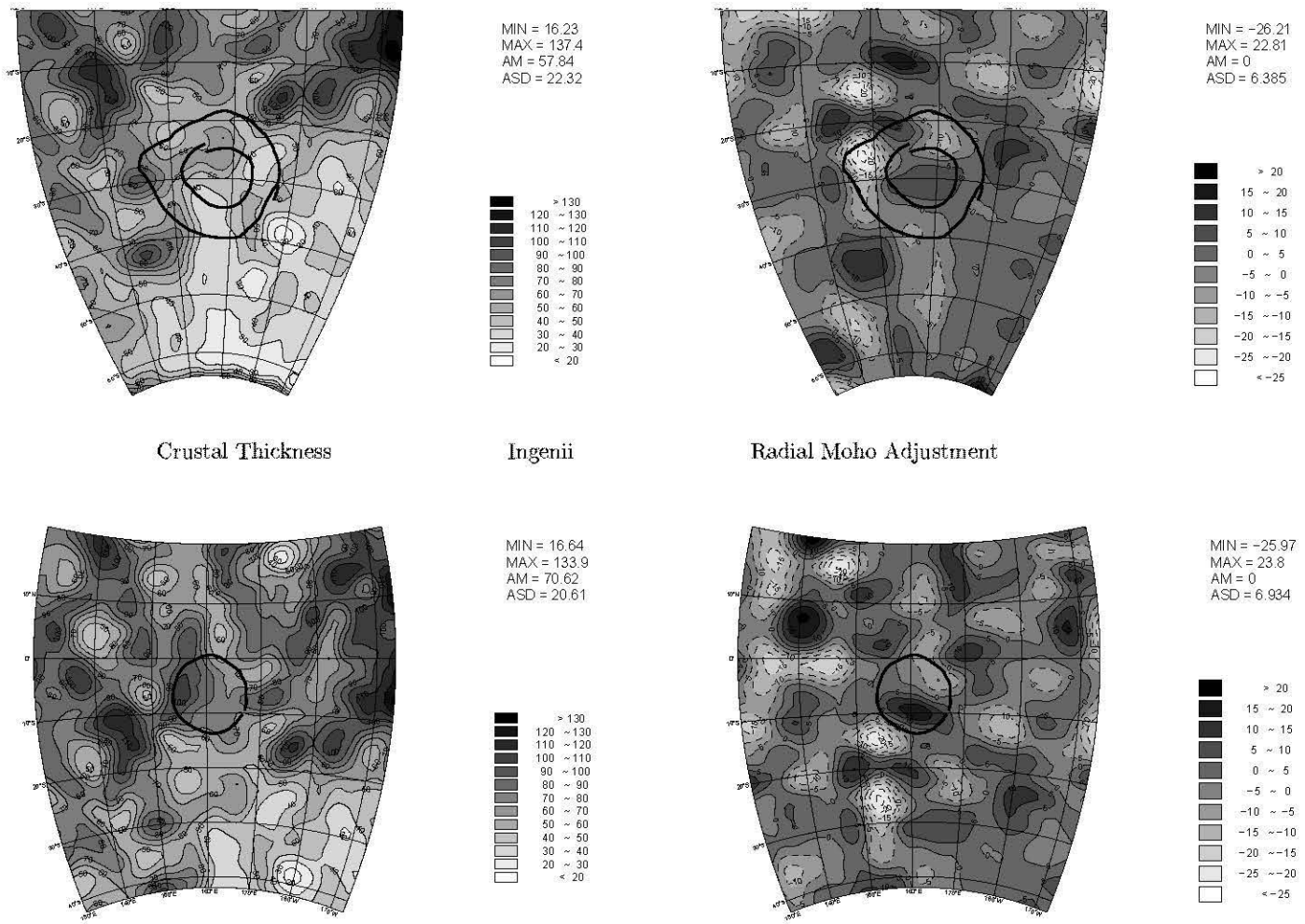

Figure 77: Crustal thickness variations (left panels) and equilibrating Moho adjustments (right panels) for the farside basins Ingenii (top) and Keeler-Heaviside (bottom).

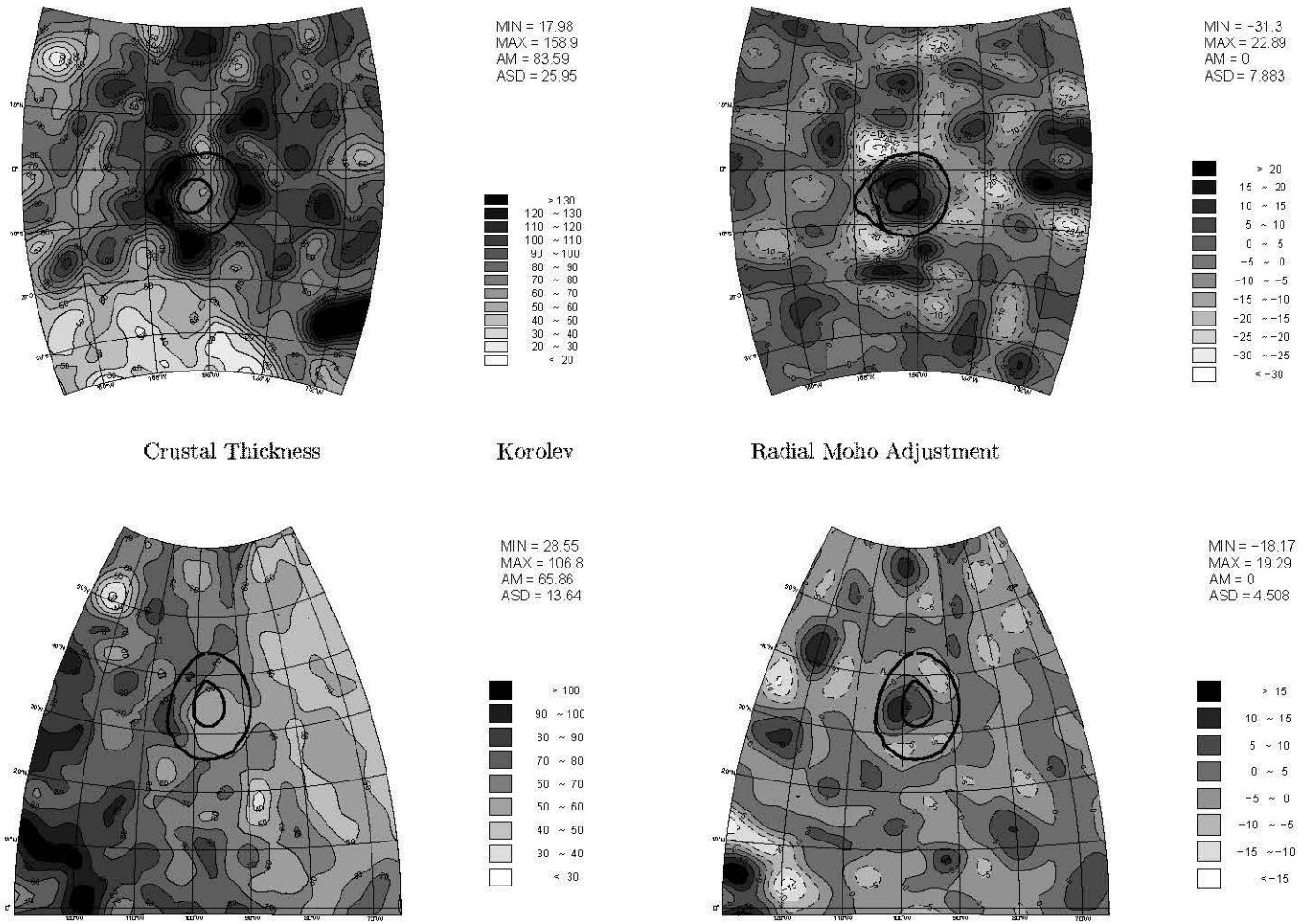

Figure 78: Crustal thickness variations (left panels) and equilibrating Moho adjustments (right panels) for the farside basins Korolev (top) and Lorenz (bottom).

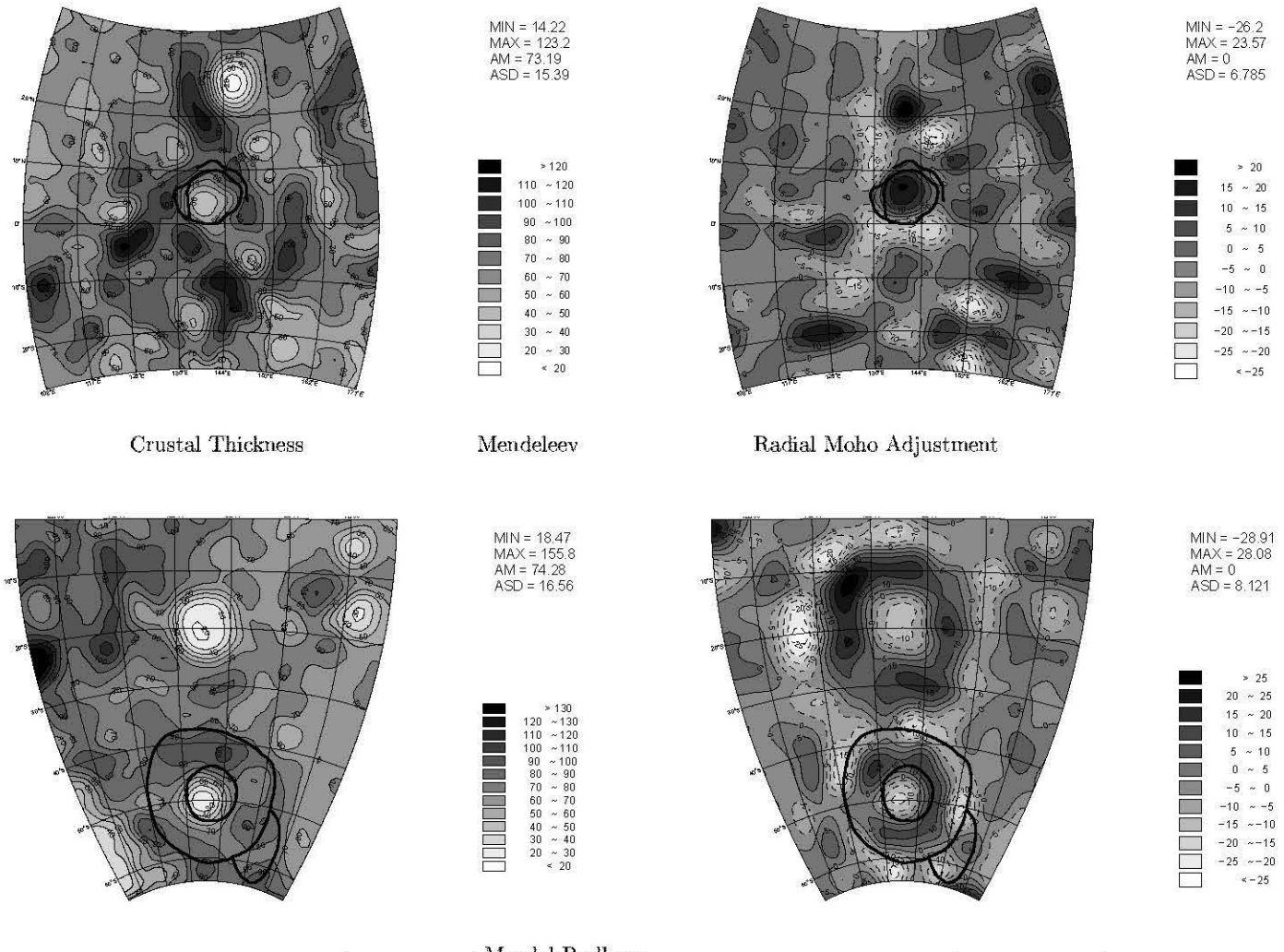

Figure 79: Crustal thickness variations (left panels) and equilibrating Moho adjustments (right panels) for the farside basins Mendeleev (top) and Mendel-Rydberg (bottom).

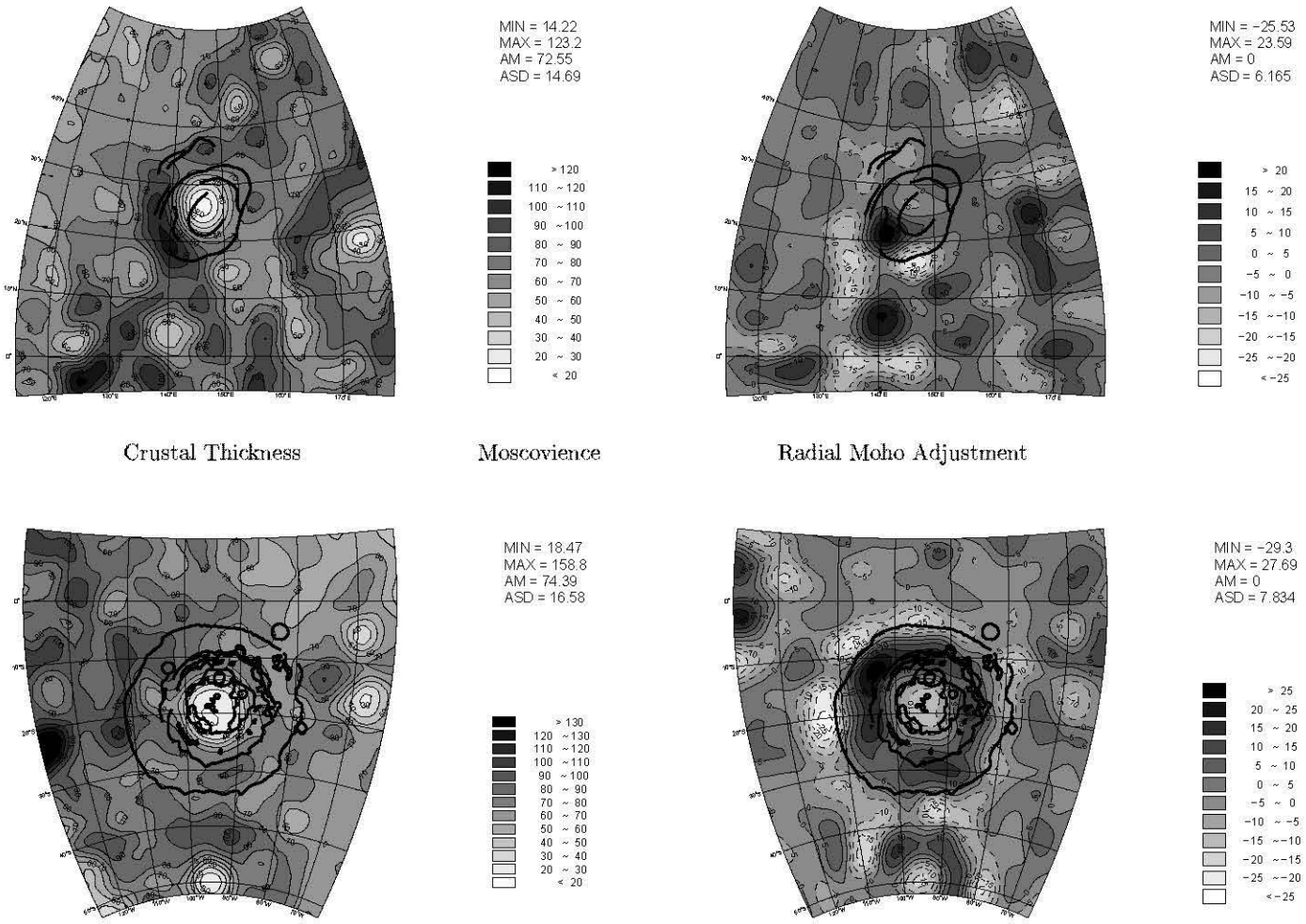

Figure 80: Crustal thickness variations (left panels) and equilibrating Moho adjustments (right panels) for the farside basins Moscovience (top) and Orientale (bottom).

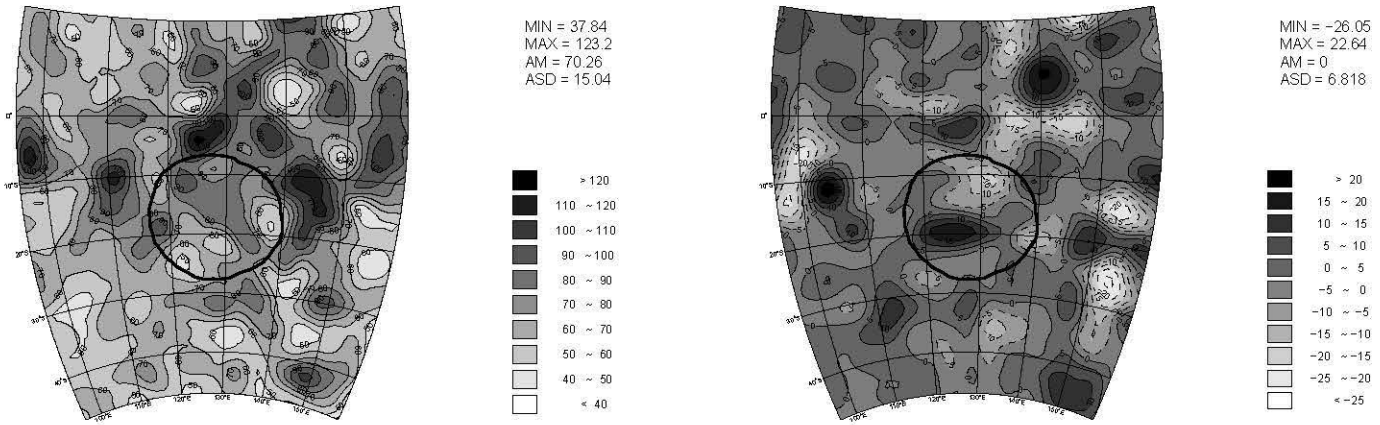

Crustal Thickness | Tsiolkovskiy-Stark | Radial Moho Adjustment

Figure 81: Crustal thickness variations (left panels) and equilibrating Moho adjustments (right panels) for the farside basin Tsiolkovskiy-Stark.

F.3 Cross-section and Profiles

This section contains the crustal cross-sections and the incipient crustal motions.

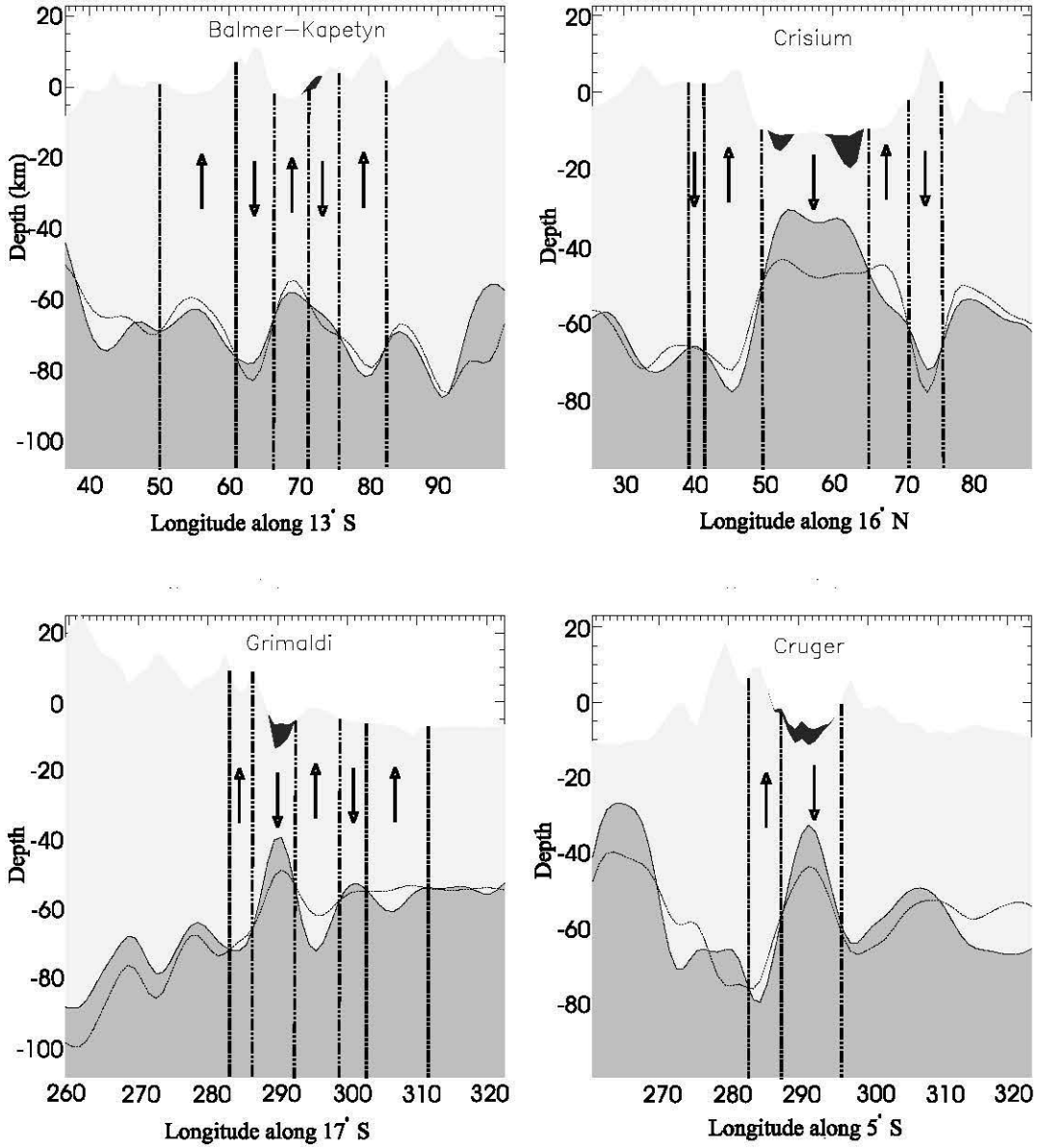

Figure 82: Crustal sections for Balmer-Kapetyn, Crisium, Grimaldi and Cruger. Each panel shows the crust and Mantle in the lighter and darker grey shading, respectively, with black shading marking inferred distribution of mare fill. The dash-dot line represents the equilibrium Moho. Arrows indicate the direction of lithospheric thrusting that can nullify *TCFAGA*. A vertical exaggeration of 5:1 was used to represent the surface topography and mare fill.

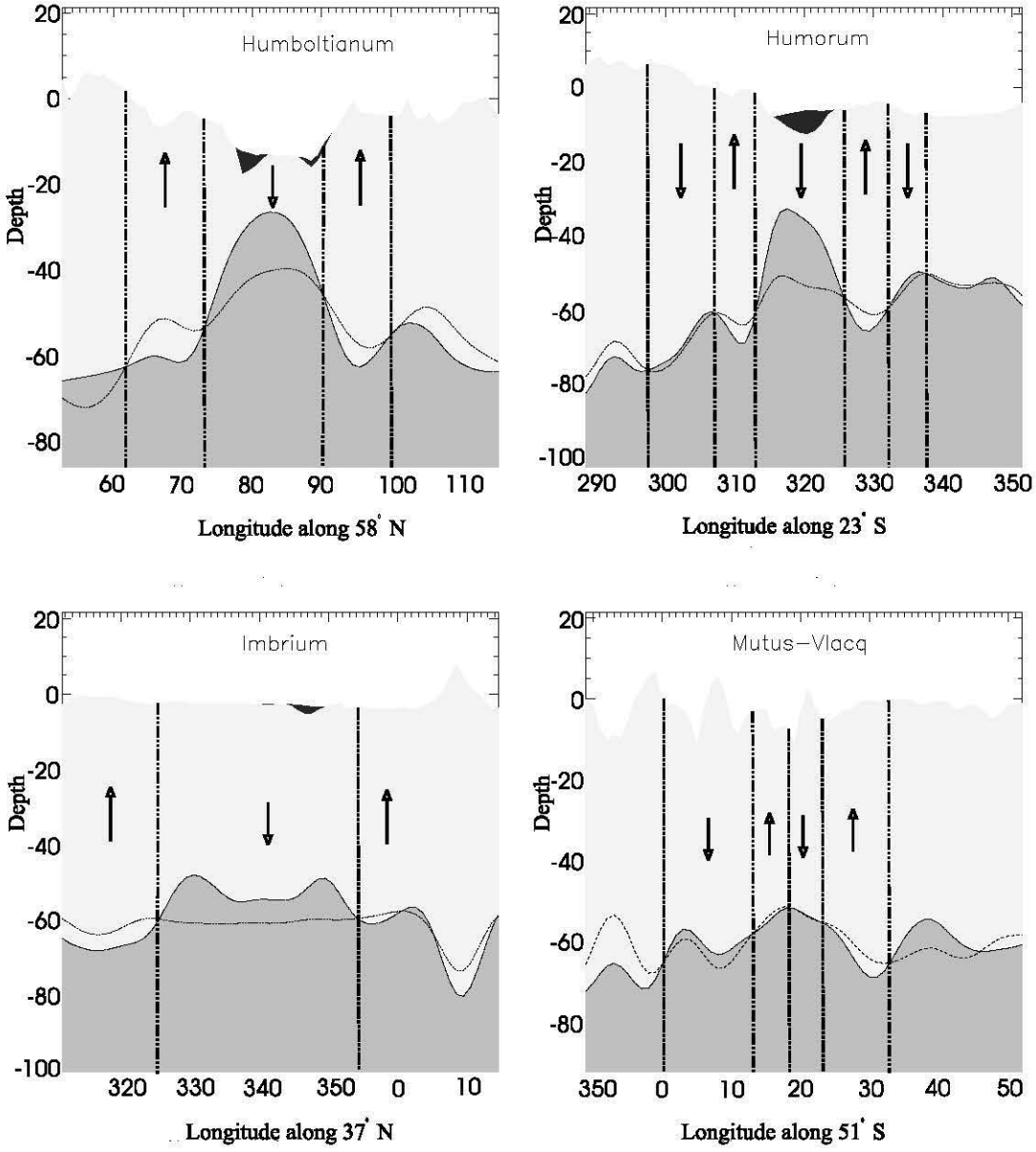

Figure 83: Crustal sections for nearside basins Humboltianum, Humorum, Imbrium and Mutus-Vlacq. Surface topography is at 5:1 vertical exaggeration.

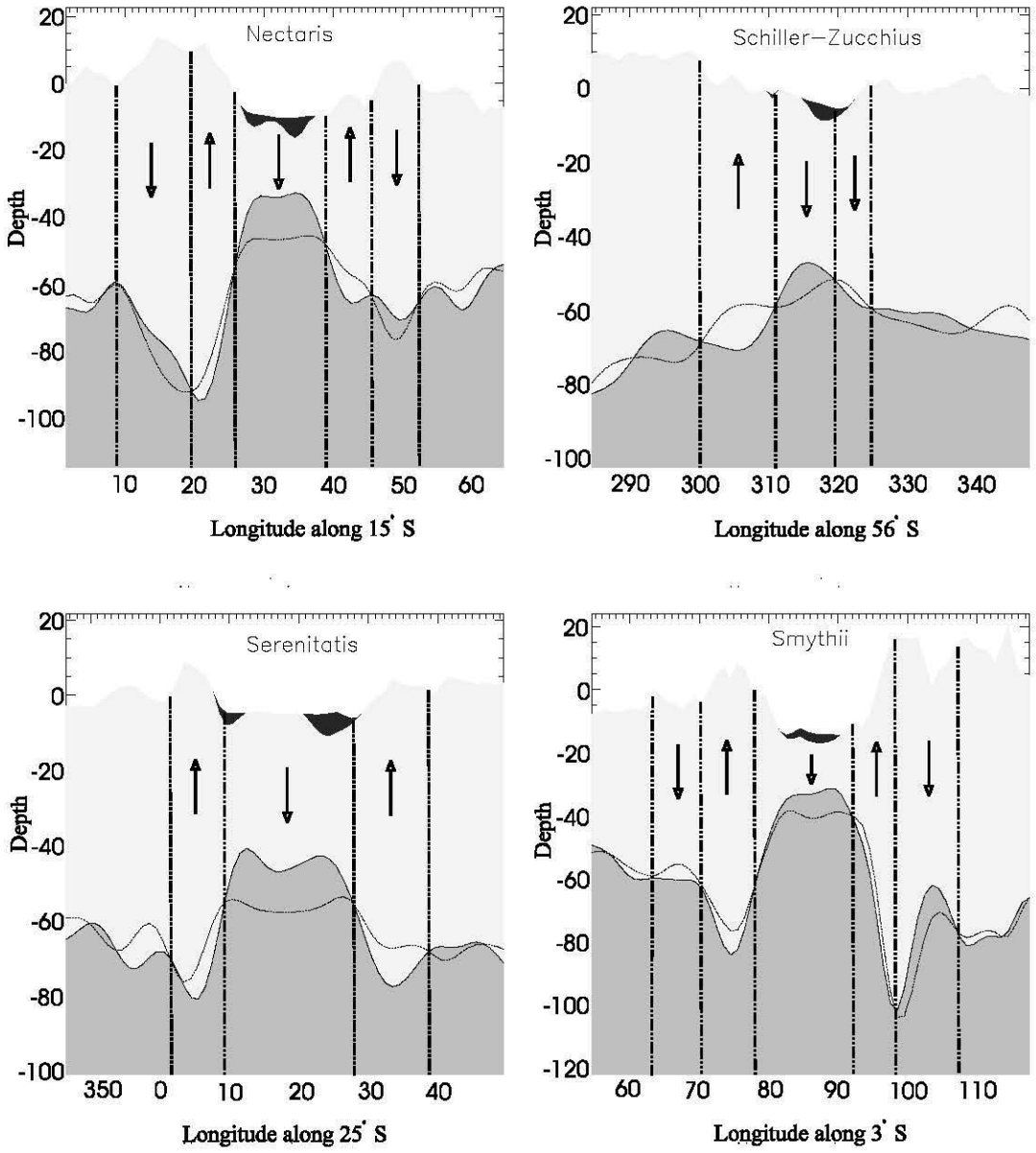

Figure 84: Crustal sections for nearside basins Nectaris, Schiller-Zucchius, Serenitatis and Smythii. Surface topography is at 5:1 vertical exaggeration.

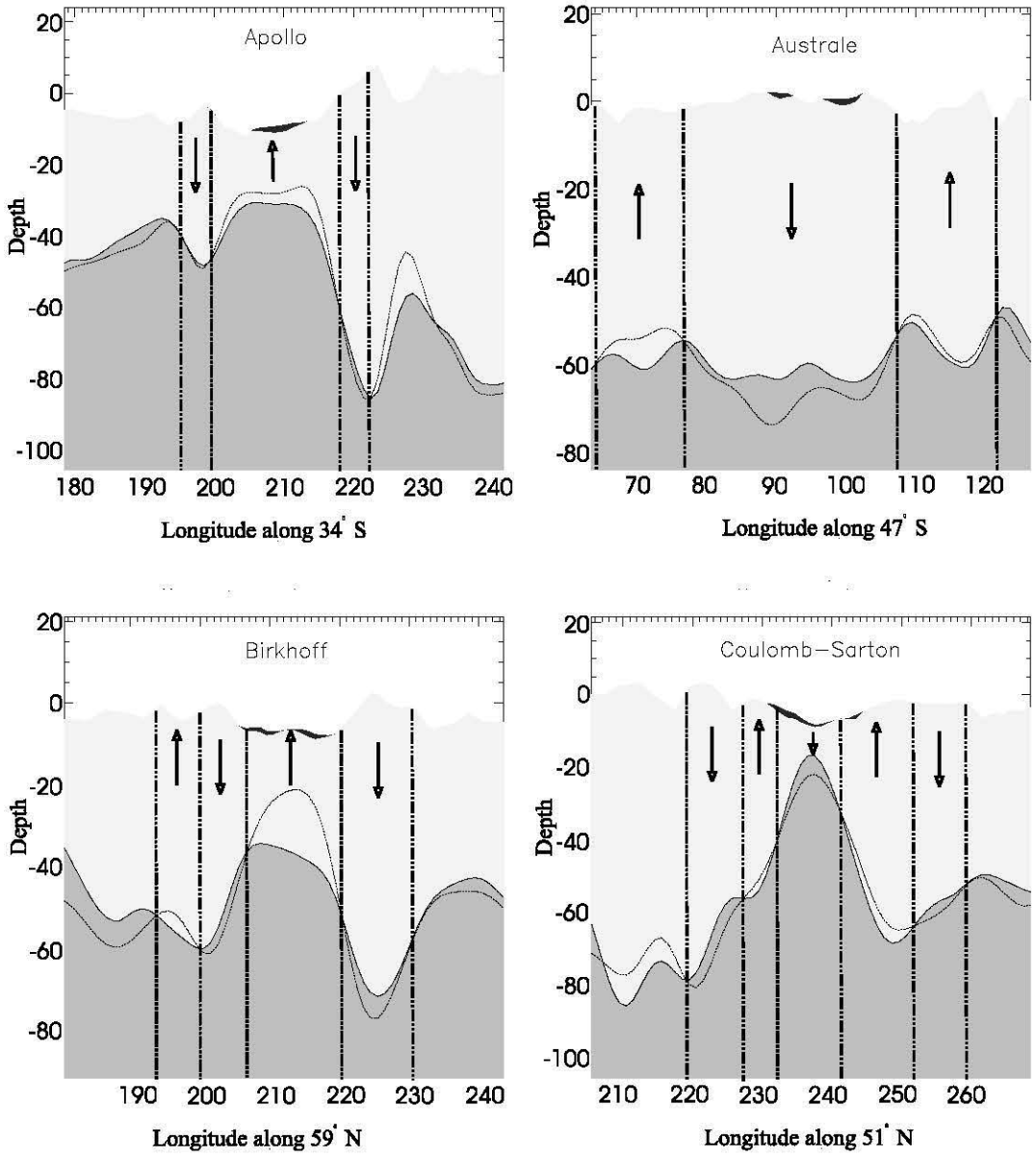

Figure 85: Crustal sections for farside basins Apollo, Australe, Birkhoff and Coulomb-Sarton. Surface topography is at 2:1 vertical exaggeration.

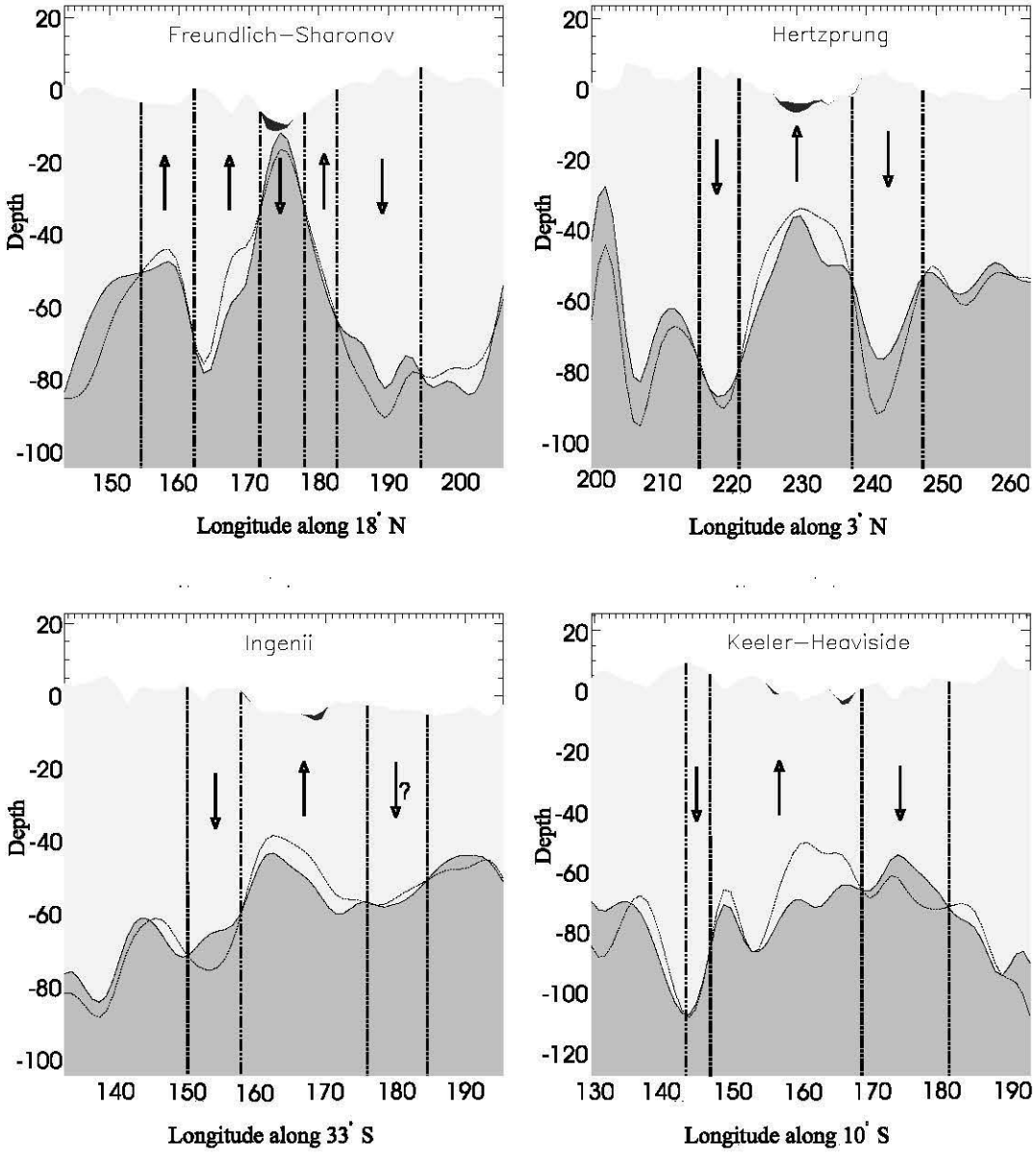

Figure 86: Crustal sections for farside basins Freundlich-Sharonov, Hertzprung, Ingenii and Keeler-Heaviside. Surface topography and mare fill is at 2:1 vertical exaggeration.

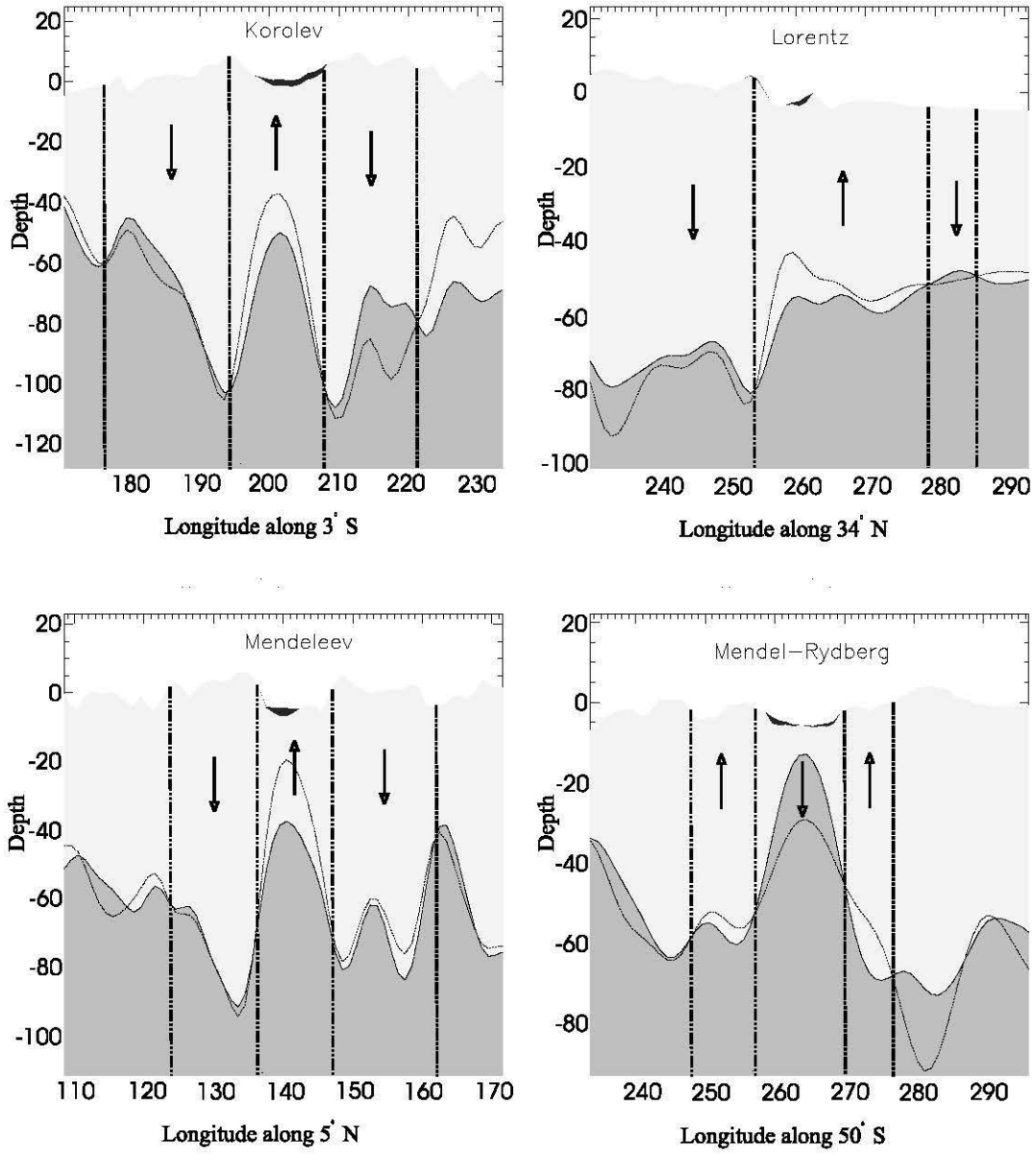

Figure 87: Crustal sections for farside basins Korolev, Lorentz, Mendeleev and Mendel-Rydberg. Surface topography is at 2:1 vertical exaggeration.

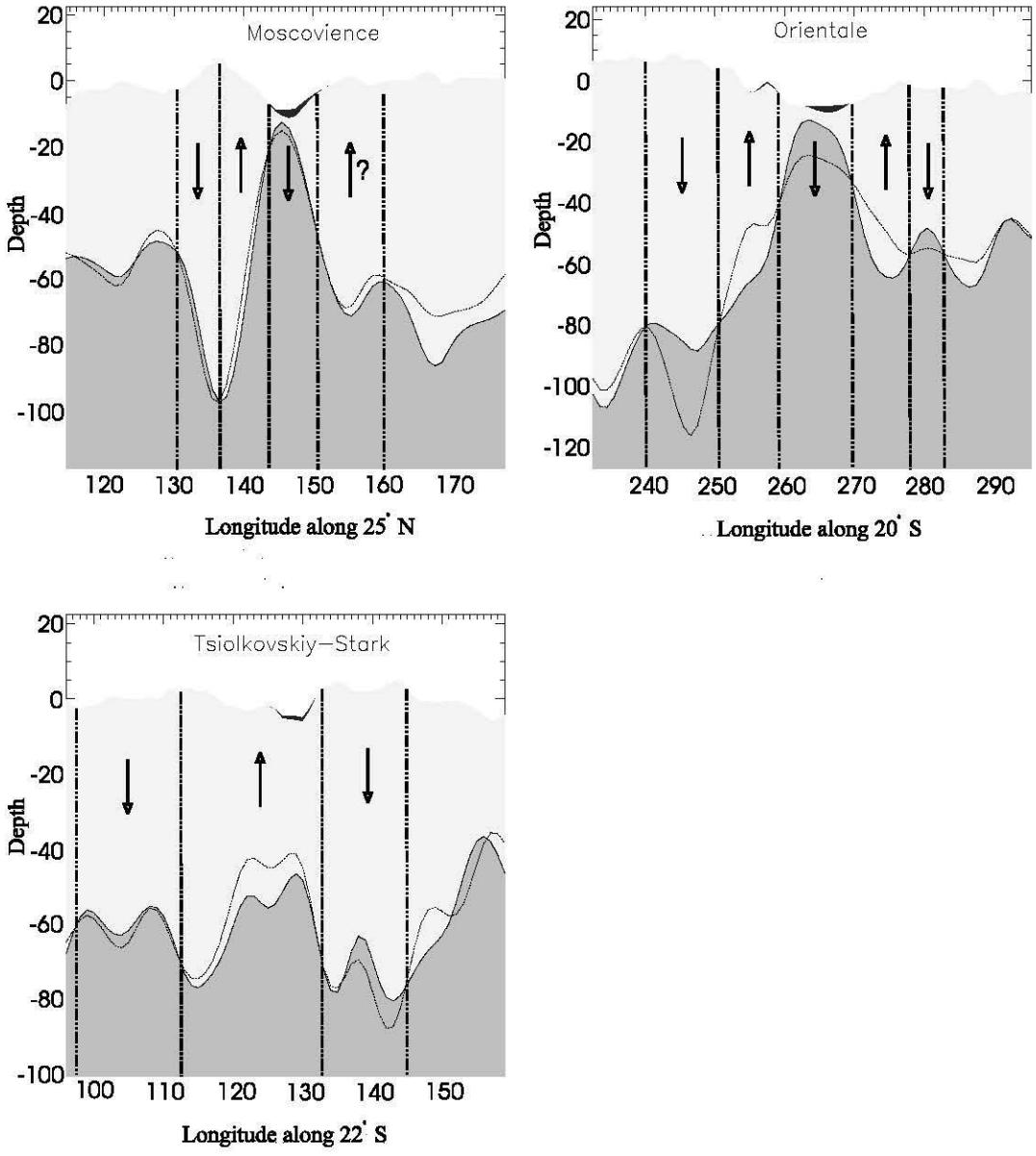

Figure 88: Crustal sections for farside basins Moscovience, Orientale and Tsiolkovskiy-Stark. Surface topography is at 2:1 vertical exaggeration.

G Stratification of the Lunar Interior

G.1 Introduction

Drawing upon seismic data, geochemical data, and lunar samples, investigators have sought to define the nature of the Moon's interior (e.g., Goins et al., 1981; Taylor, 1982; Nakamura, 1983). The existence of a lunar core was once heavily debated including the stratification of the lunar mantle (Runcorn, 1996). However, the recent analysis of the orbital characteristic of the Lunar Prospector satellite confirmed the existence of a small lunar core (Konopliv et al., 1998).

The internally stratified structure of the lunar mantle may be obtained from seismic velocities (Goins et al., 1981; Nakamura, 1983). However, the seismic network was limited to a few locations on the lunar nearside and operated for a limited time and collected poor data (Nakamura, 1983).

In the case of limited seismic data, geophysical models (Short, 1975) are generally constructed based on constraints from moments of interia (Bills and Rubincamp, 1995), cosmochemical analysis (Righter and Drake, 1996) and seismic data. A plausible geophysical model for a stratified lunar interior must be consistent with seismic and geochemical data (Taylor, 1982).

Recent advances in geochemistry modeling and its application to lunar studies provide improved understanding regarding the evolution of planetary differentiation. For example, the depth for the origin of the lunar basalt provided insight on the bouyancy forces and chemical composition of the lunar interior (Circone and Agee, 1996; Agee, 1998).

The purpose of this appendix is to construct a synthesized radial density model for the Moon that is consistent with the results of lunar heat flow modeling (Konrad and Spohn, 1997), seismic data (Moore, 1981; Goins et al., 1981; Nakamura, 1983) and geochemical models (Alley and Parmentier, 1998; Agee, 1998; Circone and Agee, 1996) so that the effects of internal mass variations of the Moon may be studied. For example, the shape and undulations of the Moon's interior density boundaries may provide insight on evolution of the Moon due to basin forming impacts. In particular, the lunar gravity field can be separated into terrain correlated and terrain decorrelated components based on a correlation analysis with the gravity effects of the lunar topography (von Frese et al., 1997b). The correlation spectrum of the terrain decorrelated free-air gravity *TDFAGA* components can be analysed in terms of the internal stratification of the Moon. For example, it is generally accepted that long wavelength features of the gravity field relate to deep-seated mass anomalies (Bowin, 1994). Hence, in order to assign a certain ensemble wavenumber components of *TDFAGA* to lateral mass variations of a particular seismic dicontinuity, the veracity of the internal structure is paramount.

This Appendix is divided into 6 sections. Section 2 describes the size and composition of the lunar core, section 3 describes the possible stratified layering of the mantle as inferred from seismic results. Geophysical models are described in section 4 and section 5 discusses geochemical constraints. Section 6 summarizes all the results and present a synthesized model for a stratified Moon.

G.2 Lunar Core Size and Composition

The existence of the lunar core has been verified from polar moment of inertia constant of 0.3932 derived from the orbital analysis of the LP satellite (Konopliv et al., 1998). Previously, a moment of inertia value of 0.3905 was derived from analysis of the Apollo seismic experiments and found to be consistent with a lunar core of about 600 km radius (Hood, 1986; Hubbard, 1984). Studies of lunar palaeomagnetics suggested that the lunar core formed 4.1 Gyr, nearly 500 Ma after the formation of the Moon (Runcorn, 1996).

The size of the lunar core was also inferred from magnetometer data, core formation studies, and moment of inertia values. For example, a re-analysis of magnetometer data from the Apollo sub-satellite suggested a core of radius 400-500 km (Russell et al., 1981). A study of core formation suggests that the lunar mantle siderophile element abundance requires the core to about 5% of the Moon's mass i.e., about a 500 km radius (Righter and Drake, 1996). The recently determined polar moment of inertia suggests an iron core of radius 220-450 km (Konopliv et al., 1998).

The composition of the lunar core has been inferred from thermal evolution models (Konrad and Spohn, 1997). In particular, a core of size 200-450 km may have a with density of 7.3 g/cm^3 (Konrad and Spohn, 1997). For a 600 km size core, the composition of the lunar core may be either iron or iron-sulphur (Runcorn, 1996). The pressure at the lunar core is only about 4.7 GPa (Circone and Agee, 1996) and interpretation of the physical libration parameters by laser ranging suggested that the core may be partially molten (Yoder, 1981).

G.3 Lunar Mantle Stratification Composition

As a result of gravitational differentiation, most terrestrial planets consist of spherical shells of various thickness and chemical composition (e.g., Morse, 1993; Righter and Drake, 1996; Rubin, 1997; Alley and Parmentier, 1998). The depths of the density interface boundaries of a stratified planet, such as Earth, may be deduced from seismic experiments.

G.3.1 Seismic Constraints

Velocities of moonquake waves, both natural and artificial, give information regarding the Moon's layered structure. Seismometers placed on the surface of the Moon during the Apollo era found that three distinct kinds of moonquakes occur on the Moon. The first kind are those produced by impacts of meteorites, the second are those produced artificially such as by small charges on the lunar surface set off during the Apollo missions or crashing the lunar modules after astronauts rejoined the orbiting section of the Apollo. The third kind are due to internal movements of the lunar globe (Moore, 1981).

Interpretation of the seismic results suggested a general structure of the Moon consisting of a lithosphere, asthenosphere, and core. The lithosphere may extend down to about 1000 km, an asthenosphere that extends from below the lithosphere to a depth of 1200 km, and a core of radius of about 500-600 km (Moore, 1981).

The stratification of the upper mantle was also interpreted from the seismic data. Density boundaries may be located at depths of about 20 km, 60 km, 150 km representing the upper crust, the crust-mantle boundary, and the upper- and middle mantle boundary, respectively. The results also suggested an upper crust may be composed of fractured basaltic material, the lower crust of anorthositic gabbro, and the upper mantle rich in olivine and pyroxenne (Moore, 1981).

Improved analysis of the Apollo era seismic data by the inversion of seismic arrival times from the lunar seismic network modified the estimated for the depths of the layers of the lunar mantle (Nakamura, 1983). The results suggested a 3-section mantle. In particular, the upper- and middle mantle boundary was located at a 270 km depth, a middle- and lower mantle boundary at 500 km depths, and the lower mantle extends down from 500 km to a depth of about 1000 km with a sharp increase in deep moonquake activity below the 800 km depth (Nakamura, 1983).

The structure of the lunar interior is poorly constrained by seismic data. A major reason is the limited coverage of the seismic network and poor data (Hubbard, 1984). In general, seismic data inversion is non-unique and the data itself is fraught with limitations. For example, constant-velocity of propagation in any particular zone is often an erroneous assumption (Nakamura, 1983). Additionally, errors associated with seismic data include reading errors and observational bias (Nakamura, 1983). For the Moon, however, a further limitation is the station/reciever network configuration because all seismic stations are located on the nearside (Hubbard, 1984).

A generalized structure of the lunar interior based on seismic data may be summarized by a 500-600 km radius high density core, a 200 km thick asthenosphere above the core, and a seismic boundary at about 550 km depth. The range of depths to the upper- and middle mantle boundary of 150 to 270 km has a large range. An average value for 210 km may be used.

G.4 Geophysical Models

Models of the radially stratified Moon are generally constructed from various geophysical data (Short, 1975). In particular, geophysical models may be constrained by electrical conductivity profiles (Sonnet et al., 1971), seismic and geochemical data (e.g., Taylor, 1982; Hubbard, 1984), and moment of interia, seismic and geochemical data (e.g., Binder, 1980; Hood, 1986; Hood and Jones, 1987).

Average electrical conductivity profiles were estimated from the magnetometer data from Apollo 12 to concieve a radially stratified Moon (Sonnet et al., 1971). The results suggested a 70-km thick crust, an upper mantle extending from the base of the crust down to about 250 km, a middle mantle extending from 250 km down to 300 and the lower mantle extend from 350 to 500 km. The model also included a core of radius 1400 km (Sonnet et al., 1971).

The combined analysis of seismic due to Goins et al. (1981) and geochemical data suggested a 70 km averaged thick crust, an upper mantle that extends down from 70 to 400 km depth and a lower mantle that extends down from 480 to 1100 km depth (Taylor, 1982). A 300 km seismic attenuation zone was located at a depth of 1100 km down to 1400 km and a core of radius of about 350 km (Taylor, 1982).

A re-interpretation of the P- and S-waves of the seismic data was based on laboratory studies on synthetic minerals consisting mostly of olivines and pyroxenes (Hubbard, 1984). The results suggested that the lunar interior may comprise a 50 km thick crust, an upper mantle that extends to a depth of about 500 km, a middle mantle that extend to a depth of about 1000 km, and a partially melted lower mantle that extend to a depth of about 1400 km. This model suggest the middle mantle composing of minerals mostly of olivines with some pyroxennes and the lower mantle, being highly opaque to S-waves, may be considered analogous to the terrestrial asthenosphere (Hubbard, 1984).

Several investigators developed geophysical models for the moon based on constraints from moment of inertia values, geochemical data, and seismic data (e.g., Binder, 1980; Hood and Jones, 1987). For example, Binder (1980) used seismic velocities from Goins et al., (1981) and suggested that the middle- and lower mantle boundary with a 0.2 g/cm^3 density contrast may be located at a depth of 850 km, assuming a high 7.4 g/cm^3 density FeS core and moment of inertia value of 0.393.

Hood and Jones, (1987) reassessed the seismic velocities of Nakamura (1983) and suggested an upper mantle extending below a 60 km thick crust to a depth of 220, a middle mantle extending from 220 down to 550 km, a lower mantle extending down from 550 to about 1300 km, and a core radius of about 450 km (Hood and Jones, 1987). These two geophysical models are in good agreement except for the depth of the middle- and lower mantle boundary.

G.4.1 Radial Densities from Moments of Inertia

Estimates of the moment of inertia value from the Apollo era are close to the recent estimates of 0.3932 obtained from the Lunar Prospector mission (Konopliv et al., 1998). The mean density and mean moment of inertia are both related to the radial moments of density distribution (Bills and Rubincamp, 1995).

A density model was computed from the moments of inertia, obtained from analysis the long wavelength features of the Clementine orbit (Nozette et al., 1996). The results shows good agreement with the density profile of geophysical model of Hood and Jones, (1985).

Table 12 gives the depth, density, composition and section estimated from the moments of interia (Bills and Rubincamp, 1995).

In summary, a synthesized model for the layered interior from the geophysical models include a crust mantle boundary, an upper- and middle mantle boundary, and a middle- and lower mantle boundary at depths of 60, 220, and 550-850 km, respectively. The corresponding density contrasts at these boundaries are 0.5, 0.1, 0.2 g/cm^3, respectively. A 150 km high viscosity zone located at a depth of about 650 km and a 300-km low viscosity zone located at a depth of about 1000 km may also be included (Binder, 1980; Hood and Jones, 1985; Bills and Rubincamp, 1995; Konrad and Spohn, 1997).

Depth (km)	Density g/cm^3	Composition	Section
0-105	2.8	anorthosite	Crust
105-208	3.3	pyroxene-olivine	upper mantle
209-549	3.4 - 3.5	olivine	middle mantle
550-1300	3.5 - 3.7		lower mantle
1300-1738	6.0 7.0 8.0	pure FeS mixture of Fe and FeS pure Fe	core

Table 12: Estimates of radial density from moment of inertia envelopes (Bills and Rubincamp, 1995). Compositional variations were adapted from Hubbard (1984), Hood (1986), Hood and Jones (1987), and Circone and Agee (1996).

G.5 Geochemical Stratification

Geochemical constraints on the separation of metals from silicates provide clues on the compositional variation that presumably resulted from the differentiation of the mantle. For example, geochemical analyses of lunar magmas for its compressibility provide clues on the depth (pressure) of crystal-liquid density inversion in the lunar mantle (Circone and Agee, 1996; Smith and Agee, 1997; Agee, 1998). Crystal-liquid density inversion is constrained by density and compressibility of crystals (Agee, 1986) and may provide insight on the compositional layering of the differentiated lunar mantle.

Petrological analysis of the mare basalts suggests that different mare basalt types were derived from different depths within the lunar mantle (Circone and Agee, 1996). In particular, the aluminous type presumably came from the shallowest depth (near surface), the high-Ti types came from the next deeper level and the low-Ti types ("black glass") from the next lower level (at a depth of about 400 - 450 km) associated with 2.0 - 2.5 GPa pressure (Circone and Agee, 1996). If the olivine-pyroxene cotectic is located at 400 - 500 km, then "black glass" melt would become buoyant relative to the residue of olivine plus a small amount of orthopyroxenne ($< 5\ \%$). The cotectic represents the range of pressure wherein different elements combine and form a magma which has a different density than both their crystaline phases (Agee, 1998). Deepest of all would be "green glass" (Agee, 1998).

Density inversion had to be present during mare volcanism. In particular, magmas generated during mare volcanism ascended from magma ocean cumulates from deep within the lunar interior, presumably at the olivine-pyroxene cotectic located at about a depth of about 400-500 km and pressure of about 2.0 - 2.5 GPa. This depth also corresponds to the phase transition boundary for the maximum depth for the buoyancy rise of high-Ti lunar basalt (e.g., Hood, 1986; Agee, 1986; Circone and Agee, 1996; Smith and Agee, 1997).

Melting of the olivine-pyroxene mantle formed the pristine volcanic glasses representing the primary magmas for high- and low-Ti mare basalt generated at pressure of about 2.5 GPa or at a depth of about 400 - 600 km (Delano, 1980; Circone and Agee, 1996; Agee, 1998; Alley and Parmentier, 1998). Low-Ti basalt are produced from the ilmenite free olivine-pyroxene cumulates at a depth

of the of 400-500 km (Smith and Agee, 1997). Hence, the generation and bouyant rise of "green glass" magma originated from this depth (Smith and Agee, 1997). If the cotectic is located less than 400 km depth then molten "black glass" would be bouyant relative to the residue of olivine and 5% orthopyoxene. Hence, the maximum depth for the bouyant rise of high-Ti basalt from its thermally equilibrated source is about 450 km (Agee, 1998) although the asthenosphere as source of high-Ti is not excluded (Delano, 1980). High-Ti magmas generated in the asthenosphere may reach the surface through overpressurization via adiabatic rise of diapirs (Hess, 1991). The seismic attenuation zone at depths of 1000-1400 km may contain some high-Ti melts that have reached this level by downward migration (Delano, 1990).

The significance of a cotectic involve the origin of pristine lunar glasses of the various mare basalt types. At liquidis conditions, density inversion may occur at pressures of 0.5-0.7 GPa and 2-2.5 GPa for orthopyroxene and olivine, respectively (Circone and Agee, 1996; Smith and Agee, 1997 Agee, 1998). In particular, at the olivine-pyroxenne cotectic, molten "green glass" is less dense than both crystaline phases (Agee, 1998). Similarly, molten "black glass" is denser than the solid residu of the orthopyroxene-olivine cotectic at a pressure of 1.5 GPa. Hence, molten "black glass" is denser than the equilibrium olivine and othopyroxene at pressure greater than 400 and 100 km in the lunar mantle (Circone and Agee, 1996).

G.6 Summary

Table 13 summarizes a synthesized model for a stratified Moon. The synthesized model for the internal structure may consist of a core, 3-section mantle that include a olivine-pyroxenne cotectic and a orthopyroxene cotectic, and an anorthositic gabbro crust. In particular, the discontinuities at the crust and upper mantle, upper- and middle mantle, middle- and lower mantle, and core-mantle boundaries, are located at depths of 60, 220, 650, and 1288 km, respectively.

The high density FeS core (7.9 g/cm^3) is associated with central pressure of 4.7 G.Pa and mean radius of 450 km (Binder, 1980; Konrad and Spohn, 1997; Konopliv et al., 1998.)

The stratified lunar mantle consists of a upper, middle, and lower parts. The upper mantle extends from about 60 km down to a depth of 220 km and include the orthopyroxenne-olive cotectic at depth of about 100 km, corresponding to a pressure of 0.6 GPa. The middle mantle ranging in depth from about 220 km to about 650 km and include the olivine-pyroxene cotectic which is located a a depth of about 450 km. The lower mantle extends from 650 km down to about 1300 km and include a 200 km high viscosity zone which extends from 800 km down to 1000 km. A 300 km low viscosity zone extend from 1000 km depth to a depth of about 1300 km.

Average densities are 3.1, 3.2 and 3.5 g/cm^3 for the upper, midle and lower mantle, respectively. An anorthositic gabrro crust has typical density ranging between 2.6 to 2.95 g/cm^3.

Depth (km)	Density g/cm^{-3}	Composition	Section
0-20	1.7-2.6	anorthosite	regolith and upper crust
21-60	2.6-3.0	pyroxenne-olivine	lower crust
61-220	3.0-3.1	pyroxenne & olivine	upper mantle
221-650	3.2-3.3	olivine	middle mantle
651-800	3.5-3.6	olivine & pyroxene	lower mantle
801-1000	3.6-3.7	partial melting high viscosity zone	
1001-1287	3.7-3.8	asthenosphere low viscosity zone	
1288-1738	7.9	pure Fe	core

Table 13: Generalized model of depth, radial density and composition for the stratified Moon derived from selenophysical models (Binder, 1980; Taylor, 1982; Hood, 1986; Hood and Jones, 1987; Bills and Rubincamp, 1995), thermal evolution model (Konrad and Spohn, 1997), and geochemical analyses (Agee, 1986; Cicone and Agee, 1996; Smith and Agee, 1997; Agee, 1998).

H Glossary

This glossary is included because of the wide ranging nature of this research that broadly covers the fields of geodesy, geophysics, geology, and remote sensing. Many of the terms in this glossary are taken verbatim from *Planetary Science: A Lunar Perspective* by S. R. Taylor and *Origin of the Moon* edited by W. K. Hartmann, R. J. Phillips and G. J. Taylor. It is intended as a simple dictionary-type aid to facilitate continuity and understanding while working through the dissertation. The glossary is divided into disciplinary sections pertaining to the fields of study namely size and shape (geodetic), interior stratification (geophysical), mineral-type (geological), and classification (remote sensing) descriptions respectively.

H.1 Estimated quantities

- **Terrain correlated free air gravity anomaly**: (*TCFAGA*) is the component of (*FAGA*) which may be related to the stress and tectonic response of the crust.
- **Terrain decorrelated free air gravity anomaly**: (*TDFAGA*) is the component of (*FAGA*) which may be related to non-isostatic effects such as the density variations inside the Moon's deep interior as well as the intra-crustal density variations within the lunar regolith.
- **Compensated terrain gravity anomaly**: (*CTGE*) may describe the isostatic properties of the lunar crust (*CTGE* = *FAGA* - *TCFAGA*).
- **Moment of Inertia**: ($I/MR^2 = 0.393$) A homogeneity constant, which provides a measure of the density distribution within a planet, where a value of 0.4 indicates a homogeneous Moon and a value less than 0.4 indicates increasing density with depth. The moments are determined from a combination of the two libration constants estimated from LLR and the J_2 and J_{22} gravitational harmonics which are estimated from tracking data of the artificial satellites. Three pricipal moments of inertia ($A < B < C$) are averaged as I = $(A+B+C)/3$.
- **Lithosphere**: The rigid part of the upper and lower mantle and includes the lunar crust.
- **Asthenosphere**: The plastic portion of the lower mantle of the Moon that extends out to 800 km depth.
- **Regolith**: Loose surface material, composed of rock fragments and soil, which overlies consolidated bedrock with an average density of 1.5 g/cm^3. Depths range from 2-8 meters in the Mare to possibly 12 meters or more in the highlands. The material is constantly tilled by micro-meteorite bombardment and solar wind abrasion.
- **Mascon**: Anomalousy positive concentration of mass in the center of the lunar basin.
- **Maslite**: Anomalousy negative concentration of mass in the center of the lunar basin.

- **Ring Mascon**: Annulus of anomalousy positive concentration of mass.
- **Ring Maslite**: Annulus of anomalousy negative concentration of mass.

H.2 Geological parameters

- **Differentiation**: The process by which planetary bodies develop radially concentric zones that differ in chemical and minerological composition due to gravity.
- **Fractionation**: The separation of elements from an initial homogenous state into different phases or systems.
- **Fractional Crystalization**: Formation and separation of mineral phases of varying composition during crystalization of a silicate melt or magma resulting in a change in composition of the magma such as from mafic (high temperature) to felsic (low temperature) compositions. According to the Bowen's Reaction series, the sequence of crystalization separate into two branches at high temperature namely olivine and magnesium-rich minerals, respectively, and a single branch consisting of quartz composition at low temperture. In particular, Olivine crystalization is a discontinuous series of Pyroxene, Amphibole and Biotite mica and the Magnesium-rich minerals crystalization series is continous through Sodium-rich minerals. When elements crystalize out of a melt they take with them some of the chemicals that originally existed in the magma. In this way they remove a specific fraction of the elements from the magma.
- **Partial melting**: The process by which magmas of more than one composition can form. For example, as rocks undergo partial melting, the early formed (low temperature) magma rise (separate) to produce a body of felsic magma. At higher temperature, the remaining portion of the rocks may melt to produce a high-temperature magma of intermediate composition. The reverse Bowen's Reaction Series suggests the process in which rocks melt over a range of temperatures to produce liquids with compositions different from the original unmelted rocks.
- **Mare**: (pronounced "Mah rey") Taken from the latin word for oceans. On the Moon they are mostly composed of dark basalts, which formed from the rapid cooling of molten rock of massive lava flows. On averages a few 100 m thick to depths of 2-4 km in the deep centers of the basins.
- **Basalt**: A fine-grained, dark colored igneous rock composed primarily of plagioclase (feldspar) and pyroxenne; usually other minerals such as olivine, ilmenite are present. Most basalts formed as lava ponds on planetary surfaces, although some formed as dikes and sills.
- **Mare basalt**: Basalts that form the lunar maria are the dark-colored areas on the Moon. Chemically similar basalts also form in breccias from the lunar highlands, indicating that such lava flows occurred there, but which is presently not discernible.

- **KREEP**: An acronym for a unique suite of minerals commonly found in lunar crustal components rich in potassium (K), the rare earth elements (REE) and phosphorous (P) and other incompatible elements.
- **Anorthosite**: An igneous rock made up almost entirely of plagioclase feldspar (a sodium-calcium silicate). It is a light low density product of magma differentiation commonly floored by high density norite. Iron is not affliatated with anorthosite.

References

Agee, C. B. (1986). Pristine lunar glasses: criteria, data, and implication. *J. Geophys. Res. 91*, 210–213.

Agee, C. B. (1993). Introduction to the special section on magma oceans. *J. Geophys. Res. 98*, 5 317.

Agee, C. B. (1998). Crystal-liquid density inversions in terrestrial and lunar magmas. *Physics of the Earth and Planetary Interiors 107*, 63–74.

Alexopoulos, J. S. and W. B. McKinnon (1994). Large impact craters and basins on Venus, with implications for ring mechanics on the terrestrial planets. *Geological Society of America Special Paper 293*, 29–50.

Alley, K. M. and E. M. Parmentier (1998, February 17). Numerical experiments on the thermal convection in a chemically stratified viscous fluid heated from below: implications for a model of lunar evolution. *Physics of the Earth and Planetary Interiors 108*(E2), 15–32.

Anderson, D. L. (1998). The scales of mantle convection. *Tectonophysics 284*, 1–17.

Arkani-Hamed, J. (1998). The lunar mascons revisited. *J. Geophys. Res. 103*, 3 709–3 739.

Arkani-Hamed, J., A. S. Konopliv, and W. L. Sjogren (1999). On the equipotential surface hypothesis of the lunar maria floors. *J. Geophys. Res. 104*, 5 921–5 931.

Artyushkov, E. V. (1973). Stress in the lithosphere caused by crustal thickness inhomogeneities. *J. Geophys. Res. 78*, 7 675–7 708.

Baldwin, R. G. (1949). *The Face of the Moon*. Chicago: Univ. Chicago Press.

Baldwin, R. G. (1963). *The Measure of the Moon*. Chicago: Univ. Chicago Press.

Baldwin, R. G. (1972). The tsunami model of the origin of ring structures concentric with large lunar craters. *Phys. Earth Plan. Interiors 6*, 327–339.

Baldwin, R. G. (1974). On the origin of mare basins. In *Proc. 5th Lunar Sci. Conf.*, pp. 1–10.

Bell, J. and B. Hawke (1984). Lunar dark-haloed impact craters: Origin and implication for early mare volcanism. *J. Geophys. Res. 89*, 6 899–6 910.

Bills, B. G. (1989). The moments of inertia of Mars. *Geophys. Res. Lett. 16*, 358–388.

Bills, B. G. (1995). Discrepant estimates of moment of inertia of the Moon. *J. Geophys. Res. 100*(E12), 26 297–26 303.

Bills, B. G. and A. J. Ferrari (1977). A lunar density model consistent with topographic, gravitational, librational and seismic data. *J. Geophys. Res. 82*, 1 306–1 314.

Bills, B. G., W. S. Kiefer, and R. L. Jones (1987). Venus gravity; a harmonic analysis. *J. Geophys. Res. 92*(B10), 10 335–10 351.

Bills, B. G. and M. Kobrick (1985). Venus topography: A harmonic analysis topography. *J. Geophys. Res. 90*(B1), 827–836.

Bills, B. G. and Lemoine (1995). Gravitational and topographic isotropy of the Earth, Moon, Mars and Venus. *J. Geophys. Res. 100*(E12), 26 275–26 295.

Bills, B. G. and R. S. Nerem (1995). A harmonic analysis of Martian topography. *J. Geophys. Res. 100*(E12), 26 317–26 326.

Bills, B. G. and D. P. Rubincamp (1995). Constraints on density models from radial moments: Applications to Earth, Moon and Mars. *J. Geophys. Res. 100*(E12), 26 305–26 315.

Binder, A. (1980). Internal structure of a moon of fission origin. *J. Geophys. Res. 85*(B9), 4 872–4 880.

Binder, A. (1998). Lunar prospector: Overview. *Science 281*, 1 475–1 476.

Blakely, R. J. (1996). *Potential Theory in Gravity and Magnetics Applications*. United Kingdom: Cambridge University Press.

Blewett, D., P. Lucey, R. Hawke, and B. Joliff (1995). Clementine images of the lunar sample-return stations: Refinement of FeO and TiO_2 mapping techniques. *J. Geophys. Res. 102*(E7), 16 319–16 325.

Bowin, C. (1994). The geoid and deep earth mass anomaly structure. In P. Vanicek and N. Christou (Eds.), *Geoid and Its Geophysical Interpretations*, pp. 203–220. CRC Press, Ann Arbor.

Bowin, C., B. Simon, and W. R. Wollenhaupt (1975, February, 25). Mascons: A two-body solution. *J. Geophys. Res. 80*(E2), 4 955–4 964.

Boyce, J. M. (1976). Ages of flow units in the nearside lunar maria based on lunar orbiter iv photographs. In *Lunar Sci. Conf.*, Volume 7, pp. 2 717–2 728.

Bratt, S. R., S. C. Solomon, J. W. Head, and C. J. Thurber (1985). The deep structure of lunar basins: Implication of basin formation and modification. *J. Geophys. Res. 190*, 3 049–3 064.

Brown, W. E. J., e. a. (1974). Elevation profiles of the Moon. In *Proc. 5th Lunar Sci. Conf.*, pp. 3 037–3 048.

Budney, C. J. and P. G. Lucey (1998). Basalt thickness in Humorum: The crater excavation method. *J. Geophys. Res. 103*(E7), 16 855–16 870.

Burša, M. (1984). Secular Love numbers and hydrostatic equilibrium of planets. *Earth, Moon and Planets 31*, 135–140.

Burša, M. (1994). Distortions of the Moon's figure due to earth. *Earth, Moon and Planets 64*, 265–271.

Cattermole, P. (1996). *Planetary Volcanism: A Study of Volcanic Activity in the Solar System* (2nd ed.). New York: John Wiley and Sons, Inc. Series in Astronomy and Astrophysics.

Chadderton, L., F. Krajenbrink, R. Katz, and A. Poveda (1969). Standing waves on the Moon. *Nature 223*, 259.

Circone, S. and C. B. Agee (1996). Compressibility of molten high-ti: Evidence for crystal-liquid density inversions in the lunar magma. *Geochimica et Cosmochimica Acta 60*(14), 2 709–2 720.

Cisowski, S. M. and M. Fuller (1986). Lunar paleointensities via the IRMS normalization method and the early magnetic history of the Moon. In W. K. Hartmann, R. J. Phillips, and G. J. Taylor (Eds.), *Origin of the Moon*, pp. 411–424. Lunar and Planetary Institute, Houston Texas.

Conel, J. E. and G. B. Holstrom (1968). Lunar mascons: A near-surface interpretation. *Science 162*, 1 403–1 405.

Croft, S. K. (1980). Implications for the excavation and transient expansion stages of crater formation. In *Proc. 11th Lunar Planet. Sci. Conf.*, pp. 2 347–2 378.

Croft, S. K. (1981). The excavation stage of basin formation: A qualitative model. In R. B. Merrill and P. H. Schultz (Eds.), *Multi-Ring Basins: Proceeding of Lunar and Planetary Science V(12A)*, pp. 207–225. New York: Pergamom.

Davies, P. A. and A. Stephenson (1977). The ages of the lunar maria and the filling of the mare basins. *Phys. Earth Planet. Inter. 14*, P13–P16.

Davis, J. C. (1986). *Statistics and Data Analysis in Geology* (2-nd ed.). New York: Wiley and Sons.

Dehon, R. A. (1974). Thickness of mare material in the Tranquilitatis and Nectaris basins. In *Proc 5th Lunar Conference*, Volume I, pp. 53–59.

Dehon, R. A. (1977). Mare Humorum and mare Nubium: Basalt thickness and basin-forming history. In *8th Lunar Planet. Sci. Conf.*, pp. 633–641.

Dehon, R. A. (1979). Thickness of the western mare basalts. In *10th Lunar Planet. Sci. Conf.*, Volume VV, pp. 2 935–2 955.

Dehon, R. A. and J. D. Waskom (1976). Geologic structure of the eastern mare basins. In *Lunar Planet. Sci. Conf.*, Volume VII, pp. 2 729–2 746.

Delano, J. W. (1980). Chemistry and liquid phase relations of Apollo 15-red glass: implications for the lunar deep interior. In *Proc. 11th Lunar Planet. Sci. Conf.*, pp. 251–288.

Delano, J. W. (1990). Bouyancy-driven melt segregation in Earth's Moon: 1. In *Proc. 20th Lunar Planet. Sci. Conf.*, pp. 3–12.

Dorman, S. and C. Lewis (1970). *Experimental isostasy, 1, Theory of the determination of the Earth's isostatic response to a concentrated load*. New York: Wiley and Sons.

Dziewonski, A. M. (1984). Mapping the lower mantle: Determination of lateral heterogeneity in p velocity up to degree and order 6. *J. Geophys. Res. 89*, 5 929–5 952.

Esposito, P. B., W. B. Banderdt, G. F. Lindal, W. Sjorgen, M. A. Slade, B. G. Bills, D. E. Smith, and G. Balmino (1992). Gravity and topography. In H. H. Kieffer, B. M. Jakosky, C. W. Snyder, and M. S. Matthews (Eds.), *Mars*, pp. 209–248. Tucson: University of Arizona Press.

Ferrari, A. J., W. S. Sinclair, W. L. Sjogren, J. G. Williams, and C. F. Yoder (1980). Geophysical parameters of the Earth-Moon system. *J. Geophys. Res. 85*(B7), 3 939–3 951.

Floran, R. J. and M. R. Dence (1976). Morphology of the Manicouagan ring-structure, Qeubec, and some comparisons with lunar basins and craters. In *Proc. Lunar Sci. Conf. 7th*, pp. 2 845–2 865.

Gaddis, L. R., A. S. McEwen, and T. L. Becker (1995). Compositional variations on the Moon: Recalibration of Galileo solid-state imaging data for the Orientale region and farside. *J. Geophys. Res. 100*(E12), 26 345–26 356.

Goins, N. R., A. M. Dainty, and M. N. Toksöz (1981). Lunar seismology: The internal structure of the Moon. *J. Geophys. Res. 86*, 5 061–5 074.

Golombek, M. (1985, March, 10). Fault type predictions from stress distribution on planetary surfaces: Importance of fault initiation depth. *J. Geophys. Res. 90*(B4), 3 065–3 074.

Greeley, R. (1976). Modes of emplacement of basalt terrains and an analysis of mare volcanism in the Orientale basin. In *7th Lunar Planet. Sci. Conf.*, pp. 2 747–2 759.

Greeley, R., S. D. Kadel, D. A. Williams, L. R. Gaddis, J. W. Head, M. A., S. L. Murchie, E. Nagel, G. Neukem, C. M. Pieters, J. M. Sunshine, R. Wagner, and M. J. Belton (1993). Galileo imaging observations of lunar maria and related deposits. *J. Geophys. Res. 98*, 17 183–17 206.

Grieve, R. A. F. (1987). Terrestrial impact structures. *Ann. Rev. Earth Planet. Sci. 15*, 245–270.

Grieve, R. A. F. and M. J. Cintala (1997). Planetary differences in impact melting. *Adv. Space Res. 20*(8), 1 551–1 560.

Grieve, R. A. F., M. R. Dence, and P. B. Robertson (1977). Cratering processes: As interpreted from the occurrence of impact melts. In D. J. Roddy, R. D. Peppin, and R. B. Merrill (Eds.), *Impact and explosion cratering: Planetary and terrestrial implications*, pp. 791–814. New York: Pergamom.

Grieve, R. A. F., P. B. Robertson, and M. R. Dence (1980). Constraints on the formation of ring impact structures, based on terrestrial data. In R. B. Merrill and P. H. Schultz (Eds.), *Multi-Ring Basins: Proc. 12th Lunar Planet. Sci. Conf., Part A*, pp. 37–57. New York: Pergamom.

Hartmann, W. K. and G. P. Kuiper (1962). Concentric structures surrounding lunar basins. *Commun. Lunar Planetary Lab. 1*, 51–66.

Hartmann, W. K. and C. A. Wood (1971). Moon: Origin and evolution of multi-ring basins. *The Moon 3*, 3–78.

Haskin, L. A. (1998). The Imbrium impact event and the thorium distribution at the lunar highlands surface. *J. Geophys. Res. 103*, 1 679–1 690.

Head, J. W. (1974). Orientale multi-ringed basin interior and implications for the petrogenesis of lunar highland samples. *Moon 11*, 327–356.

Head, J. W. (1976). Lunar volcanism in space and time. *Rev. Geophys. 14*, 265–300.

Head, J. W. (1982). Lava flooding of ancient planetary crusts: Geometry, thickness, and volumes of flooded lunar impact basins. *Moon and Planets 26*, 61–88.

Head, J. W., S. Murchie, J. F. Mustard, G. Pieters, A. Neukum, R. McEwen, R. Greeley, and M. J. S. Belton (1993). Lunar impact basins: New data for the western limb and fraside (Orientale and South Pole-Aitken basins) from the first Galileo flyby. *J. Geophys. Res. 96*, 17 149–17 181.

Head, J. W., M. Settle, and R. S. Stein (1975). Volume of material ejected from major lunar basins and implications for the depth of excavation of lunar samples. In *Proc. 6th Lunar Sci. Conf.*, pp. 2 805–2 829.

Head, J. W. and S. C. Solomon (1981). Tectonics of terrestrial planets. *Science 213*, 62–76.

Heiskanen, W. A. and H. Moritz (1967). *Physical Geodesy*. Graz, Austria: Institute of Physical Geodesy.

Henkel, H. and W. U. Reimold (1998). Integrated geophysical modeling of a giant, complex impact structure: anatomy of the Vredefort structure, South Africa. *Tectonophysics 287*, 1–20.

Hess, P. C. (1991). Diapirism and the origin of high TiO_2 mare glasses. *Geophys. Res. Lett. 81*, 2 069–2 072.

Hide, R. and S. R. C. Malin (1970). Novel correlations between global features of the Earth's gravitational and magnetic fields. *Nature 225*, 605–609.

Hood, L. and J. H. Jones (1985). Lunar density models consistent with mantle seismic velocities and other geophysical constraints (abstract). In *Proc. 16th Lunar Planet. Sci. Conf.*, pp. 360–361. Lunar and Planetary Science Institute, USA.

Hood, L. and J. H. Jones (1987). Geophysical constraints on lunar bulk composition and structure: A reassessment. *J. Geophys. Res. 92*, E396–E410.

Hood, L. L. (1986). Geophysical constraints on the lunar interior. In W. K. Hartmann, R. J. Phillips, and G. J. Taylor (Eds.), *Origin of the Moon*, pp. 453–468. Lunar and Planetary Institute, Houston Texas.

Hörz, F. (1978). How thick are lunar mare basalts? In *Proc. 9th Lunar Planet. Sci. Conf.*, pp. 3 311–3 331.

Hubbard, W. B. (1984). *Planetary Interiors*. New York: Van Nostrand Rienhold Company.

Hubbard, W. B. (1999). Gravitational signature of Jupiter's deep zonal flows. *Icarus 135*, 357–359.

Jeffreys, H. (1924). *The Earth*. New York: Wiley-Interscience.

Johnson, G. G., V. Vand, and F. Dachille (1968). Additional rims around Ries Kessel meteorite crater. *Nature 201*, 592.

Joliff, B. L., J. J. Gillis, L. A. Haskin, R. L. Korotev, and M. A. Wieczorek (2000). Major lunar crustal terranes: Surface expressions and crust-mantle origins. *J. Geophys. Res. 105*(E2), 4 217–4 235.

Kaula, W. M. (1966). *Theory of Satellite Geodesy*. Waltham, Mass., Blaisdell.

Kaula, W. M. (1993). Higher order statistics of planetary gravities and topographies. *J. of Geophys. Res. 20*(23), 2 583–2 586.

Kiefer, W. S., B. G. Bills, and R. S. Nerem (1996). An inversion of gravity and topography for mantle and crustal structure on Mars. *J. Geophys. Res 101*, 9 239–9 252.

Kiefer, W. S., A. Richards, B. H. Hager, and B. G. Bills (1986). A dynamical model of Venus' gravity field. *Geophys. Res. Lett. 13*, 14–17.

Koch, K.-R. (1987). *Parameter Estimation and Hypothesis Testing in Linear Models*. New York, Springer-Verlag.

Konopliv, A. S., A. B. Binder, L. L. Hood, A. B. Kucinskas, W. L. Sjorgen, and J. G. Williams (1998). Improved gravity field of the Moon from lunar prospector. *Science 281*, 1 476–1 480.

Konopliv, A. S. and W. L. Sjogren (1994). Venus spherical harmonic gravity model to degree and order 60. *Icarus 112*, 42–54.

Konrad, W. and T. Spohn (1997, 12). Thermal history of the Moon: Implication for an early core dynamo and post-accretional magmatism. *Adv. Space Res. 19*(10), 1 511–1 521.

Kopal, Z. (1972). Moments of inertia of the lunar globe, and their bearing on chemical differentiation of its outer layers. *The Moon 4*, 448–454.

Kopal, Z. (1978). *Dynamics of Close Binary Systems*. Dordrecht: D. Reidel Publishing Company.

Korotev, R. (2000). The great lunar hot spot and the composition and origin of the apollo mafic ("LFKM") impact-melt breccias. *J. Geophys. Res. 105*(E2), 4 317–4 346.

Kucinskas, A. and D. Turcotte (1994). Isostatic compensation of equatorial highlands on Venus. *Icarus 112*, 104–116.

Lambeck, K. and S. Pullan (1980). The lunar fossil bulge revisited. *Phys. Earth Planet. Inter. 22*, 29–35.

Langel, R. A., E. V. Slud, and P. J. Smith (1984). Reduction of satellite magnetic anomaly data. *J. Geophys. 541*, 207–212.

Lawson, R. L. and R. J. Hanson (1974). *Solving Least Squares Problems*. Englewood Cliffs, N. J., Prentice-Hall, Inc.

Lemoine, F., D. Smith, M. Zuber, G. Neumann, and D. Rowland (1997). A 70th degree lunar gravity model (GLGM-2) from Clementine and other tracking data. *J. Geophys. Res. 90*, 16 339–16 359.

Lenardic, A., W. M. Kaula, and D. L. Bindschadler (1993). A mechanism for crustal recycling on Venus. *J. Geophys. Res. 98*, 18 697–18 708.

Lucey, P., G. Taylor, and E. Malaret (1995). Abundance and distribution of iron on the Moon. *Science 268*, 1 150–1 153.

Lucius, J. E. and R. B. B. von Frese (1988). Aeromagnetic and gravity anomaly constraints on the crustal geology of Ohio. *Geol. Soc. America Bull. 100*, 104–116.

Mason, B. and W. G. Melson (1970). *The Lunar Rocks*. New York, Wiley-Interscience.

Matsumoto, K., K. Heki, and D. D. Rowlands (1999). Impact of far-side satellite tracking on gravity estimation in the selene project. *Adv. Space Res. 23*(11), 1 809–1 812.

Melosh, H. J. (1982). A schematic model of crater modification by gravity. *J. Geophys. Res. 87*, 371–380.

Melosh, H. J. and W. B. McKinnon (1978). The mechanics of ringed basin formation. *Geophys. Res. Lett. 5*, 985–986.

Melosh, J. H. (1989). *Impact Cratering: A Geologic Process*. New York, NY, USA, Oxford University Press.

Mikhail, E. and F. Ackerman (1976). *Observations and Least Squares*. New York, University Press of America.

Moore, P. (1981). *The Moon*. New York, Rand McNally and Co.

Morelli, A. and A. M. Dziewonski (1987). Thermal evolution of Earth and Moon growing by planetesimal impacts. *Nature 325*, 678–683.

Moritz, H. (1989). *Advanced Physical Geodesy*. Karlsruhe, Wichmann.

Morse, S. A. (1993). Behaviour of a perched crystal layer in a magma ocean. *J. of Geophys. Res. 98*(E3), 5 347–5 353.

Muller, P. M. and W. L. Sjogren (1968). Mascons: Lunar mass concentrations. *Science 161*, 680–684.

Munk, W. H. and G. J. F. MacDonald (1960). *The Rotation of the Earth: A Geophysical Discussion*. New York, Cambridge University Press.

Murray, J. B. (1980). Oscillating peak model of basin and crater formation. *Moon and Planets 22*, 269–291.

Murtaugh, J. G. (1972). Shock metamorphism in the Manicouagan crypto-explosion structure. In *Proc. 24th Geol. Congr., Sect. 15*, pp. 133–139.

Naidu, P. S. and M. P. Mathew (1998). Analysis of geophysical potential fields: A digital signal processing approach. In A. J. Berkhout (Ed.), *Advances in Exploration Geophysics*, Volume 5. Elsevier.

Nakamura, Y. (1983). Seismic velocity structure of the lunar mantle. *J. Geophys. Res. 88*(B1), 677–686.

Nakamura, Y., G. Latham, and H. J. Dorman (1982). Apollo lunar seismic experiment: Final summary. In *Proc. 13th Lunar Planet. Sci. Conf.*, pp. 117–123.

Nakamura, Y., G. V. Latham, H. J. Dorman, A. K. Ibrahim, J. Koyama, and P. Horvath (1979). Shallow moonquakes: Depth, distribution and implications as to the present state of the lunar interior. In *Proc. 10th Lunar Planet. Sci. Conf.*, pp. 2 299.

Neumann, G. A., M. T. Zuber, D. E. Smith, and F. G. Lemoine (1996). The lunar crust: Global structure and signature of major basins. *J. Geophys. Res. 101*(E7), 16 841–16 843.

Nozette, S., D. E. Smith, and F. G. Lemoine (1996). The Clementine mission to the Moon: Scientific overview. *Science 266*, 1 835–1 838.

O'Keefe, J. D. (1968). Isostacy on the Moon. *Science 261*, 1405–1406.

O'Keefe, J. D. and T. J. Ahrens (1993). Planetary cratering mechanics. *J. Geophys. Res. 98*, 17011–17028.

Pavlis, N. K. and R. H. Rapp (1990). The development of a isostatic gravitational model to degree 360 and its use in global gravity modeling. *Geophys. J. Int. 100*, 369–378.

Phillips, R. J., J. E. Conel, E. A. Abbott, J. B. Sjogren, and J. B. Morton (1972). Mascons: Progress toward a unique solution for mass distribution. *Science 77*, 7 106–7 112.

Pieters, C., G. He, and S. Thompkins (1996). Anorthosite and olivine layers of the farside upper crust at tsiolkovsky. In *Proc. 27th Lunar Planet. Sci. Conf.*, Volume XXVII, pp. 1 035–1 036. Abstracts.

Pieters, C. M., J. W. Head, J. M. Sunshine, E. M. Fischer, S. L. Murchie, M. Belton, A. McEwen, L. Gaddis, R. Greely, G. Neukem, R. Jaumann, and H. Hoffmann (1993). Crustal diversity of the Moon: Compositional analyses of galileo solid state imaging data. *J. Geophys. Res. 98*(E9), 17 127–17 148.

Pike, R. A. (1974). Depth/diameter relations of fresh lunar craters: Revision from spacecraft data. *Geophys. Res. Lett. 1*, 291–294.

Rapp, R. (1989). The decay of the spectrum of the gravitational potential and the topography of the Earth. *Geophys. J. Int. 99*, 449–455.

Rapp, R. (1994). Global geoid determination. In P. Vanicek and N. Christou (Eds.), *Geoid and Its Geophysical Interpretations*, pp. 57–76. CRC Press, Ann Arbor.

Rapp, R. H. and N. K. Pavlis (1990). The development and analysis of geopotential coefficient models to spherical harmonic degree 360. *J. Geophys. Res. 95*, 21 885–21 911.

Rappaport, N. and J. J. Plaut (1994). A 360-degree and order model of Venus topography. *Icarus 112*, 27–33.

Ridgway, J. R. and W. J. Hinze (1986). Magsat scalar anomaly map of South America. *Geophysics 51*, 1 472–1 479.

Righter, K. and M. J. Drake (1996). Core formation in the Earth's Moon, Mars and Vesta. *Icarus 124*, 513–519.

Rubin, A. E. (1997). A history of the mesosiderite asteroid. *American Scientist 41*, 26–35.

Rukl, A. (1976). *A concise Guide in Colour: Moon, Mars and Venus*. New York, Hamlyn.

Runcorn, S. K. (1974). On the origin of mascons and moonquakes. In *Proc. 5th Lunar Planet. Sci. Conf.*, Volume V, pp. 3115–3126.

Runcorn, S. K. (1996). The formation of the lunar core. *Geochimica et Cosmochimica Acta 60*(7), 1 205–1 208.

Runcorn, S. K., D. W. Collinson, W. O'Reilly, M. H. Battey, A. Stephenson, J. M. Jones, A. J. Manson, and P. W. Readman (1970). Magnetic properties of Apollo 11 lunar samples. In *Apollo 11 Lunar Sci. Conf.*, pp. 2 369–2 387. Lunar and Planetary Institute, Houston Texas.

Russell, C. T., P. J. Coleman (Jr), and B. E. Goldstein (1981). Measurements of the lunar induced magnetic moment in the geomagnetic tail: Evidence for a lunar core. In *Proc. 12th Lunar Planet. Sci. Conf., Part B*, pp. 831–836. Lunar and Planetary Institute, Houston Texas.

Short, N. M. (1975). *Planetary Geology*. New Jersey: Prentice Hall, Inc.

Sjogren, W. L. (1977). Lunar gravity determinations and their implications. In *Philos. Trans. R. Soc. London, Ser. A*, Volume 285, pp. 219–226.

Sjogren, W. L. and J. C. Smith (1976). Quantitative mass distribution models for mare Orientale. In *Proc. 7th Lunar Sci. Conf.*, pp. 2 639–2 648.

Sjogren, W. L. and W. R. Wollenhaupt (1973). Lunar shape via the Apollo laser altimeter. *Science 179*, 275–278.

Sjogren, W. L. and W. R. Wollenhaupt (1976). Lunar global figures from mare surface elevations. *Moon 15*, 143–154.

Smith, D. E., J. F. Lerch, S. R. Nerem, M. T. Zuber, G. B. Patel, S. K. Fricke, and F. G. Lemoine (1993). An improved gravity model for Mars: Goddard mars model 1. *J. Geophys. Res. 98*, 20 871–20 890.

Smith, D. E., M. T. Zuber, G. A. Neumann, and F. G. Lemoine (1997). Topography of the Moon from the Clementine lidar. *J. Geophys. Res. 102*(E1), 1 591–1 611.

Smith, J. R. and C. B. Agee (1997). Compressibility of molten "green glass" and the crystal-liquid density crossover in low-Ti lunar magma. *Geochimica et Cosmochimica Acta 61*(10), 2 139–2 145.

Smith, W. H. F. and P. Wessel (1990). Gridding with continuous curvature splines in tension. *Geophysics 55*, 293–305.

Solomon, S. C. (1975). Mare volcanism and lunar crustal structure. In *Lunar and Planetary Science Conference*, Volume VI, pp. 1 021–1 042.

Solomon, S. C., R. P. Comer, and J. W. Head (1982). The evolution of impact basins: Viscous relaxation of topographic relief. *J. Geophys. Res. 87*, 3 975–4 000.

Solomon, S. C. and J. W. Head (1979). Vertical movement in mare basins: Relation to mare emplacement, basic tectonics and thermal history. *J. Geophys. Res., 84*, 1 667–1 682.

Solomon, S. C. and J. W. Head (1980). Lunar mascon basins: Lava filling, tectonics and evolution of the lithosphere. *Rev. Geophys. Space Phys. 18*, 107–141.

Sonnet, C. P., D. S. Colburn, P. Dyal, C. W. Parkin, B. F. Smith, G. K. Schubert, and K. Schwartz (1971). Lunar electrical conductivity profile. *Nature 230*, 359–362.

Spudis, P. (1993). *The geology of multi-ring impact basins: The Moon and other planets*. New York, NY, USA, Cambridge University Press.

Spudis, P. D. (1982). Orientale basin ejecta: Depths of derivation and implications for basin-forming process (abstract). In *Proc. 13th Lunar Planet. Sci. Conf.*, pp. 760–761.

Spudis, P. D. (1983). The excavation of the multi-ringed basins: Additional results for the four nearside basins (abstract). In *Proc. 14th Lunar Planet. Sci. Conf.*, pp. 735–736.

Spudis, P. D., B. R. Hawke, and P. Lucey (1984). Composition of orientale basin deposits and implications for the lunar basin-forming process. *J. Geophys. Res. 89*(Suppl.), C197–C210.

Stacey, F. D. (1969). *Physics of the Earth*. New York, John Wiley & Sons. Inc.

Stevenson, D. J. (1980). Lunar asymmetry and palaeomagnetism. *Nature 287*, 520–521.

Stipe, J. G. (1968). Iron meteorites as mascons. *Science 162*, 1 402–1 403.

Stroud, A. H. and D. Secrest (1966). *Gaussian Quadrature Formulas*. Englewood Cliffs, N. J., Prentice-Hall.

Taylor, S. T. (1982). *Planetary Science: A Lunar Perspective*. Houston, Texas: Lunar and Planetary Science Institute.

Thurber, C. H. and S. C. Solomon (1978). An assesment of crustal thickness variations on the nearside: Models, uncertainties and implications for crustal differentiation. In *Proc. 9th Lunar Planet. Sci. Conf.*, pp. 3 418–3 497.

Toksöz, M. N., A. M. Dainty, S. C. Solomon, and A. K. R. (1974). Structure of the Moon. *Rev. Geophys. Space. Phys. 12*, 539–567.

Torge, W. (1989). *Gravimetry*. Berlin, New York, de Gruter.

Turcotte, D. L. (1996, February, 25). Magellan and comparative planetology. *J. Geophys. Res. 101*(E2), 4 765–4 773.

Turner, J. S. (1986). Turbulent entrainment: The development of entrainment assumption, and its application to geophysical flows. *J. Fluid Mech. 173*, 431–471.

Van Dorn, W. G. (1968). Tsnumamis on the Moon? *Nature 220*, 1102.

Van Dorn, W. G. (1969). Lunar maria: Structure and evolution. *Science 165*, 693.

von Frese, R., L. Potts, L. Tan, J. W. Kim, T. E. Leftwich, C. J. Merry, and J. Bossler (1998). Comparative crustal modeling of the Moon and Earth from topographic and gravity correlations. In *29th Lunar Planet. Sci. Conf.* Abstract # 1870, (CDROM).

von Frese, R. R. B., W. J. Hinze, L. W. Braile, and A. J. Luca (1981). Spherical earth gravity and magnetic anomaly modeling using gauss-legendre quadrature integration. *J. Geophysics 49*, 234–242.

von Frese, R. R. B., M. B. Jones, J. W. Kim, and W. Li (1997). Spectral correlation of magnetic and gravity anomalies of ohio. *Geophys 62*(1), 365–380.

von Frese, R. R. B., J. W. Kim, and J. Kim (1997). Analysis of anomaly correlations. *Geophys 62*(1), 342–351.

von Frese, R. R. B., D. N. Ravat, W. J. Hinze, and C. A. McGue (1988). Improved inversion of geopotential field anomalies for lithopsheric investigations. *Geophysics 53*(3), 375–385.

Warren, P. H. (1993). The magma ocean as an impediment to lunar plate tectonics. *J. Geophys. Res. 98*(E3), 5 335–5 345.

Whitaker, E. A. (1981). The lunar Procellarum basin, in multi-ring basins. In *Proc. Lunar Planet. Sci. 12A*, pp. 105–111.

Wichman, R. W. and P. Schultz (1995). Floor-fractures craters in mare Smythii and west of Oceanus Procellarum: Implication of crater modification by viscous relaxation and igneous intrusion models. *J. Geophys.Res. E10*, 21 201–21 218.

Wieczorek, M. A. and R. J. Phillips (1997). The structure and compensation the lunar highland crust. *J. Geophys. Res. 102*(E5), 10 933–10 943.

Wieczorek, M. A. and R. J. Phillips (1998). Potential anomalies on a sphere: Applications to the thickness of the lunar crust. *J. Geophys. Res. 103*(E1), 1 715–1 724.

Wieczorek, M. A. and R. J. Phillips (1999). Lunar multi-rings basins and the cratering process. *Icarus 139*, 246–259.

Wilhelms, D. E. (1987). The geologic history of the Moon. *USGS Professional Paper 1348*, 1–302.

Williams, K. K. and M. T. Zuber (1998). Re-evaluation of mare thicknesses based on lunar crater depth-diameter relationship. *Icarus 103*(E1), 1 715–1 724.

Wise, D. U. and M. T. Yates (1970). Mascons as structural relief on a lunar "moho". *J. Geophys. Res. 75*, 261–268.

Wollenhaupt, W. R., R. K. Osburn, and G. A. Ransford (1972). Comments on the figure of the Moon from Apollo landmark tracking. *Moon 5*, 149–157.

Yingst, R. A. and J. W. Head III (1998). Characteristics of lunar mare deposits in Smythii and Marginis basins: Implication for magma transport mechanisms. *J. Geophys. Res. 103*(E5), 11 135–11 158.

Yoder, C. F. (1981). The free librations of a dissipative moon. *Phil. Trans. Roy. Soc. London A-303*, 327–338.

Zhang, C. Z. (1994). A note on the physical parameters of the Moon. *Earth, Moon and Planets 64*, 31–38.

Zhang, C. Z. (1997). A comparison between Venus and the Earth. *Earth, Moon and Planets 75*, 135–139.

Zuber, M. T., D. E. Smith, F. G. Lemoine, and G. A. Newmann (1994). The shape and internal structure of the Moon from the Clementine mission. *Science 266*, 1 839–1 843.